

# **Time-dependent Behaviour of Cracked Steel Fibre Reinforced Concrete:**

from Single Fibre Level to Macroscopic Level

by

**Pieter Daniel Nieuwoudt**



Dissertation presented for the degree of  
**Doctor of Philosophy in Engineering**  
At the Stellenbosch University

Promotor: Prof. W.P. Boshoff  
Department of Civil Engineering

March 2016

# DECLARATION

By submitting this dissertation electronically, I declare that the entity of the work contained therein is my own, original work, that I am the authorship owner thereof (unless to the extent explicitly otherwise stated) and that I have not previously in part submitted it for obtaining any qualification.

Date: March 2016

Copyright © 2016 Stellenbosch University  
All rights reserved

# ABSTRACT

The addition of steel fibres to a concrete matrix is known to improve the material's post crack mechanical behaviour under short term loading conditions. However, limited information is available on the material's post-crack behaviour under long-term loading, particularly under sustained uni-axial tensile loading.

The purpose of this research study is to investigate and quantify the time-dependent Crack Mouth Opening Displacement (CMOD) behaviour of cracked Steel Fibre Reinforced Concrete (SFRC) under sustained uni-axial tensile loading, and to develop a mathematical model which is able to simulate the time-dependent crack width opening behaviour of cracked SFRC under sustained uni-axial tensile loading.

To reach this goal, experimental investigations were performed at two levels, namely macroscopic level and single fibre level. At the macroscopic level, the short term mechanical properties of SFRC were investigated by performing compressive and uni-axial tensile strength tests. To investigate the long term mechanical properties of cracked SFRC, sustained uni-axial tensile load tests were performed at stress levels ranging from 30 % to 85 % of the residual tensile strength. To understand the mechanisms causing the time-dependent CMOD as well as the factors that can influence the behaviour, single fibre pull-out rate tests and single fibre sustained load tests were performed on hooked-end steel fibres.

The SFRC showed significant toughness and energy absorption capacity after cracking, both under compression and uni-axial tensile loading. The sustained uni-axial tensile load results showed that the time-dependent CMOD increases with the applied sustained stress level. Over the measured time period of 240 days none of the tested specimens fractured even for stress levels as high as 85 % of the residual tensile strength. Significant variability was found in the results at each load level and it was concluded that the variation in the crack plane fibre count for each specimen is one possible reason for the variability at each load level.

The single fibre pull-out rate results showed significant rate sensitivity for the slip at maximum pull-out force. This rate effect is induced by the interface between the hooked-end

of the fibre and the surrounding matrix. The fibre embedment inclination angle and the geometry of the mechanical hooked-end of the fibre have been found to significantly affect the pull-out behaviour. The single fibre sustained load results showed that the pull-out due to a sustained load is dependent on the applied load level. The pull-out due to a sustained load is referred to as pull-out creep and is defined as the relative movement between the fibre and the matrix interface under sustained loading. It is found that the pull-out creep is induced by the localised compression of the surrounding matrix by the hooked-end of the fibre. The mechanisms responsible for the pull-out creep are therefore believed to be similar as the creep for bulk normal concrete under compression.

A constitutive model was developed based on the theory of rheology to simulate the single fibre pull-out creep behaviour of an aligned hooked-end steel fibre. The model was then generalised to simulate the CMOD of cracked SFRC under sustained uni-axial tensile loading by assuming a uniform fibre distribution over the crack plane. It was found that the orientation of the fibres at the crack plane was a relevant factor that affects the time-dependent CMOD. The generalised model was able to simulate the CMOD under various applied sustained stress levels (30 % to 85 %) with relative high accuracy.



# OPSOMMING

Dit is wel bekend dat die byvoeging van staalvesels by 'n betonmengsel die meganiese gedrag van gekraakte beton verbeter. Die informasie beskikbaar oor die langtermyn gedrag van gekraakte staalvesel beton is beperk, veral onder volgehoue eenassige trekbelasting.

Die doel van hierdie navorsingstudie is om die tydafhanklike kraakwydte verplasings gedrag van Staalvesel Versterkte Beton (SVVB) te ondersoek en te kwantifiseer, asook om 'n wiskundige model te ontwikkel wat die tydafhanklike kraakwydte verplasings gedrag van SVVB kan simuleer onder volgehoue eenassige trekbelasting.

Om die doelwit te bereik, is eksperimentele ondersoeke uitgevoer op twee vlakke, naamlik makroskopiese vlakke en enkelvesel vlakke. Vir die makroskopiese vlak is korttermyn meganiese eienskappe van Vesel Versterkte Beton (VVB) ondersoek deur die uitvoering van drukkrag en eenassige trekkrag toetse. Die langtermyn meganiese eienskappe van gekraakte SVVB is ondersoek deur volgehoue eenassige trek toetse te doen met spanningsvlakke wat wissel van 30% tot 85% van die oorgeblewe trekkrag. Om die meganismes wat die tydafhanklike kraakwydte verplasing en die faktore wat die gedrag kan beïnvloed te verstaan, is enkelvesel uittrek snelheid toetse en enkelvesel volgehoue belasting toetse uitgevoer op staalvesels met haakvormige ente.

Die SVVB het beduidende sterkte en energie absorpsie vermoë getoon, beide onder kompressie sowel as onder eenassige trekbelasting. Die volgehoue eenassige trekbelasting resultate het getoon dat die tydafhanklike kraakwydte verplasing vergroot met die aangewende volgehoue spanningsvlak. Oor die toetsperiode van 240 dae het geen van die proefstukke gebreek nie, selfs nie eens vir spanningsvlakke so hoog as 85% van die oorgeblewe trekkrag sterkte nie. 'n Duidelike variasie in die resultate vir elke spanningsvlak is opgemerk en die gevolgtrekking is gemaak dat die variasie in die hoeveelheid vesels wat getel is op die kraakvlak een moontlike rede vir die variasie vir elke spanningsvlak is.

Enkelvesel uittrek snelheid resultate het beduidende snelheid sensitiwiteit getoon vir die glip wat ooreenstem met die maksimum uittrekkrag. Die snelheid effek word veroorsaak deur die

raakvlak tussen die haakvormige ent van die vesel en die omringende betonmatriks. Daar is gevind dat die hoek waarteen die vesel ingegiet is en die geometrie van die vesels se haakvormige ente die uittrek gedrag beduidend beïnvloed. Die enkelvesel volgehoue belasting resultate het getoon dat die veseluittrek as gevolg van die volgehoue belasting afhanklik is van die aangewende spanningsvlak. Die veseluittrek onder volgehoue belasting word na verwys as die uittrek kruipgang, en omskryf as die relatiewe beweging tussen die vesel en die matriks raakvlak onder volgehoue belasting. Dit is bevind dat die uittrek kruipgang veroorsaak word deur die lokale druk van die omringende betonmatriks deur die haakvormige ente van die vesel. Die meganismes verantwoordelik vir die uittrek kruipgang word daarom aangeneem om dieselfde te wees as die kruipgang vir normale massa beton onder kompressie.

'n Konstituerende model is ontwikkel wat gebaseer is op die teorie van reologie om die enkelvesel uittrek kruipgang gedrag van staalvesels met haakvormige ente te simuleer. Die model is veralgemeen om die kraakwydte verplasing van gekraakte SVVD onder volgehoue eenassige trekbelasting te simuleer deur aan te neem dat die vesels eweredig verspreid is oor die kraakvlak. Daar is bevind dat die oriëntasie van die vesels by die kraakvlak 'n relevante faktor is wat die tydsafhanklike kraakwydte verplasing beïnvloed. Die veralgemeende model simuleer die kraakwydte verplasing onder verskeie toegepaste volgehoue spanningsvlakke (30% tot 85%) met relatiewe hoë akkuraatheid.

# ACKNOWLEDGEMENTS

I would like to thank the following people for their assistance and support,

- Prof. W.P. Boshoff, my supervisor for his guidance and support. His broad knowledge on fibre reinforced concrete helped me to understand the concepts and the identification of problems.
- My family and friends for their continuous support throughout this dissertation.
- The staff of the Civil Engineering Department laboratory at Stellenbosch University.

# NOTATIONS AND SYMBOLS

## ABBREVIATIONS

---

1D, 2D, 3D	One, two and three-dimensions
CH	Calcium-hydroxide
CMOD	Crack mouth opening displacement
CoV	Coefficient of variation
C-S-H	Calcium silica hydrate
CSIR	Council for Scientific and Industrial Research
CT	Computed Tomography
FA	Fly ash
<i>fib</i>	Fédération Internationale du Béton
FM	Finess modulus
FPZ	Fracture process zone
FRC	Fibre reinforce concrete
GCM	Generalised constitutive model
GFRP	Glass fibre reinforced polymer
GGBS	Ground granulated blastfurnace slag
ITZ	Interfacial transition zone
LVDT	Linear variable displacement transducer
NA	Neutral axis
OGCM	Oriented generalised constitutive model
PVA	Polyvinyl alcohol fibres
SCC	Self-compacting concrete
SE	Scanning electron
SF	Silica fume
SFRC	Steel fibre reinforced concrete
SFRSCC	Steel fibre reinforced self-compacting concrete
SRC	Steel reinforced concrete
UHPC	Ultr-high performance concrete

## SYMBOLS

**Chapter 2: Mechanical and Time-dependent Behaviour of SFRC**

$C$	Unhydrated cement	–
$\delta$	Displacement	mm
$d_f$	Fibre cross-sectional diameter	mm
$\Delta\sigma_i$	Stress relaxation magnitudes	N/mm <sup>2</sup>
$\varepsilon$	Strain	–
$\varepsilon_{bc}$	Measured basic creep	–
$\varepsilon_{dc}$	Drying creep	–
$\varepsilon_{fs}$	Drying shrinkage	–
$\varepsilon_{tot}$	Total measured creep strain	–
$H_y$	Hydration products	–
$l_f$	Fibre length	mm
$\eta$	Limit of proportionality under sustained loading	–
$P$	Total pull-out force	N
$P_x$	Force component on the x-axis	N
$\sigma$	Stress	N/mm <sup>2</sup>
$\sigma_{cr}$	First cracking strength	N/mm <sup>2</sup>
$\sigma_{ut}^1$	Maximum post crack strength (Strain softening behaviour)	N/mm <sup>2</sup>
$\sigma_{ut}^2$	Maximum post crack strength (Strain hardening behaviour)	N/mm <sup>2</sup>
$t_i$	Loading age's	days
$\tau$	Interfacial toughness	N/mm <sup>2</sup>
$V$	Voids generated by hydration	–
$V_{cr}$	Critical fibre volume	–
$V_f$	Volumetric fibre fraction	–
$w$	Crack width	mm
$W$	Unhydrated water	–

**Chapter 3: Mechanical and Time-dependent Behaviour of SFRC**

$d_f$	Fibre diameter	mm
$\dot{\Delta}$	Single fibre pull-out rate	mm/s
$l_b$	Fibre embedment length	mm
$l_f$	Fibre length	mm
$L_0$	Pull-out length immediately after application of sustained load	mm
$L_n$	Pull-out length at time step $n$	mm

$n$	Time steps between the measurement of pull-out creep	days
$\theta$	Fibre embedment inclination angle	°
$V_f$	Fibre volume fraction	–

## Chapter 4: Mechanical and Time-dependent Behaviour of SFRC on a Macroscopic Level

$CMOD_{inst}$	Instantaneous crack mouth opening displacement	mm
$CMOD_{irr}$	Irrecoverable crack mouth opening displacement	mm
$CMOD_{sus}$	Crack mouth opening displacement due to the applied sustained load	mm
$CMOD_{tot}$	Total time-dependent crack mouth opening displacement	mm
$A_c$	Cross-sectional area of compressive test specimen's	mm <sup>2</sup>
$\delta_{sh}$	Measured drying shrinkage displacement	mm
$\delta_u$	The deformation corresponding to $\sigma_u$	mm
$\dot{\Delta}$	Single fibre pull-out loading rate	mm/s
$\bar{e}$	Normalised error	–
$\varepsilon_{exp}$	Experimental shrinkage strain	–
$\varepsilon_{model}$	Predicted shrinkage strain	–
$f_{cm}$	Compressive strength	mm <sup>2</sup>
$L_{gauge}^{shrinkage}$	Gauge length over which the drying shrinkage were measured	mm
$L_{gauge}^{pre-cracked}$	Gauge length of pre-cracked sustained load specimen's	mm
$\bar{\eta}$	Equivalent real applied load level	%
$N_f$	Crack plane fibre count	–
$P$	Compressive crushing load	N
$\sigma$	Stress	N/mm <sup>2</sup>
$\sigma_r$	Residual strength after the post-peak drop	N/mm <sup>2</sup>
$\sigma_{r,max}$	Maximum post-crack strength	N/mm <sup>2</sup>
$\sigma_{sus}^{Theoretical}$	Theoretical applied sustained load	MPa
$\sigma_{sus}^{Real}$	Real applied sustained load	MPa
$\sigma_u$	Ultimate strength of the matrix under uni-axial tensile loading	N/mm <sup>2</sup>
$w$	Crack width opening	mm
$w_r$	The deformation corresponding to $\sigma_r$	mm
$w_{r,max}$	The deformation corresponding to $\sigma_u$	mm
$\gamma(t)$	Coefficient of $CMOD_{sus}$	–

## Chapter 5: Mechanical and Time-dependent Behaviour on a Single Fibre Level

$\delta_{creep}$	Single fibre pull-out creep	mm
$\delta_{inst}$	Instantaneous pull-out during application of sustained load	mm
$G_{1mm}$	Pull-out energy up to a slip of 1 mm	N.mm
$G_{max}$	Average pull-out energy at maximum pull-out force	N.mm
$l_b$	Fibre embedment length	mm
$N_{max}$	Average maximum pull-out force	N
$S_{max}$	Average slip at maximum pull-out force	mm
$t$	Generic time instances	days
$\theta$	Fibre embedment inclination angle	°
$\gamma_{creep}(t)$	Coefficient of pull-out creep	–

## Chapter 6: Predicting the Single Fibre Pull-out Creep Behaviour

$\alpha$	Parameter describing the pre-peak branch of bond stress-slip response	–
$s_1, \alpha'$	Parameters describing the post-peak branch of the bond stress-slip response	–
$A, B$	Parameters describing the non-linear pull-out creep behaviour	–
$A_f$	Cross-sectional area	mm <sup>2</sup>
$A_{exp}$	Area under the experimental force-slip graph	mm <sup>2</sup>
$A_{num}$	Area under the numerical force-slip graph	mm <sup>2</sup>
$\Delta_{max,s}$	Total simulated pull-out creep at maximum pull-out force	mm
$\bar{e}$	Normalised error	–
$E_f$	Young's modulus	MPa
$\varepsilon_f(x)$	Fibre strain	–
$H_1, H_2$	History variables	–
$k$	Spring stiffness	N/mm
$N$	Numeric force entity	N
$\eta$	Non-linear pull-out creep load ratio	–
$N_1$	Applied sustained load	N
$\bar{N}$	Pull-out force data captured during pull-out test	N
$N_{dashpot}$	Dashpot force	N
$N(x)$	Axial force	N
$\bar{N}_{max}$	Experimental maximum pull-out force	N
$N_{sp}$	Mechanical bond component	N
$N_{spring}$	Spring force	N

$N_u$	Maximum pull-out force	N
$P_f$	Cross-sectional perimeter of fibre	mm
$s$	Generalised Kelvin-Voigt Displacement	mm
$s_{model}$	Modelled pull-out creep	mm
$s_{exp}$	Experimental pull-out creep	mm
$s_m$	Slip corresponding to the bond strength	mm
$\bar{s}_{max}$	Slip corresponding to $\bar{N}_{max}$	mm
$s(x)$	Slip along fibre bond length	mm
$s_{max}$	Slip at maximum pull-out force	mm
$s_{max,static}$	Simulated slip at maximum pull-out force	mm
$s_{max,exp}$	Average experimental slip at maximum pull-out force	mm
$s_{max,sim}$	Average simulated slip at maximum pull-out force	mm
$t_i$	Time increments	s
$\tau$	Retardation time	days
$\tau(x)$	Bond shear stress between fibre and matrix	MPa
$\tau(s)$	Bond stress-slip relationship	MPa
$\tau_m$	Bond strength	MPa
$\varphi$	Non-linear factor	–
$\varphi_{exp}$	Non-linear factor	–
$\varphi_{predicted}$	Non-linear factor	–
$\nu$	Viscosity	N.s/mm

## Chapter 7: Predicting the Macroscopic Time-dependent crack Mouth Opening Displacement

$A_f$	Cross-sectional area of a single fibre	mm <sup>2</sup>
$A_{sec}, A_c$	Area of cracked section	mm <sup>2</sup>
$\alpha$	Orientation factor	–
$CMOD_{sus}(t)$	Simulated crack mouth opening displacement due to sustained load	mm
$CMOD_{sus}^{model}$	Modelled $CMOD_{sus}$	mm
$CMOD_{sus}^{exp}$	Average experimental $CMOD_{sus}$	mm
$\bar{e}$	Normalised error	–
$\zeta$	Pull-out force factor	–
$k$	Spring stiffness	N/mm
$l_f$	Fibre embedment length	mm
$N$	Load carried by each fibre bridging the crack	N



$N_f$	Crack plane fibre count	–
$N_{max,\theta}$	Maximum pull-out force of a inclined fibre	N
$N_{max,0^\circ}$	Maximum pull-out force of a aligned fibre	N
$\bar{\eta}$	Equivalent real applied load level	%
$P$	Applied sustained load over the crack plane	N
$s_{creep}$	Single fibre pull-out creep	mm
$\sigma$	Applied sustained load	N/mm <sup>2</sup>
$\sigma_r$	Average residual strength	N/mm <sup>2</sup>
$t$	Generic time instances	days
$\tau$	Retardation time	days
$\theta$	Fibre orientation angle	°
$V_f$	Volumetric fibre fraction	–
$w_{creep}$	Crack width opening due to pull-out creep of a single aligned fibre	mm
$w_{creep,\theta}$	Crack width opening due to pull-out creep of a oriented fibre	mm

# Table of Contents

<b>Chapter 1: Introduction.....</b>	<b>1</b>
1.1 Statement of the Research Problem .....	2
1.2 Justification of this Research Study .....	3
1.3 Outline of Content.....	4
<b>Chapter 2: Mechanical and Time-dependent Behaviour of SFRC.....</b>	<b>5</b>
2.1 Mechanical Behaviour of SFRC .....	5
2.1.1 Macroscopic level .....	6
2.1.1.1 Compression properties .....	6
2.1.1.2 Tensile properties .....	7
2.1.1.3 Flexural properties .....	9
2.1.2 Microscopic level.....	11
2.1.2.1 Fibre/matrix interface .....	11
2.1.2.2 Bridging mechanisms .....	14
2.1.2.2.1 Aggregate bridging.....	14
2.1.2.2.2 Fibre bridging .....	17
2.1.2.2.3 Combined aggregate and fibre bridging.....	21
2.1.2.3 Factors influencing the pull-out behaviour of a single fibre .....	22
2.1.2.3.1 Fibre type.....	22
2.1.2.3.2 Fibre geometry .....	23
2.1.2.3.3 Fibre embedment length and diameter .....	24
2.1.2.3.4 Fibre inclination angle.....	25
2.1.2.3.5 Fibre volume fraction .....	28
2.1.2.3.6 Matrix composition and its mechanical properties.....	29
2.1.2.3.7 Specimen preparation method .....	29
2.1.2.3.8 Loading rate.....	30
2.2 Time-dependent Behaviour of Cement-Based Materials .....	30
2.2.1 Shrinkage mechanisms.....	30
2.2.2 Creep and its nature in concrete.....	34
2.2.2.1 Instantaneous deformation.....	35
2.2.2.2 Creep recovery.....	35
2.2.2.3 Relaxation of stress.....	36
2.2.3 Creep mechanisms .....	37

2.2.4	Factors affecting creep .....	39
2.2.4.1	Influence of aggregates .....	39
2.2.4.2	Influence of water/cement ratio .....	40
2.2.4.3	Influence of cement type and cement extenders .....	40
2.2.4.4	Influence of relative humidity .....	41
2.2.4.5	Influence of temperature .....	41
2.2.4.6	Influence of age at loading .....	42
2.2.4.7	Influence of specimen size .....	42
2.2.4.8	Influence of stress level .....	42
2.2.5	Creep fracture .....	43
2.3	Background on Time-dependent Behaviour of SFRC .....	43
2.3.1	Strain rate effect .....	44
2.3.2	Review on creep of SFRC .....	45
2.3.2.1	Structural level .....	45
2.3.2.2	Macroscopic level .....	46
2.3.2.3	Single fibre level .....	48
2.4	Concluding Summary .....	49
<b>Chapter 3: Experimental Framework .....</b>		<b>50</b>
3.1	Concrete Mix Materials and Mixing Procedure .....	51
3.1.1	Concrete mix materials .....	51
3.1.2	Mixing procedure .....	51
3.1.3	Workability of concrete in the fresh state .....	52
3.2	Mechanical and Time-dependent Behaviour of SFRC on a Macroscopic Level .....	54
3.2.1	Compression strength test .....	54
3.2.2	Uni-axial tensile test .....	54
3.2.2.1	Research programme .....	54
3.2.2.2	Specimen preparation .....	55
3.2.2.2.1	Preparation of moulds .....	55
3.2.2.2.2	Casting procedure .....	56
3.2.2.2.3	Curing of specimens .....	57
3.2.2.2.4	Preparation of samples for testing .....	57
3.2.2.3	Experimental methodology and setup .....	57
3.2.2.4	Experimental programme .....	59
3.2.3	Pre-cracked sustained load tests .....	59
3.2.3.1	Research programme .....	59
3.2.3.2	Specimen preparation .....	59
3.2.3.3	Experimental methodology and setup .....	59

3.2.3.4	Experimental programme .....	61
3.2.4	Drying shrinkage test .....	62
3.3	Mechanical and Time-dependent Behaviour on a Single Fibre Level .....	63
3.3.1	Quasi-static single fibre pull-out tests.....	63
3.3.1.1	Research programme .....	63
3.3.1.2	Specimen preparation .....	64
3.3.1.3	Experimental methodology and setup .....	64
3.3.1.4	Experimental programme .....	65
3.3.1.4.1	Pull-out loading rate .....	66
3.3.1.4.2	Fibre embedment length .....	67
3.3.1.4.3	Fibre inclination angle .....	67
3.3.1.4.4	Fibre mechanical anchorage .....	68
3.3.2	Single fibre sustained load tests .....	69
3.3.2.1	Research program .....	69
3.3.2.2	Specimen preparation .....	69
3.3.2.3	Experimental methodology and setup .....	70
3.3.2.4	Experimental programme .....	71
3.3.2.4.1	Applied sustained load .....	72
3.3.2.4.2	Fibre inclination angle .....	73
3.3.2.4.3	Fibre mechanical anchorage .....	73
3.3.2.4.4	Pre-damaged sustained load .....	73
3.4	Concluding Summary.....	74

<b>Chapter 4: Mechanical and Time-dependent Behaviour of SFRC on a Macroscopic Level.....</b>	<b>75</b>
4.1 Compressive Strength .....	76
4.1.1 Results.....	76
4.1.2 Discussion .....	76
4.2 Uni-axial Tensile Strength Test.....	77
4.2.1 Results.....	78
4.2.2 Discussion .....	80
4.2.3 Experimental observations during testing of specimens.....	82
4.2.4 Effect of crack plane fibre count on $\sigma$ - $w$ response.....	84
4.3 Pre-cracked Sustained Load Tests.....	86
4.3.1 Results.....	86
4.3.2 Discussion .....	90
4.3.3 Effect of crack plane fibre count on the variability of $CMOD_{sus}$ .....	95
4.4 Drying Shrinkage Test .....	97

4.4.1 Results.....	98
4.4.2 Discussions .....	98
4.5 Concluding Summary.....	100

## **Chapter 5: Mechanical and Time-dependent Behaviour on a Single Fibre**

### **Level.....102**

5.1 Quasi-Static Single Fibre Pull-out Tests .....	103
5.1.1 Results.....	103
5.1.1.1 Pull-out loading rate .....	103
5.1.1.2 Fibre embedment length .....	106
5.1.1.3 Fibre inclination angle .....	107
5.1.1.4 Fibre mechanical anchorage .....	110
5.1.2 Discussions .....	112
5.1.2.1 Failure modes .....	112
5.1.2.2 Pull-out loading rate .....	114
5.1.2.3 Fibre embedment length .....	116
5.1.2.4 Fibre inclination angle .....	118
5.1.2.5 Fibre mechanical anchorage .....	119
5.2 Single Fibre Sustained Load Tests .....	121
5.2.1 Results.....	121
5.2.1.1 Applied sustained load.....	121
5.2.1.2 Fibre inclination angle .....	124
5.2.1.3 Fibre mechanical anchorage .....	127
5.2.1.4 Pre-damage sustained load test.....	130
5.2.2 Discussions .....	133
5.2.2.1 Applied sustained load.....	133
5.2.2.2 Fibre inclination angle .....	136
5.2.2.3 Fibre mechanical anchorage .....	137
5.2.2.4 Pre-damaged sustained load tests .....	138
5.2.3 Mechanisms causing the crack widening under sustained loading.....	139
5.3 Concluding Summary.....	140

## **Chapter 6: Predicting the Single Fibre Pull-out Creep Behaviour.....142**

6.1 Constitutive Pull-out Creep Model .....	143
6.1.1 Mathematical derivation of linear pull-out creep behaviour.....	143
6.1.2 Model adaption to include non-linear pull-out creep behaviour.....	146
6.1.3 Implementation of pull-out creep model.....	147
6.1.3.1 Linear visco-elastic material parameters .....	147
6.1.3.2 Non-linear pull-out creep behaviour.....	150

6.2	Verification of Pull-out Creep Model using Rate Tests .....	152
6.2.1	Analytical modelling of the quasi-static pull-out behaviour.....	154
6.2.1.1	Local bond-slip relationship .....	154
6.2.1.2	Pull-out load-slip relationship .....	155
6.2.1.3	Numerical simulations .....	157
6.2.2	Model adaption to include time-dependent behaviour.....	159
6.2.2.1	Mathematical derivation of time-dependent model.....	161
6.2.2.2	Verification of adapted model .....	162
6.3	Concluding Summary.....	164
<b>Chapter 7: Predicting the Macroscopic Time-dependent Crack Mouth Opening Displacement.....</b>		<b>166</b>
7.1	Conceptual Basis .....	167
7.2	Generalised Constitutive Model (GCM).....	168
7.2.1	Identifying factors that affects the $CMOD_{sus}$ .....	168
7.2.1.1	Crack plane fibre distribution .....	168
7.2.1.2	Propagation of $CMOD_{sus}$ .....	170
7.2.1.3	Fibre embedment inclination angle distribution over crack plane .....	170
7.2.1.4	Sustained load distribution over crack plane .....	170
7.2.1.5	Fibre embedment length distribution over crack plane .....	170
7.2.2	Generalised formulation.....	170
7.2.3	Experimental validation .....	171
7.2.4	Calibration of generalised constitutive model (GCM).....	175
7.3	Oriented Generalised Constitutive Model (OGCM).....	177
7.3.1	Experimental validation .....	181
7.4	Concluding summary .....	184
<b>Chapter 8: Conclusions and Recommendations.....</b>		<b>185</b>
8.1	Conclusions .....	185
8.1.1	Macroscopic Level.....	185
8.1.2	Single Fibre Level.....	186
8.1.2.1	Quasi-static single fibre pull-out tests .....	186
8.1.2.2	Single fibre sustained load tests.....	187
8.1.3	Single Fibre Pull-out Creep Modelling.....	188
8.1.4	Time-dependent Modelling of Cracked SFRC .....	188
8.2	Recommendations .....	189

<b>References.....</b>	<b>191</b>
<b>APPENDIX I: Experimental Quasi-static Single Fibre Pull-out Results.....</b>	<b>209</b>
<b>APPENDIX II: Experimental Single Fibre Pull-out Creep Results.....</b>	<b>215</b>

# Chapter 1

---

## Introduction

To date concrete is the most widely used construction material and the usage of this material can be dated back to the ancient times (Sparavigna, 2011). The reason for its popularity in the construction industry is its ability to be cast into almost any shape or size, its relative high compressive strength compared to other construction materials, and its durability. The only disadvantage of ordinary concrete is that it is a brittle material, i.e. it has a relatively low tensile strength and poor resistance to crack opening and propagation (Brandt, 2008). To compensate for its low tensile strength, steel reinforcement is used in the tensile region. Steel Reinforced Concrete (SRC) has been used successfully over the years and is still being used in the industry as the main reinforcement in concrete structures (Yakut, 2004). Cracking however still occurs in the tensile regions when steel reinforcement is used. These cracks lead to durability problems because they create pathways for water and gaseous substances to penetrate the material that in turn cause the steel reinforcement to corrode resulting in structural degradation (Cigna, et al., 2003; Song & Saraswathy, 2007).

The concept of fibre reinforcement of concrete is a more recent development. However according to Brandt (2008) it is not a new concept as the use of fibre-like materials to strengthen brittle building materials, e.g. the clay bricks, can be traced back to biblical times (approximately 3500 years ago) where horse-hair, straw and other vegetable fibres were used as reinforcement. Today various types of fibres are available, namely glass fibres (Majumdar



---

& Nurse, 1974), carbon fibres (Toutanji, et al., 1993), polymeric fibres (Oh, et al., 2007) and steel fibres (Olivito & Zuccarello, 2010). According to Brandt (2008) steel fibres can be considered the most important for structural concrete. It is a common misconception by users of Fibre Reinforced Concrete (FRC) that by adding any amount of fibres will increase the tensile strength of concrete. Scholars have showed that the addition of low volume steel fibres to concrete, typically ranging between 0.5 – 1 %, does not significantly improve the tensile strength of concrete but significantly improves the post-crack behaviour (de Oliveira, 2010; Rossi, 1992). Most of the research done by scholars concerns the short-term loading behaviour of Steel Fibre Reinforced Concrete (SFRC). However, the properties of concrete changes due to aging and the behaviour of the material is dependent on the duration of the load. Before SFRC can be considered as a commercial construction material, design models are required in order to establish the time-dependent behaviour of SFRC.

## **1.1 Statement of the Research Problem**

Numerous studies on the post-cracking behaviour of SFRC have been done over the last 40 years, see e.g. Lim et al. (1988), Soroushian & Bayasi (1991), Barros & Figueiras (1999), Barros et al. (2005), Soranakom & Mobasher (2007), Fantilli et al. (2009). These studies are based on short-term loading rates. The long-term behaviour of SFRC has been studied before, see e.g. Chern & Chan (1989), Tan et al. (1995), Altoubat & Lange (2003), however it was only recently that the long-term behaviour of cracked SFRC has been investigated, see e.g. Kanstad & Zirgulis (2012), Mouton & Boshoff (2012). The investigations done by Mouton & Boshoff (2012) showed that even though the tensile creep of SFRC is relatively low, compared to ordinary concrete, the creep increased significantly after the SFRC has cracked. This phenomenon can be associated with the time-dependent crack widening that is probably caused by fibre pull-out over time, but the mechanisms causing this increased time-dependent crack widening still needs to be investigated and identified. This investigation is necessary as this increased time-dependent crack widening can have a significant influence on the serviceability limit state design of SFRC structures as typical Fibre Reinforced Concrete (FRC) model codes, e.g. fib (fib Special Activity Group 5, 2010) model code, only consider the time-dependent behaviour of conventionally reinforced concrete.

---

## 1.2 Justification of this Research Study

SFRC structures already exist, see e.g. Oslejs (2008), and model codes for FRC exist, e.g. *fib* Model Code (*fib* Special Activity Group 5, 2010). However in these model codes the time-dependent behaviour of SFRC is based on the time-dependent behaviour of conventionally reinforced concrete, making it difficult for designers to accept this material. Before this material can be accepted as a construction material, research is required on the time-dependent behaviour of SFRC. The long term behaviour of SFRC has been investigated before. Bissonnette & Pigeon (1995) and Bissonnette, et al. (2007) showed that the addition of steel fibres tended to increase the tensile creep of uncracked concrete. In contrast Garas et al. (2009) showed that the addition of short straight steel fibres decreased the tensile creep of uncracked Ultra-high Performance Concrete (UHPC). They proposed that the decrease in creep was due to the enhancements at the fibre/matrix interface during thermal treatment. It is only recently that the long term behaviour of cracked SFRC has been included in the investigations. Mouton and Boshoff (2012) and Zhao et al. (2014) are among the few that investigated the long-term crack widening of pre-cracked SFRC under sustained uni-axial tensile loading. Babafemi and Boshoff (2015) did similar work on the creep of macro-synthetic fibre reinforced concrete. Research is also available on the long-term crack widening of pre-cracked SFRC under flexural loading (Abrishambaf, et al., 2015; Garacia-Taengua, et al., 2014; Tan & Saha, 2005; Zerbino & Barragán, 2012). These investigations showed that even though the creep is similar to that of conventional concrete, the creep increased significantly after the concrete had cracked. This phenomenon is associated with the crack widening over time as a result of fibre pull-out under sustained load and is referred to as pull-out creep. It is defined as the relative movement between the fibre and the matrix interface under sustained loading. The mechanisms involved during the pull-out creep are still unknown and need to be investigated.

Modelling of the time-dependent behaviour of cracked SFRC is still a concern and according to the author of this dissertation no literature is available on the time-dependent modelling of cracked SFRC subjected to sustained uni-axial tensile loading. Also typical FRC structural design codes, e.g. *fib* Model Code (*fib* Special Activity Group 5, 2010), lack information on the time-dependent behaviour. This needs urgent attention as this could significantly influence the long-term deflections of SFRC.

This research study investigated, quantified and modelled the time-dependent crack width opening behaviour of cracked SFRC under sustained uni-axial tensile loading.

### **1.3 Outline of Content**

A comprehensive review of the literature background is given in Chapter 2 on FRC and the typical time-dependent behaviour found for cement-based materials. In addition the literature available on the time-dependent behaviour of FRC is included of which the focus was on cracked FRC.

Chapter 3 provides a detailed description of the experimental methodology performed in this research project. The experimental investigations conducted were divided according to the level of magnification at which the material is studied, namely: macroscopic and single fibre level. The test methods described on the macroscopic level include compressive, uni-axial tensile and pre-cracked sustained uni-axial tensile tests. The test methods described on the single fibre level were quasi-static single fibre pull-out and single fibre sustained load tests.

In Chapter 4, the experimental results on the macroscopic level (compressive strength, uni-axial tensile test and pre-cracked sustained uni-axial tensile tests) are presented and discussed in detail.

The experimental results and discussions on the single fibre level (quasi-static single fibre pull-out tests and single fibre sustained load tests) are presented in Chapter 5.

In Chapter 6 a constitutive model that is able to simulate the time-dependent pull-out behaviour of aligned hooked-end steel fibres is elaborated on.

Chapter 7 generalises the model developed in Chapter 6 to a macroscopic level so that it can simulate the time-dependent behaviour of cracked SFRC directly.

Chapter 8 presents the significant findings of this study and aspects that have been identified for further investigation.

# Chapter 2

---

## Mechanical and Time-dependent Behaviour of SFRC

Steel fibres were originally proposed as a dispersed reinforcement for concrete in the early 1960's (Brandt, 2008) and were commercially introduced to the European market in the second half of the 1970's (Ross, 2009). At that time no standards or recommendations were available making it difficult to accept this new concrete technology. Steel fibres were initially used as a substitute for secondary reinforcement or for crack control in the less critical regions of the construction. Today steel fibres are widely used as the main reinforcement in industrial and suspended floor slabs (Oslejs, 2008), shotcrete and prefabricated concrete products (Ross, 2009).

Numerous studies have been done on the mechanical behaviour of SFRC. However the literature available on the time-dependent behaviour of SFRC is limited. In this chapter an extensive background study on the mechanical behaviour and time-dependent behaviour of SFRC is presented.

### **2.1 Mechanical Behaviour of SFRC**

Steel Fibre Reinforced Concrete (SFRC) consist of ordinary concrete ingredients, i.e. water, cement and cement extenders, aggregates and additives to modify the workability. The

percentage and type of steel fibres added depends on the type of mechanical response required (Fantilli, et al., 2009). The post-cracking behaviour under tensile loading is what distinguishes SFRC from ordinary concrete. The steel fibres added to the cement composite bridge the crack or cracks which gives an improved ductile post-cracking response in comparison to normal concrete (Fantilli, et al., 2009). The utilisation of steel fibres is more advantageous over conventional steel reinforcement because it reduces the cost of labour and construction time (Ou, et al., 2012).

In this section the mechanical behaviour of SFRC is reviewed on both a Macroscopic and Microscopic Level.

### 2.1.1 Macroscopic level

To better understand the mechanical behaviour of SFRC the compression, tensile and flexural properties of SFRC is reviewed on a Macroscopic Level.

#### 2.1.1.1 Compression properties

In current concrete design, transverse steel reinforcement is used to improve the toughness of the concrete in compression. Transverse reinforcement confines the lateral expansion of concrete induced by compression. In contrast, steel fibres bridge longitudinal cracks caused by the lateral expansion of concrete under compression, see Figure 2.1. The pull-out of the fibres as the crack widens increases the toughness of the material (Ou, et al., 2012).

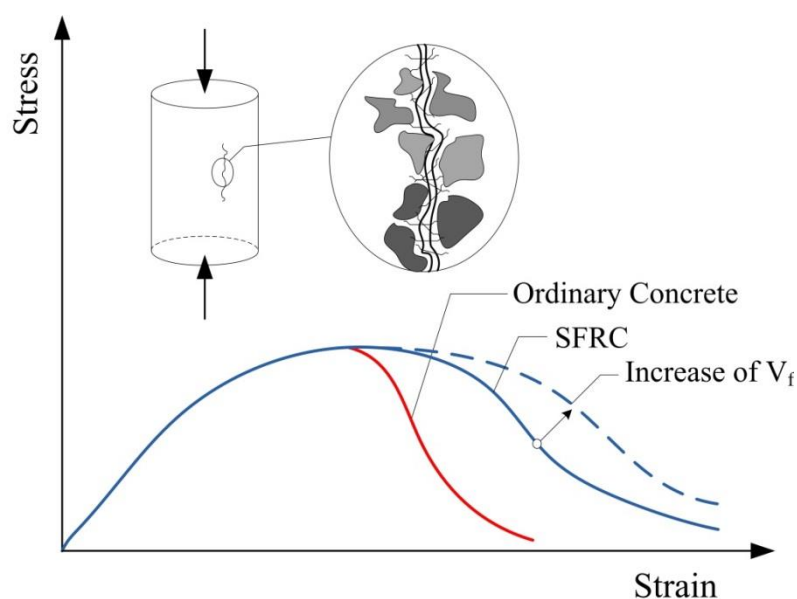


Figure 2.1. Schematic description of the behaviour of ordinary concrete and SFRC in compression (based on Löfgren 2005)

---

A typical comparison of the performance of SFRC versus ordinary concrete is schematically shown in Figure 2.1 where it is indicated that steel fibres increase both the toughness and the strain at peak stress and that this increase continues as the volumetric fibre content is increased. It was found that an increase in the volumetric fibre content leads to a relatively flatter post-peak softening branch in the stress-strain curve of mortar with steel fibres (Fanella & Naaman, 1985), see Figure 2.1. The mechanical response of SFRC in compression is highly dependent on the type of fibres used, the volumetric fraction of fibres and the properties of the matrix (Dhakal, et al., 2005; Ou, et al., 2012).

Researchers have proposed a number of models to calculate the beneficial behaviour of steel fibres; see e.g. Ezeldin and Balaguru (1992), Barros and Figueiras (1999), Nataraja et al. (1999), Dhakal et al. (2005) and Ou et al. (2012). These models can analytically model the compression stress-strain relationship of SFRC for different fibre content volumes.

### **2.1.1.2 Tensile properties**

A typical tensile response for SFRC is schematically shown in Figure 2.2. It depicts that SFRC is a ductile material when compared to the brittle nature of ordinary concrete and has a post-crack tensile residual strength. The post crack tensile response is characterised by a non-linear behaviour. The mechanical response of the material during the non-linear phase is dependent on several factors, namely the mechanical characteristics of the fibres, the shape and size of the fibres, the volume of fibres within the matrix and the fibre orientation as well as external conditions such as the curing procedure, loading application rates and ambient temperatures to which the material is exposed (Chanvillard, et al., 1990).

The tensile stress-strain response of SFRC can be characterised by three distinct phases, refer to Figure 2.2: (1) the linear elastic phase, during which the material performance is similar to ordinary concrete and represents the material behaviour of the matrix before cracking; (2) the non-linear phase, during which the fibres are activated at the onset of the first crack by crack bridging, providing resistance to crack propagation; and (3) the failure phase, during which ultimate failure of the material occurs and which can be a result of two phenomena. These are discussed later in this section.

According to Lim et al. (1988) many researchers have assumed that the linear-elastic behaviour of SFRC is equal to the normal failure behaviour of the matrix (Aveston, et al., 1974; Pakotiprapha, et al., 1983). However, experimental results showed that the first crack

for SFRC appears at a slightly higher strain level than for the unreinforced matrix, and that this increases with the increase in fibre volume fraction (Naaman, et al., 1974). This increase can be considered negligible for fibre volume fractions limited to 1 %. The structural performance of SFRC is generally characterised by its post-cracking behaviour (Dupont, 2003). Thus, the initial elastic phase of SFRC can be considered as similar to that of ordinary concrete.

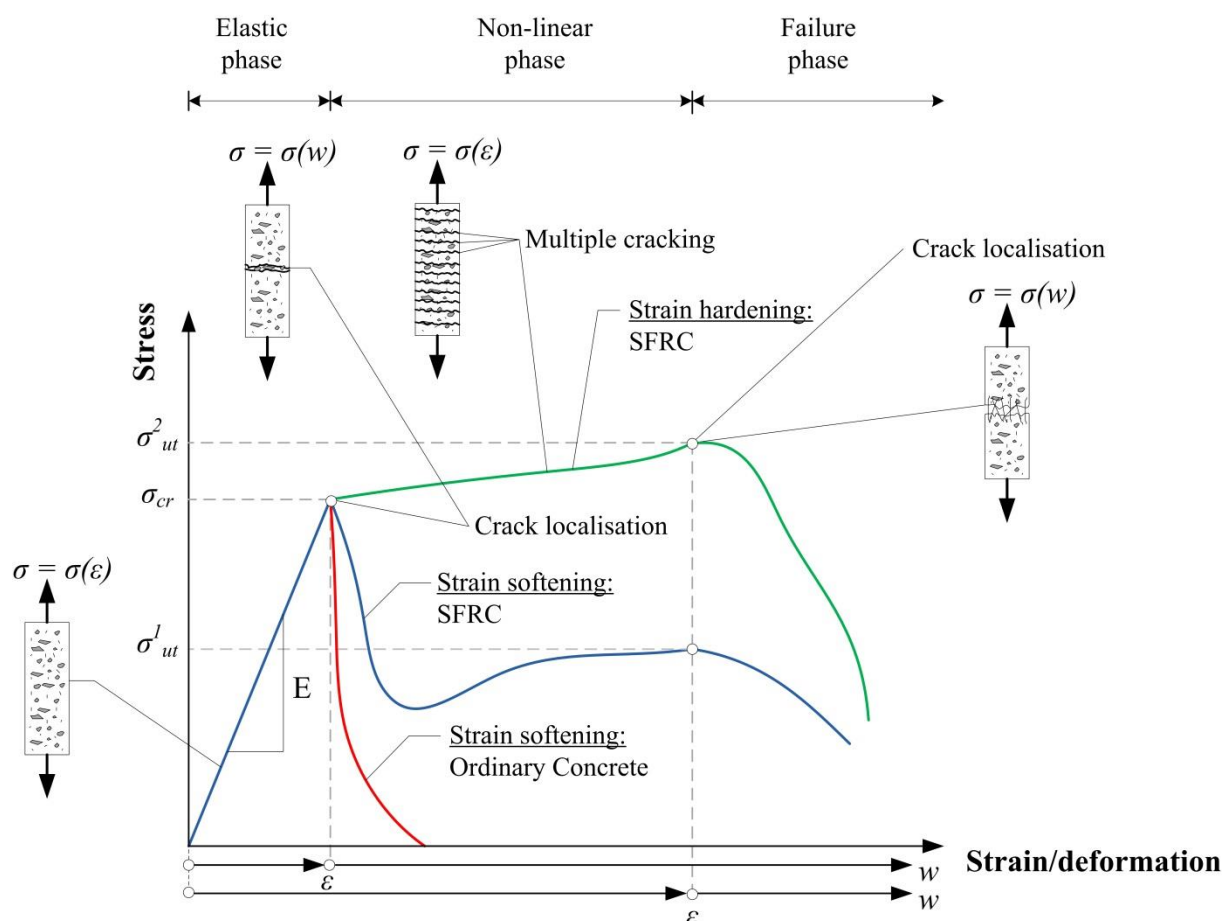


Figure 2.2. The tensile response of SFRC compared to ordinary concrete schematically (based on Löfgren 2005)

SFRC is characterised by the non-linear post cracking tensile behaviour. Depending on the fibre characteristics and their volume percentage within the mix, the post-cracking phase of SFRC can undergo either strain hardening or strain softening when subjected to axial tensile loading, see Figure 2.2. Strain hardening is a property in which the tensile stress increases as the tensile strain increases after cracking and during this phenomenon multiple cracking occurs before reaching the maximum post-cracking strength, see Figure 2.2. Strain softening is a property in which the tensile stress decreases to the post cracking residual stress as the

---

strain increases after cracking and is characterised by the formation of a single localised crack (fib Special Activity Group 5, 2010), see Figure 2.2. The two phenomena can be distinguished by determining the volume fraction of fibres that defines the transition between the two phenomena for a certain type of fibre and mix. This is defined as the critical fibre volume ( $V_{cr}$ ) and if the fibre volume ( $V_f$ ) added to the mix is more than the critical fibre volume strain hardening will occur after cracking. If the fibre volume added to the mix is less than the critical fibre volume strain softening will occur after cracking (Lim, et al., 1988; Fantilli, et al., 2009).

Once the material has reached its maximum post-cracking strength, failure of the material begins to take place that can be a result of either two phenomena that take place: rupture of fibres as a result of stress concentrations or pull-out of fibres from the matrix. Fibre rupture occurs when the matrix-fibre bond strength is greater than the strength of the fibre (Bentur & Mindess, 2007). Fibre rupture is generally associated with Fibre Reinforced Composites (FRC) that is reinforced with synthetic fibres but can also occur in steel fibres used with ultra-high strength concretes (Robins, et al., 2002; Boshoff, et al., 2009). Fibre rupture is normally associated with a brittle failure. Fibre pull-out occurs when the bond between the fibre and the surrounding matrix is exceeded. Resistance to crack propagation is provided by frictional forces between the fibres and the surrounding concrete matrix. Fibre pull-out is normally associated with a more ductile failure compared to fibre rupture (Fantilli, et al., 2009).

Models to analytically predict the stress-strain relationship of SFRC in tension for different volumetric fibre contents have been developed by researchers: see e.g. Lim et al. (1987), Li et al. (1993), and Vrech et al. (2010).

### **2.1.1.3 Flexural properties**

The flexural behaviour of SFRC is a complicated phenomenon. At the onset of cracking on the material surface the tensile capacity changes to the resistance provided by the fibres bridging the crack, and the depth of the neutral axis changes accordingly to maintain the equilibrium between the compression and tensile forces in the flexural element, see Figure 2.3 (Jarrat, 2011).

When SFRC is subjected to flexural loading, strain softening materials can undergo deflection softening or deflection hardening, see Figure 2.4. Deflection softening is when the material fails with no increase in the flexural load capacity after cracking, whereas for deflection



hardening an increase in flexural load capacity is found after cracking due to the extra stiffness contributed by the fibres in the cracked zone of the tensile region (Soranakom & Mobasher, 2007). For deflection hardening to occur it is required that the strain softening material has sufficient post-peak tensile strength to significantly change the stress distribution across the sample depth (Soranakom & Mobasher, 2007). At the initiation of cracking the fibres are activated by bridging the cracks, which gives the material a post-peak residual strength. At the crack locations a residual resisting force is provided by the fibres (see Figure 2.3), which gives the material a ductile response in flexure compared to ordinary concrete.

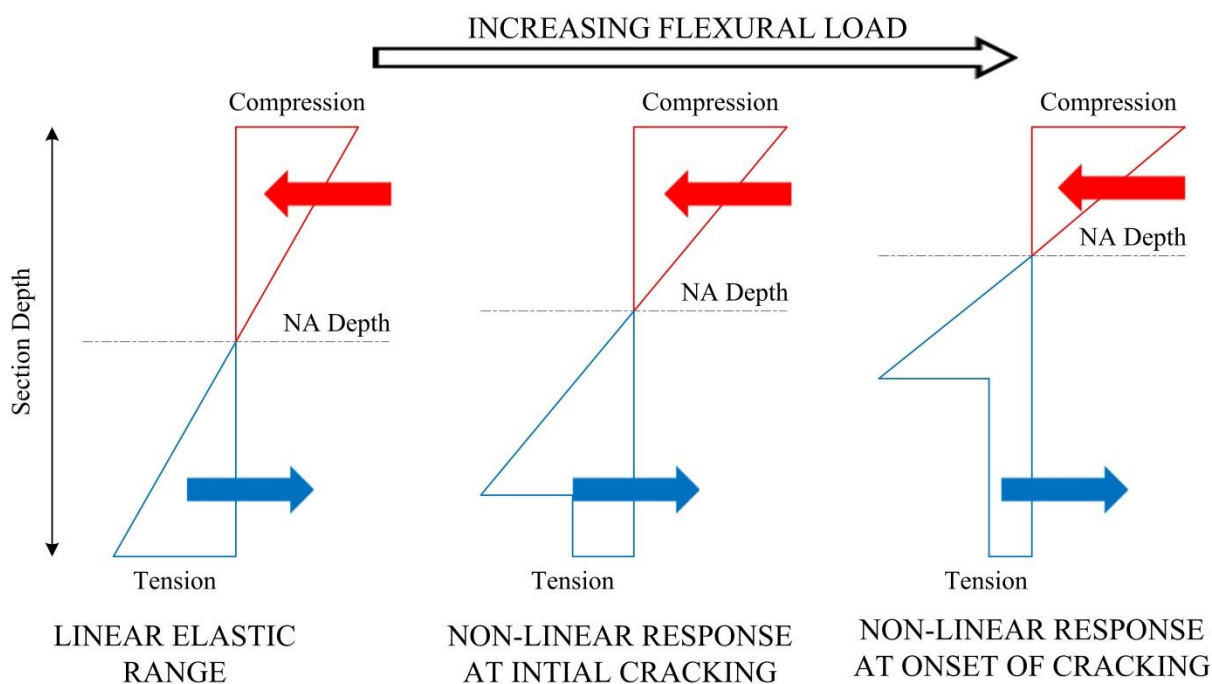


Figure 2.3. Schematic representation of the stress distribution and shift in neutral axis depth through the section height (based on Jarred 2011)

The mechanical response of SFRC during flexural loading is dependent on several factors, namely the mechanical characteristics of the fibres, the shape and size of the fibres (Soroushian & Bayasi, 1991), the volume of fibres within the matrix and the fibre orientation as well as external conditions such as the curing procedure, loading application rates and ambient temperatures to which the material is exposed (Chanvillard, et al., 1990; Bayramov, et al., 2004). It was shown that an increase in the volumetric fibre content increases the flexural tensile strength and flexural residual tensile strength of the concrete (Bayramov, et al., 2004; Barros, et al., 2005).

Models to analytically predict the tensile load-deflection relationship of SFRC under bending for different volumetric fibre content have been developed by researchers: see e.g. Lim et al. (1988), Barros et al. (2005), Soranakom & Mobasher (2007), and Soranakom & Mobasher (2008).

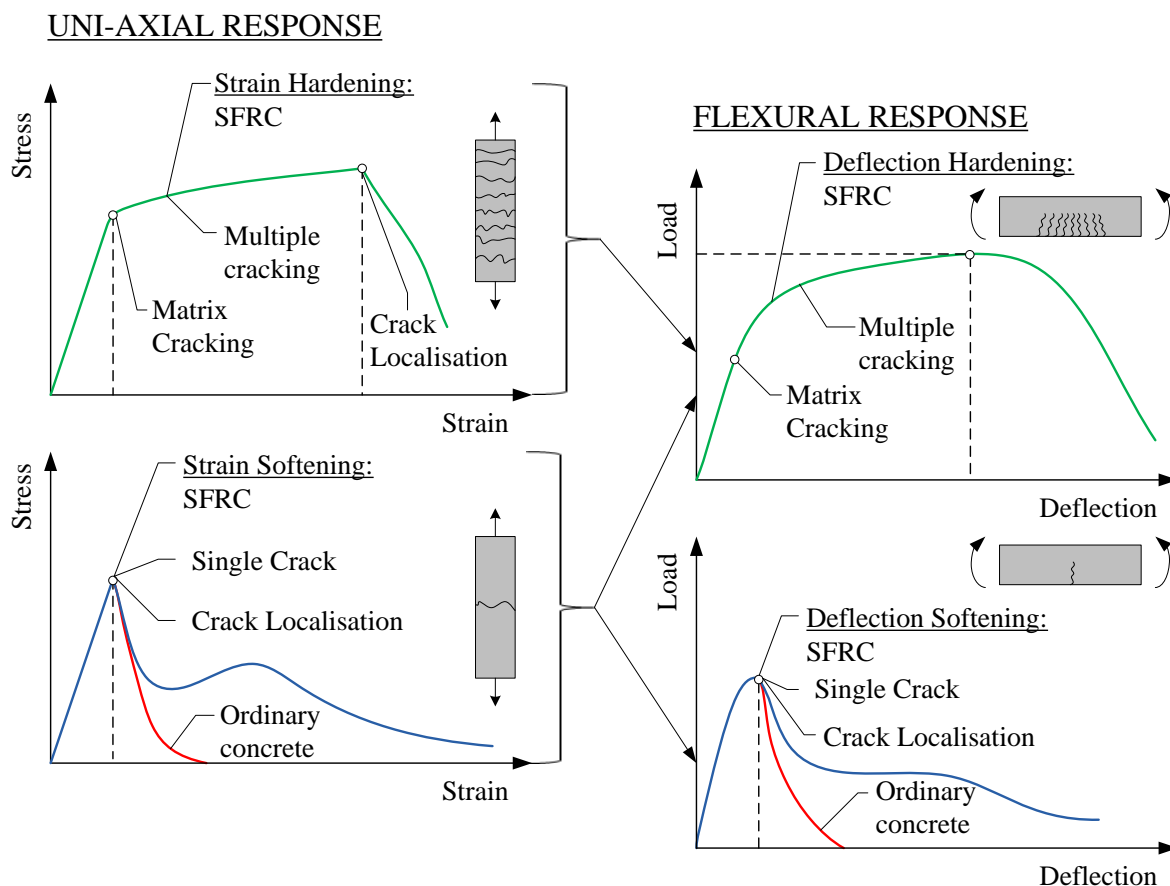


Figure 2.4. Characterisation between tensile and flexural response of SFRC (based on Löfgren 2005)

## 2.1.2 Microscopic level

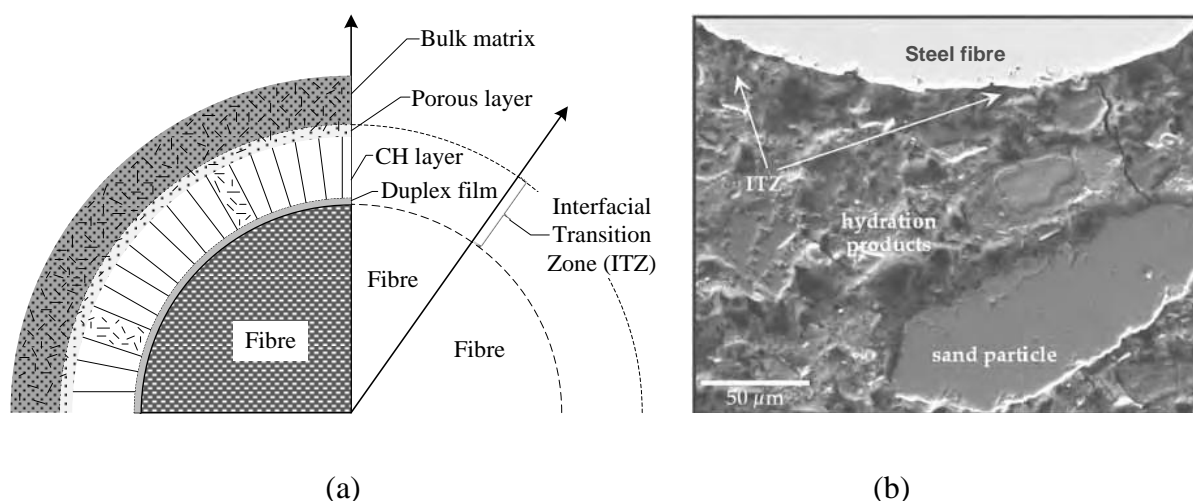
In this section the interface between the fibre and matrix, and the bridging mechanisms of FRC are reviewed on a microscopic level as well as factors that influence the pull-out behaviour of steel fibres from a cementitious matrix.

### 2.1.2.1 Fibre/matrix interface

The microstructure of concrete is developed during the hydration process. The hydration process involves a chemical reaction of the cement and/or other binder ingredients and water, whereby concrete becomes a firm hardened mass, which makes it capable of supporting an

applied load. The cement hydration is initiated immediately after the mixing of cement and water. During the hydration process a sequence of overlapping chemical reactions between clinker components, calcium sulphate, and water occur, leading to the setting and hardening of the cement paste.

The addition of steel fibres neither changes the hydration reactions nor the development of the microstructure in the bulk matrix. The pull-out behaviour and the bond of a fibre are significantly influenced by the microstructure at the interface between the fibre and the matrix. This interface is referred to as the Interfacial Transition Zone (ITZ) and its composition differs from the rest of the concrete matrix due to the presence of the fibre (Dupont, 2003). In Figure 2.5(a) the ITZ is schematically represented and in Figure 2.5(b) a scanning electron (SE) image of SFRC is shown to illustrate the scale of the microstructure.



*Figure 2.5. Interfacial Transition Zone (ITZ): (a) Schematic representation of the interfacial transition zone (based on Löfgren 2005); and (b) an SE image of the ITZ close to the fibre (Löfgren 2005)*


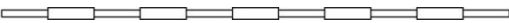





The ITZ generally consists of a cement paste layer of varying thickness, which is a consequence of the wall effect caused by the presence of the fibre. In this cement layer there may be a number of voids present due to the bleeding water getting trapped in this region during the hydration process or inefficient packing of the cement grains surrounding the fibre (Dupont, 2003; Löfgren, 2005; Bentur & Mindess, 2007).

Several explanations for the formation of the ITZ exist. The main deduction is that during the formation of the ITZ the presence of all these phenomena at this zone result in a significant higher porosity than in the bulk matrix, and also in an increased amount of calcium-hydroxide

(CH) crystals, Figure 2.5(a). The result is that the ITZ has a substantially lower strength and stiffness when compared to the bulk cement matrix (Diamond and Huang 2001, sien Cunha 2010). Wei et al. (1986) tested the micro-hardness of concrete around a steel fibre and showed that the micro-hardness in the ITZ is lower than in the bulk cement matrix. He also showed that the width of the ITZ is about 75  $\mu\text{m}$ . According to Bentur and Mindess (1990) the width of the ITZ ranges between 20-50  $\mu\text{m}$ , whereas Li and Stang (1997) reported values in the order of 40-70  $\mu\text{m}$ .

The density and packing of the ITZ is influenced by several factors namely, the size of the fibres in relation to the other constituents, the size and packing of the matrix material, and the surface roughness and chemistry of the fibre. Löfgren (2005) and Bentur & Mindess (2007) showed that by improving the mixing techniques and using cement fillers improved the strength of ITZ thus improving the bond between the fibre and the ITZ and this increased the pull-out load for a fibre. Bentur & Mindess (2007) showed that the ITZ can be decreased by using fibres of smaller diameters. This decreases the formation of voids that improves the composite performance. Not only can the strength of the ITZ be improved through improved adhesion and friction of the surrounding matrix and the fibre, but it can also be improved by mechanical anchorage of the fibre (Bentur & Mindess, 2007). This is achieved by modifying the shape of the fibre. In steel fibres the shape of the fibre can easily be modified, e.g. the introduction of hooked-end steel fibres or crimped steel fibres etc. In Table 2.1 examples of different steel fibre shapes are shown schematically (Cunha, et al., 2007). The application of shaped fibres results in using a much lower fibre dosage than with straight fibres, without reducing the ductility or the toughness of the fibre concrete (Dupont, 2003).

*Table 2.1: Schematic representation of different steel fibre profiles*

<b>Fibre type</b>	<b>Longitudinal profile</b>	<b>Cross-section profile</b>
Straight		Round, flat or any shape
Indented		
Crimped		
Flat-end		Round or flat
Button-end		Round
Hooked-end		
Twisted		Polygonal (triangular or rectangular)

A problem with refined fibres is that they increase the probability of fibre balling (Soroushian & Bayasi, 1991; Dupont, 2003). This was resolved by using fibres that are glued together with water-soluble glue. The fibres that are glued together form plates of fibres and the slenderness ratio of these plates of fibres is much smaller than that of an individual fibre, which solves the problem of fibre balling (Soroushian & Bayasi, 1991; Dupont, 2003).

### 2.1.2.2 Bridging mechanisms

In ordinary concrete the aggregates contribute to the energy dissipation during matrix cracking. The aggregates provide bridging traction that gradually decreases towards zero for a crack opening of 0.3 mm (Li, et al., 1993; Löfgren, 2005), see Figure 2.6. Only after cracking has occurred do the fibres start bridging the crack. The addition of fibres increases the tensile ductility that means that the toughness or fracture energy is increased and is represented by the area under the stress-crack opening curve, see Figure 2.6. The total response of the stress-crack opening is a result of the combined phenomena of aggregate bridging and fibre bridging.

In this section the mechanisms behind aggregate bridging, fibre bridging, and the combined action between aggregate and fibre bridging are reviewed.

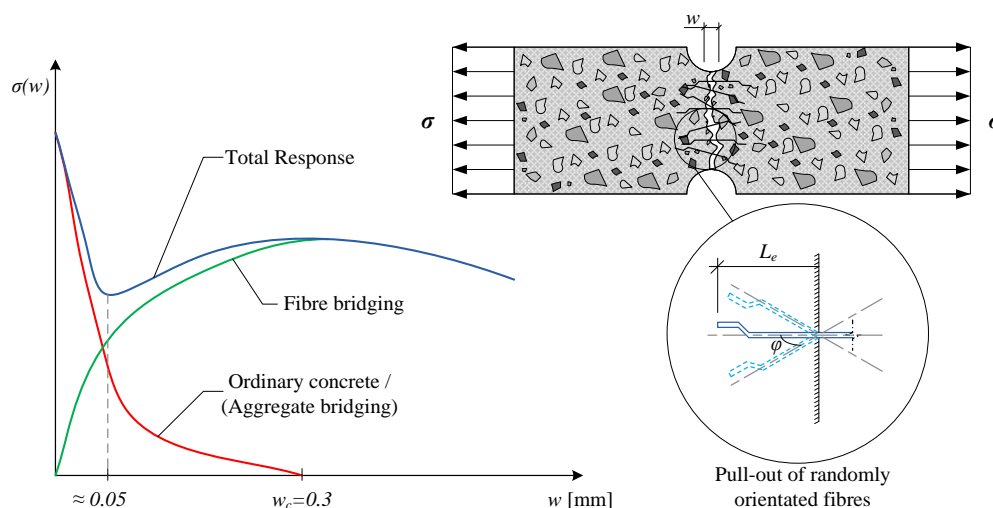


Figure 2.6. Combined fibre and aggregate bridging of FRC (based on Löfgren 2005 and Li et al. 1993) loaded in uni-axial tension

#### 2.1.2.2.1 Aggregate bridging

In quasi-brittle materials like concrete the fracture toughness is mainly related to the action of aggregate bridging that leads to the presence of a Fracture Process Zone (FPZ) ahead of the

stress-free macro-crack tip (Schlangen & van Mier, 1992; Zhang & Xu, 2007), see Figure 2.7. The FPZ is the zone of discontinuous micro-cracking ahead of a continuous macro-crack tip (Schlangen & van Mier, 1992). In this zone the opening of the crack is restrained by the bridging traction of the aggregates (Zhang & Xu, 2007), See Figure 2.7.

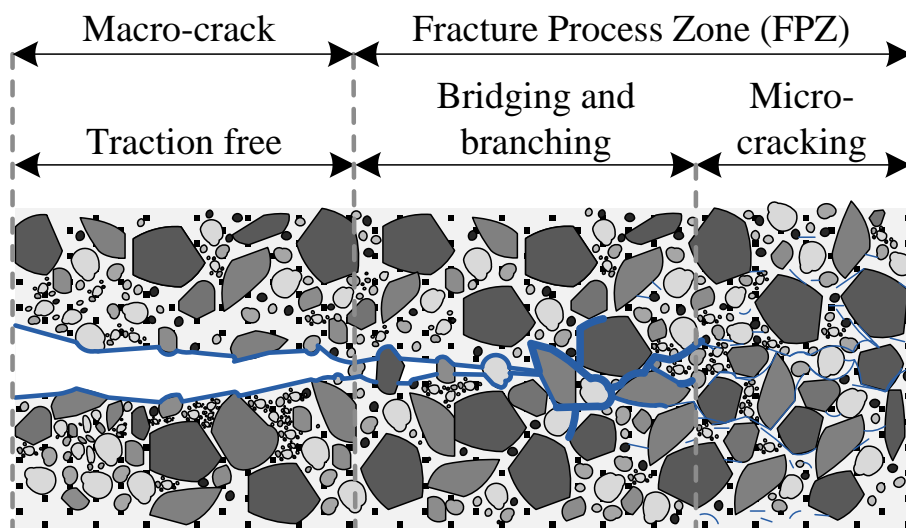


Figure 2.7. Schematic representation of the Fracture Process Zone (FPZ) (based on Löfgren 2005 and Schlangen & van Mier 1992)

In ordinary concrete the different toughening mechanisms that are involved during the fracture process include (see Figure 2.8): (a) crack shielding, (b) crack deflection, (c) aggregate bridging, (d) crack surface roughness-induced closure, (e) crack tip blunted by void and (f) crack branching (Shah, et al., 1995). Aggregate bridging is the major toughening mechanism in ordinary concrete and as a result it can be expected that the stress-crack opening response should be dependent on the characteristics of the aggregates and as well as on the characteristics of the cement and any supplementary materials, e.g. microsilica, fly ash and fillers (Löfgren, 2005). The effect that aggregates play (e.g. type, size, shape, volume fraction, etc.), the effect of additions etc., and the techniques used such as acoustic emission monitoring and X-ray observations have been investigated by several researchers: see e.g. van Mier (1991), van Mier (1997), Giaccio & Zerbino (1997), Buyukozturk & Hearing (1998), Otsuka & Date (2000), Tasderi & Karihaloo (2001), Darwin, et al. (2001), Wu, et al. (2001). Researchers also found that by modelling and simulating the fracture process of ordinary concrete it provided additional information and a better understanding of the fracture process: see e.g. Schlangen & van Mier (1992), Zhang & Xu (2007).



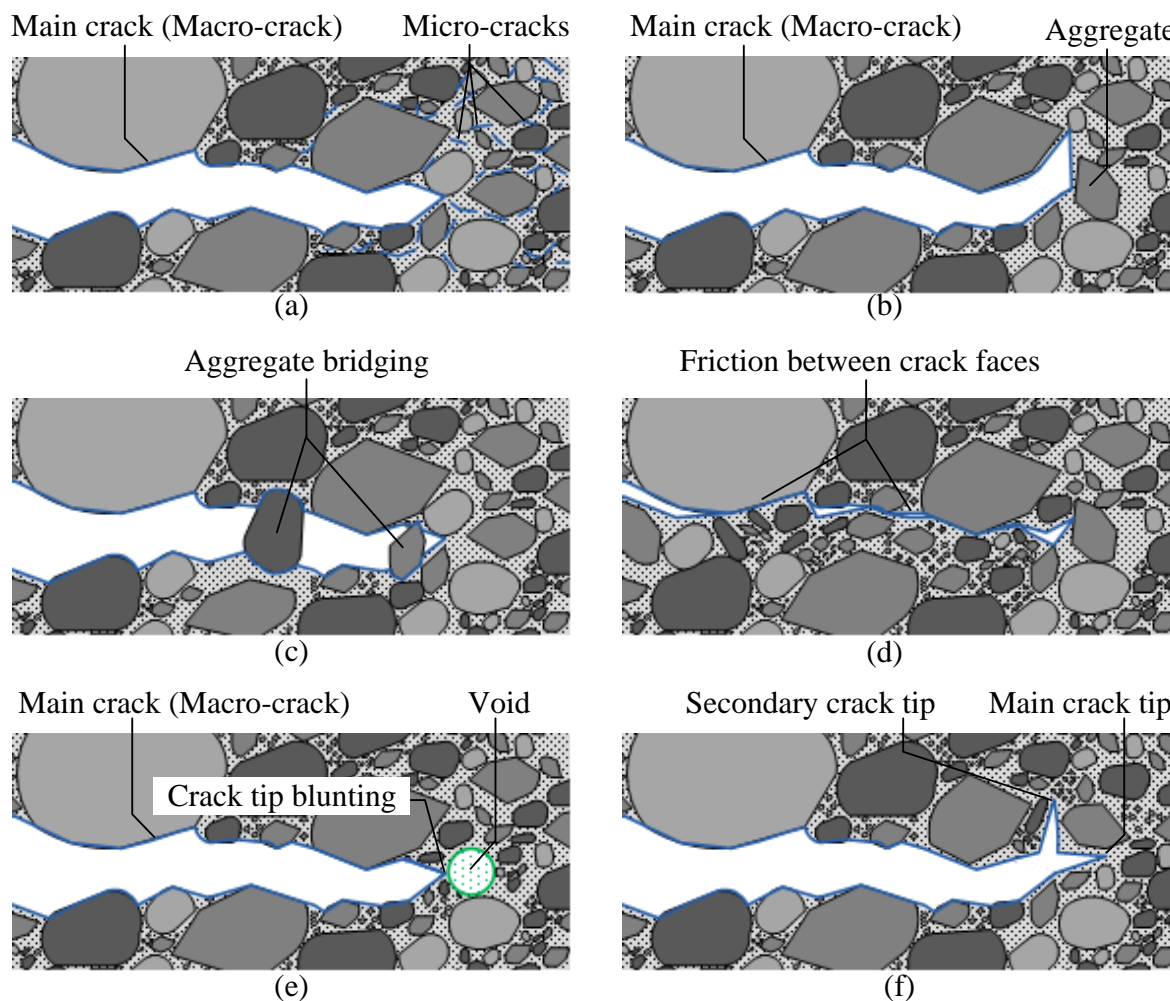


Figure 2.8. Toughening mechanisms involved during the fracture process in ordinary concrete (based on Löfgren 2005 and Shah et al. 1995)

The uni-axial tensile response of ordinary concrete can be explained as represented in Figure 2.9 (Schlangen & van Mier, 1992; Löfgren, 2005; Zhang & Xu, 2007). Internal restraints within concrete (caused by aggregates, shrinkage and thermal deformations) cause pre-existing micro-cracks within concrete, even before any stresses have been applied. When a stress is applied to an ordinary concrete specimen, additional micro-cracks will arise and the pre-existing micro cracks will develop further (A). This initially originates at the interface between the cement paste and the aggregates, but eventually the micro-cracks propagate into the mortar (B). Crack localisation occurs at the peak stress (C) and is the result of the micro-cracks that propagate in an unstable manner and coalesce to form a macro-crack throughout the specimen, leading to the stress drop (D). Due to the crack bridging and crack branching caused by the aggregates, the long softening tail (D-E) originates.

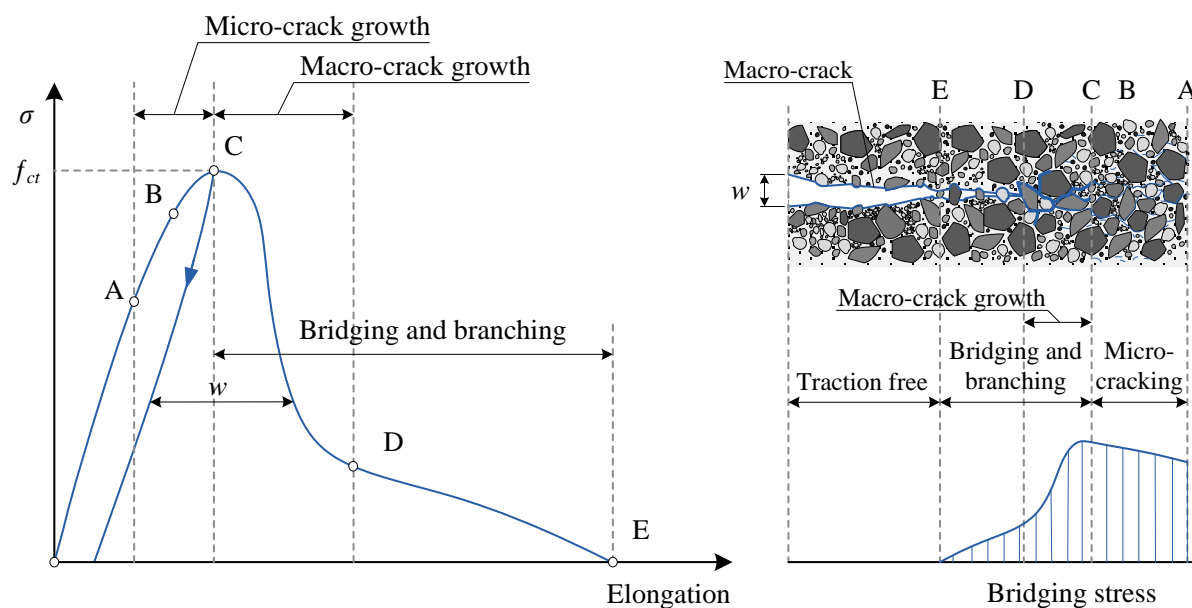


Figure 2.9. Schematic representation of the fracture process of ordinary concrete in uni-axial tension and the resulting stress-crack opening relationship (based on Löfgren 2005)

As mentioned previously, the fracture process of ordinary concrete depends largely on the characteristics of the aggregates and their bond to the matrix. However this is different for high-strength concrete and lightweight aggregate concrete. For these two types of concrete the aggregates may be the weakest link in the matrix and aggregate rupture may occur, which may result in a reduction in the bridging effect of the material and eventually initiate a more brittle fracture process (Schlangen & van Mier, 1992).

#### 2.1.2.2.2 Fibre bridging

The fracture process of FRC is a complex phenomenon and is dependent on a number of parameters; e.g. the type of fibre used and the geometry of the fibre, the fibre length and diameter, fibre orientation with respect to the loading direction, matrix composition and its mechanical properties, fibre volumetric fraction in the composite, specimen preparation method, loading rate etc. (NG, et al., 2012).

The mechanical behaviour of FRC is not only related to the amount and orientation of fibres, but also largely to the pull-out versus load (or load-slip) behaviour of individual fibres. In Figure 2.10 the pull-out responses for aligned straight and hooked-end steel fibres are schematically compared to each other. The ascending part OA is associated with the elastic or adhesive bond between fibre and matrix. In the part AB of the pull-out response the debonding process is initiated until full debonding occurs at point B. Due to the mechanical



anchorage of the fibre the pull-out force is attained and the load can be increased (BC). At the maximum pull-out load the curvatures 1 and 2 are both deformed that leads to a decrease in the mechanical anchorage (CD). As the curvature 2 passes the last corner of the fibre imprint made in the matrix, another peak load is observed (DE). Afterwards the fibre end is fully straightened and the pull-out occurs under frictional resistance (EF), which decays as the slip increases. Robins et al. (2002) showed that the pull-out response of a hook-end fibre is predominately influenced by three parameters: (1) fibre embedment length; (2) fibre orientation; and (3) matrix strength.

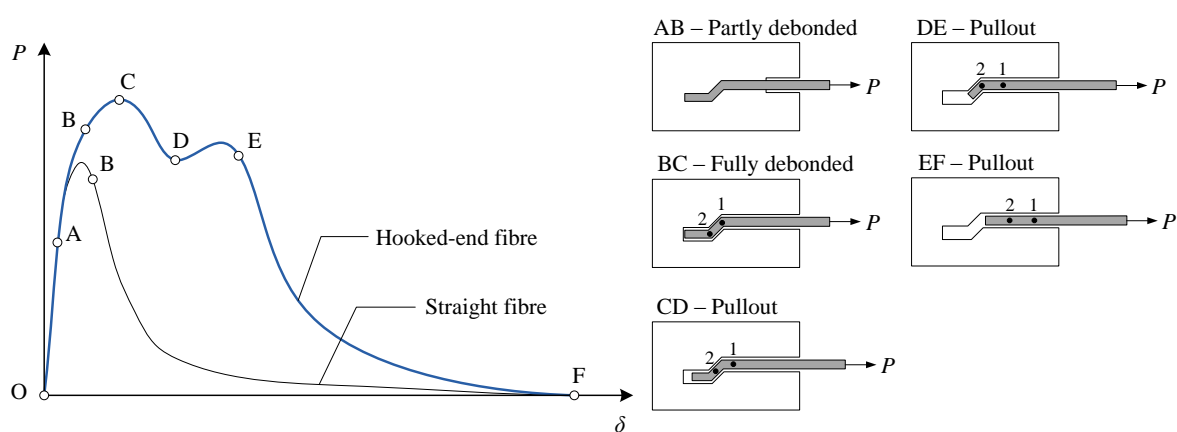


Figure 2.10. Typical pull-out response versus slip in hooked-end steel fibre (based on Ghoddousi et al.2010)

In FRC the fibres are randomly distributed and not all the fibres are aligned in the direction of the applied load. When a crack crosses a fibre that is not perpendicular to the crack plane and the crack is opening, the fibre is found to bend at the exit point (snubbing effect), i.e. at the crack surface (Dupont, 2003; NG, et al., 2012). At this point the fibre is subjected to a combination of shear, bending and tensile stresses, see Figure 2.11. The pull-out of inclined fibres results in the generation of high concentrated stresses at the place where the fibre is forced to bend and may cause local spalling (Dupont, 2003; Löfgren, 2005; NG, et al., 2012). Spalling is when the concrete between the fibre and the crack plane is crushed or pushed off, see Figure 2.12. If concrete spalling occurs the fibre can easily bend and the stress carried by the fibre is reduced (Dupont, 2003). For ductile fibres (e.g. steel fibres) the pull-out load increases for an inclination angle up to  $45^\circ$  and then decreases, while for flexible fibres (e.g. synthetic fibres) the pull-out load increases up to high inclination angles, and for brittle fibres (e.g. carbon fibres) the pull-out load decreases for all inclination angles (Löfgren, 2005).

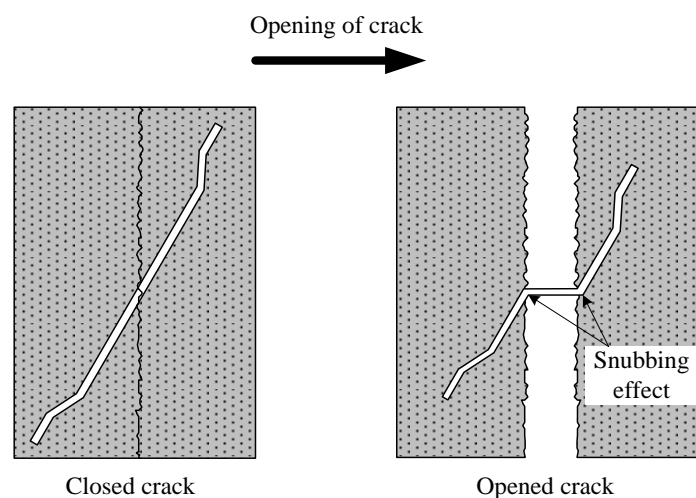


Figure 2.11. Schematic illustration of snubbing effect (based on Dupont 2003)

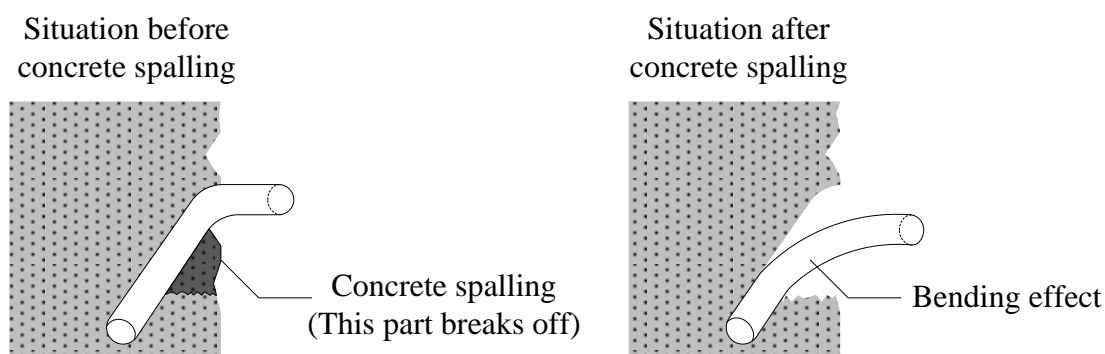


Figure 2.12. Schematic illustration of concrete spalling (based on Dupont 2003)

The bond between the fibre and matrix allows forces to be transmitted between the fibre and the matrix. Debonding of the interface surrounding a fibre is the result of fibre pull-out, and is followed by frictional slip and pull-out of the fibre from the matrix (Löfgren, 2005). There are a few factors that influence the bond between fibre and matrix and they can be classified as follows: (1) the physical and/or chemical adhesion between fibre and matrix; (2) the frictional resistance; (3) the mechanical component (dependent on the particular fibre geometry, e.g. crimped, or hooked-end fibres); and (4) the fibre to fibre interlock (Löfgren, 2005). After the initiation of debonding two interfacial zones will arise, a bonding and debonding zone, see Figure 2.13(a). Several models exist to describe the fibre pull-out behaviour: see e.g. Stang & Shah (1986), Desarmot & Favre (1991), Gorbatkina (1992), Scheer & Nairn (1995), Nairn (2000). The debonding criterion can be described by two different approaches: a strength-based criterion (or stress-based) and a fracture-based criterion (Li & Stang, 1997; Löfgren, 2005; Zhandarov & Mader, 2005; Cunha, et al., 2008; Ghoddousi, et al., 2010), see Figure

2.13(a). In the strength-based models, it is assumed that debonding initiates when the interfacial shear stress exceeds the shear strength. For the fracture-based models, the debonding zone is treated as an interfacial crack. To drive the debonded zone forward, i.e. interfacial crack propagation, adequate energy must be supplied. At the debonding zone the stress transfer will be governed by the frictional shear bond (Gopalaratnam & S.P., 1987). Different relationships can be used to describe the frictional bond (see Figure 2.13(b)): (1) constant friction, (2) decaying friction (or slip softening), and (3) slip hardening friction (Li & Stang, 1997; Löfgren, 2005). The controlling mechanism will determine which model and relationship to use to describe the pull-out behaviour of a fibre.

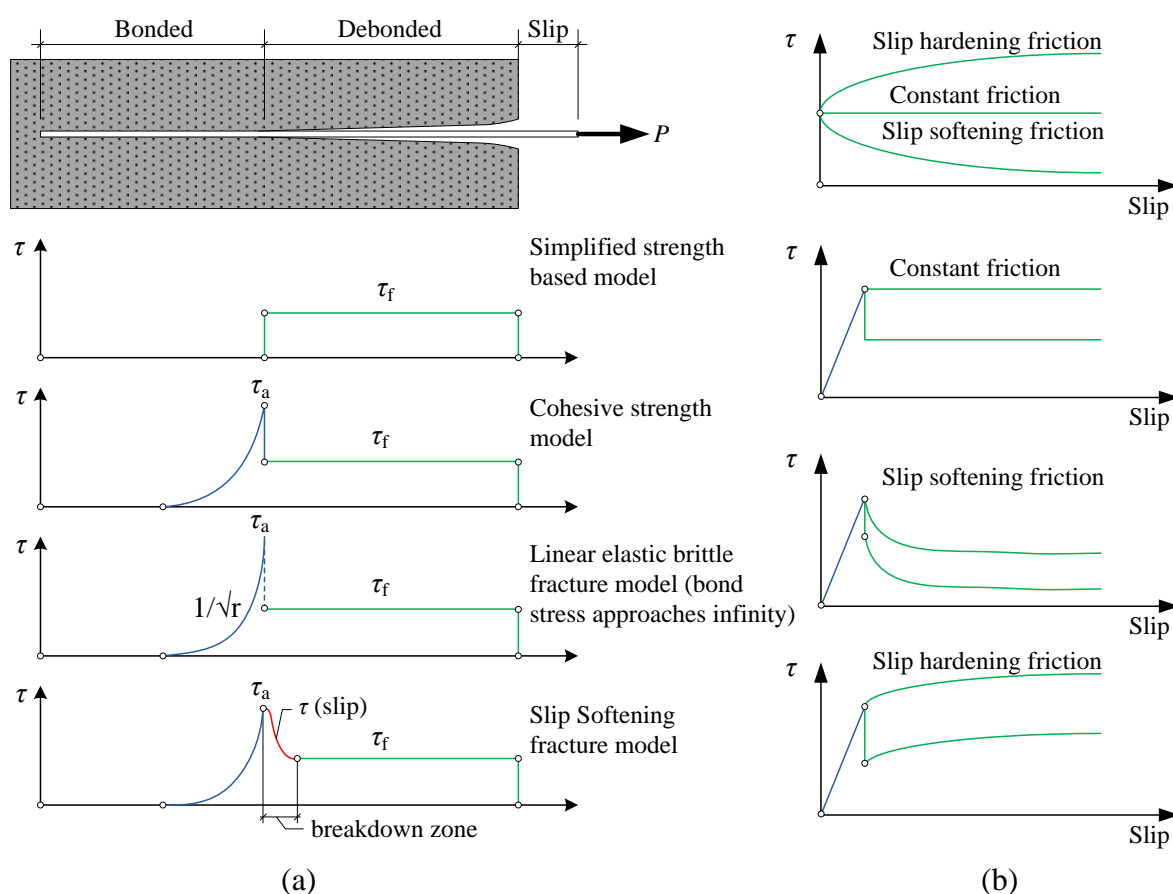


Figure 2.13. (a) Different debonding models for fibre pull-out (based on Li and Stang 1997) and (b) different relationships for describing the frictional bond-slip relationship (based on Löfgren 2005)

The use of straight fibre models is not adequate to predict the pull-out behaviour of fibres with an end anchorage, since the behaviour of hooked-end fibres is dominated by the mechanical anchorage (Cunha, et al., 2008). Models to predict the pull-out behaviour of

hooked-end steel fibres have been developed by Alwan et al. (1999), Cunha et al. (2008) and Ghoddousi et al. (2010).

### 2.1.2.2.3 Combined aggregate and fibre bridging

The tensile bridging stress and energy dissipation in fibre reinforced concrete is due to a number of mechanisms acting simultaneously. These have been explained separately in Section 2.1.2.2.1 and 2.1.2.2.2. Fibres act as an additional bridging mechanism when compared to ordinary concrete. It has been shown that the critical crack opening (the stress-free crack opening) and fracture energy can increase by a factor larger than 10 if fibres are added to the matrix (Soroushian & Bayasi, 1991; Groth, 2000). As mentioned in Section 2.1.1.2 the addition of fibres has no effect on the linear-elastic behaviour of FRC and it is the same as for ordinary concrete, but during the post cracking behaviour of FRC the maximum fibre bridging stress depends on the parameters described for the single fibre pull-out and the additional effects caused by randomly orientated fibres (Löfgren, 2005). During the fracture process of FRC there will be a combined effect of aggregate and fibre bridging, see Figure 2.14. The aggregate bridging has a relatively short functioning range in comparison to the fibres. When a single crack is observed, three distinct zones can be identified (see Figure 2.14): (1) a traction-free zone, which occurs at relatively large crack openings; (2) a bridging zone, here stresses are transferred by fibre pull-out and aggregate bridging; and (3) a micro-cracking and macro-cracking zone.

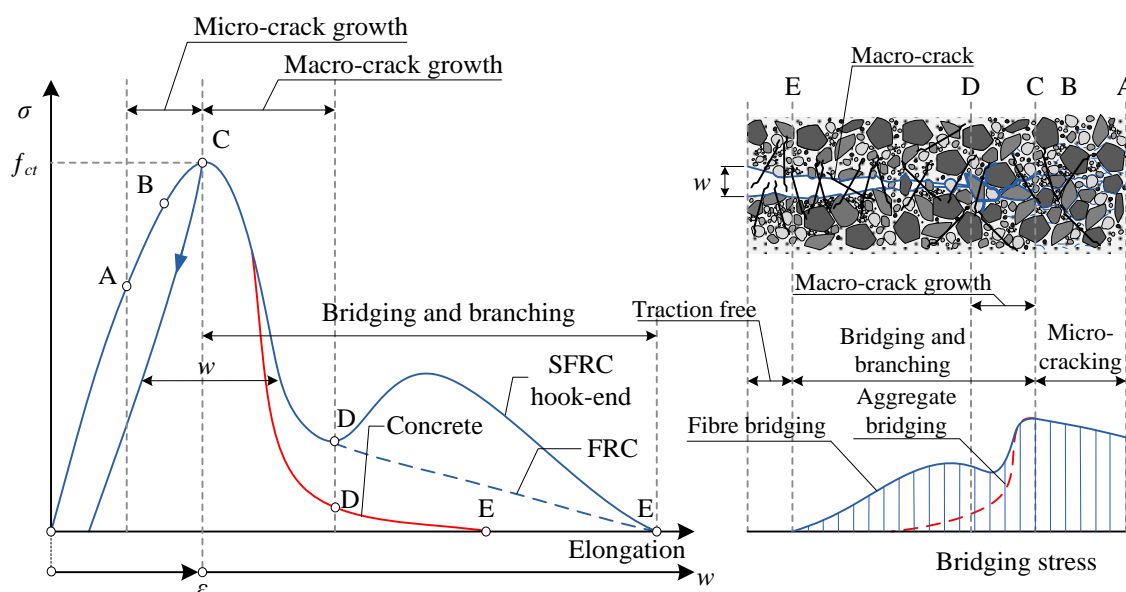


Figure 2.14. Schematic description of the effect of fibre bridging in the fracture process in uni-axial tension (based on Löfgren 2005)

---

The stress-crack opening response (see Figure 2.14) starts with a descending part (C-D) for small crack openings, e.i.  $w < 0.1$  mm (Löfgren, 2005). Fibre bridging only starts to have a major influence when a crack opening of at least 0.05 mm has been reached, see Figure 2.6. Depending on the fibre characteristics, the curve will slowly decrease with an increase in fibre slip (or crack opening) until it becomes zero (D-E); for some fibre types, e.g. hooked-end fibres, the fibres will first undergo an ascending part for which the stress increases as the fibre is straighten during the pull-out process (see Figure 2.10), but eventually the stress will start to decrease until zero.

### **2.1.2.3 Factors influencing the pull-out behaviour of a single fibre**

As far as the author could determine the factors that can have an effect on the pull-out of a single fibre from the matrix are summarised in Table 2.2. These factors were investigated by researchers (see Table 2.2) under static and/or dynamic loading conditions. In this section some factors that can have an effect on the pull-out behaviour of a single fibre from a cementitious matrix are discussed based on research done by previous researchers.

#### **2.1.2.3.1 Fibre type**

Gokoz & Naaman (1981) investigated the pull-out behaviour for three types of fibres, namely smooth steel, glass and polypropylene. They investigated the effect of strain rate and concluded that glass fibres fractured at all loading rates and steel fibres showed a pull-out failure mode at all loading rates. Polypropylene on the other hand showed a mixed behaviour between the two types of failure modes, which is dependent on the loading rate. They also concluded that polypropylene fibres are very sensitive to the loading rate, while steel fibres are insensitive to the loading rate. They found that the post peak response of steel fibres, which is a representative of the frictional effects between the fibre and the matrix, is almost insensitive to the loading rate. It should be noted that smooth steel fibres were used during this research.

Banthia & Trottier (1991) did single fibre pull-out tests of deformed steel fibres from cement-based matrixes to investigate the effect of strain rate on the pull-out behaviour. They concluded that deformed steel fibres embedded in cementitious matrixes in general support a higher load under impact than under static pull-out. Also the pull-out energy is greater under impact provided the fibre failure mode is maintained from static to impact loading.

*Table 2.2. Factors that affects the pull-out behaviour of fibres from a cementitious matrix*

<b>Factors</b>	<b>References</b>
Fibre type	Gokoz and Naaman (1981); Banthia and Trottier (1991); Yang and Li (2005);
Fibre geometry	Banthia (1990); Naaman & Najm (1991); Burakiewicz (1996); Alwan et al. (1999); Abu-Lebdeh et al. (2010); Htut (2010);
Fibre Embedment length and diameter	Gopalaratnam & Abu-Mathkour (1987); Naaman & Najm (1991); Chanvillard & Aitcin (1996); Alwan et al. (1999); Robins et al. (2002); NG et al. (2012);
Fibre inclination angle	Morton & Groves (1974); Naaman & Shah (1987); Ouyang et al. (1994); Robins et al. (2002); Htut (2010)
Fibre volume fraction	Maage (1977); Naaman & Shah (1987) ; Naaman & Najm (1991); Markovic et al. (2003); Trckova & Prochazka (2009)
Matrix composition and its mechanical properties	Banthia (1990); Naaman & Najm (1991); Guerrero & Naaman (2000); Markovic et al. 2003
Specimen preparation method	Gray & Johnston (1984); Banthia & Trottier (1989); NG et al. (2012)
Loading rate	Gokoz & Naaman (1981); Banthia (1990); Banthia & Trottier (1991)

Yang & Li (2005) investigated the single fibre pull-out behaviour of Polyvinyl Alcohol fibres (PVA) at different loading rates. The results showed that the pull-out behaviour of PVA fibres is very sensitive to the loading rate. They found that the chemical bond between the fibre and the matrix becomes more evident at higher loading rates.

### **2.1.2.3.2 Fibre geometry**

The pull-out behaviour of a fibre from a matrix is influenced by the geometry of the fibre. Alwan et al. (1999) mentioned that the maximum pull-out load is a function of the fibre embedment length and the mechanical anchorage with the binding matrix. In the industry steel fibres with different mechanical anchorage are available, see Table 2.1.

Naaman & Najm (1991), Burakiewicz (1996), Alwan et al. (1999), and Htut (2010) did single fibre pull-out tests on hooked-end steel fibres and concluded that the plastic deformation of the hooks significantly contributed to the maximum pull-out load when compared to straight steel fibres. Naaman & Najm (1991) and Htut (2010) noted, by isolating the frictional bond

---

component from the mechanical bond component that the mechanical bond component of the fibre is responsible for the improvement in the maximum pull-out load. The contribution of the hook is dependent on the fibre properties and the hook geometries i.e. the inclination angle of the hook, the hook length and fibre diameter.

Abu-Lebdeh et al. (2010) did single fibre pull-out tests on flat-end steel fibres. They found that the fibres ruptured at all embedment lengths when pulled out at high loading rates. The mode of failure changed from a complete pull-out under quasi-static loading to fibre rupture under dynamic loading.

According to Banthia (1990), corrugated or indented fibres usually have a more non-linear crack opening displacement response than that of hooked-end steel fibres. This means that more energy is required to pull-out these types of fibres. However, these types of fibres are best suited for a low strength matrix, as in a high strength matrix a fracture failure mode of the fibre may occur resulting in a reduction in the pull-out energy.

Naaman (2003) did single fibre pull-out tests on twisted triangular cross section steel fibres and found that the ductility is significantly improved when compared to other steel fibre types. He also reported that although the maximum pull-out load of twisted and hook-end fibres is almost the same, twisted steel fibres maintain the high level of pull-out load for slips of 70% to 90% of the embedment length. This means that the pull-out work and pull-out energy of twisted steel fibres are approximately 80% to 130% higher than for hooked-end steel fibres.

#### **2.1.2.3.3 Fibre embedment length and diameter**

The fibre embedment length and diameter can also influence the pull-out behaviour from a cementitious matrix (NG, et al., 2012). A larger fibre embedment length and/or diameter means that a larger surface area of the fibre is in contact with the cementitious matrix. A larger contact area suggests that a larger pull-out load and pull-out energy can be expected. Gopalaratnam & Abu-Mathkour (1987) mentioned that this only holds true for straight steel fibres and is not usually true for hooked-end steel fibres (Naaman & Najm, 1991; Alwan, et al., 1999). However according to Robins et al. (2002) the pull-out response of hooked-end steel fibres is influenced by the fibre embedment length, fibre orientation and the matrix strength. They also found that the toughness and magnitude of the pull-out responses are

proportional to the initial fibre embedment length. Similar results were found by Chanvillard & Aitcin (1996) for corrugated steel fibres.

#### 2.1.2.3.4 Fibre inclination angle

Fibre reinforced cement-based composites contain randomly distributed fibres, meaning that not all the fibres are aligned in the direction of the applied load. Thus when a crack has formed the inclined fibres that bridge the crack will bent between the two crack surfaces and will realign to the direction of the applied load. Due to this phenomenon the inclined fibres will experience a combination of shear, bending and tensile stresses (NG, et al., 2012).

Snubbing of fibres and/or spalling of the matrix at the exiting point of the fibre are expected for fibres with high inclination angles (Morton & Groves, 1974). According to Ouyang et al. (1994) the increase in the maximum pull-out load is due to the pulley effect and the bending mechanisms. Only the force component  $P_x$  of the total pull-out force  $P$  in the direction of the fibre axis (see Figure 2.15) contributes to the pull-out of an inclined fibre and is referred to as the pulley effect (Ouyang, et al., 1994).

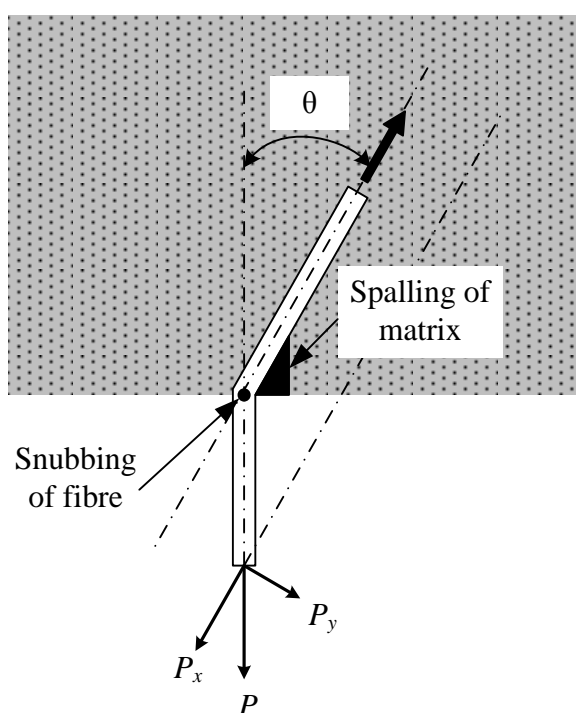


Figure 2.15. Inclined fibre mechanisms at pull-out (based on Ouyang et al. 1994)

Naaman & Shah (1987) mentioned that the snubbing of a fibre/and or spalling of the matrix due to the fibre inclination angle cause the pull-out load to reduce substantially. However,



according to Htut (2010) snubbing incorporates a mechanical anchorage component. This is because fibres subjected to snubbing action undergoes a combination of shear, bending and tensile stresses and, consequently, the pull-out load is maintained longer when compared to that of aligned fibres (NG, et al., 2012).

NG et al. (2012) mentioned that the bending resistance of fibres depends on the fibre inclination angle, type of fibre, fibre material properties and the quality of the surrounding cementitious matrix. Figures 2.16 and 2.17 shows the relationship between the embedded inclination angle of the fibre and the maximum pull-out load reached for single straight and hooked-end steel fibres, respectively. The results from Figure 2.16 and 2.17 are from different researchers who are indicated in the figures.

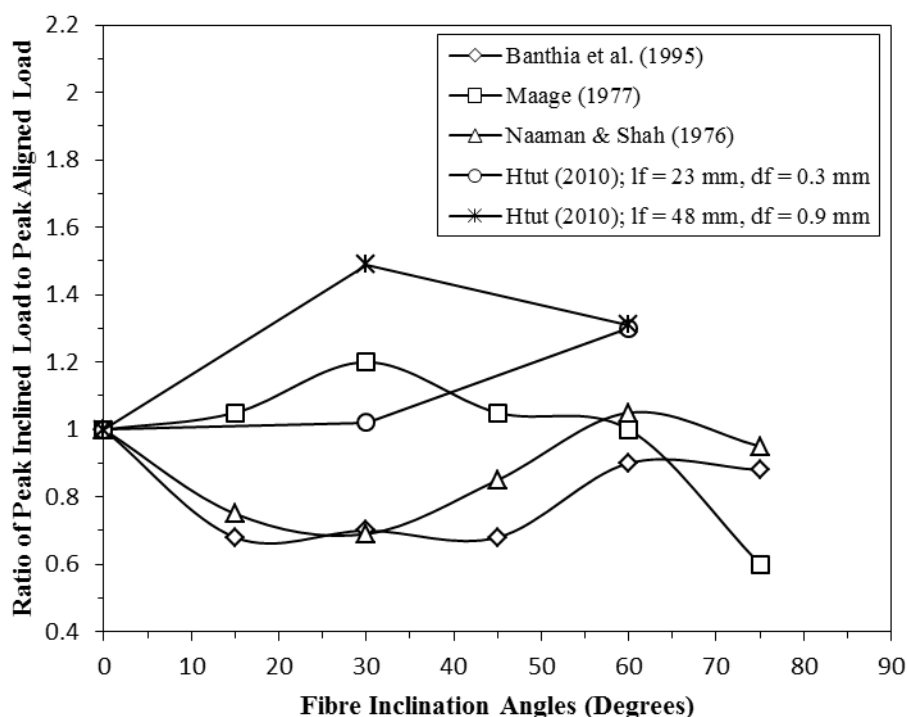


Figure 2.15. Effect of the inclination angle on the pull-out capacity of a single straight fibre embedded in a cementitious matrix (based on NG et al. 2012)

Figure 2.16 demonstrates that a straight fibre can carry a fairly large load when embedded in a cementitious matrix at a high inclination angle (Htut, 2010). This is mainly due to the snubbing effect which incorporates a mechanical anchorage.

Figures 2.16 and 2.17 demonstrate that the difference in the pull-out load, between fibres embedded at high inclination angles and aligned fibres, is small. According to Robins et al.

(2002) the mechanical properties of the fibre become more influential as the fibre embedment angle increases and, consequently, a high fibre inclination angle may cause the fibre to rupture due to the snubbing effect which causes high stress concentrations (due to the bending effect) at the exiting point of the crack surface. However, the fibre slip at maximum pull-out was usually significantly greater for inclined fibres than for aligned fibres (Robins, et al., 2002).

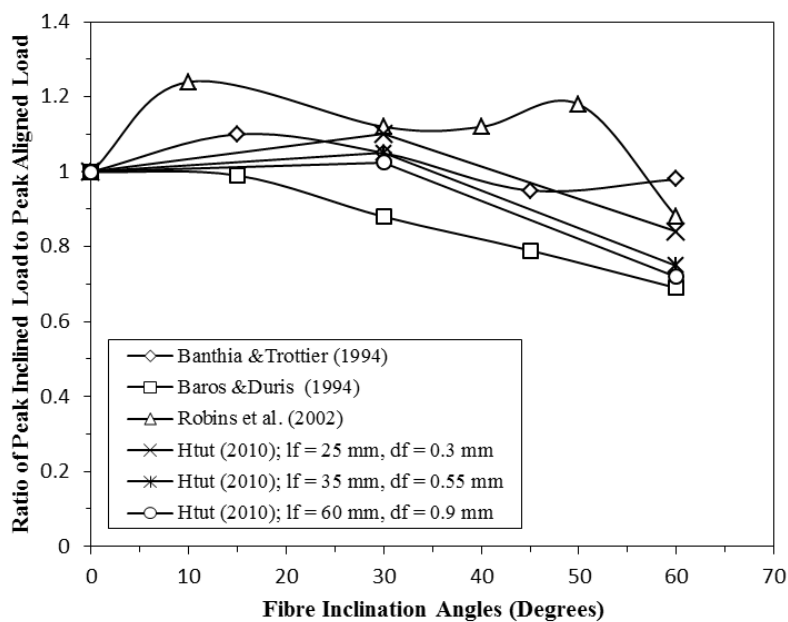


Figure 2.17. Effect of the inclination angle on the pull-out capacity of a single hooked-end fibre embedded in a cementitious matrix (based on NG et al. 2012)

Local crushing and spalling of the matrix occurs during the pull-out of an inclined fibre and is influenced by the work undertaken during the fracture process, which is measured as the area under the pull-out load versus slip curve (NG, et al., 2012). Figure 2.18 shows the relationship between the pull-out energy and the fibre embedment angle for tests conducted on single hooked-end steel fibres.

In Figure 2.18 it is clearly demonstrated that the maximum toughness response of the pull-out load versus slip will occur for fibre inclination angles between  $0^\circ$  and  $20^\circ$ . It can also be seen from Figure 2.18 that beyond a critical angle (approximately  $30^\circ$ ) the pull-out energy reduces. This reduction in the pull-out energy can be due to fibre fracture occurring and according to Robins et al. (2002) this phenomenon occurs when the embedment length is greater than 5 mm and the fibre embedment angle is greater than  $20^\circ$ . As mentioned earlier fibre fracture is

caused by relatively high stress concentration (due to fibre snubbing effect) at the crack surface.

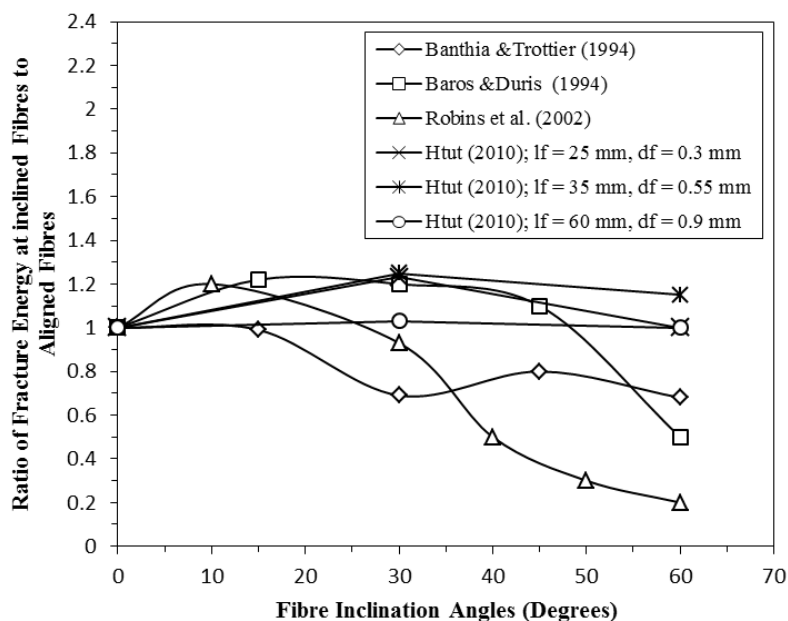


Figure 2.18. Effect of inclination angle on the pull-out energies of a single hook-end fibre (based on NG et al. 2012)

### 2.1.2.3.5 Fibre volume fraction

Usually, only single fibre pull-out test from a cementitious matrix is performed. However on a macroscopic level the fibres are more closely spaced in the cementitious composite. Naaman & Najm (1991) and Markovic et al. (2003) mentioned that by adding additional fibres around a fibre acts as secondary reinforcement and improves the fibre pull-out response. They assumed that by adding shorter micro-fibres together with longer fibres can improve the pull-out response due to the lateral confinement provided by the short or micro-fibres. Besides the micro-fibres bridge the secondary micro-cracks caused by the mechanical anchorage (Markovic, et al., 2003).

Maage (1977), Naaman & Shah (1987), and Trckova & Prochazka (2009) conducted pull-out tests on a group of aligned fibres and concluded that increasing the number of fibres from the same pull-out medium does not significantly affect the mean pull-out load per fibre. However, Naaman & Shah (1987) found that the fibre matrix bond is inversely proportional to the number of fibres being pulled out from the same area. They mentioned that this is due to the disruption of the matrix in the pull-out region when the number of fibres is increased.

#### **2.1.2.3.6 Matrix composition and its mechanical properties**

The presence of fine cementitious materials in ordinary Portland cement concrete improves the particle packing of the matrix and improves the interfacial microstructure of the concrete. These fine cementitious materials are ground cement, silica fume, fly ash, metakaolin, slag and latex. Thus by improving the interfacial microstructure of the concrete the frictional bond strength between the fibre and the matrix is improved and it increases the debonding energy (Banthia, 1990; Naaman & Najm, 1991; Guerrero & Naaman, 2000; Markovic, et al., 2003).

Guerrero & Naaman (2000) mentioned that if very fine sand is used in a cementitious matrix it improves the pull-out behaviour of smooth, hooked-end and twisted fibres. They found that the pull-out energy increases by more than 100% for smooth steel fibres, of which the frictional bond component is dominant, embedded in a fine sand cementitious matrix. A 50% increase in the pull-out energy was found for hooked-end and twisted steel fibres. Guerrero & Naaman (2000) also reported that the maximum pull-out force is improved up to 150% for smooth steel fibres and approximately 50% for hooked-end steel fibres. The aggregate composition and its fineness have an indirect influence on the fibre pull-out response, since the debonding between the fibre and the matrix localises within the Interfacial Transitional Zone (ITZ) around the fibre. Thus by compacting FRC the bond between the fibre and matrix is improved, consequently, an improvement in the pull-out response can be expected (Pinchin & Tabor, 1987). However, when coarse aggregates are used in FRC it will affect the compaction effort and thus a weaker ITZ will form around the fibre that will influence the pull-out load.

#### **2.1.2.3.7 Specimen preparation method**

There exists a degree of contradiction in the literature based on the various pull-out experiments that have been undertaken. According to NG et al. (2012) it is assumed that this is due to the natural variability between the different concrete mixes as well as the various methods used during the specimen preparation and environmental test conditions.

It has been reported that the method of specimen preparation, such as casting the specimen at different directions of the applied load and different curing ages, can have a significant effect on the bond strength between the fibre and the matrix (Gray & Johnston, 1984; Banthia & Trottier, 1989). Also the environmental conditions, such as temperature and humidity, under

---

which the experiments are undertaken, affect the bond strength between fibre and matrix (Banthia & Trottier, 1989).

#### **2.1.2.3.8 Loading rate**

Gokoz & Naaman (1981) and Banthia (1990) investigated the effect of strain rate on the pull-out behaviour of steel fibres. A wide range of loading rates was explored ranging from  $4.2 \times 10^{-2}$  mm/s to 3000 mm/s. They developed a special experimental procedure that allowed them to pull-out a group of fibres simultaneously. They concluded that steel fibres did not fail for the range of loading rates but rather showed a pull-out mode. They also concluded that steel fibres are insensitive to the loading rate. They found that the post peak response of steel fibres, which is a representative of frictional effects between the fibre and the matrix, is almost insensitive to the loading rate. It should be noted that smooth steel fibres were used during this research.

Banthia & Trottier (1991) did single fibre pull-out tests of deformed steel fibres from cement-based matrixes to investigate the effect of strain rate on the pull-out behaviour. The loading rate varied from  $8.46 \times 10^{-6}$  m/s to 1.5 m/s. They concluded that deformed steel fibres embedded in cementitious matrixes in general support a higher load under impact than under static pull-out. Also the pull-out energy is greater under impact provided the fibre failure mode is maintained from static to impact loading.

## **2.2 Time-dependent Behaviour of Cement-Based Materials**

Creep and shrinkage are the best known time-dependent phenomena of cement-based materials. Numerous research and literature has been published on these time-dependent phenomena. In this section the different mechanisms causing and affecting the time-dependent behaviour of cement-based materials are explained and discussed.

### **2.2.1 Shrinkage mechanisms**

Shrinkage of concrete takes place in two distinct stages (Holt, 2001): (1) early age shrinkage, and (2) long term shrinkage, see Figure 2.19. On the macroscopic level various types of shrinkage phenomena can be observed, namely plastic shrinkage, drying shrinkage, autogenous shrinkage and carbonation shrinkage. These shrinkage phenomena occur within each of the two distinct stages as shown in Figure 2.19. The definition of early age and long term shrinkage depends on the circumstances and time frame of the measurements. Holt

(2001) defined early age shrinkage as the volume changes occurring immediately after concrete placing up to the age of about 24 hours. This period includes the time when the concrete is fluid or liquid, the transition period when it is undergoing early stiffening by the formation of the skeletal frame, and the initial hardening when the concrete is rigid and the formwork or moulds can be removed. Long term shrinkage is generally measured from the starting point of 24 hours after the time of concrete mixing or placing; at the time the mould or framework is removed.

Plastic shrinkage is the change in length on a macroscopic level while the concrete is in its fresh state, i.e. before the concrete has attained any significant strength (Ghoddousi, et al., 2004). Although the material is in its fresh state, cracking can occur. When the rate of evaporation is higher than the rate of bleeding the phenomenon defined as plastic shrinkage occurs. Plastic shrinkage mostly occurs in floor slabs and can sometimes be impossible to prevent. Hasanain et al. (1989) showed that if concrete is shadowed off from direct intense sun light the rate of evaporation can be reduced by as much as 50%. On the contrary Van Dijk & Boardman (1971) showed that slabs cast in the shade can have more cracks than slabs cast in the sun. This phenomenon can be explained by the fact that although the sun raises the surface temperature of the concrete and the evaporation rate, it also increases the rate of hydration of the cement, thus increasing the surface strength of the concrete.

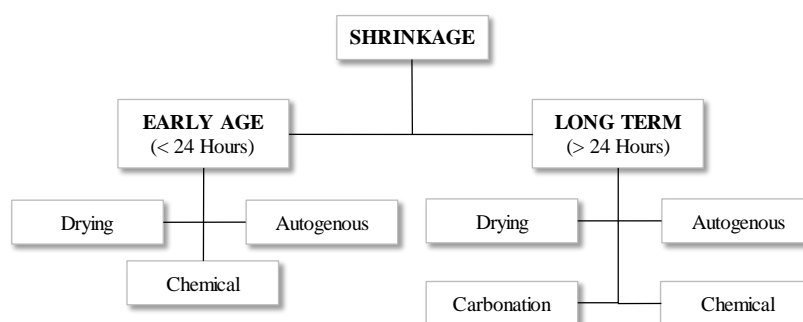


Figure 2.19. Diagram of shrinkage stages and types (based on Holt 2001)

Drying shrinkage is traditionally defined as the reduction in volume or length of cement-based materials resulting from a loss of water from the concrete due to drying (Holt, 2001; Boshoff, 2007). Initially, free excess water escapes to the surface as bleed water, as the heavier aggregate particles settles. This bleeding water can evaporate to the surrounding environment causing the concrete to be subjected to drying. This will cause excess water to be extracted from the interior of the concrete mass (extracted from the capillary voids), which

causes drying shrinkage to an unrestrained hydrated cement paste. The drying mechanisms causing shrinkage are dependent on the internal pore spaces (Holt, 2001). The description of various pore sizes is schematically represented in Figure 2.20 along with the solid particles of the hydrated cement paste. Capillary voids are spaces that were filled with excess water that were removed during the cement hydration reactions. Neville (1970) mentioned that for a matrix with higher cement paste (decrease in the water cement ratio) the relationship between weight loss and shrinkage becomes more linear. It is expected that for a matrix with a lower water cement ratio a denser microstructure will be formed that is composed of smaller pores and a lower pore volume compared to a standard mixture. This will result in a reduction in the drying shrinkage.

Chemical shrinkage occurs mostly during the plastic stage and is a result of the reactions between cement and water, which leads to a volume reduction (Boshoff, 2007). The ingredient in concrete that provides the chemical reactions to bind the mass is the cement particles. The chemical reaction of Portland cement is too complex to be shown by simple chemical equations. One of the most common reactions that take place during hydration when cement and water are added together is:



The volume reduction due to solidification of free water in Equation 2.1 can be theoretically calculated to be up to 10.87 % (Tazawa, et al., 1995). Tazawa et al. (1995) predicted the chemical shrinkage by simple stoichiometric calculations by determining the hydration equations and verified it experimentally. He found that most of the chemical shrinkage turns into internal air voids within the hardened cement paste and did not play a large role in the macroscopic volume or length change of the material.

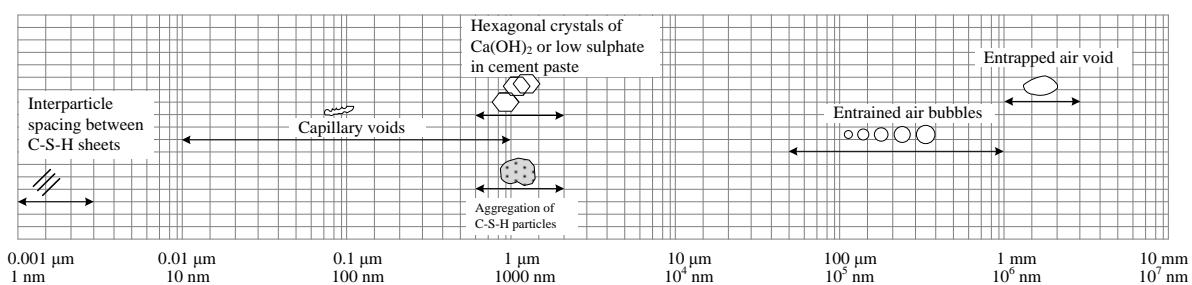


Figure 2.20. Distribution of solids and pores in hydrated cement paste (based on Mehta & Monteiro 1993)

Autogenous shrinkage is defined as the macroscopic volume or length change of cement paste and concrete when moisture transportation to or from the material is prevented. Autogenous shrinkage is a result of chemical shrinkage affiliated with the hydration of cement particles (Japan Concrete Institute, 1999). In Figure 2.21 a schematic description of the composition change due to the cement hydration reactions is presented. It shows how autogenous shrinkage is a portion of the chemical shrinkage (Tazawa, et al., 1995). The chemical shrinkage is an internal volume reduction due to most of the shrinkage turning into air voids, while autogenous shrinkage is an external volume or length change due to the extraction of water from the capillary pores during the hydration of unhydrated cement. It has been shown by Tazawa et al. (1995) that if the water cement ratio is reduced the autogenous shrinkage increases and the drying shrinkage decreases. It has been shown that for a water cement ratio of 0.17 all the change in length during drying can be attributed to autogenous shrinkage and that drying shrinkage did not play a role (Tazawa, et al., 1995).

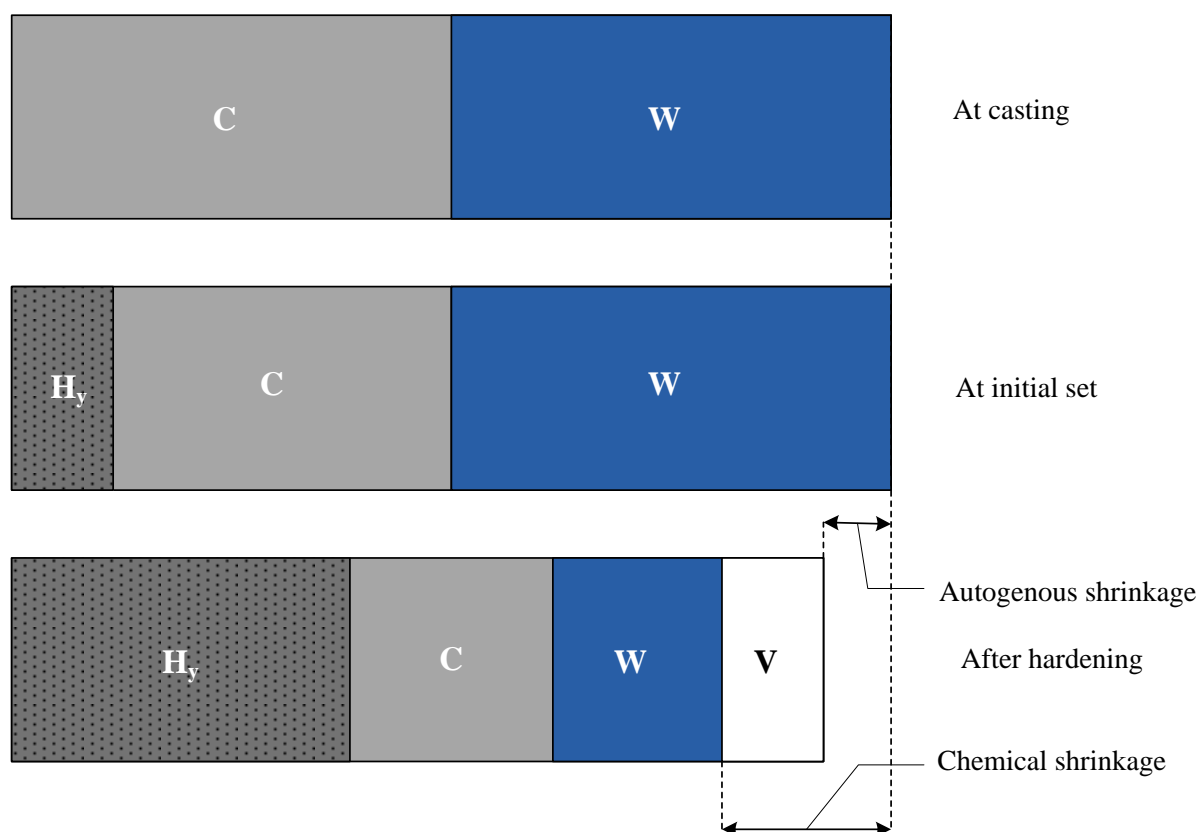
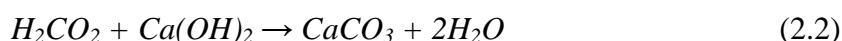


Figure 2.21. Cement hydration reactions causing chemical and autogenous shrinkage (based on Holt 2001); C = unhydrated cement, W = unhydrated water,  $H_y$  = hydration products, and V = voids generated by hydration



Carbonation shrinkage occurs when the hydrated cement paste in the concrete reacts with moisture and carbon dioxide (CO<sub>2</sub>) from the ambient environment (Mehta & Monteiro, 1993), see Equation 2.2. This will cause a slight (almost negligible) shrinkage and a reduction in the pH of the concrete. When the pH of concrete is lowered it can be detrimental to other forms of deterioration; e.g. when the reinforcing steel is exposed due to cracking it can cause corrosion, which can lead to expansion cracking and spalling of the concrete (Kosmatka & Panarese, 1988).



The first step of the reaction is the dissolving of carbon dioxide in the pore water, thus if there is an inadequate amount of water in the pores, carbonation shrinkage will not occur (Boshoff, 2007).

### 2.2.2 Creep and its nature in concrete

The physical nature and mechanisms of creep have been studied for many decades, but they are still not fully understood. A number of materials are subjected to creep; e.g. steel exposed to relatively high temperatures, some rocks that are subjected to high stresses, plastics, and concrete. Creep can be defined as the slow, continuous deformation of a material under constant load (Yanni, 2009).

Depending on the ambient humidity of the environment, the creep of concrete can be separated into two types of creep, namely basic creep and drying creep (Kovler, 1999). Basic creep is defined as the component of concrete under conditions of no moisture movement to or from the surrounding environment. In theory, the measured total length change of a specimen subjected to a sustained load under drying conditions should be the same as the addition between the measured basic creep ( $\epsilon_{bc}$ ) and drying shrinkage ( $\epsilon_{fs}$ ), in the same environmental conditions (Boshoff, 2007). This is however not the case as the total measured creep ( $\epsilon_{tot}$ ) is more than the predicted creep ( $\epsilon_{bc} + \epsilon_{fs}$ ). This difference between the measured creep and the predicted creep is attributed to an apparent mechanism, named drying creep, see Figure 2.22. This extra strain called drying creep ( $\epsilon_{dc}$ ) was first pointed out by Picket (1942). Thus the total strain can be represented as follows:

$$\epsilon_{tot} = \epsilon_{fs} + \epsilon_{bc} + \epsilon_{dc} \quad (2.3)$$

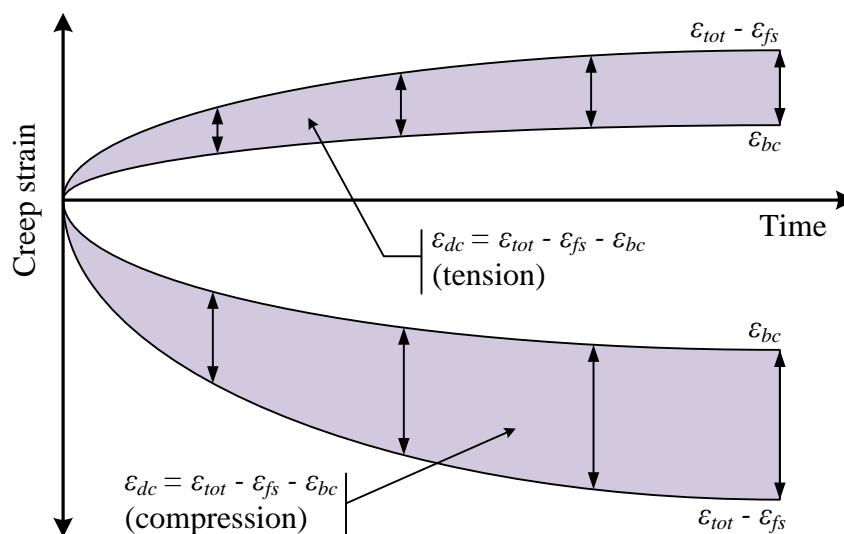


Figure 2.22. Drying creep strain under tension and compression as extra creep strain component (based on Kovler 1999)

### 2.2.2.1 Instantaneous deformation

Concrete like any other structural material exhibits an elastic behaviour when a stress is applied (Atrushi, 2003). The strain at loading is elastic and is indirectly proportional to the static modulus of elasticity at the time the load is applied. During the execution of an experiment the application of the load cannot be applied instantaneously. This will cause the strain to increase due to creep of the concrete during the loading period. This means that the response does not only include an elastic deformation but also a certain creep deformation, that depends on the rate of application of the load (Atrushi, 2003). This makes it difficult to separate the elastic deformation at application of the load and the subsequent creep. However, for practical purposes and for interpretation of test data, the deformations taking place during the loading time (seconds or minutes) is considered as elastic, and the subsequent increase in strain is considered as creep (Atrushi, 2003). This means that all the deformations that takes place during the application of the load is considered as elastic, and is called the instantaneous deformation see Figure 2.23.

### 2.2.2.2 Creep recovery

When the sustained stress is completely removed, the strain immediately decreases by an amount defined as the instantaneous recovery (Atrushi, 2003; Chong, 2004), see Figure 2.23. The instantaneous recovery is less than the instantaneous deformation at loading, since the E-modulus is higher at the time of unloading than at the time of loading. Subsequent to the

instantaneous recovery is the creep recovery, see Figure 2.23. Creep recovery is a gradual decrease in strain over time. Initially the creep recovery exhibits a rapid increase with time but reaches an asymptotic value (Atrushi, 2003). The creep strain developed over the sustained loading period cannot be recovered entirely (permanent creep), with only a relatively small amount being recoverable through creep recovery. Generally the recoverable creep is less than 30% of the total creep strain (Neville, 1970; Chong, 2004).

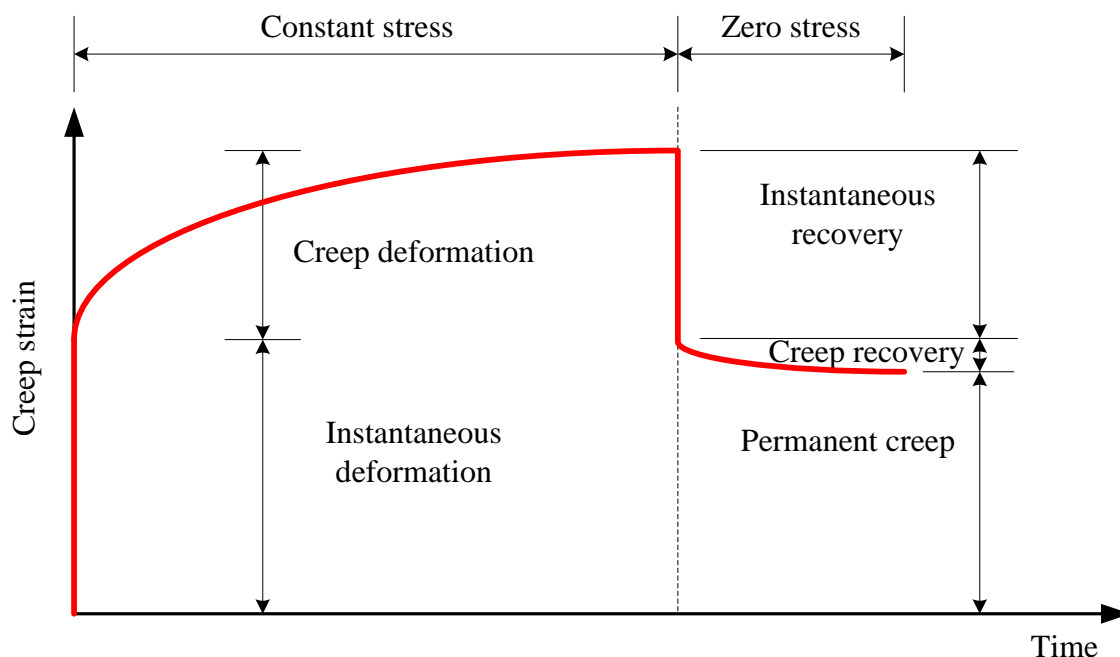


Figure 2.23. Schematic representation of creep over time (based on Atrushi 2003)

### 2.2.2.3 Relaxation of stress

Creep is often denoted as the phenomenon of creep deformation and that of relaxation of stress, but they are of course not the same phenomenon (Atrushi, 2003). Creep and relaxation in concrete is two different expressions of which the strain and stress is a function of time (Neville, 1970). Relaxation is defined as the reduction in stress with time at a constant strain; see Figure 2.24(a). Thus if the creep deformation of a structural element is prevented, then the stress will reduce over time.

Just as in the case of creep, the rate of stress relaxation is higher when loaded at an early age rather than at later ages. This is schematically illustrated in Figure 2.24(b) when comparing the stress relaxation magnitudes  $\Delta\sigma_0$ ,  $\Delta\sigma_1$  and  $\Delta\sigma_2$  at the different loading age's  $t_i$ .

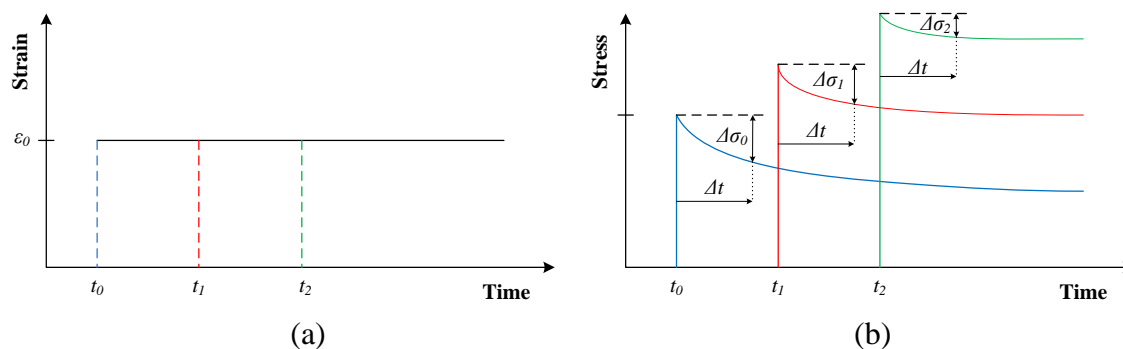
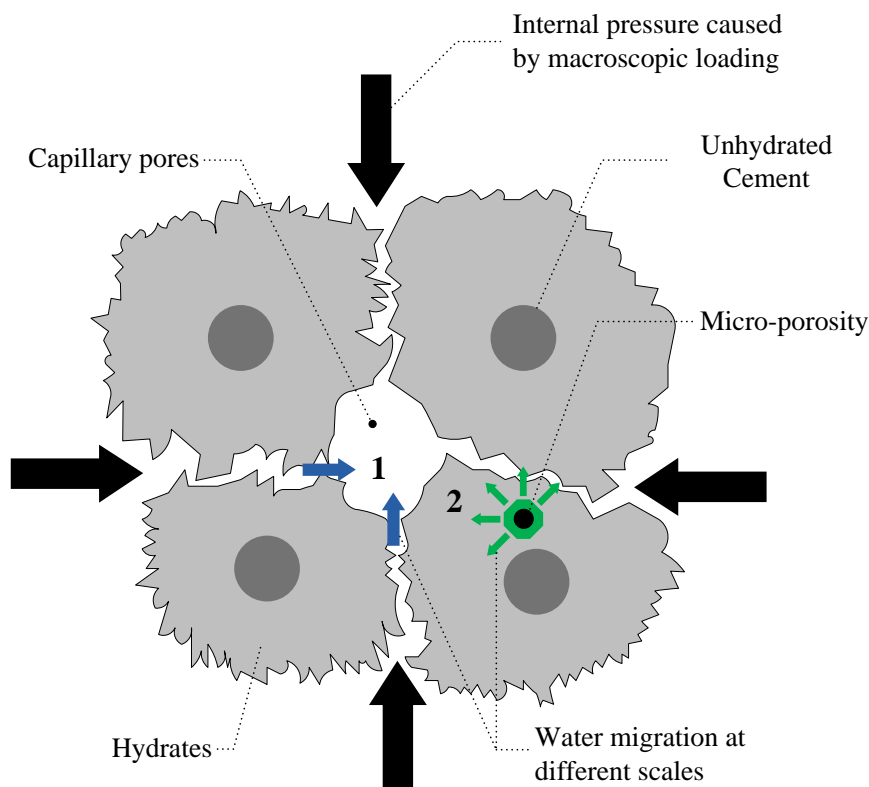


Figure 2.24. (a) Schematic representation of Strain vs. time for stress relaxation of concrete, and (b) effect of loading age on relaxation in concrete specimens subjected to equal initial strains (based on Atrushi 2003)

### 2.2.3 Creep mechanisms

Many theories of creep mechanisms for concrete have been proposed over the years namely, mechanical deformation theory, plastic theory, viscous and visco-elastic theory, elastic after-effect theory, solid solution theory, seepage theory and micro-cracking theory. Neville (1970) and Bissonnette et al. (2007) have narrowed down the theories to be a combination of three mechanisms: (1) Consolidation due to seepage and redistribution of pore water under stress; (2) Viscous-flow of the cement paste caused by sliding or shear of the gel particles; and (3) Micro-cracking.

The first mechanism states that creep is caused due to the water seepage and the redistribution of pore water when under stress. Water seepage occurs at the interface between hydrates (reversible) and the hydrates intrinsic porosity (irreversible) (Benboudjema, et al., 2003). First the macroscopic loading is transmitted to the water absorbed between the hydrated products, in the form of pressure. The absorbed water will then migrate reversibly to the non-saturated capillary pores, see 1 in Figure 2.25. When all the water absorbed between the hydrated products have migrated to the capillary pores the macroscopic loading is then retransmitted to the water absorbed in the intrinsic porosity of the hydrates, which will then also migrate (irreversible) to the capillary pores, see 2 in Figure 2.25. The migration of the absorbed water between the hydrated products is related to the short-term creep. The migration of the water absorbed in the intrinsic porosity is related to the long-term creep, because the migration of the water is much slower due to the high complexity of the microstructure of the hydrated products (Benboudjema, et al., 2001).



*Figure 2.25. Schematic illustration of the creep due to water seepage and redistribution of pore water when under stress (based on Benboudjema et al. 2001 and Benboudjema et al. 2003)*

The second mechanism states that creep is caused by the viscous-flow of the cement paste caused by sliding or shear of the gel particles. During the sliding or shear of the Calcium Silicate Hydrate (C-S-H) sheets, bonds are broken and re-established. This phenomenon occurs in the nano-porosity, dimension of about 1 nm (Benboudjema, et al., 2003). The water absorbed near the C-S-H gel sheets (see 1 in Figure 2.26) contains great absorption energy and is responsible for the reversible creep after unloading. After some water layers (see 2 in Figure 2.26), the absorption energy of the water is much lower than the absorption energy of the water close to the C-S-H gel sheets, thus the movement of this water is irreversible (Benboudjema, et al., 2001). The irreversible part is due to the rupture of the hydrogen bridges in the absorbed water.

Lastly, the formation of micro-cracks in the matrix tends to increase the creep at a higher rate and is the cause of the non-linearity of creep (Neville, 1970). The absence of micro-cracking will not lead to failure if the material is subjected to a sustainable load over a long period. Then again, when micro-cracks are present, creep under sustained loading will propagate these cracks that will lead to failure of the material. This failure of the material applies only

for stress-strength ratios exceeding 0.7 (Neville, 1970). Micro-cracking is responsible for only a part of the total creep and according to Neville (1970) it is about 10% to 25% of the total creep deformation.

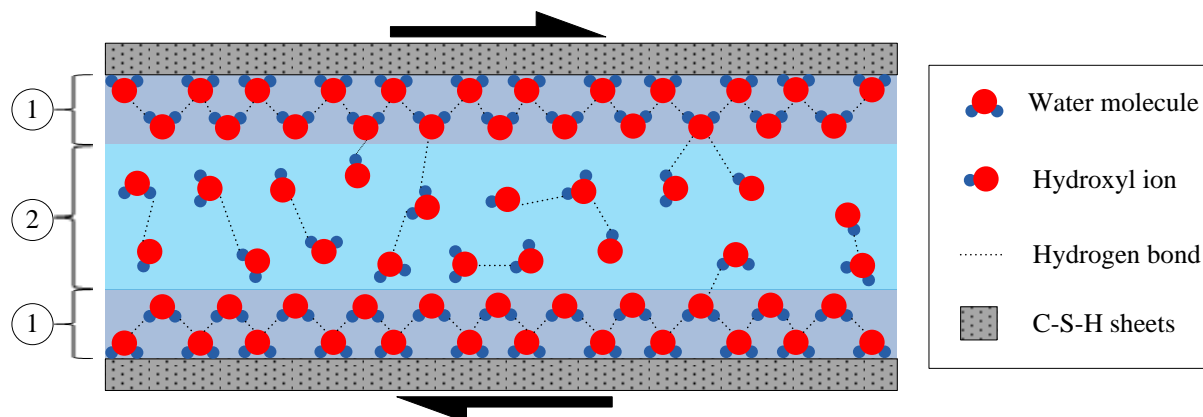


Figure 2.26. Schematic illustration of creep due to viscous-flow of the cement paste caused by sliding or shear of the gel particles (based on Benboudjema et al. 2001 and Benboudjema et al. 2003)

## 2.2.4 Factors affecting creep

The creep of concrete is influenced by a large number of factors. These factors can be subdivided into intrinsic factors and extrinsic factors. Table 2.3 provides a list of the most significant factors that are included in the most widely known creep prediction models (Adam & Taha, 2011). The material factors that are fixed during the whole service life of the concrete are referred to as intrinsic factors. The factors that can have an effect on the creep after casting the concrete are referred to as extrinsic factors (Atrushi, 2003).

Some of these factors are described briefly in the following sections. For a detailed description of the factors affecting the creep of concrete refer to Neville (1970) and Alexander & Beushausen (2009).

### 2.2.4.1 Influence of aggregates

As mentioned in Section 2.2.3, it is the cement paste that undergoes creep but in concrete aggregates are added that do not undergo creep. Research has shown that there is a relation between the aggregate content and the creep of the concrete (Neville 1970) and if the aggregate content is increased a decrease in the creep is found (Atrushi, 2003).

Aggregates contain certain mechanical and physical properties that influence the creep of concrete. According to Neville (1970) these properties include shrinkage and creep of the aggregate itself, and its bond, elasticity, porosity, shape, particle size and grading, and the petrological and mineralogical characteristics. According to Neville (1970) the factor that influences the creep of concrete most is the modulus of elasticity of aggregates. The higher the modulus the better is the restraint against creep of the cement paste.

*Table 2.3. Factors considered in existing creep prediction models*

Intrinsic Factors	Slump
	28-day mean compression strength
	28-day mean modulus of elasticity
	Modulus of elasticity at loading
	Water-cement ratio
	Cement type
	Cement content
	Aggregate content
Extrinsic Factors	Relative humidity
	Temperature
	Curing Regime
	Age at the end of moist curing
	Age at loading
	Specimen size
	Specimen shape
Creep stress ratio	

#### **2.2.4.2 Influence of water/cement ratio**

The water/cement ratio controls the strength, the stiffness and the permeability of the cement paste, and therefore influences the creep of cement paste (Alexander & Beushausen, 2009). It is well known that a decrease in the water cement ratio increases the strength and stiffness of cement paste and an increase in the stiffness decreases the creep of the cement paste. Neville (1970) mentioned that the creep is approximately proportional to the square of the water/cement ratio.

#### **2.2.4.3 Influence of cement type and cement extenders**

Different cement types have different compositions that influence the creep of cement paste. The creep is higher for cements containing a higher  $C_3A$  (tri-calcium Aluminate) content or a lower  $C_3S$  (tri-calcium Silicate) content (Alexander & Beushausen, 2009). Also different

---

cement types have different strengths and fineness, which also affects the creep of cement paste (an increase in both factors implies reduced creep).

The addition of cement extenders like Fly Ash (FA), Silica Fume (SF) and Ground Granulated Blastfurnace Slag (GGBS) has different rates of hydration and therefore the development of strength is different while under loading (Atrushi, 2003). FA and SF reduce the creep if it is incorporated in the concrete mix (Ram, et al., 1981; Buil & Acker, 1985). There exists conflicting results in literature concerning the reduction of creep due to the addition of GGBS. Chern & Chan (1989) reported that the creep increases when GGBS is incorporated in the concrete mix, but according to Neville (1970) the creep can be reduced when GGBS is incorporated.

#### **2.2.4.4 Influence of the relative humidity**

The surrounding environment has an environmental influence on the creep. Relative humidity and temperature are considered as environmental influences and affect the cement gel and the water in it after the concrete has set (Neville 1970). In this section the influence on the creep due to the relative humidity is discussed.

The creep of cement paste is associated to the mobile water in it and the relative humidity affects the mobile water. It is known that the greater the mobile water in the cement paste the greater the creep. However there are two important effects that should be noted, before loading and during loading (Atrushi, 2003; Alexander & Beushausen, 2009). Firstly, if the cement paste is allowed to become in equilibrium with the relative humidity of the surrounding environment (meaning the cement paste is allowed to dry) before loading a decrease in the creep will be experienced if the relative humidity is reduced. This is due to the fact that less mobile water is available in the cement paste. Secondly, cement paste subjected to a lower relative humidity during loading will experience greater creep than when it is subjected to a higher relative humidity. This increase in the creep can be associated with the additional drying creep called the Pickett Effect explained in Section 2.2.2.

#### **2.2.4.5 Influence of the temperature**

As mentioned in the previous section temperature is considered as an environmental influence on the creep of cement paste. In this section the influences of elevated temperatures are



---

discussed, but for the influences of low temperatures on the creep of cement paste the reader is referred to Johansen & Best (1962), CSIR (1988), Marzouk (1992).

The influence of elevated temperatures on creep depends on when the temperature is raised relative to the time of loading (Alexander & Beushausen, 2009). According to Neville (1970) for concrete stored continuously at higher temperatures the creep is significantly less compared to concrete where the temperature is raised a short time before loading. An increase prior to loading for a long time will accelerate the hydration process and gain a higher strength, resulting in a reduction in the creep. According to Alexander & Beushausen (2009) temperatures raised a short time before loading the creep will increase up to about 50 °C, decrease between 50 °C and about 120 °C, and will further increase between 120 °C and about 400 °C. The initial increase in the creep is due to the extrusion of the evaporable water from the cement paste. After the extrusion of all this water the creep is reduced and becomes equal to cement paste stored continuously at higher temperatures a long time before loading. The further increase in the creep for temperatures between 120 °C and about 400 °C is due to the change in the hydrated products at these high temperatures.

#### **2.2.4.6 Influence of age at loading**

The strength of concrete or the cement paste increases with time if adequately cured. Thus concrete loaded at a later age will creep less than when loaded at an earlier age (Alexander & Beushausen, 2009). Also an important factor is that the rate of creep is significantly greater when loaded at an early age compared to when loaded at later age (Atrushi, 2003).

#### **2.2.4.7 Influence of specimen size**

Under drying conditions the creep decreases with an increase in specimen size (Neville, 1970; Atrushi, 2003). This is due to the fact that drying in larger specimens is slower as the core of the specimen has conditions that are similar to being fully saturated (meaning the drying creep will be less). Neville (1970) mentioned that if the thickness of a specimen exceeds 900 mm the size effect becomes negligible. This means that structures as large as dams would exhibit no drying creep, however they do. Thus in literature it is normally found that the size effect is expressed in terms of the volume/surface ratio of the structure (Atrushi, 2003). This is done because the structure size determines the drying rate, which in turn influences the creep rate.

#### 2.2.4.8 Influence of the applied stress level

From the review of literature a direct proportionality between creep and the applied stress (Neville, 1970; Neville, 1996; Atrushi, 2003; Alexander & Beushausen, 2009) is found with a possible exception of specimens loaded at an age less than 24 hours. The stress level is generally expressed as a ratio of the ultimate short-term strength (stress/strength ratio) and is considered as a practical approach to express the relationship between creep and the subjected sustained load. According to Neville (1996) there is no lower limit of proportionality because concrete undergoes creep even at very low stress levels.

The upper limit of proportionality for concrete subjected to uniform compression varies between 0.3 and 0.75 (Neville, 1996; Atrushi, 2003). This limit is reached when severe micro-cracking develops in the concrete. Above the limit of proportionality ( $\eta$ ) the creep increases non-linear with an increase in the stress/strength ratio, this is schematically represented in Figure 2.27.

#### 2.2.5 Creep fracture

For ordinary concrete creep fracture occurs when a sustained load higher than the peak of the creep limit (called the creep fracture limit) is applied, see Figure 2.28. The creep limit is defined as a test that is done over a long period of time (e.g. 30 years) until no more creep occurs (Boshoff, 2007). Research has shown that the creep fracture limit for ordinary concrete can be as low as 60% of the ultimate short term resistance in flexure (Boshoff & van Zijl, 2007). Zhou (1992) found that the creep fracture of notched concrete beams is close to the softening branch of the force-crack mouth opening displacement response. According to the author's knowledge no literature has been published on the creep fracture of SFRC.

### 2.3 Background on Time-dependent Behaviour of SFRC

The time-dependent behaviour of SFRC is still an unfamiliar topic and existing model codes, e.g. the *fib* (*fib* Special Activity Group 5, 2010) Model Code does not include the time-dependent behaviour of SFRC. Before this material can be considered as an established construction material the time-dependent behaviour of SFRC needs to be incorporated in model codes. In this section the time-dependent behaviour of SFRC is discussed based on published literature in this field.

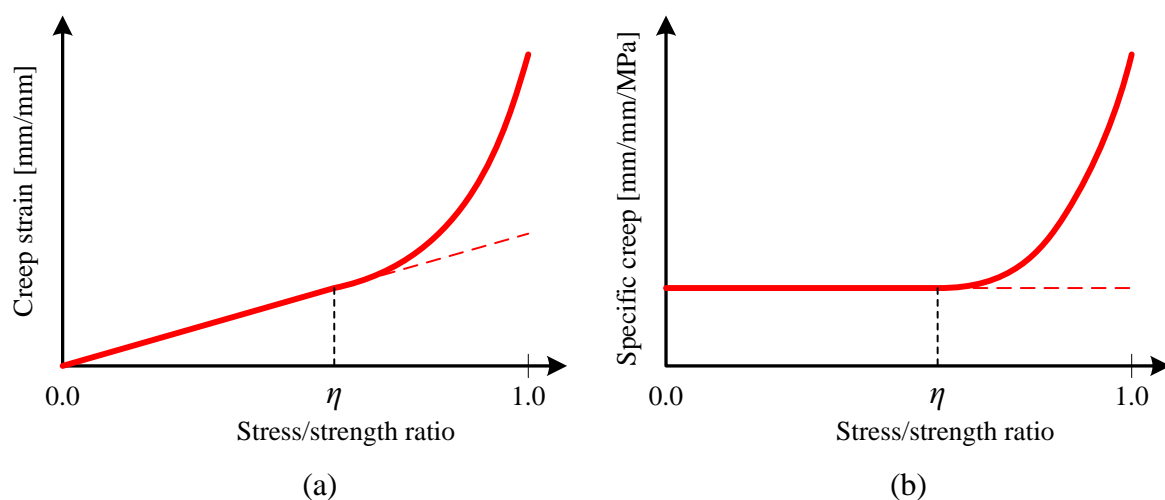


Figure 2.27. (a) Creep strain in relation to the stress/strength ratio, and (b) specific creep in relation to the stress/strength ratio (based on Boshoff 2007)

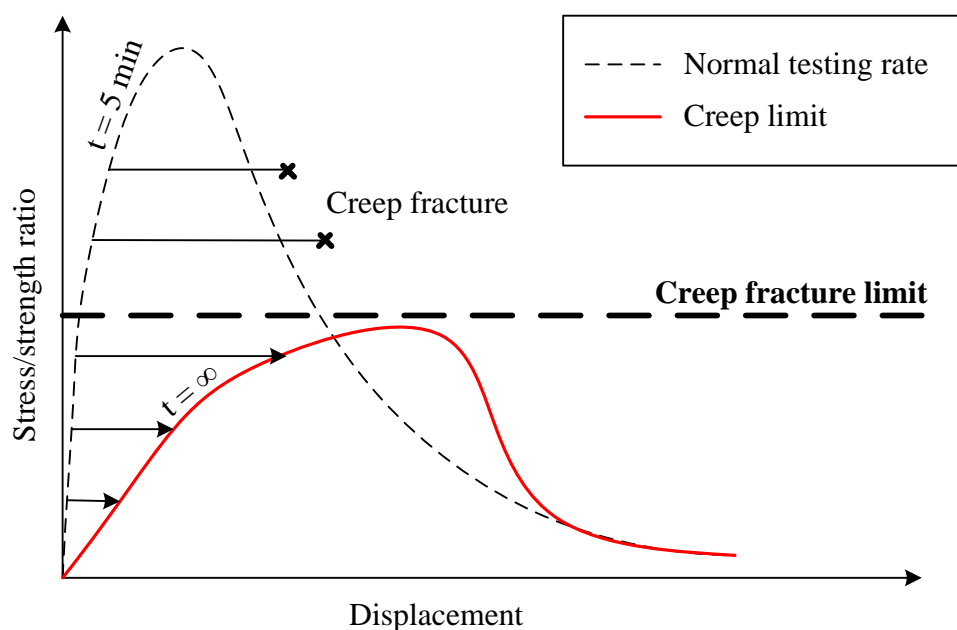


Figure 2.28. Schematic representation of creep fracture and creep limit (based on Boshoff 2007)

### 2.3.1 Strain rate effect

The increase in strength of cement-based materials with an increase in loading rate is well known. Much research has been done in this field for cement-based materials to quantify and model the increase in strength. In this section the effect of strain rate on SFRC is discussed on a macroscopic level based on published researchers.

---

Kormeling & Reinhardt (1987) investigated the effect of strain rate on SFRC in uni-axial tension. Three different strain rates were used:  $1.25 \times 10^{-6}/s$ ,  $2.5 \times 10^{-3}/s$  and  $1.5/s$  to  $20/s$ . They found a significant increase in the tensile strength with the increase in strain rates. The fracture energy and strain at maximum stress also increased at higher strain rates. The fracture energy of SFRC is up to a hundred times larger than that of plain concrete.

Banthia et al. (1993) also reported that for SFRC the strength and toughness increases at higher strain rates. They however found that the improvements were more pronounced at higher fibre volume fractions. In a further research Banthia et al. (1996) concluded that SFRC is effective in improving the fracture energy under impact loading, however the improvements are dependent on fibre type and geometry but are not as pronounced as observed under static conditions.

### **2.3.2 Review on creep of SFRC**

The creep of ordinary concrete has been well studied and quantified for many years. The investigation done by Davis & Davis (1931) was one of the first and most extensive studies done on the creep of concrete under the action of sustained loads. On the other hand, the amount of literature available on the creep of SFRC is insufficient. What sets SFRC apart from ordinary concrete is that even after it has cracked the crack is bridged by the fibres and over time the crack width can increase due to fibre pull-out (Mouton & Boshoff, 2012). In this section previous research done on the creep of SFRC are discussed on a structural, macroscopic and single fibre level.

#### **2.3.2.1 Structural level**

The application of steel fibres in the industry is escalating fast and is becoming an important material in the use of structures (Oslejs, 2008; Ross, 2009), due to the high ductility, high post-cracking tensile strength, high compressive stiffness and strength (Mendes, et al., 2012).

Mendes et al. (2012) executed experimental and numerical studies on a pedestrian bridge of 12 meter span. The bridge is composed of a Steel Fibre Reinforced Self-Compacting Concrete (SFRSCC) deck with a thickness of 40 mm and 2 m wide (hooked-end steel fibres were used), and Glass Fibre Reinforced Polymer (GFRP) I-shape profiles. The load applied to the bridge corresponds to the load combination for the serviceability limit state. From the experimental results it was found that the deflection increased by 151% after 51 days compared to the

---

instantaneous deflection, due to creep effect. The analytical approach used to estimate the creep deflection for 50 and 100 years predicts an increase of 158% and 186%, respectively, when compared to the instantaneous deflection.

It was only recently that researchers have started to investigate the time-dependent behaviour of cracked FRC subjected to flexural loading. A majority of these investigations have been focussed on SFRC (Arango et al., 2012; Barragan et al., 2008; Barragan & Zerbino, 2008; Chanvillard & Roque, 1999; Garcia-Taengua et al., 2014; Granju et al., 2000; Kanstad & Zirgulis, 2012; Nakov & Markovski, 2012; Zerbino & Barragan, 2012).

Blanco (2013) performed sustained load tests on pre-cracked SFRC beams over a period of 150 days. Three pre-cracking widths were considered, namely 0.25 mm, 1.5 mm and 2.5 mm. At each pre-cracking width two theoretical load levels were investigated, 50 % and 60 % of the load registered for the pre-cracking width. The results showed that at each pre-crack width the crack width increased due to creep with an increase in sustained load level. It was also showed that the average crack width due to creep was higher for specimens pre-cracked at larger crack widths. The creep rate over the measured time period decreased with a linear tendency with the logarithm of time. After 100 days the creep rate was barely measurable, averaging around 0.001 mm/day. Similar findings regarding the creep rate were found by Granju et al. (2000). They showed that for cracked SFRC under sustained stress of 60 % of the residual flexural strength the creep strain stabilised after a period of six months.

From the published researchers given above it is shown that significant attention has been given to the investigation of cracked SFRC under sustained flexural loading. However, information on predicting this behaviour is still lacking.

### **2.3.2.2 Macroscopic level**

The amount of information on the tensile creep of FRC is limited and the majority of these investigations were performed over a short-term period (Bissonnette et al., 2007; Gutsch & Rostasy, 1995; Kamen et al., 2009; Kanakubo, 2006; Ostergaard et al., 2001; Swaddiwudhipong et al., 2003). The limited amount of information can be related to the sophisticated equipment required to perform such investigations. This equipment prevents prejudicial hindrances, such as load eccentricity and stress concentrations.

---

The amount of information available on the uni-axial tensile creep of cracked FRC is limited. Among the few published research results are those by Babafemi & Boshoff (2015); Boshoff et al., (2009a); Boshoff & Adendorff (2013), Mouton & Boshoff (2012) and Zhao et al., (2014). The investigations done by Mouton & Boshoff (2012) and Zhao et al., (2014) were on SFRC the rest were on synthetic FRC.

Mouton and Boshoff (2012) did sustained uni-axial load tests on pre-cracked notched prismatic beams made from self-compacting concrete. The specimens were pre-cracked to a crack width of 0.5 mm in a uni-axial tensile test setup and then the specimens were transferred to a uni-axial tensile creep frame where they were subjected to sustained loads of 50 % of the residual axial tensile strength. A large scatter in the results was reported with a total crack opening ranging from 0.07-1.23 mm after a period of three months. They showed that for each specimen the total crack width opening due to the sustained load was almost double to the instantaneous crack opening after the three months. The same specimen configuration and test setup was used in this dissertation and are discussed in Chapter 3.

Zhao et al., (2014) investigated the uni-axial tensile creep of cracked SFRC. The variables investigated were restricted to the pre-cracked width and subjected load level. The specimens had a cylindrical configuration and were cored from prisms. The cylindrical specimens were notched and then initially cracked in a uni-axial tensile test setup to a crack width of 0.05 mm and 0.2 mm after which the specimens were transferred to the creep frames where they were subjected to sustained loads of 30 % of the maximum pre-cracking load. The specimens were subjected to this sustained load for a period of 180 days after which they were unloaded for one week in order to measure the deferred recovery and then reloaded to 60 % (or 30 %) of the maximum pre-cracking load. The results showed that the crack opening due to creep was almost the same magnitude as the instantaneous crack opening after 100 days for sustained load levels of 30 %, ranging between 0.019-0.038 mm. After unloading most of the instantaneous crack opening was immediately recovered, this can thus be considered as an elastic behaviour. The deferred recovery was found to be insignificant after one week with an average of 0.003 mm. After the one week of unloading the specimens were reloaded again to 60 % (or 30 %). For the specimens reloaded to 30 % the instantaneous crack width opening was about the same magnitude as the instantaneous recovery. However, those reloaded to 60 % showed a significantly increase in the instantaneous crack width opening (more than

---

double of those who were reloaded to 30 %). Also the specimens that were reloaded to 60 % showed an increase in the crack width opening.

### 2.3.2.3 Single fibre level

Information regarding the mechanisms that are involved during the time-dependent crack width opening is still lacking. According to the author's knowledge Babafemi & Boshoff (2015) and Boshoff (2007) are the only researchers who conducted sustained single fibre pull-out tests. To perform such tests can be a difficult task due to the sensitivity of the tests.

Boshoff (2007) performed single fibre sustained load tests on micro synthetic fibres (PVA) at a load level of 50 % of the maximum interfacial shear resistance. The test program was divided into two groups, i.e. a group of which the fibres were not debonded before the test started, and another group of which the fibres were fully debonded along the embedment length of the fibre. The latter was achieved by pulling the fibre out at a constant rate until the response indicated that full debonding occurred. All fibre pull-out creep tests pulled out within 70 hours at a load as low as 50 % of the expected strength. The average time for non-debonded creep tests was 57 hours while for the debonded tests it was 16 hours. For PVA fibres no clear trend for the rate of pull-out at a constant load was observed. It was concluded by Boshoff (2007) that the single fibre pull-out creep tests are not representative of the true conditions on a macroscopic scale due to three reasons. Firstly, the embedment lengths of the test were not representative to those on the macroscopic level. Secondly, fibre orientation was not considered and lastly, the load applied to the single fibre creep tests was higher than the load per fibre in a tensile test on a macroscopic level. However, the results showed that the time-dependent crack widening of a macroscopic specimen subjected to a sustained load can be attributed to the time-dependent pull-out of fibres.

Babafemi & Boshoff (2015) performed single fibre sustained pull-out tests on macro synthetic fibres (polypropylene fibres) embedded in a concrete matrix. Five sustained load levels ranging from 50 % to 80 % of the average maximum interfacial shear resistance of specimens tested at 25 mm embedment length were applied to the fibres individually. All single fibre pull-out specimens loaded at 50 % of the quasi-static capacity pulled out over time. Also the results showed that the time-dependent pull-out of the single fibres was dependent on the magnitude of the stress applied: the higher the stress, the quicker the pull-out. Babafemi & Boshoff (2015) mentioned that an important characteristic of polymeric materials, such as

---

polypropylene, is creep. They performed a single fibre creep tests by subjecting 30 % of the average tensile strength over 4 days. The results indicated that a polypropylene fibre can lengthen with up to 40 % at a load as low as 30 % of its maximum capacity over a period of 4 days. From the aforementioned results Babafemi & Boshoff (2015) concluded that the time-dependent crack widening under sustained load has been identified to be caused by two mechanisms: (1) time-dependent fibre pull-out and (2) time-dependent fibre creep.

The mechanisms involved during the time-dependent crack widening of SFRC is still unknown. It is expected that steel fibres would not creep under normal testing conditions. The identification of the mechanisms involved during the time-dependent crack widening of SFRC forms an important part of the investigation done in this dissertation and are investigated comprehensively.

## **2.4 Concluding Summary**

An extensive background study on the mechanical and time-dependent behaviour of SFRC is reported in this chapter. This is not only required to understand the material behaviour so that further research can be done on the material, but also to recognise where research on the material is deficient.

Literature available on the time-dependent behaviour of SFRC is insufficient, especially on the time-dependent crack opening after the material has cracked. Only few published research studies have been done in this field (Kanstad & Zirgulis, 2012; Mouton & Boshoff, 2012; Nakov & Markovski, 2012; Zhao, 2014). The factors causing the time-dependent crack opening after the material has cracked is still unknown. The only way to understand these factors is to explore them on a single fibre level. According to the authors knowledge there is no published literature available on the single fibre time-dependent pull-out behaviour of steel fibres.

Before SFRC can commercially be utilised as a construction material, guidelines need to be instituted on how to predict the time-dependent behaviour. Thus is it important to understand the factors causing the time-dependent crack opening of SFRC so that they can be incorporated in these guidelines and then be used to predict the time-dependent crack opening of SFRC.



# Chapter 3

---

## Experimental Framework

In this chapter the experimental methodology for the investigations done on cracked SFRC is explained. In this study cracked SFRC was investigated under short- and long-term loading conditions. To understand the post-crack behaviour of cracked SFRC under the aforementioned loading conditions, experimental investigations were performed at two levels, namely: macroscopic and single fibre level. The investigations performed at the macroscopic level were to determine the compressive strength of the concrete with and without steel fibres, the uni-axial tensile strength and the time-dependent Crack Mouth Opening Displacement (CMOD) behaviour under uni-axial tensile sustained loading. To study the mechanisms involved during the post-crack behaviour and the factors affecting it, investigations were performed on a single fibre level under short- and long-term loading conditions. Quasi-static single fibre pull-out tests were performed to investigate the factors affecting the pull-out behaviour of steel fibres. In this study the factors that were investigated were the fibre embedded inclination angle, the fibre embedment length, fibre mechanical anchorage and the rate of loading application. Single fibre sustained load tests were performed to study the mechanisms involved during fibre pull-out creep and the factors affecting it. The following factors were investigated: the applied sustained load, the embedded fibre inclination angle and the mechanical anchorage of the fibre. Single fibre sustained load tests were also performed on pre-damaged specimens to investigate whether the pre-damaged process has an effect on the pull-out creep behaviour.

A thorough description of the materials and methodologies used in performing the aforementioned investigations are presented in this chapter. This includes the mix materials used during the mixing procedure, the preparation of the specimens, the experimental methodologies and test setup, and the experimental programmes followed in performing these tests.

### 3.1 Concrete Mix Materials and Mixing Procedure

#### 3.1.1 Concrete mix materials

Three types of hooked-end fibres were used in this research project, namely DRAMIX 3D-65/60-BG, 4D-65/60-BG and 5D-65/60-BG hooked-end fibres, see Figure 3.1. The three types of hooked-end steel fibres are designated by TYPE A, TYPE B and TYPE C, see Table 3.1. The fibres were supplied by BEKAERT in Belgium. Table 3.1 gives the properties of the fibres as received from the suppliers. Only one mix of SFRC was used for all the tests. The materials used in the mix composition were: Portland cement CEM I 52.5N, Dynamon SP1 superplasticiser supplied by MAPEI South Africa, water, crushed greywacke stone and natural sand (known locally as Malmesbury sand). At least 90 % of the coarse aggregate (crushed greywacke stone) passed through the 6 mm sieve size and retained on the 4.75 mm sieve. The fine aggregate (Malmesbury sand) had a finess modulus (FM) of 2.3 and the grading as obtained from a sieve analysis is shown in Figure 3.2. The mix constituents and proportions are given in Table 3.2.



Figure 3.1. The hooked-end steel fibres used in this study




#### 3.1.2 Mixing procedure

All mixes were done in a 50 litre Gustav Eirich concrete pan mixer. The mix proportions given in Table 3.2 were decreased proportionally to the required mix size. The following sequenced procedure was followed during each mix:

- The mixing drum was saturated with water and dried with industrial tissue paper. This ensured minimum water absorption by the mixing drum during the mixing process.
- The dry constituents were added to the mixing drum in the following order: sand, cement and stone. This ensured a minimum loss of the fine cement particles during the mixing process. The dry constituents were mixed for about 60 seconds.
- The water was then added to the mix and allowed to mix for another 60 seconds.
- Next the super plasticiser was slowly added over a period of about 30 seconds and the mix was continued for another 60 seconds.
- The mixing process was then stopped to perform a slump test to verify the workability of the mix without fibres, refer to Section 3.1.3.
- For mixes without fibres the mixing procedure stopped at this point. However, for mixes with fibres, the fibres were added over a period of 60 seconds to ensure that the fibres were uniformly dispersed. The mixing process was then continued for another 60 seconds.
- Finally, the mixing process was stopped and a slump test was performed on the SFRC mix to investigate the effect of fibres on the workability of the concrete, refer to Section 3.1.3.

Upon completion of the mixing process the fresh concrete was cast into the moulds that had been prepared prior to the mixing process.

*Table 3.1. Properties of the hooked-end steel fibres used in this study*

Fibre type	A	B	C
Trade name: DRAMIX	3D-65/60-BG	4D-65/60-BG	5D-65/60-BG
Profile			
Tensile strength (on the wire) [MPa]	1160	1500	2300
Relative density	7.85	7.85	7.85
Modulus of elasticity [GPa]	210	210	210
Length ( $l_f$ ) [mm]	60	60	60
Diameter ( $d_f$ ) [mm]	0.9	0.9	0.9
Aspect ratio ( $l_f/d_f$ )	67	67	67

### 3.1.3 Workability of concrete in the fresh state

The workability characteristics of SFRC are complex and are influenced by many factors of which the most important are the shape of the fibres, their aspect ratio and volume fraction (Swamy, 1974; Swamy & Mangat, 1974, Swamy & Jojagha, 1982). The addition of fibres to

concrete increases its viscosity; this is due to the larger surface area than the aggregates thus, fibres take up more cement to coat which increases the concrete's internal resistance to flow. Also fibres can form a network structure in concrete, which can effectively restrain the segregation of the aggregates. Fibres thus decrease the ability of the concrete to flow in the fresh state (Chen & Liu, 2005). This can pose serious implications on compaction during in-situ casting of concrete. Therefore the concrete mix must be designed to accommodate the fibres.

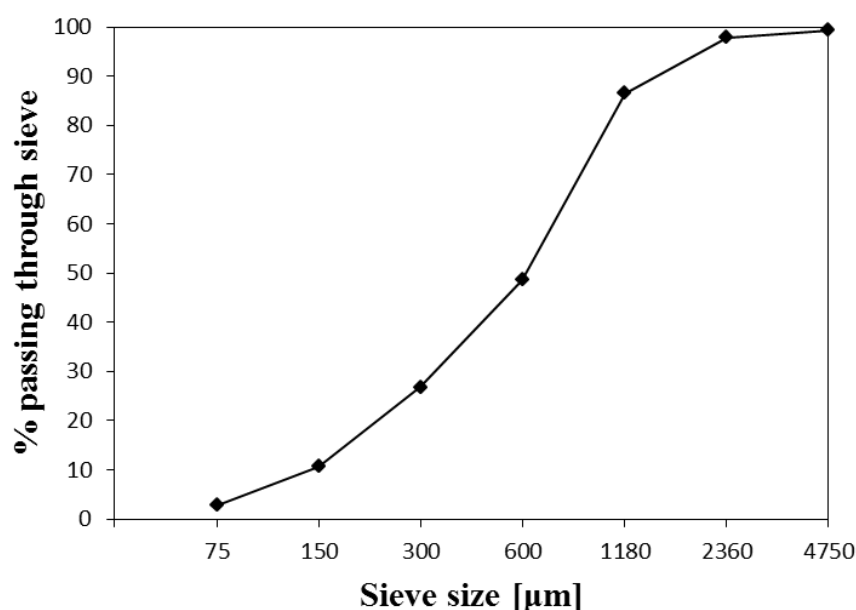


Figure 3.2. Fine aggregate grading: Malmesbury sand

Table 3.2. Mix constituents for SFRC

Material type	kg/m <sup>3</sup>
Cement (CEM I 52.5N)	395
Water	190
Sand (Malmesbury, FM = 2.3)	990
Stone (Greywacke, 6 mm nominal size)	800
Superplasticiser (0.5% by weight of binder)	1.975
Fibres (0.5% by volume)	39.25

For this research study a normal concrete mix was designed to accommodate a fibre volume of  $V_f = 0.5\%$ . The workability of the concrete mixes without and with fibres was investigated with the slump test (BS EN 12350-2, 2000). An average slump value of 230 mm was obtained for the normal concrete mixes without the addition of fibres. The concrete with the addition of

fibres showed an average slump value of 130 mm. Thus by adding 0.5 % of TYPE A hooked-end steel fibres to the concrete mix a 43.5 % reduction in the slump value was observed.

## 3.2 Mechanical and Time-dependent Behaviour of SFRC on a Macroscopic Level

### 3.2.1 Compression strength test

Compressive strength tests were performed on the concrete mixes with (SFRC) and without fibres (plain concrete) to investigate the influence of TYPE A hooked-end steel fibres on the compressive strength of concrete. The specimen size and test procedure was done according to the requirements of BS EN 12390 (2002). Cubic specimens with an edge length of 100 mm were tested for both mixes, with and without fibres, which had been cured for 28 days. The tests were performed at a loading rate of 0.3 MPa/s in a Contest Material Testing Machine that has a capacity of 2000 kN. The test programme is summarised in Table 3.3.

*Table 3.3. Compressive strength test programme*

Concrete Mix	Specimen size [mm <sup>3</sup> ]	No. of Mixing Batches	No. of specimens tested
Plain concrete	100 x 100 x 100	8	30
SFRC		3	16

### 3.2.2 Uni-axial tensile test

#### 3.2.2.1 Research programme

The post-cracking tensile behaviour of concrete reinforced with low fibre content is best simulated by the stress-crack width,  $\sigma$ - $w$ , relationship (Montaignac, et al., 2011) and can be directly obtained from uni-axial tensile tests (RILEM TC 162-TDF, 2001). This type of test setup requires sophisticated equipment to prevent prejudicial hindrances, such as load eccentricity. Due to the high cost of the aforementioned equipment it is not always possible to perform direct uni-axial tensile tests. Therefore, other more simple and economic methods for determining the  $\sigma$ - $w$  response of SFRC are assessed by an inverse procedure that are obtained by indirect tensile tests that include experimental test results, such as: splitting tensile tests (ASTM C496, 2004; Abrishambaf, et al., 2015); three-point notched beam bending tests (RILEM TC162-TDF, 2000); wedge splitting test (Skocek & Stang, 2008). However, Cunha (2010) showed that when comparing the  $\sigma$ - $w$  relationships acquired from the indirect tests

with the uni-axial tensile  $\sigma$ - $w$  response a vast discrepancy was observed. Therefore, the uni-axial tensile test is the most appropriate method for obtaining the tensile material properties of concrete composites (Boshoff, 2007; van Mier & van Vliet, 2002; Wille, et al., 2014).

Uni-axial tensile tests were performed to determine the post-crack uni-axial tensile strength of SFRC. Because of the complexity of performing such a test no accorded standard test method for performing such a test is yet reported. Test setups for performing a direct tensile test have been reported by a number of scholars which was comprehensively reviewed by Wille, et al. (2014). They mentioned that aspects such as the specimen shape, which can be distinguished into dogbone shape, unnotched and notched prisms or cylinders, and the type of gripping system (fixed or rotating boundary conditions), can significantly influence the test results

The design of the specimen preparation and test setup used in this study were based on Mouton (2012). Only TYPE A hooked-end steel fibres were used during the mixing procedure (see Section 3.1.2).

### 3.2.2.2 Specimen preparation

#### 3.2.2.2.1 Preparation of moulds

Steel moulds used to cast  $100 \times 100 \times 500 \text{ mm}^3$  concrete prisms were modified to incorporate specially designed steel anchors, see Figure 3.3. The anchors were embedded in the specimen moulds prior to casting the concrete protruding at both ends of the steel moulds, see Figure 3.4. Eye-like steel hooks required to connect the specimens to the test setup were welded to the ends of the anchors.

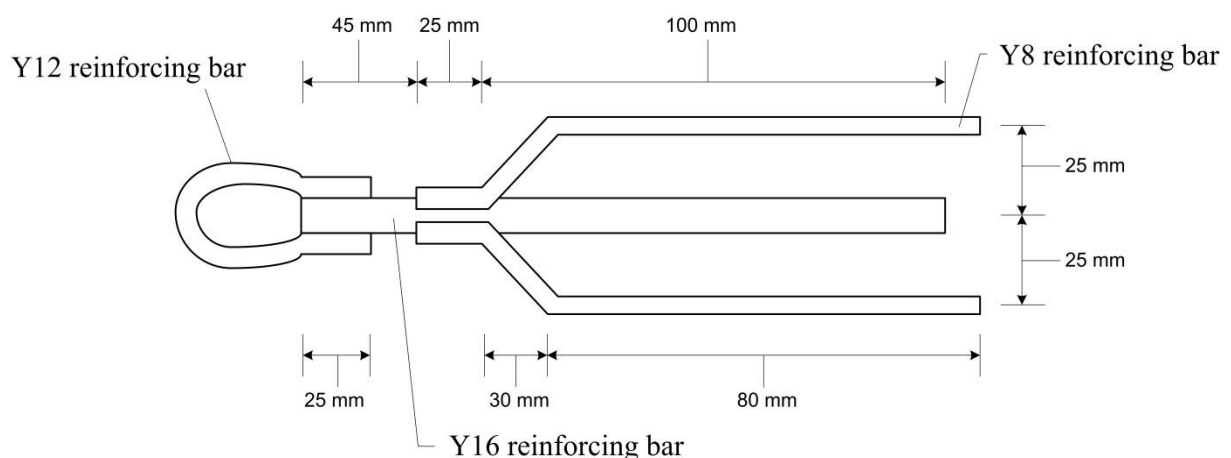


Figure 3.3. Dimensions of steel anchors (Mouton 2012)



Figure 3.4. Steel anchors positioned in steel mould

### 3.2.2.2.2 Casting procedure

The casting procedure was done in two layers on a vibration table. The fibre concrete was placed in the middle portion of the mould and allowed to gently flow under vibration to fill up the anchors, see Figure 3.5. This procedure ensured that the positioning of the anchors was undisturbed during the casting of the fibre concrete. After casting, all specimens were moved to a climate controlled room with a temperature of  $23 \pm 1$  °C and a relative humidity of  $65 \pm 5$  %.

Step 1: Place 1ste scoop of SFRC in middle of the mould



Step 2: Vibrate



Step 3: Add 2de scoop while vibrating



Figure 3.5. The casting procedure for uni-axial tensile specimens proceeding in steps



### 3.2.2.2.3 Curing of specimens

All specimens were demoulded after  $24 \pm 2$  hours and transferred to a curing tank where they were submerged in water and cured at a temperature of  $23 \text{ }^\circ\text{C}$  for a further 27 days before testing at an age of 28 days. A uni-axial tensile specimen with end anchors is shown in Figure 3.6.

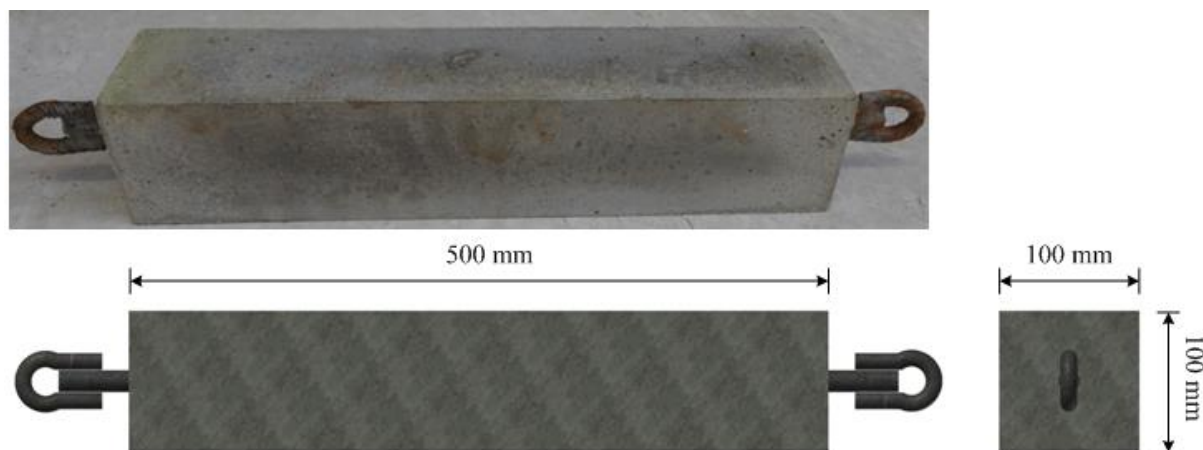


Figure 3.6. Dimensions of uni-axial tensile specimen with end anchors

### 3.2.2.2.4 Preparation of samples for testing

After aging for 28 days the specimens were removed from the curing tank and prepared for testing. A peripheral notch, with a depth of 10 mm, was made with a 3 mm diamond blade at the centre of the specimens, see Figure 3.7. This resulted in an effective cross-section area of  $6400 \text{ mm}^2$ .

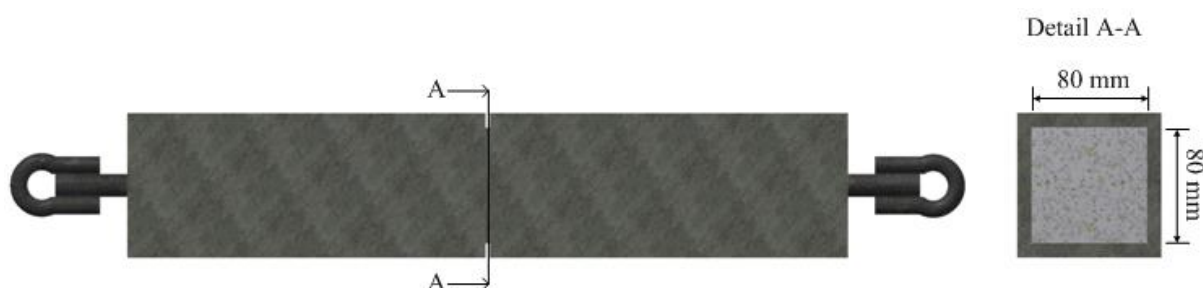


Figure 3.7. Uni-axial tensile specimen with a peripheral notch at the centre

### 3.2.2.3 Experimental methodology and setup

The uni-axial tensile tests were performed in a Zwick Z250 Universal Testing Machine that has a capacity of 250 kN, see Figure 3.8. The specimens were connected to the test machine by means of the Eye-like steel hooks that were welded to the ends of the steel anchors. In



Figure 3.8 a detailed description of the connection between the specimen and the test machine is schematically presented. The specimen was connected to the test machine through specially designed links. Each link consisted out of two steel plates of 10 mm thickness. On both sides of the specimen a link was connected through the eye-like steel hooks of the specimen and a central supporting plate (10 mm thick), by passing two galvanised bolts (20 mm diameter) through each link. The supporting plates were gripped by the hydraulic clamps of the test machine. This type of connection ensured a rotational degree of freedom around the two horizontal axes at each support. This ensured that no prejudicial hindrances that cause internal moments are subjected to the specimen.

The test machine is equipped with a 250 kN load cell that was used to measure the load during testing. The displacement readings over the notch were measured with two HBM Linear Variable Displacement Transducers (LVDTs). The LVDTs were attached to the specimen by means of a removable aluminium frame with a gauge length of 100 mm. The readings were recorded with an electronic data acquisition system supplied with the testing system.

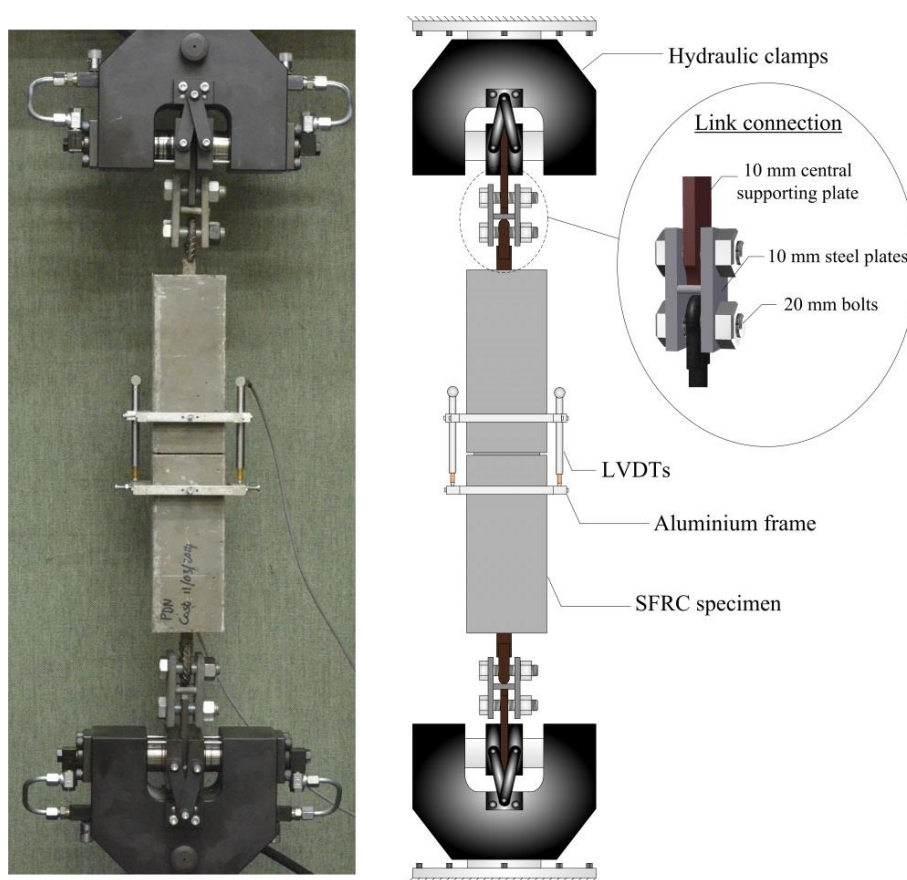


Figure 3.8. Uni-axial tensile test setup

### **3.2.2.4 Experimental programme**

A total of six specimens were tested. The specimens were cast from two batches, three specimens from each batch. The specimens were pre-loaded to 1 kN to stiffen the connection links between the specimen and the test machine. Thereafter the tests commenced at a loading rate of 0.01 mm/s that was controlled by the speed of the crossheads of the machine. The tests were aborted once a crack width opening of 6 mm was reached.

### **3.2.3 Pre-cracked sustained load tests**

#### **3.2.3.1 Research programme**

The primary objective of this research programme is to investigate the Crack Mouth Opening Displacement (CMOD) of pre-cracked SFRC specimens under sustained uni-axial tensile loading. Performing sustained uni-axial tensile load tests on pre-cracked specimens can be an intricate task, due to the sophisticated test setup required to perform such experiments (Babafemi & Boshoff, 2015; Boshoff, 2007; Mouton & Boshoff, 2012; Zhao, et al., 2014).

Due to the post-crack residual strength of SFRC it is important to understand the post-crack behaviour before performing the pre-cracked sustained loading tests, see Section 3.2.2 The applied sustained loads were based on the post-crack residual strength to ensure that complete fracture would not take place when the loads were applied. The experimental setup used for the sustained loading tests were designed by Mouton (2012). Only TYPE A hooked-end steel fibres were used during the mixing procedure (see Section 3.1.2).

#### **3.2.3.2 Specimen preparation**

The preparation and configuration of the pre-cracked sustained loading specimens was the same as described in Section 3.2.2. At an age of 28 days the specimens were pre-cracked, before being moved to the sustained loading setup. Crack initiation occurred abruptly and as soon as the crack appeared the load was removed. The same tests setup as described in Section 3.2.2 was used to pre-crack the specimens.

#### **3.2.3.3 Experimental methodology and setup**

Mouton (2012) designed eight loading frames that were erected in a climate controlled room, with a temperature of  $23 \pm 1$  °C and a relative humidity of  $65 \pm 5$  %, see Figure 3.9. Each loading frame could accommodate two specimens at a time, connected in series. A detailed

description of a loading frame is schematically presented in Figure 3.10. Free hanging weights attached to two pivot beams were used to apply a sustained load to the specimens. Before the specimens were inserted into the frame the pivot beams were positioned horizontally with a stopper mechanism. The free hanging weights were then applied to the pivot beams that were transmitted to the stopper mechanism. This allowed the specimens to be inserted into the frames load free. The sustained load was then transferred to the specimens by slowly releasing the stopper mechanism. The stopper mechanism also functioned as a safety mechanism to stop the sudden drop of the pivot beams during failure of one or both specimens under sustained loading. The specimens were connected to the loading frames with the same connection links as described in Section 3.2.2. This ensured that no internal moments were induced in the specimens during testing.

The displacement readings over the notch were measured with two 10 mm HBM LVDTs. The LVDTs were attached to the specimen by means of a removable aluminium frame with a gauge length of 70 mm. A HBM Spider8 data acquisition system was used to record the readings. The acquisition system was started before the application of the loads. The load was applied within 60 seconds by releasing the stopper, as mentioned above, while ensuring that no dynamic loading occurred.



*Figure 3.9. The loading frames used for pre-cracked sustained loading tests*

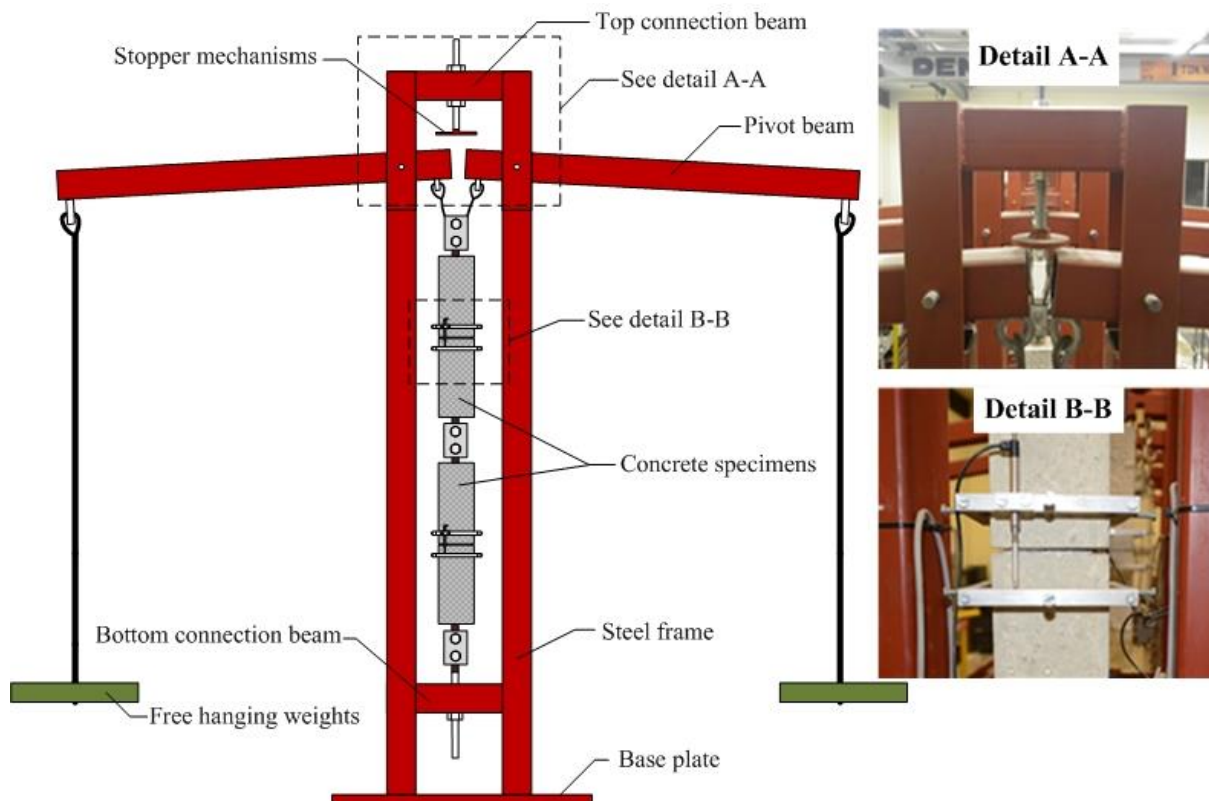


Figure 3.10. Schematic representation of the loading frames used in the sustained loading tests.

The loading frames were calibrated prior to the setting up of the pre-cracked specimens. The calibration process was necessary to determine the weight needed to apply the required load. The calibration process was done with a HBM 50 kN load cell that was placed in the position to be occupied by the specimens, see Figure 3.11. The load cell was connected to a HBM Spider8 data acquisition system. The pivot beams were positioned by the stopper mechanism so that no load was applied to the load cell. The load cell was then zeroed by the software program provided with the acquisition system before the stopper mechanism was released transferring the load provided by the pivot beams to the load cell. One free weight at time was placed simultaneously on each cable connected to the pivot beams until the correct load output was achieved. The free hanging weights were conventional steel weights of 3 kg, 4 kg, 5 kg and 10 kg. Lead weights weighing 100 kg each were also used. Smaller weights were used to calibrate the loading frames to the nearest 0.1 N.

### 3.2.3.4 Experimental programme

A total of 12 specimens were prepared from four separate mixing batches. In Table 3.4 the required load levels investigated together with the number of specimens tested at each load

level are shown. The required load levels considered for the study were based on a percentage of the post-crack residual strength of each specimen. However, it should be remarked that the average applied load is the same in the two tensile beams of each loading frame, and given the natural differences between the post-crack residual strength of each specimen, the actual applied load level percentage is slightly different from the required load level percentage.

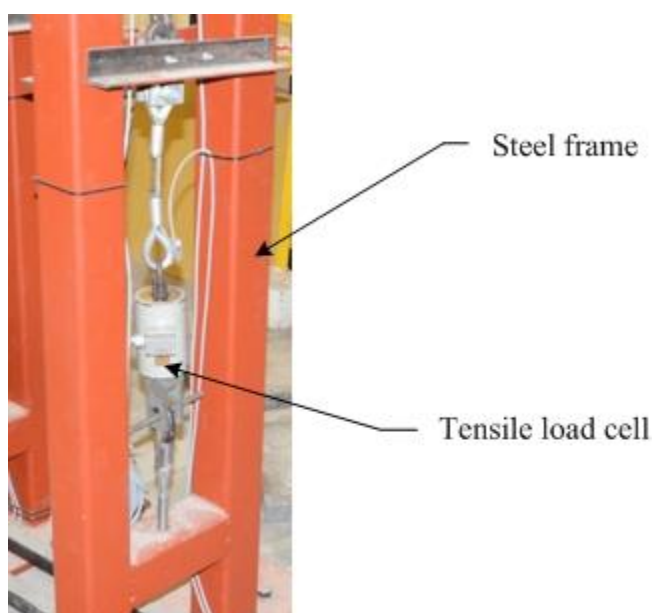


Figure 3.11. The load cell positioned in the loading frame during calibration process

The specimens were tested unsealed meaning that moisture movement to and from the specimens were allowed; therefore basic creep, drying creep, crack widening and drying shrinkage occurred at the same time. If the specimens were sealed only basic creep would have occurred. The tensile creep of the material was found to be insignificant compared to the CMOD under uni-axial tensile loading (Mouton & Boshoff, 2012), while the drying shrinkage was measured separately and could be subtracted from the readings recorded over the cracked notched area, see Section 3.2.4.

Table 3.4. Pre-cracked uni-axial tensile sustained loading test programme

Required load level	30%	50%	70%	85%
Number of specimens tested	3	3	3	3

### 3.2.4 Drying shrinkage test

The drying shrinkage of the SFRC was measured on three 100 x 100 x 500 mm<sup>3</sup> unrestrained specimens, see Figure 3.12. The specimens were placed on PVC rollers to minimise the restraint against shrinkage. The shrinkage deformation was measured with two 10 mm HBM



LVDTs. The LVDTs were fixed to a removable aluminium frame with a gauge length of 300 mm. A HBM Spider8 data acquisition system was used to record the readings. The shrinkage strain was multiplied by the gauge length (70 mm) of the sustained loading specimens to determine the drying shrinkage displacements caused in the sustained loading specimens. These displacements were subtracted from the displacements measured during the sustained loading test to obtain the load-related CMOD under sustained loading.

The preparation of the drying specimens was the same as described in Section 3.2.2 except that the moulds were not modified to incorporate the steel hooks and neither were they notched. The drying shrinkage test was performed under the same climate conditions as the pre-cracked sustained load tests.



*Figure 3.12. Drying shrinkage test setup*

### **3.3 Mechanical and Time-dependent Behaviour on a Single Fibre Level**

#### **3.3.1 Quasi-static single fibre pull-out tests**

##### **3.3.1.1 Research programme**

The post-crack behaviour of SFRC is governed by the cumulative individual interactions of each bridging fibre with the concrete matrix. The individual contribution of a single bridging fibre between randomly distributed fibres is often represented by the response of a single fibre pull-out test. In a single fibre pull-out test the pull-out force is represented as a function of the pull-out slip (Boshoff et al. 2009; Cunha et al. 2010; Robins et al. 2002; Wille & Naaman

2012). There are several factors that can affect the pull-out behaviour of steel fibres, see Section 2.1.2.3.

Single fibre pull-out tests were performed to investigate certain factors affecting the pull-out behaviour of steel fibres. The investigation was restricted to the influence of the fibre embedded inclination angle, the fibre embedment length, fibre mechanical anchorage and the rate of loading application.

### **3.3.1.2 Specimen preparation**

The concrete matrix of the single fibre pull-out specimens contained no fibres except for the single embedded fibre. The mixing procedure is described in Section 3.1.2. A specimen configuration was chosen so that it can fit into the hydraulic clamps of the testing machine. 100 x 100 x 100 mm<sup>3</sup> cube moulds were modified in order that the specimens could be cast into a rectangular prism shape. The modified cube moulds and dimensions of the test specimens are presented in Figure 3.13.

After the mix was cast into the mould a single fibre was carefully inserted to the correct embedment length in the middle of the specimen. The fibres that were embedded at a certain inclination angle were bent prior to the insertion of the fibres at the specific embedded inclination angles to be tested. Straight steel fibres were obtained by cutting off the hooked-ends of the TYPE A fibres with pliers. Care was taken to ensure that no rough edges were created after cutting the hooked ends. Figure 3.14 shows a TYPE A fibre with the hooked-ends removed. After the fibres were inserted the moulds were gently vibrated to ensure that no voids were formed between the fibre and the matrix. Adequate care was taken to ensure that the fibre remained vertical and at the correct embedment length. All specimens were demoulded after  $24 \pm 2$  hours and transferred to a curing tank where they were cured by submerging in water at a temperature of 23 °C for a further 27 days before testing at an age of 28 days.

### **3.3.1.3 Experimental methodology and setup**

The pull-out tests were performed in a Zwick Universal Materials Testing Machine that has a capacity of 250 kN. The specimens were gripped with the fitted hydraulic clamps. A protruding fibre gripping setup was designed to ensure that the bond between the protruding fibre and the matrix was not damaged when gripping the fibre. A small hole was drilled in the

head of a bolt to thread the fibre and a gripping screw was used to clamp the fibre in position, see Figure 3.15. A 500 kg load cell connected in series was used to take the readings of the force exerted during the test. The fibre pull-out slip was measured with two 50 mm HBM LVDTs. The LVDTs were fixed to the fibre gripping setup. A HBM Spider8 data acquisition system was used to record the readings. Care was taken during testing to ensure that no slippage took place between the hydraulic clamps and the specimen, and between the protruding fibre and the fibre grip setup.

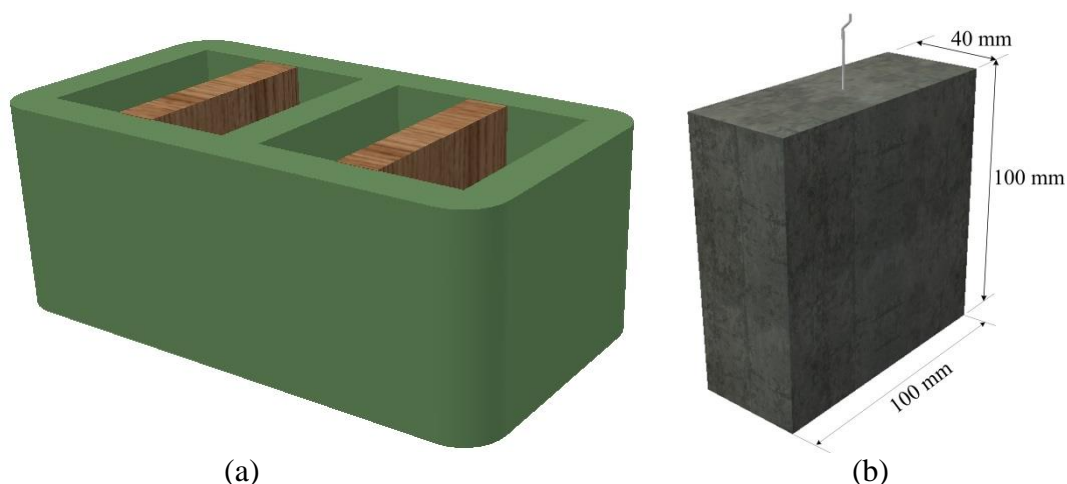


Figure 3.13. (a) Modified cube moulds to cast single fibre pull-out specimens, (b) the dimensions of the single fibre pull-out specimens

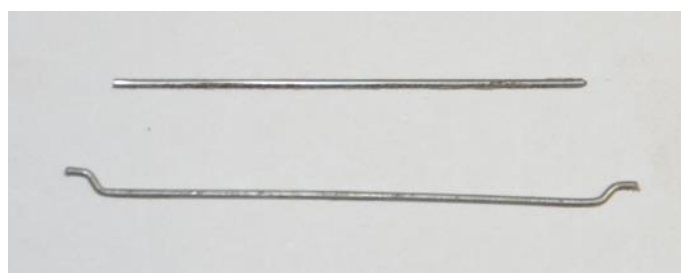


Figure 3.14. Straight steel fibre obtained by cutting the hooked-ends of a TYPE A fibre.

### 3.3.1.4 Experimental programme

As mentioned previously, the single fibre pull-out behaviour can be affected by numerous factors. The factors that were investigated in this research project were the rate of loading application, the fibre embedment length, the fibre embedment inclination angle and the fibre mechanical anchorage. All tests were performed in a climate controlled room with a temperature of  $23 \pm 1$  °C and a relative humidity of  $65 \pm 5$  %. The experimental programme for the investigation of each factor is discussed next. The labels given to each test series were



based on alphanumeric characters separated by underscores. The first string indicates the fibre anchorage type which also represents the fibre type (S-straight, A, B and C), the second string indicates the fibre embedment length,  $l_b$  in mm (for instance lb15 represents a fibre embedment length of 15mm), the third numeral indicates the embedded inclination angle,  $\theta$ , with respect to the fibre pull-out force direction in degrees and finally the last numeral indicates the pull-out rate,  $\dot{\Delta}$ , in mm/s.

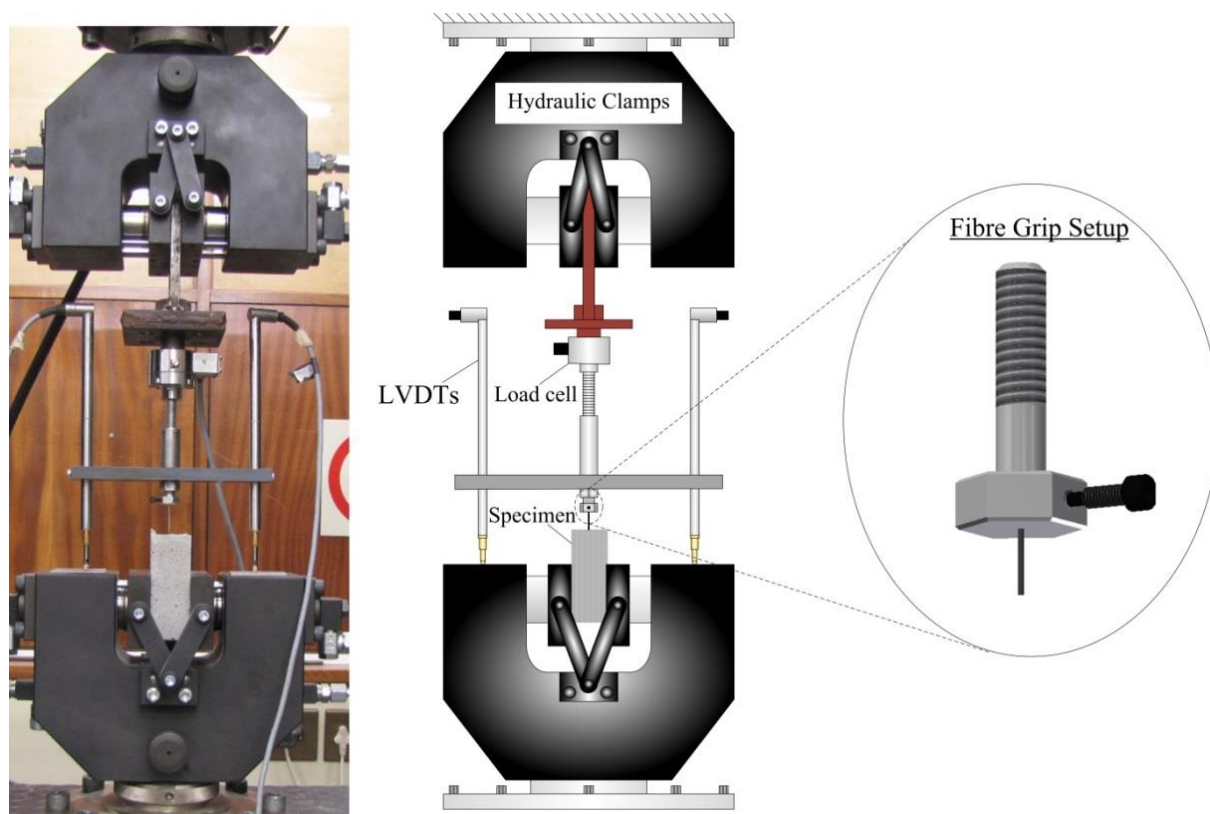


Figure 3.15. Single fibre pull-out test setup

#### 3.3.1.4.1 Pull-out loading rate

Five different pull-out loading rates were investigated for straight and TYPE A hooked-end fibres, namely: 0.00025 mm/s, 0.0025 mm/s, 0.025 mm/s, 0.25 mm/s and 2.5 mm/s. All fibres were embedded at an inclination angle of  $0^\circ$  and an embedment length of 15 mm. For the straight series S\_lb15\_0\_2.5, S\_lb15\_0\_0.25, S\_lb15\_0\_0.0025 and S\_lb15\_0\_0.00025 were cast from the same mixing batch. The results of test series S\_lb15\_0\_0.025 in Section 3.3.1.4.4 were used in this test programme. For the TYPE A hooked-end series A\_lb15\_0\_2.5, A\_lb15\_0\_0.25, A\_lb15\_0\_0.0025 and A\_lb15\_0\_0.00025 were cast from the same mixing batch. The results of test series A\_lb15\_0\_0.025 in Section 3.3.1.4.3 were used in this test program. A summary of the test programme for straight and TYPE A hooked-end

fibres are shown in Tables 3.5 and 3.6, respectively, together with the number of specimens tested at each loading rate.

*Table 3.5. Quasi-static single fibre pull-out test programme for different loading rates on straight fibres*

Series	Anchorage	$l_b$ [mm]	$\theta$ [°]	$\dot{\Delta}$ [mm/s]	No. of specimens
S_lb15_0_0.00025	Straight	15	0	0.00025	5
S_lb15_0_0.0025				0.0025	4
S_lb15_0_0.025				0.025	4
S_lb15_0_0.25				0.25	3
S_lb15_0_2.5				2.5	7

*Table 3.6. Quasi-static single fibre pull-out test programme for different loading rates on TYPE A hooked-end fibres*

Series	Anchorage	$l_b$ [mm]	$\theta$ [°]	$\dot{\Delta}$ [mm/s]	No. of specimens
A_lb15_0_0.00025	A	15	0	0.00025	5
A_lb15_0_0.0025				0.0025	7
A_lb15_0_0.025				0.025	8
A_lb15_0_0.25				0.25	6
A_lb15_0_2.5				2.5	9

### 3.3.1.4.2 Fibre embedment length

Three embedment lengths were investigated for TYPE A hooked-end fibres, namely: 7.5 mm, 15 mm and 30 mm. All fibres were embedded at an inclination angle of 0°. The tests were performed at a pull-out rate of 0.025 mm/s. Series A\_lb7.5\_0\_0.025 and A\_lb30\_0\_0.025 were cast from the same mixing batch. The results of test series A\_lb15\_0\_0.025 in Section 3.3.1.4.3 were used in this test programme. A summary of the test programme is shown in Table 3.7 together with the number of specimens tested at each embedment length.

### 3.3.1.4.3 Fibre inclination angle

Five embedded inclination angles were investigated for TYPE A hooked-end fibres, namely: 0°, 15°, 30°, 45° and 60°. The fibres had an embedment length of 15 mm. The tests were performed at a pull-out rate of 0.025 mm/s. All specimens were cast from the same mixing

batch. A summary of the test programme is shown in Table 3.8 together with the number of specimens tested at each inclination angle.

*Table 7. Quasi-static single fibre pull-out test programme for different embedment lengths*

Series	Anchorage	$l_b$ [mm]	$\theta$ [°]	$\dot{\Delta}$ [mm/s]	No. of specimens
A_lb7.5_0_0.025	A	7.5	0	0.025	8
A_lb15_0_0.025		15			8
A_lb30_0_0.025		30			6

*Table 3.8. Quasi-static single fibre pull-out test programme for different embedded inclination angles*

Series	Anchorage	$l_b$ [mm]	$\theta$ [°]	$\dot{\Delta}$ [mm/s]	No. of specimens
A_lb15_0_0.025	A	15	0	0.025	8
A_lb15_15_0.025			15		8
A_lb15_30_0.025			30		9
A_lb15_45_0.025			45		8
A_lb15_60_0.025			60		8

#### 3.3.1.4.4 Fibre mechanical anchorage

Three different types of hooked-end steel fibres were investigated. Single fibre pull-out tests were performed on straight steel fibres to distinguish the mechanical bond mechanism from the cohesive and friction mechanisms. The configuration of the different mechanical anchorages and properties of the fibres are presented in Table 3.1. All fibres were supplied by BEKAERT in Belgium. As mentioned previously the straight fibres were obtained by cutting off the hooked-ends of the TYPE A hooked-end fibres with pliers. All fibres were embedded at an inclination angle of 0° and an embedment length of 15 mm. The tests were performed at a pull-out rate of 0.025 mm/s. Series S\_lb15\_0\_0.025, B\_lb15\_0\_0.025 and C\_lb15\_0\_0.025 were cast from the same mixing batch. The results of test series A\_lb15\_0\_0.025 in Section 3.3.1.4.3 were used in this test programme. A summary of the test programme is shown in Table 3.9 together with the number of specimens tested at each anchorage type.

*Table 3.9. Quasi-static single fibre pull-out test programme for different mechanical anchorages*

Series	Anchorage	$l_b$ [mm]	$\theta$ [°]	$\dot{\Delta}$ [mm/s]	No. of specimens
S_lb15_0_0.025	Straight				4
A_lb15_0_0.025	A	15	0	0.025	8
B_lb15_0_0.025	B				8
C_lb15_0_0.025	C				8

### 3.3.2 Single fibre sustained load tests

#### 3.3.2.1 Research program

The time-dependent behaviour of pre-cracked SFRC under sustained uni-axial tensile loading has only recently been investigated (Mouton & Boshoff, 2012; Zhao, et al., 2014). Therefore the mechanisms causing the increase in the time-dependent CMOD under sustained uni-axial tensile loading is still not fully apprehended.

Single fibre sustained load tests were performed to investigate the mechanisms causing pull-out creep. The single fibre pull-out behaviour is affected by numerous factors as mentioned in Section 3.3.1. It is therefore expected that the pull-out creep would also be affected by these factors. In this study the investigation was restricted to the applied sustained load, the fibre embedded inclination angle and the fibre mechanical anchorage. In addition the pull-out creep behaviour of pre-damaged specimens was also investigated.

#### 3.3.2.2 Specimen preparation

The same specimen preparation procedure was followed as in Section 3.3.1.2 except the specimens were cast in cube moulds with 100 mm side lengths. The cube moulds and dimensions of the test specimens are presented in Figure 3.16. The specimens were removed from the curing baths a day prior to testing. A 12 mm hole was drilled in the concrete specimens on the opposite side of the protruding fibre to a depth of about 40 mm. Threaded bars (10 mm diameter) were affixed in the holes with epoxy glue, see Figure 3.17. Care was taken to ensure that the threaded bars stayed perpendicular to the surface into which the holes were drilled. The specimens were then left in the climate room for a further 24 hours before testing commenced.

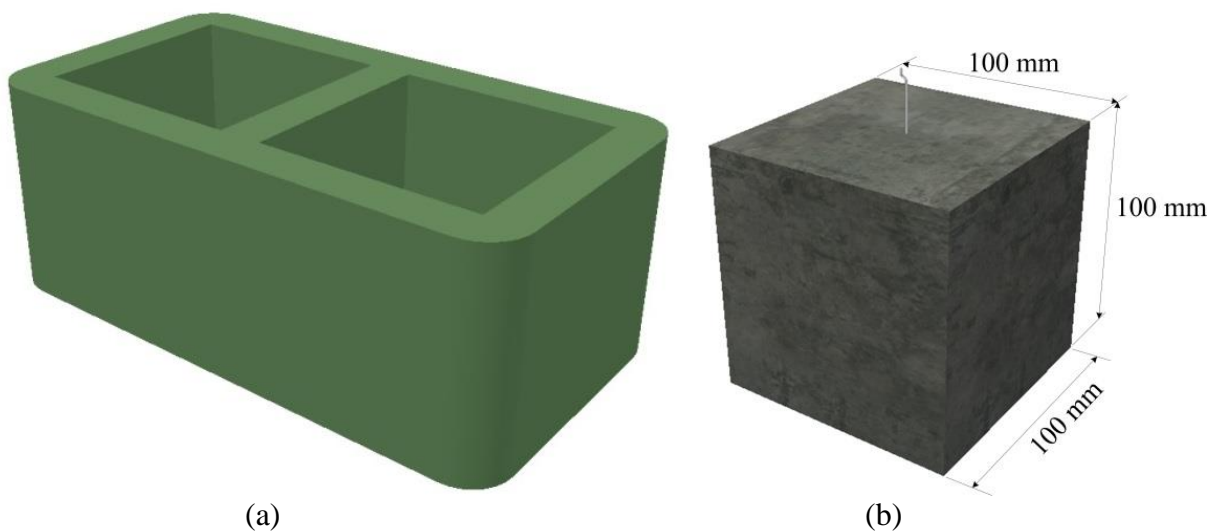


Figure 3.16. (a) Cube moulds to cast single fibre sustained load specimens, (b) the dimensions of the single fibre sustained load specimens

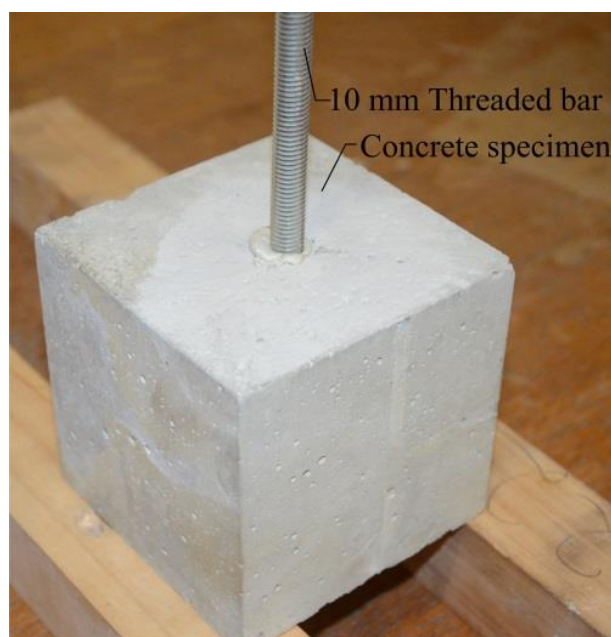


Figure 3.17. Sustained load specimen after threaded bar is affixed

### 3.3.2.3 Experimental methodology and setup

A simple test setup was designed where free hanging weights were used to apply the load, see Figure 3.18. Three supporting frames were designed of which each can hold eight specimens at a time. Each specimen was anchored to the frames using the 10 mm threaded bar that was affixed in the concrete specimen on the opposite side of the protruding fibre. A similar gripping setup as shown in Section 3.3.1.3 was used with the addition that free hanging weights can be used to apply the load, see Figure 3.18. The pull-out creep was measured

optically by taking digital images with a microscope that contains a 3.1 Mega-pixel EC 3 Leica camera. These images were scaled with a fixed calibration plate to give the correct measurements. An example of the measuring method is demonstrated in Figure 3.19. The images were taken at different time periods  $n$ . The pull-out creep at time  $n$  was calculated by measuring the difference between lengths  $L_n$  and  $L_0$ . Length  $L_0$  is the length immediately after the load was applied. The free hanging weights were conventional steel weights of 3 kg, 4 kg, 5 kg and 10 kg. Smaller weights were used to correctly apply the load to the nearest 0.1 N. The load was applied to the single fibre within 60 seconds by adding weights carefully and ensuring that no dynamic loading occurred.

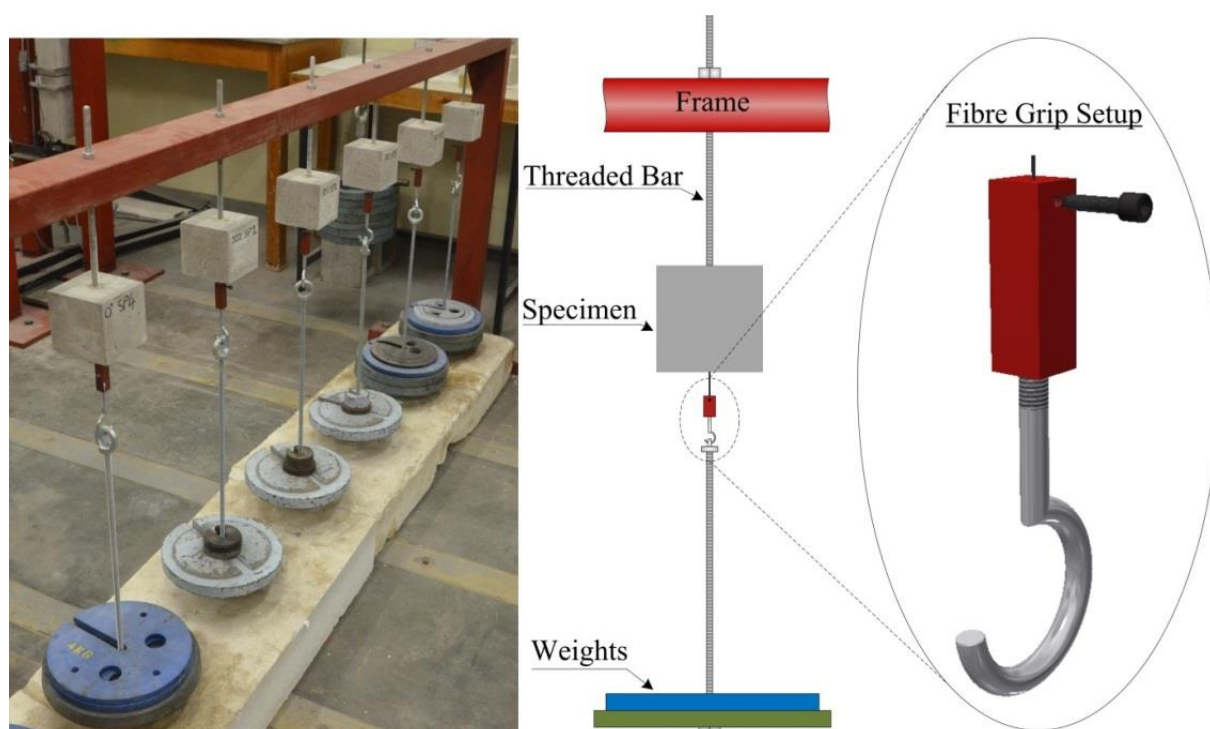


Figure 3.18. Single fibre sustained load test setup

### 3.3.2.4 Experimental programme

As mentioned earlier the pull-out creep can be affected by numerous factors. Due to the limited number of specimens that can be tested at a time, the investigation in this research project was restricted to the applied sustained load, the fibre embedded inclination angle and the fibre mechanical anchorage. A set of single fibre sustained load tests were also performed on pre-damaged specimens. All tests were performed in a climate controlled room with a temperature of  $23 \pm 1$  °C and a relative humidity of  $65 \pm 5$  %. The experimental programme for the investigation of each factor is discussed in the following sections.



Labels were given to each test series that were based on alphanumeric characters separated by underscores. The first string indicates the fibre anchorage type which also represents the fibre type (A, B and C), the second numeral indicates the fibre embedment inclination angle,  $\theta$ , with respect to the fibre pull-out force direction in degrees and finally the last numeral indicates the sustained load level in a percentage of the average maximum pull-out rate force. All specimens cast for single fibre sustained load tests had a fibre embedment length ( $l_b$ ) of 15 mm.

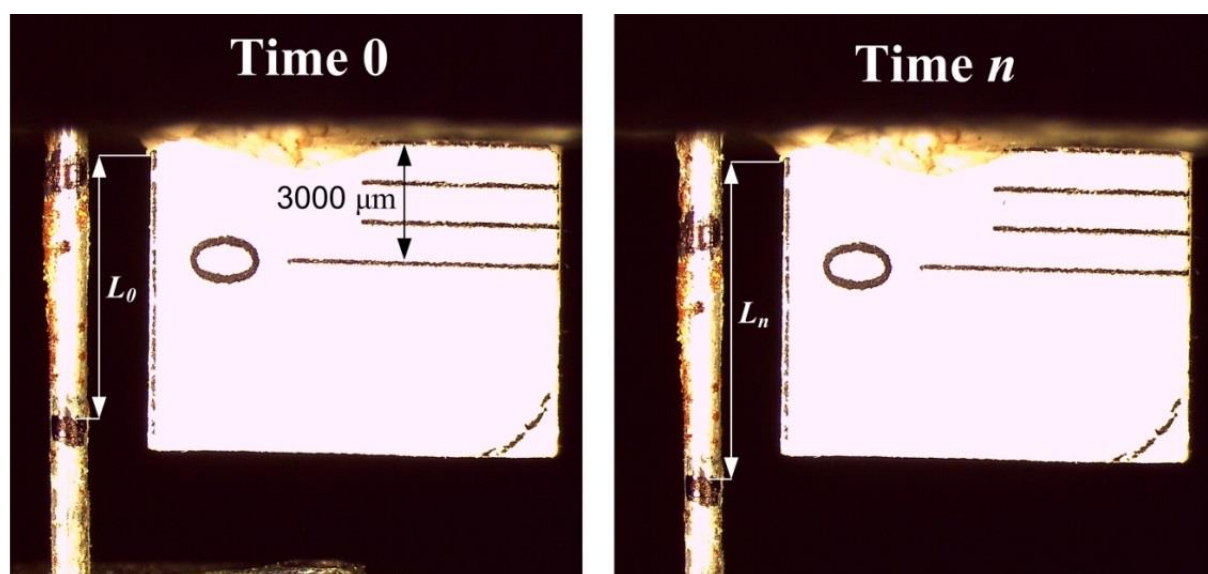


Figure 3.19. An example of the pull-out creep calculation using the microscope images.

#### 3.3.2.4.1 Applied sustained load

Four different applied sustained load levels were tested for TYPE A hooked-end fibres, namely: 30 %, 50 %, 70 % and 85 % of the average maximum pull-out rate force, determined from the single fibre pull-out rate tests, see Section 3.3.1.4.1. All fibres were embedded at an inclination angle of  $0^\circ$ . All specimens were cast from the same mixing batch. A summary of the test programme is shown in Table 3.10 together with the number of specimens tested at each sustained load level.

Table 3.10. Single fibre sustained load test programme for different sustained load levels.

Series	Anchorage	$\theta$ [ $^\circ$ ]	Load level [%]	No. of specimens
A_0_30	A	0	30	3
A_0_50			50	3
A_0_70			70	3
A_0_85			85	3

### 3.3.2.4.2 Fibre inclination angle

Three inclination angles were tested for TYPE A hooked-end fibres, namely: 0°, 30° and 60°. All tests were performed at a sustained load level of 50 % of the average maximum pull-out force, determined from the single fibre pull-out tests at different embedded inclination angles, see Section 3.3.1.4.1. Series A\_30\_50 and A\_60\_50 were cast from the same mixing batch. The results of test series A\_0\_50 in Section 3.3.2.4.1 were used in this test programme. A summary of the test programme is shown in Table 3.11 together with the number of specimens tested at each embedded inclination angle.

*Table 3.11. Single fibre sustained load test programme for different embedded inclination angles*

Series	Anchorage	$\theta$ [°]	Load level [%]	No. of specimens
A_0_50	A	0	50	3
A_30_50		30		3
A_60_50		60		3

### 3.3.2.4.3 Fibre mechanical anchorage

Three different types of hooked-end steel fibres were tested, namely: TYPE A, TYPE B and TYPE C, see Section 3.1.1 for the definition of the types of hooked-end steel fibres. All tests were performed at a sustained load level of 50 % of the average maximum pull-out force, determined from the single fibre pull-out tests for different mechanical anchorage types, see Section 3.3.1.4.3. All fibres were embedded at an inclination angle of 0°. Series B\_0\_50 and C\_0\_50 were cast from the same mixing batch. The results of test series A\_0\_50 in Section 3.3.2.4.1 were used in this test programme. A summary of the test programme is shown in Table 3.12 together with the number of specimens tested for each mechanical anchorage type.

*Table 3.12. Single fibre sustained load test programme for different mechanical anchorages*

Series	Anchorage	$\theta$ [°]	Load level [%]	No. of specimens
A_0_50	A	0	50	3
B_0_50	B			3
C_0_50	C			3

### 3.3.2.4.4 Pre-damaged sustained load

For the pre-damaged sustained load tests the single fibre specimens were pre-damaged prior to the sustained loads being applied. The same test setup that was used for the quasi-static



---

single fibre pull-out tests (see Section 3.3.1.3) were used to pre-damage the specimens. The pre-damaged process was performed up to a certain pull-out slip which is discussed in Section 5.2.1.4. The specimens were pre-damaged at a pull-out loading rate of 0.025 mm/s.

Pre-damaged sustained load tests were performed on TYPE A hooked-end steel fibres at a sustained load level of 50 % of the average maximum pull-out force, determined from the single fibre pull-out rate tests, see Section 3.3.1.4.1. A total of three specimens that were cast from the same mixing batch were tested. For each specimen the fibre was embedded at an inclination angle of 0°.

### **3.4 Concluding Summary**

This chapter presented a description of the concrete mix materials used, the mixing procedure and the preparation of the specimens for the experimental test programmes performed on a macroscopic and single fibre level. A thorough description of the experimental methodologies and test setups to perform these experimental test programmes was also presented.

The investigations performed at the macroscopic level were done on SFRC. The short- and long-term behaviour was investigated. The short-term investigations performed were compressive and uni-axial tensile tests. Pre-cracked sustained uni-axial tensile load and drying shrinkage tests were performed to investigate the long-term behaviour of SFRC. The specimens were unsealed meaning that moisture movement to and from the specimens were allowed. This allows drying creep and drying shrinkage to occur which are not present in sealed conditions.

The investigations performed at a single fibre level were quasi-static single fibre pull-out and single fibre sustained load tests. The quasi-static single fibre pull-out tests were performed to investigate the factors affecting the pull-out behaviour. Whereas the single fibre sustained load tests were performed to investigate the mechanisms involved during fibre pull-out creep. These mechanisms are thought to be the cause of the time-dependent crack opening of SFRC under sustained loading.

The results of all experimental test programmes and the discussions of the findings are presented in the subsequent chapters.

# Chapter 4

---

## Mechanical and Time-dependent Behaviour of SFRC on a Macroscopic Level

In this chapter the experimental results performed on SFRC at a macroscopic level are presented and discussed. The addition of steel fibres to the matrix of normal concrete was investigated under short- and long-term loading conditions. The chapter commences with the results of the short-term mechanical responses of SFRC. This includes compressive and uni-axial tensile strength results. The uni-axial tensile strength test was performed to acquire information about the post crack behaviour of SFRC. The long-term result includes the time-dependent CMOD behaviour of cracked SFRC. Sustained uni-axial tensile load tests on pre-cracked SFRC specimens were performed over a period of 240 days. Drying shrinkage tests were performed to distinguish between the drying shrinkage and the time-dependent CMOD. Also presented is a brief discussion of the restraining ability of steel fibres on the drying shrinkage of normal concrete.

## 4.1 Compressive Strength

In this section the results of the compressive strength tests performed on the concrete mixes with (SFRC) and without fibres (plain concrete) are presented. The tests were performed to investigate the influence of steel fibres on the compressive strength of concrete.

### 4.1.1 Results

In Table 4.1 the compressive strength results of plain concrete and SFRC are presented. The compressive strength is calculated as follow:

$$f_{cm} = \frac{P}{A_c} \quad (4.1)$$

where  $f_{cm}$  is the compressive strength [MPa],  $P$  is the crushing load [N] and  $A_c$  is the cross-sectional area [ $\text{mm}^2$ ] perpendicular to the load.

*Table 4.1. Average compressive strength at 28 days and density of the prismatic square cubes*

Concrete Mix	$f_{cm}$ [MPa]	CoV of $f_{cm}$ [%]	Density [ $\text{kg/m}^3$ ]	CoV of density [%]
Plain concrete	54.35	4.50	2314.64	1.21
SFRC	60.22	2.74	2370.63	1.19

The results presented in Table 3.1 shows that the addition of 0.5 % of TYPE A hooked-end steel fibres to plain concrete increased the compressive strength with 10.8 %. The Coefficient of Variation (CoV) of the  $f_{cm}$  for plain concrete and SFRC was 4.5 % and 2.74 %, respectively. The density for both plain and SFRC was also determined. The addition of the steel fibres at the dosage used increased the density by an insignificant amount of 2.42 %. The CoV of the density for plain concrete and SFRC was 1.21 % and 1.19 %, respectively. The CoV of the  $f_{cm}$  and the density for plain concrete and SFRC were relatively low. This indicates a good repeatability and consistency of the respective mixing batches.

### 4.1.2 Discussion

The compression behaviour of FRC is dependent on various factors, namely: the type of fibre added, the volume fraction of fibres added, the fibre geometry, the fibre orientation, the dispersion of the fibres, the concrete mix design, and the casting method (Alani & Aboutalebi, 2013; Bencardino, et al., 2008; Bencardino, et al., 2013; Swamy & Mangat, 1974; Yazici, et

al., 2007). The results of this experimental investigation have shown that the addition of steel fibres to plain concrete increases the compressive strength of the concrete. Similar results were found by Bencardino (2014), Holschemacher et al. (2010) and Yazici et al. (2007). They added hooked-end steel fibre to plain concrete and found that the compressive strength of concrete increased with the increase in fibre volume fraction. However, Boulekbache et al. (2012) found that the addition of hooked-end steel fibres to the concrete slightly reduced the compression strength. They mentioned that introducing fibres to the concrete matrix substantially disrupts the concrete matrix by introducing voids. Additional defects are also induced to the matrix through insufficient compaction that results in an increase in the porosity of the concrete matrix. Bencardino (2014) added hooked-end fibres to plain concrete at volume fractions of 1 %, 1.6 %, 3 % and 5%. He concluded that the compressive strength of plain concrete increased for volume fractions up to 1.6 % and decreased slightly for volume fractions higher than 1.6 %. This slight decrease in the compressive strength can be the result of the reasons mentioned above by Boulekbache et al. (2012).

From the literature mentioned above there are conflicting results regarding the influence of steel fibres on the compressive strength of plain concrete. However, all of these scholars concluded that the addition of steel fibres to concrete significantly improves the post-peak compressive behaviour. The addition of fibres increased the toughness of the concrete under compression. They also found that the toughness and the strain at peak stress increased with increasing volumetric fibre content. On this point an important observation of the failure pattern of the specimens tested under compression was that the plain concrete specimens showed a more brittle failure mode with matrix spalling whereas the SFRC showed a more ductile failure mode as the fibres provided resistances to the propagation of cracks.

## **4.2 Uni-axial Tensile Strength Test**

As previously mentioned, the uni-axial tensile test is the most appropriate method to obtain the tensile material properties of concrete composites. The stress-crack width opening ( $\sigma-w$ ) relationship can be obtained directly with this test. The result also enables the investigation of the post-cracking behaviour. In this section the results and a discussion of the results of the uni-axial tensile tests are presented. Some experimental observations and the effect of the crack plane fibre count are also discussed in this section.

### 4.2.1 Results

Presented in Figure 4.1 are the  $\sigma$ - $w$  responses for the six specimens tested at a loading rate of 0.01 mm/s. The  $\sigma$ - $w$  response ignores the linear elastic response of the concrete matrix. In Figure 4.2 the linear elastic response of the concrete matrix is included. The crack width opening ( $w$ ) was calculated by subtracting the average displacement at peak stress from the average readings recorded by the LVDTs and neglecting the linear elastic response. The stress ( $\sigma$ ) was calculated by dividing the recorded force readings by the notched effective cross-sectional area (6400 mm<sup>2</sup>) of the specimen.

In order to conduct a quantitative analysis of the behaviour of the specimens under uni-axial tensile loading, several parameters were defined in terms of the stress-displacement ( $\sigma$ - $\delta$ ) relationship and stress-crack width opening ( $\sigma$ - $w$ ) relationship, denoted in Figure 4.3.  $\sigma_u$  is the ultimate strength of the matrix before cracking occurs,  $\delta_u$  is the deformation corresponding to  $\sigma_u$ ,  $\sigma_r$  is the residual strength after the post-peak drop,  $w_r$  is the crack width opening corresponding to  $\sigma_r$ , and  $\sigma_{r,max}$  is the maximum post-crack strength with a corresponding crack width opening of  $w_{r,max}$ .

In Table 4.1 the calculated parameters for each individual specimen, determined from the  $\sigma$ - $\delta$  and  $\sigma$ - $w$  relationships, are presented. It should be noted that all specimens tested cracked at the notched area, which was expected as this was the point of stress concentration. Crack propagation thus occurred over the notched area. From the results three distinct phases can be observed during the uni-axial tensile behaviour, namely: the linear elastic phase, the crack formation phase and the post cracking phase; see Figure 4.3.

An average ultimate strength ( $\sigma_u$ ) of 3.65 MPa and corresponding displacement ( $\delta_u$ ) of 0.0103 mm was obtained indicated as Point A in Figure 4.2. The CoV for  $\sigma_u$  and  $\delta_u$  are 9.1 % and 25.51 %, respectively, which seem to be in the same range as for the modulus of rupture of concrete matrixes without fibres. The calculated average residual strength ( $\sigma_r$ ) and corresponding crack width opening ( $w_r$ ) are 1.76 MPa and 0.53 mm, respectively indicated as Point B in Figure 4.1. The CoV for  $\sigma_r$  and  $w_r$  are 19.74 % and 15.93 %, respectively. At this point the fibres are fully engaged to control the crack opening of the specimen. Beyond this point a pseudo-hardening behaviour was observed for each specimen. The load carrying capacity increased until an average post-crack strength ( $\sigma_{r,max}$ ) of 2.13 MPa with a corresponding crack width opening ( $w_{r,max}$ ) of 1.45 mm indicated as Point C in Figure 4.1.

The CoV for  $\sigma_{r,max}$  and  $w_{r,max}$  are 19.49 % and 21.45 %, respectively. Beyond  $\sigma_{r,max}$  the load bearing capacity started to decay and continued so until 6 mm, where after the test was aborted. This phenomenon is expected to continue until complete pull-out of the fibres occurred, which is the characteristic failure mechanism. This distinct phenomenon is thoroughly investigated in Section 5.1.

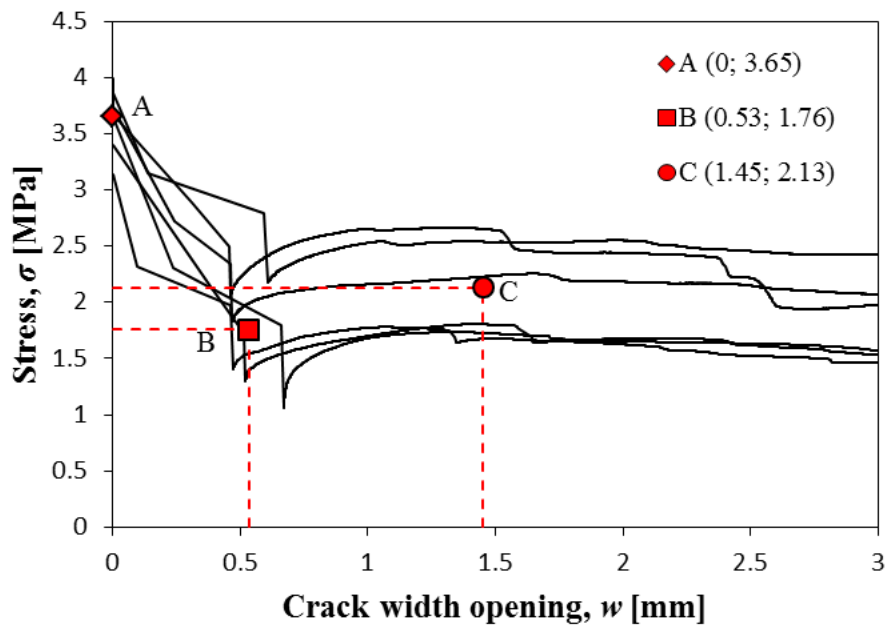


Figure 4.1. Stress-crack width opening ( $\sigma$ - $w$ ) response of SFRC under uni-axial tensile loading

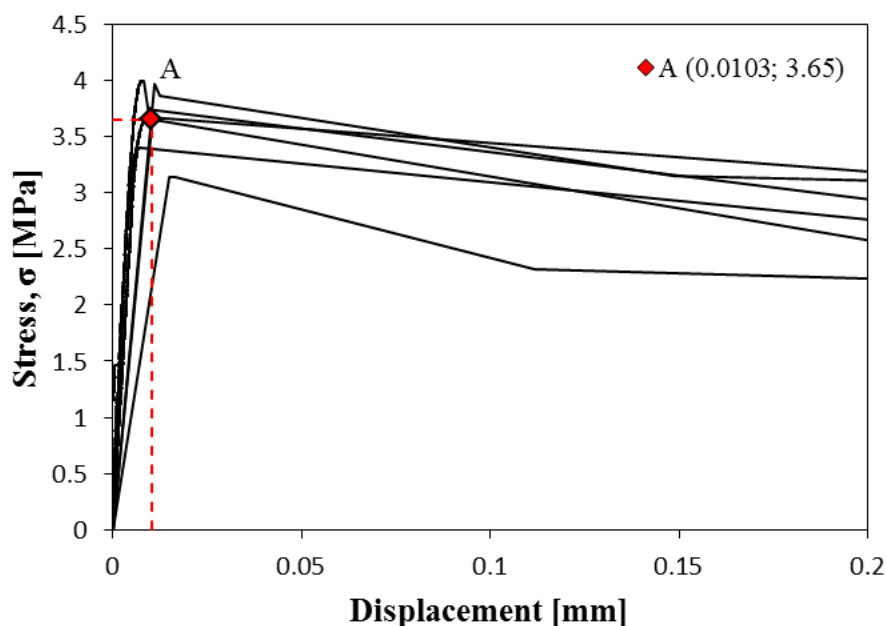


Figure 4.2. The linear elastic response of SFRC up to ultimate strength ( $\sigma_u$ )

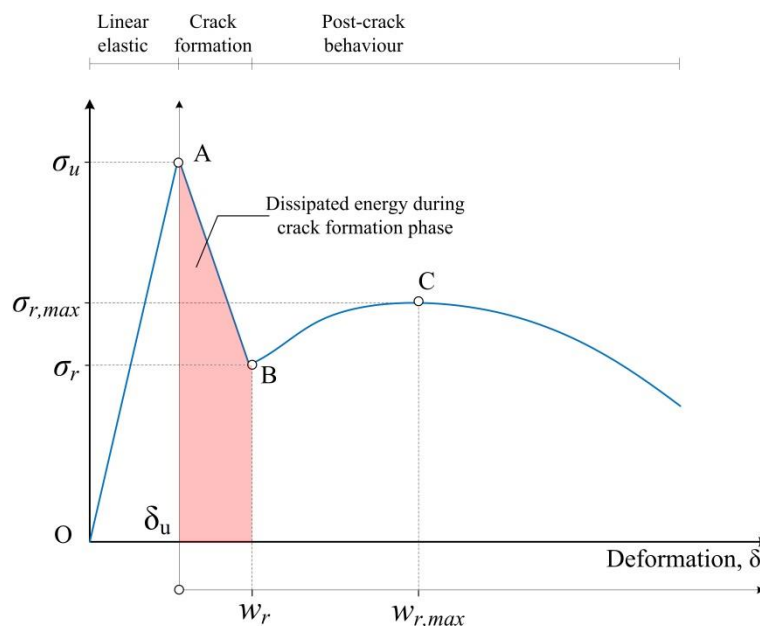


Figure 4.3. A schematic representation of the  $\sigma$ - $\delta$  and  $\sigma$ - $w$  relationships and the parameters determined

Table 4.1. The parameter determined from the  $\sigma$ - $\delta$  and  $\sigma$ - $w$  relationships

Specimen no.	$\sigma_u$ [MPa]	$\delta_u$ [mm]	$\sigma_r$ [MPa]	$w_r$ [mm]	$\sigma_{r,max}$ [MPa]	$w_{r,max}$ [mm]
1	3.73	0.0107	1.83	0.47	2.25	1.65
2	3.65	0.0096	1.79	0.66	1.73	1.33
3	3.40	0.0071	1.30	0.52	1.80	1.42
4	3.99	0.0083	2.04	0.46	2.66	1.30
5	3.97	0.0111	2.18	0.61	2.55	1.95
6	3.14	0.0150	1.40	0.47	1.78	1.06
Average	3.65	0.0103	1.76	0.53	2.13	1.45
CoV [%]	9.10	26.51	19.74	15.93	19.49	21.45

## 4.2.2 Discussion

It would be expected that the addition of high-strength and high-modulus fibres (210 GPa) to a relatively low modulus concrete matrix (about 35 GPa) would increase the  $\sigma_u$  of the matrix, due to some of the tensile load being transferred to the fibres. However, Li and Maalej (1996), Mindess (1995) and Shah (1992) showed that the addition of fibre reinforcement did not substantially improve the strength of the matrix compared to a corresponding matrix without fibres. They concluded that this could be the result of the brittle behaviour of the matrix, the low tensile strain capacity of the cementitious matrixes, and due to the additional defects that

are induced to the matrix, e.g. voids and increased porosity. These studies are based on fibre volumes that can conveniently be incorporated into conventional mortars and concretes. However, Naaman et al. (1974) showed that the strain at the first crack appears at a slightly higher strain than for the unreinforced matrix, and this increases with increasing fibre volume fraction. This increase can be considered negligible for cementitious matrixes reinforced with fibre volume fractions up to and less than 1 %.

As soon as the ultimate strength ( $\sigma_u$ ) of the concrete matrix is reached a significant drop in the stress is observed, see Figure 4.1. In general this is the failure characteristic of concrete. However, an average residual strength of 1.76 MPa is observed resulting from the load being transferred through the fibres (Point A to Point B in Figure 4.3). During this stage the crack is formed and controlled by the engaged fibres. An abrupt dissipation of energy is observed during this phase (see shaded area in Figure 4.3) which resulted in an average crack opening ( $w_r$ ) of 0.53 mm indicated as Point B in Figure 4.1. Banthia and Trottier (1995) concluded that the sudden release of energy during the crack formation phase has a significant influence on the load-displacement response. Because the fracture energy is calculated as the area under the  $\sigma$ - $w$  graph it would be deceptive to calculate the fracture energy from the obtained results (Banthia & Trottier, 1995), since an inadequate amount of data points was captured during the crack formation phase, see Point A to Point B in Figure 4.1. The inadequate amount of data points captured was a consequence of the slow reaction time of the testing machine used, see Section 3.2.2.3.

At Point B the concrete matrix had fractured completely at the notch area resulting in the formation of a crack plane. At this point the entire load capacity is being transferred through the fibres. It is expected that complete debonding of the fibre/matrix interface and some form of fibre pull-out has occurred at this point ( $w_r = 0.53$  mm). Thus beyond this point the crack width opening is controlled by the fibre pull-out mechanisms. The pull-out behaviour of a single fibre will be thoroughly investigated in the course of this dissertation.

Beyond Point B a significant crack width opening is observed. As the crack width opening ( $w$ ) propagates beyond Point B a pseudo-hardening response is observed as mentioned in the results. During this phenomenon the stress increased to an average maximum post-cracking strength ( $\sigma_{r,max}$ ) of 2.13 MPa (Point C in Figure 4.1) which is 21 % more than the average residual strength ( $\sigma_r$ ). The pseudo-hardening behaviour occurred until an average crack width opening ( $w_{r,max}$ ) of 1.45 mm was reached. A number of reasons could be attributed for the



possible pseudo-hardening response during the post-crack behaviour. One possible reason is the improved bond strength provided by the hooked-ends of the steel fibre which requires more energy to straighten the hooked-ends during pull-out of the fibres as the crack width increases. Cunha et al. (2010) also reported that the number of effective fibres increases as the crack width opening ( $w$ ) increases, this is also attributed as a possible reason. A final reason could be that the fibres crossing the crack plane at various angles are eventually aligned to the direction of the applied pull-out load as the crack width opening increases. Due to the ductility of the steel fibres, more energy is required to bend the inclined fibres at the protruding point of the crack plane to the aligned direction of the applied load, see Figure 4.4.

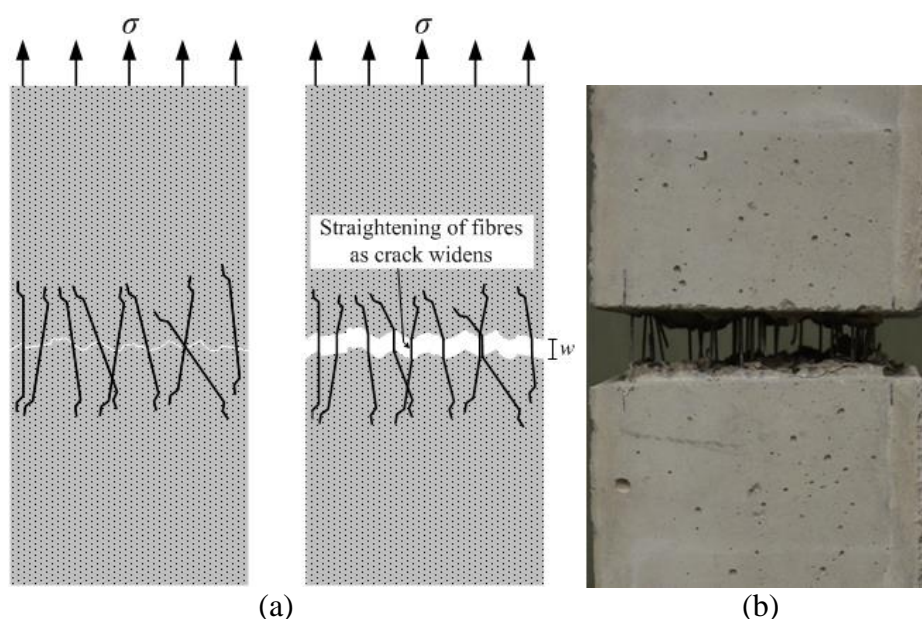


Figure 4.4. (a) Schematic presentation of inclined fibres being bent to the aligned direction of the applied load, (b) photo of fibres aligned in the direction of loading

### 4.2.3 Experimental observations during testing of specimens

It was assumed that the stress distribution over the crack plane is uniform, but according to Dupont (2003) this is not the case. During each uni-axial tensile test a combination of non-uniform (out-of-plane) and uniform crack propagation was observed. This phenomenon has also been observed by other scholars (Babafemi, 2015; Barragan, et al., 2003; Dupont, 2003). As mentioned in Section 3.2.2.3 two LVDTs were used, adjacent to each other, to measure the crack width opening over the notched area of the specimen.

An example of the crack propagation process observed during the uni-axial tensile tests is demonstrated in Figure 4.5. The stress versus the displacement readings of the two LVDTs for

Specimen 1 (see Table 4.1) is presented in Figure 4.5(a). During the linear elastic phase the readings of the two LVDTs were very similar, indicating that the stress distribution was uniform over the measured notched area during this phase, see readings up to Point A in Figures 4.5(a) and 4.5(b). During the crack formation phase (Between Points A and B) a slight variation in the two LVDT readings were observed. A possible reason for this could be due to the non-uniform distribution of fibres over the crack plane (Dupont, 2003). As the average crack width increased up to Point C (The crack width corresponding to the maximum post-crack strength,  $\sigma_{r,max}$ ) the variation between the two LVDTs increased even more. During this stage the specimen rotated slightly resulting in a non-uniform crack width opening, see Figure 4.5(c). The non-uniform crack propagation started to disappear beyond Point C which resulted in a uniform crack width opening as the average crack width increased, see Figure 4.5(d). The crack propagation process explained above was observed for each specimen tested during the uni-axial tensile tests.

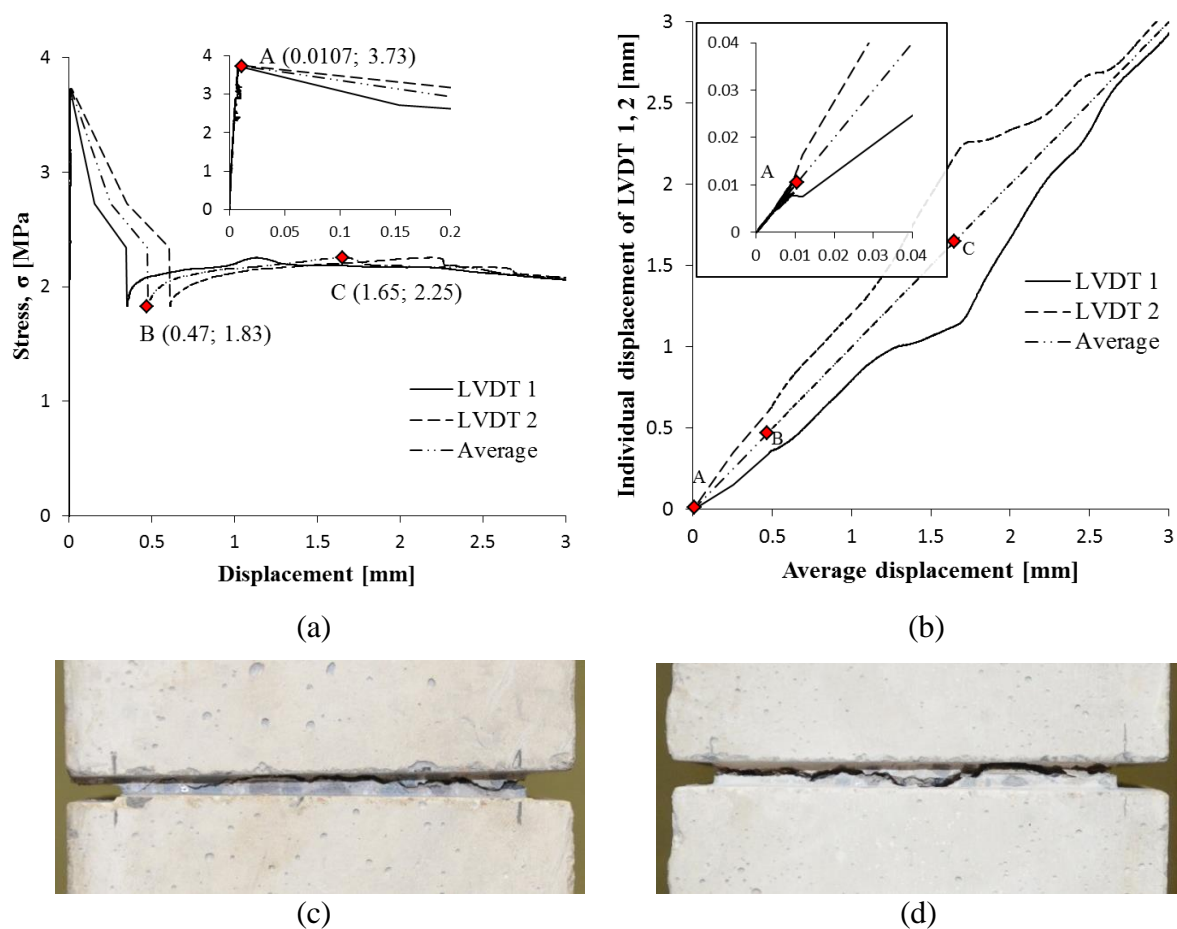


Figure 4.5. The crack propagation process: (a) stress versus LVDT readings, (b) comparison of the individual LVDT readings, (c) example of a non-uniform crack width opening, and (d) example of a uniform crack width opening.

#### 4.2.4 Effect of crack plane fibre count on $\sigma$ - $w$ response

The results of the uni-axial tensile tests showed variability in the  $\sigma$ - $w$  responses, see Figure 4.1. A possible reason for this variability could be the variations in the crack plane fibre count ( $N_f$ ) of each specimen (Barragan, et al., 2003). To prove this the fibres were counted on the crack plane of each specimen. After the specimen was tested it was split into two, see Figure 4.6. The total fibres visible on both sides of the crack plane area ( $6400 \text{ mm}^2$ ) were counted manually and added together. This gave the total crack plane fibre count ( $N_f$ ). It should be noted that a fractured fibre can give the incorrect  $N_f$ , for the reason that it can be double counted. A thorough examination was done to check whether fibre fracture occurred. To do this the total number of fibres protruding the one side of the specimen was compared to the total number of holes on the other side of the specimen, from which the fibres pulled out. For each specimen the total number of fibres and total number of holes were exactly the same, therefore it was concluded that no fibre rupture occurred. The result of the crack plane fibre count for each specimen tested for the uni-axial tensile strength is presented in Table 4.2.

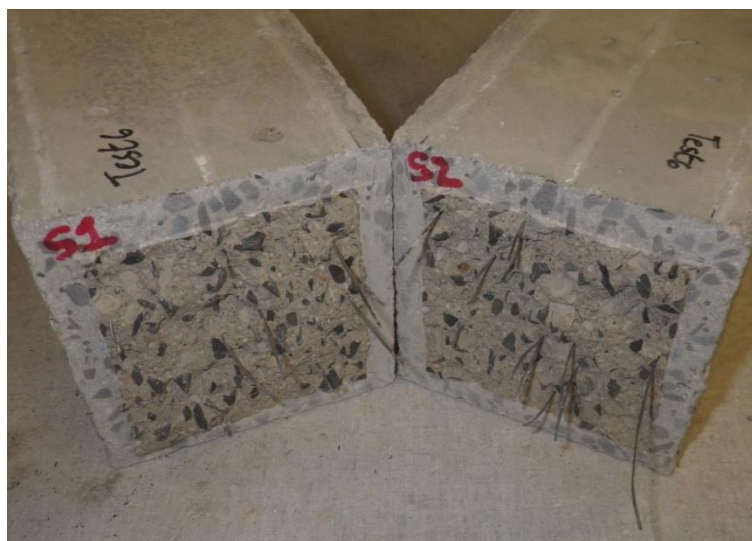


Figure 4.6. Specimen separated into two for crack plane fibre count

Table 4.2. Crack plane fibre count ( $N_f$ ) of the specimens tested for uni-axial tensile strength

Specimen no.	1	2	3	4	5	6	Average	CoV [%]
Fibre count, $N_f$	36	26	26	41	41	27	32.83	22.42

The  $N_f$  ranged between 26 and 41 with a CoV of 22.42 %. This relatively high variation in the  $N_f$ , as mentioned previously, may be the possible reason for the variability in the  $\sigma$ - $w$

responses. To further investigate this matter the values of three representative parameters (i.e.,  $\sigma_u$ ,  $\sigma_r$  and  $\sigma_{r,max}$ ) determined from the  $\sigma$ - $w$  responses, see Table 4.1, are plotted in Figures 4.7(a) to 4.7(c) against the  $N_f$ . Note that the lines plotted in Figures 4.7(a) to 4.7(c) are the linear least square fit of the data points and  $R^2$  is the coefficient of determination for the regression.

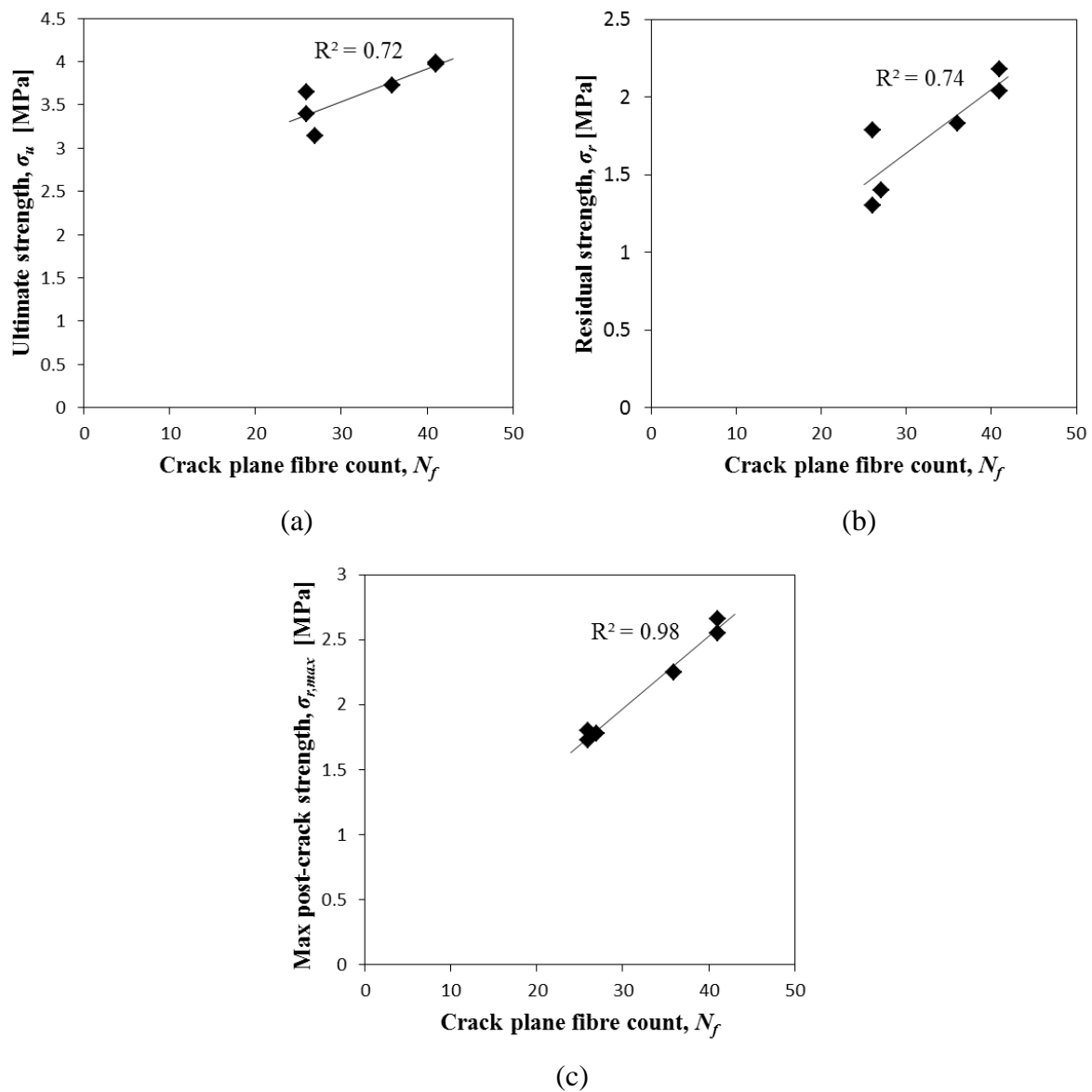


Figure 4.7. Values of (a) ultimate strength,  $\sigma_u$ , (b) residual strength,  $\sigma_r$ , and (c) maximum post-crack strength,  $\sigma_{r,max}$ , versus the crack plane fibre count,  $N_f$

The ultimate strength ( $\sigma_u$ ) and the residual strength ( $\sigma_r$ ), see Figures 4.7(a) and 4.7(b), show very similar and some dependence on the  $N_f$ . This indicates the combined influence of the matrix and fibres on the linear elastic and crack formation phases. The maximum post-crack

strength shows a linear dependence on the  $N_f$ , see Figure 4.7(c). This correlation explains the variability of the post-crack behaviour observed in Figure 4.1. Similar results were found by (Barragan, et al., 2003). He mentioned that further and more extensive investigations in this field could yield relations between the post-crack behaviour of fibre reinforced concrete and the dosage of fibres.

### 4.3 Pre-cracked Sustained Load Tests

The time-dependent Crack Mouth Opening Displacement (CMOD) of pre-cracked SFRC samples was investigated under four stress levels, namely: 30 %, 50 %, 70 % and 85 % of the residual strength ( $\sigma_r$ ). In this section the results and discussions of the results of time-dependent CMOD are presented. Also discussed in this section is the effect of the crack plane fibre count on the time-dependent CMOD.

#### 4.3.1 Results

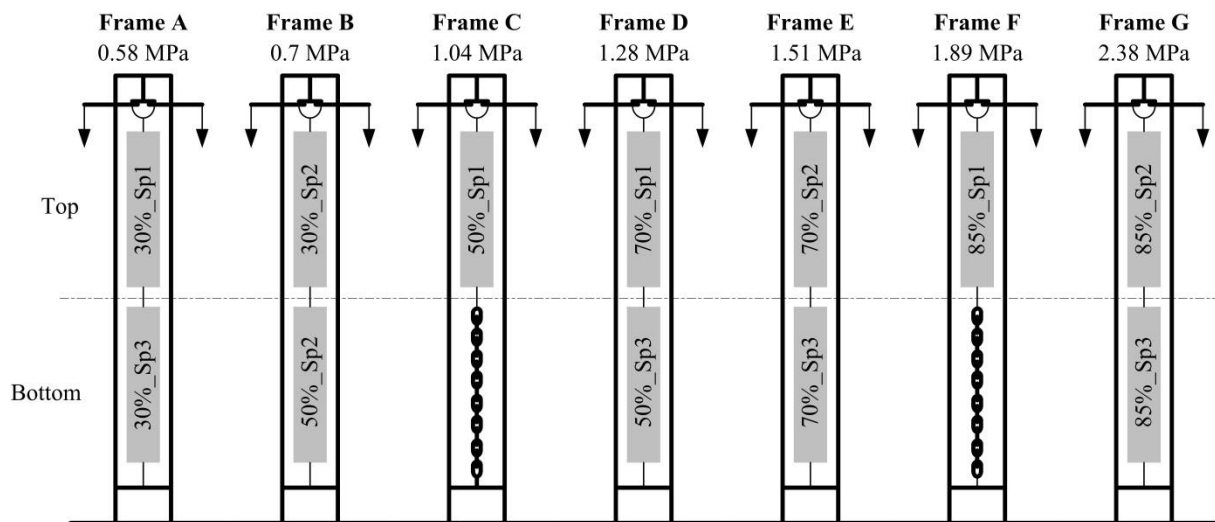
Each specimen was pre-cracked and then unloaded. As mentioned previously the crack occurred abruptly during the crack formation phase and as soon as the crack initiated the load was removed which caused an irrecoverable Crack Mouth Opening Displacement ( $CMOD_{irr}$ ). Presented in Table 4.3 are the residual strength ( $\sigma_r$ ) and  $CMOD_{irr}$  of each specimen determined after the pre-cracking phase. Also presented in Table 4.3 are the required ( $\sigma_{SUS}^{Required}$ ) and actual applied sustained load ( $\sigma_{SUS}^{Actual}$ ) and the equivalent actual load level ( $\bar{\eta}$ ) for each specimen. The seven steel frames were alphabetically numbered from A to G. Figure 4.8 schematically shows the location of each specimen in the steel frames together with the applied load to each frame.

In Figure 4.9 the  $\sigma$ - $w$  response of a specimen that was loaded, unloaded after the crack formation phase and then reloaded up to a crack width opening of 3 mm is presented. This was done to investigate the reloading response under uni-axial tension. This response is also a representative of the behaviour of the specimens that were pre-cracked, unloaded after the crack formation phase and then taken to the loading frames where they were subjected to sustained loads. It should be noted that during the pre-cracking of the specimens a similar crack propagation process was observed during the crack formation phase for each specimen as discussed in Section 4.2.3. Point B in Figure 4.9 represents the residual strength ( $\sigma_r$ ) of the

specimen. The arrows represent the magnitude of the sustained loads applied ( $\sigma_{sus}$ ) to each specimen in the loading frames, see Table 4.3.

*Table 4.3. The residual strength, irrecoverable crack mouth opening displacement and calculated sustained load for each specimen determined after the pre-cracking phase*

Required stress level	Specimen no.	$\sigma_r$ [MPa]	$CMOD_{irr}$ [mm]	$\sigma_{sus}^{Required}$ [MPa]	$\sigma_{sus}^{Actual}$ [MPa]	Position in frame	$\bar{\eta}$ [%]	Notation
30%	1	1.870	0.404	0.561	0.580	A_Top	31.02	30%_Sp 1
	2	2.023	0.547	0.607	0.700	B_Top	34.60	30%_Sp 2
	3	1.988	0.549	0.596	0.580	A_Bottom	29.18	30%_Sp 3
50%	1	2.080	0.433	1.040	1.040	C_Top	50.00	50%_Sp 1
	2	1.585	0.451	0.793	0.700	B_Bottom	44.16	50%_Sp 2
	3	2.679	0.429	1.340	1.280	D_Bottom	47.77	50%_Sp 3
70%	1	1.760	0.441	1.232	1.280	D_Top	72.71	70%_Sp 1
	2	2.078	0.518	1.455	1.510	E_Top	72.67	70%_Sp 2
	3	2.250	0.468	1.575	1.510	E_Bottom	67.10	70%_Sp 3
85%	1	2.227	0.376	1.893	1.890	F_Top	84.87	85%_Sp 1
	2	2.720	0.333	2.312	2.380	G_Top	87.49	85%_Sp 2
	3	2.887	0.765	2.454	2.380	G_Bottom	82.44	85%_Sp 3



*Figure 4.8. Location of specimens in loading frames*

The time-dependent CMOD of each specimen during the sustained load tests was measured as the crack width opening from the irrecoverable Crack Mouth Opening Displacement ( $CMOD_{irr}$ ). As mentioned previously the specimens were tested unsealed, therefore basic creep, drying creep, crack widening and drying shrinkage occurred at the same time. The tensile creep of the matrix over the measured gauge length (70 mm) was found to be negligible when compared to the crack width increase due to the sustained load. The drying shrinkage was measured separately on three unrestrained specimens (see Section 4.4) and



subtracted from the measured time-dependent displacements of each specimen. The displacement measured during the load application was also subtracted from the time-dependent displacements, which was defined as the instantaneous Crack Mouth Opening Displacement ( $CMOD_{inst}$ ). This gave the Crack Mouth Opening Displacement caused by the applied sustained load ( $CMOD_{sus}$ ). Thus is the total time-dependent Crack Mouth Opening Displacement ( $CMOD_{tot}$ ) calculated as:

$$CMOD_{tot} = CMOD_{irr} + CMOD_{inst} + CMOD_{sus} \quad (4.2)$$

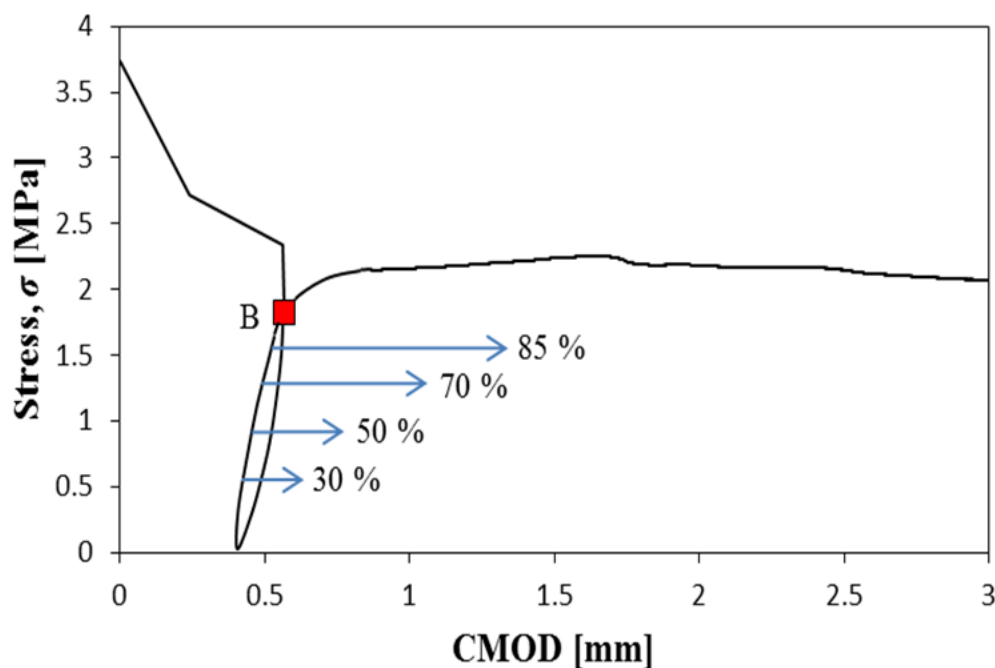


Figure 4.9. The  $\sigma$ - $w$  response of a specimen that was unloaded and reloaded during a uniaxial tensile test

The results of the  $CMOD_{sus}$  for each individual specimen at the various sustained load levels are depicted in Figures 4.10 to 4.13. The averages for each sustained load level are shown in Figure 4.14. All specimens tested showed an initial increase in the  $CMOD_{sus}$  as soon as the sustained load was applied. At all sustained load levels investigated a decrease in the  $CMOD_{sus}$  rate is observed with time. Another important effect observed from the results is that the  $CMOD_{sus}$  is dependent on the applied sustained load level. If the sustained load level is increased, the  $CMOD_{sus}$  also increased.

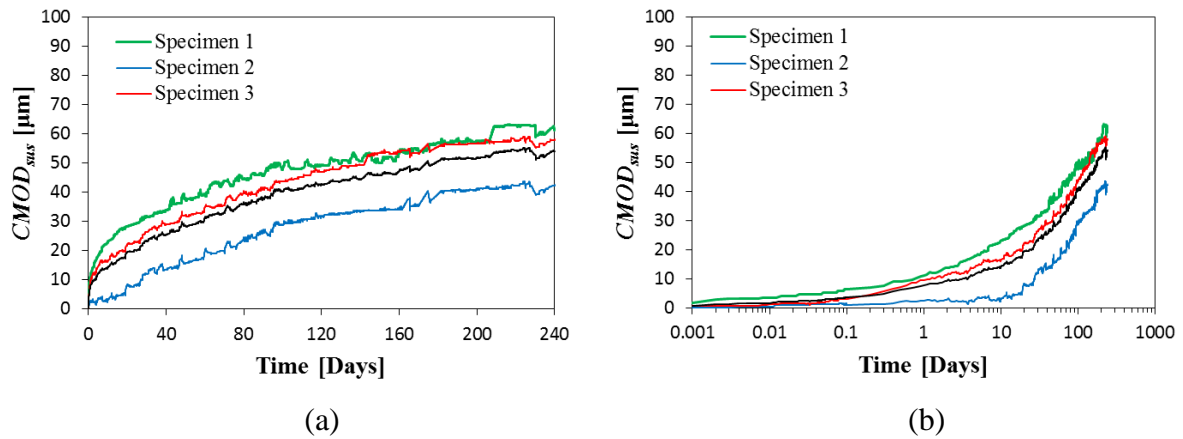


Figure 4.10. (a) Linear and (b) semi-logarithmic plot of the  $CMOD_{sus}$  for each individual specimen at a sustained load level of 30 %

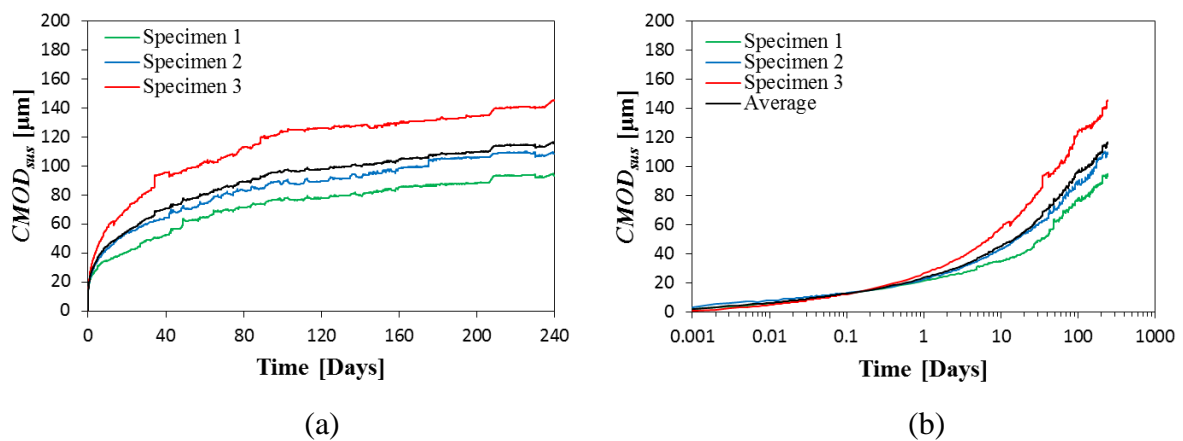


Figure 4.11. (a) Linear and (b) semi-logarithmic plot of the  $CMOD_{sus}$  for each individual specimen at a sustained load level of 50 %

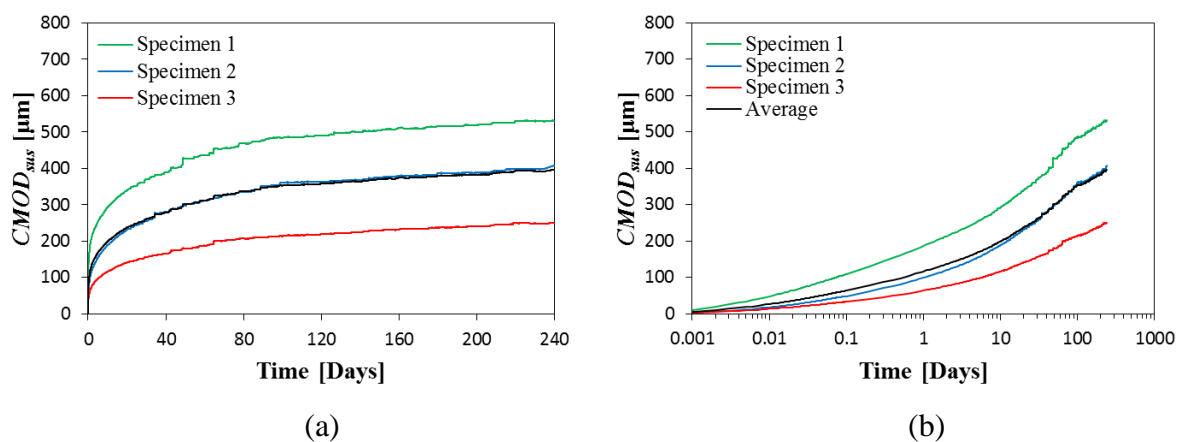


Figure 4.12. (a) Linear and (b) semi-logarithmic plot of the  $CMOD_{sus}$  for each individual specimen at a sustained load level of 70 %



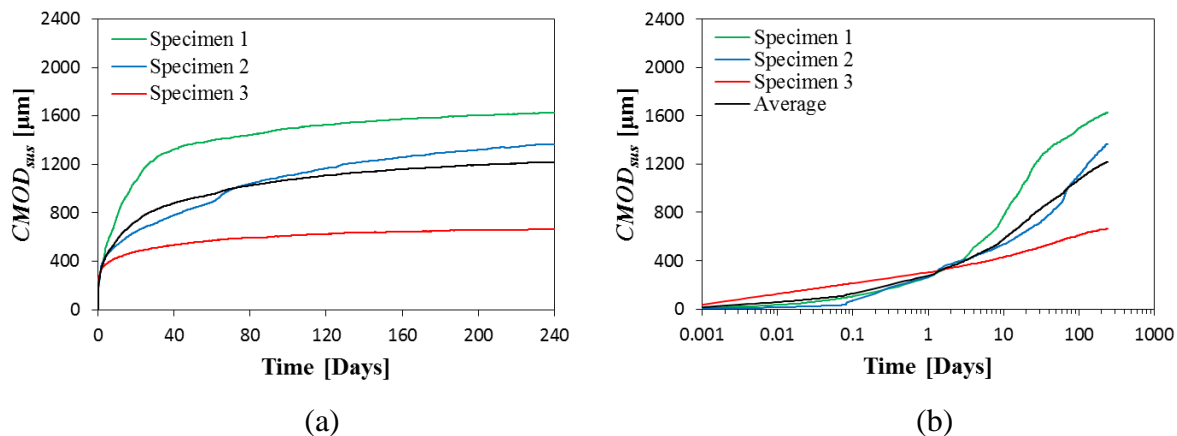


Figure 4.13. (a) Linear and (b) semi-logarithmic plot of the  $CMOD_{sus}$  for each individual specimen at a sustained load level of 85 %

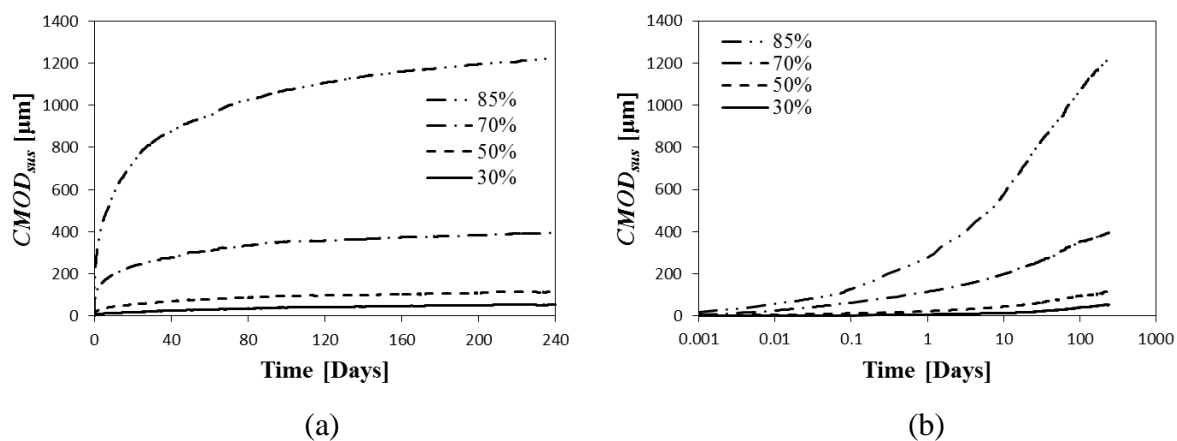


Figure 4.14. (a) Linear and (b) semi-logarithmic plot of the average  $CMOD_{sus}$  for each sustained load level

### 4.3.2 Discussion

In Figures 4.10(b) to 4.14(b) the abscissa are scaled logarithmically to get a better understanding of the early age  $CMOD_{sus}$ . None of the specimens fractured over the measured time period, even for loads as high as 85 % of the residual strength ( $\sigma_r$ ) of the specimen. From here on the average  $CMOD_{sus}$  response at the various applied load levels were used to further analyse the performance of the time-dependent CMOD. The  $CMOD_{tot}$  (see Equation 4.2) after 30, 100, 170 and 240 days at the various applied load levels are shown in Table 4.4.

The results are presented graphically in Figure 4.15(a) to 4.15(d). The results indicate that the  $CMOD_{tot}$  increases with time and applied load level. The increase seems to be linear up to a sustained load level of 50 %. For higher load levels an exponential increase is observed. To get a better understanding of this behaviour the  $CMOD_{inst}$  and  $CMOD_{sus}$  are presented

graphically at the various load levels (see Table 4.4) in Figures 4.16 and 4.17, respectively. The  $CMOD_{inst}$  increases with the applied load level, whereas the  $CMOD_{sus}$  increases with time and applied load level. The  $CMOD_{inst}$  and  $CMOD_{sus}$  at the various load levels appear to increase linearly up to a load level of 50 %, explaining the linear increase in  $CMOD_{tot}$ . As in the case of the  $CMOD_{tot}$ , an exponential increase in the  $CMOD_{ins}$  and  $CMOD_{sus}$  was observed for load levels higher than 50 %. This non-linear increase in the  $CMOD_{ins}$  and  $CMOD_{sus}$  is thought to be the result of the non-linear increase in the instantaneous pull-out and pull-out creep of the fibres, respectively.

Table 4.4.  $CMOD_{tot}$  after 30, 100, 170 and 240 days

Load level [%]	$CMOD_{irr}$ [mm]	$CMOD_{inst}$ [mm]	$CMOD_{sus}$ [mm]				$CMOD_{tot}$ [mm]			
			30 days	100 days	170 days	240 days	30 days	100 days	170 days	240 days
30	0.500	0.059	0.023	0.040	0.047	0.054	0.582	0.599	0.606	0.613
50	0.438	0.133	0.064	0.096	0.105	0.116	0.634	0.666	0.676	0.686
70	0.476	0.347	0.261	0.352	0.375	0.396	1.083	1.175	1.197	1.219
85	0.492	0.581	0.823	1.072	1.169	1.219	1.895	2.145	2.241	2.291

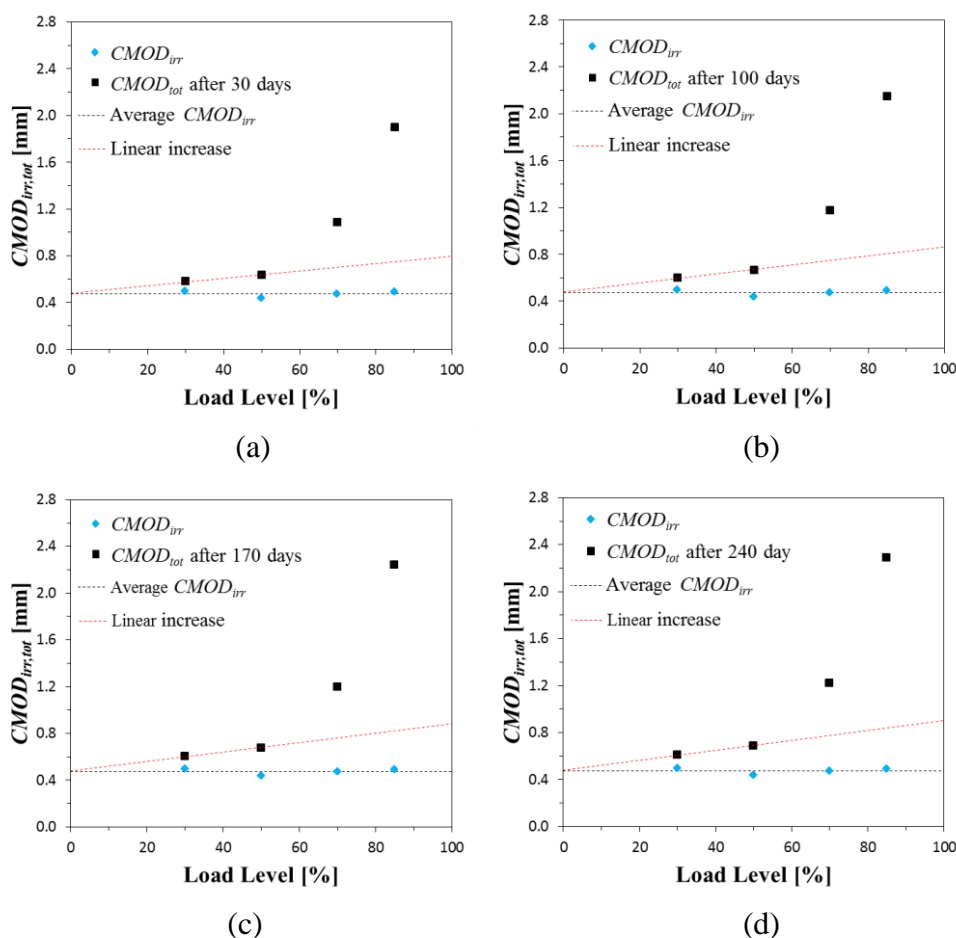


Figure 4.15. The  $CMOD_{irr}$  and  $CMOD_{tot}$  at the various load levels after (a) 30 day, (b) 100 days, (c) 170 days and (d) 240 days

With the aim to analyse in detail the measured  $CMOD_{sus}$ , the values of the  $CMOD_{sus}$  at 30, 100, 170 and 240 days are presented in Table 4.5. Also shown in Table 4.5 is the percentage difference in  $CMOD_{sus}$  between 30 and 100 days (30-100), 100 and 170 days (100-170), 170 and 240 days (170-240).

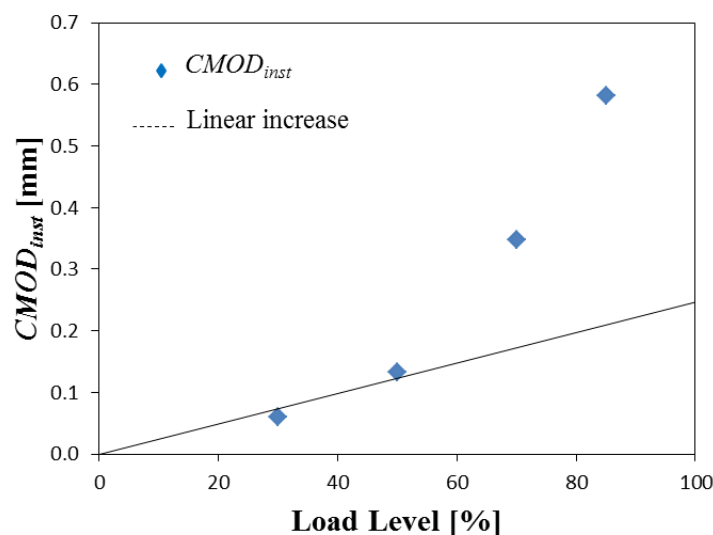


Figure 4.16. The  $CMOD_{inst}$  at the various load levels

The values presented in Table 4.5 reveal that the highest increments in the percentage increase in  $CMOD_{sus}$  appeared during the time interval between 30 and 100 days. The percentage increase in  $CMOD_{sus}$  decreased with age, indicating that the  $CMOD_{sus}$  rate decreases with age. It would be expected that the percentage increase in  $CMOD_{sus}$  would increase as the applied load level increases. This behaviour was observed by Babafemi (2015) who did sustained load tests on pre-cracked macro-synthetic FRC. However, the results in Table 4.5 reveal otherwise. A decrease in the percentage  $CMOD_{sus}$  is observed as the applied load level increases. This decreasing behaviour was the most significant during the time interval between 30 and 100 days. To understand this decreasing behaviour, the  $CMOD_{sus}$  rate was determined at the respective time instances as mentioned previously for each applied load level, see Table 4.6. The  $CMOD_{sus}$  rate was determined by differentiating the  $CMOD_{sus}$  response with respect to time. The  $CMOD_{sus}$  rates calculated at the respective time instances presented in Table 4.6 are presented graphically in Figure 4.18. The ordinate axis is scaled logarithmically to compare the  $CMOD_{sus}$  rate values at each applied load level. Table 4.6 reveals that even though the  $CMOD_{sus}$  rate increases with increasing applied load level, the percentage decrease in the  $CMOD_{sus}$  rate increases with increasing applied load level. This decrease was the most

significant in the time interval between 30 and 100 days. The increase in the percentage decrease in the  $CMOD_{SUS}$  rate explains the decrease in the percentage increase in the  $CMOD_{SUS}$  as the applied load level increases. The mechanisms causing this decreasing behaviour in the percentage  $CMOD_{SUS}$  are investigated thoroughly in the course of this dissertation.

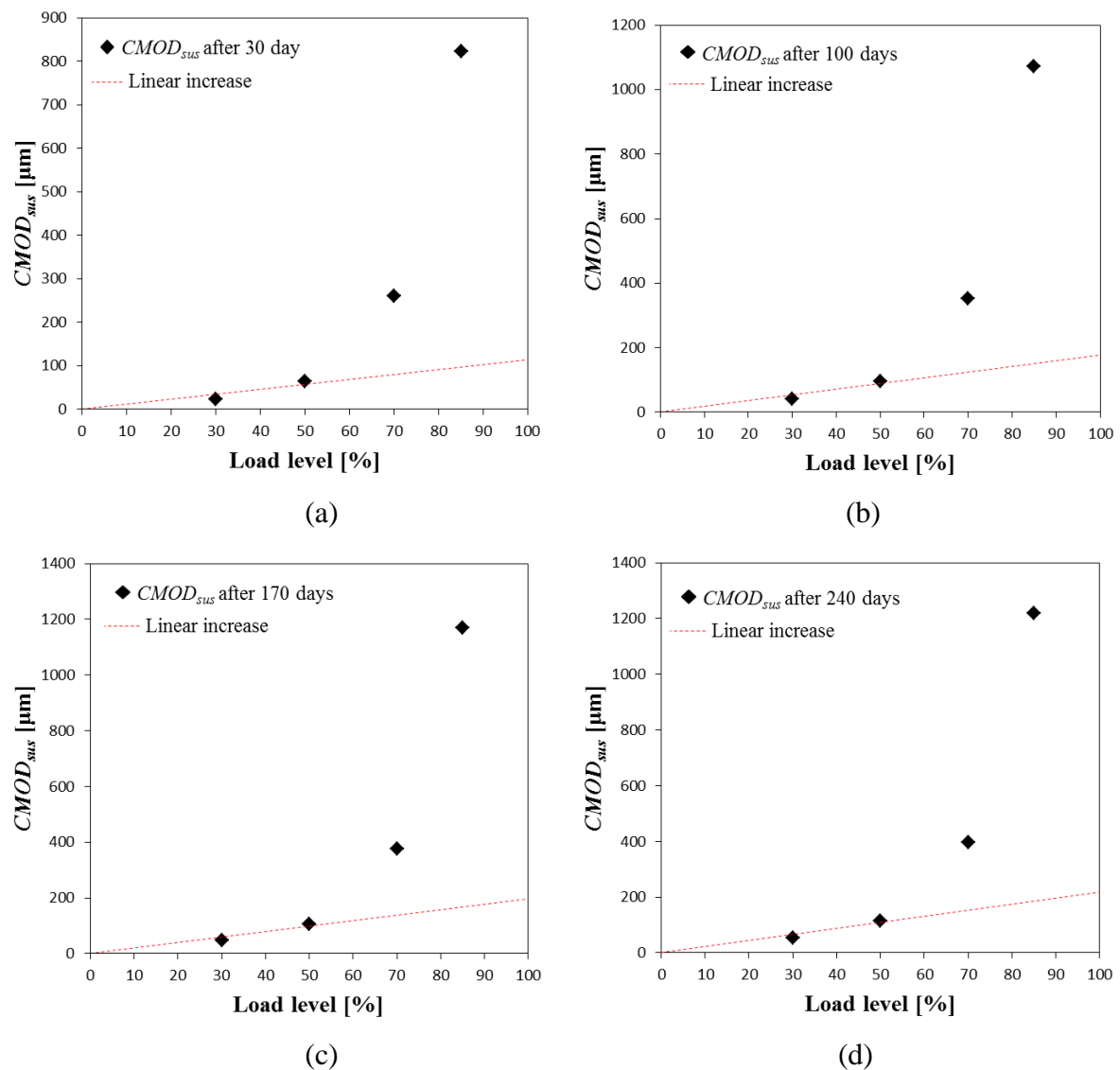


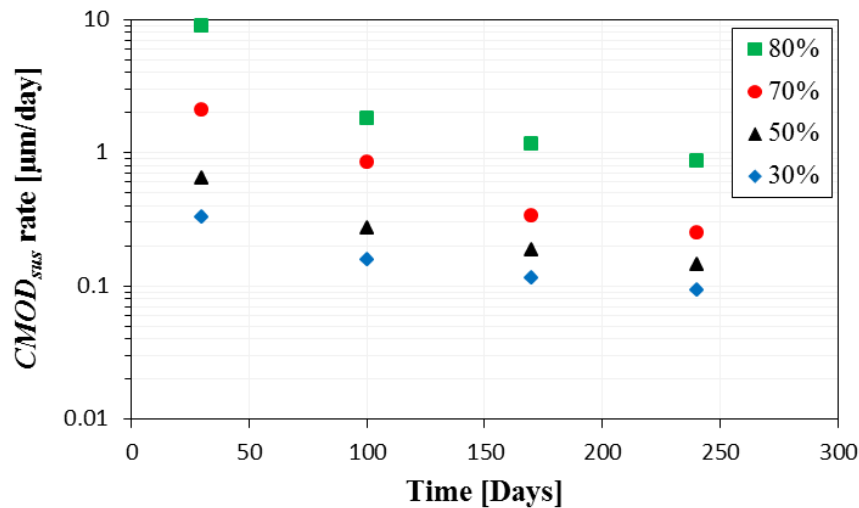
Figure 4.17. The  $CMOD_{SUS}$  at the various load levels after (a) 30 day, (b) 100 days, (c) 170 days and (d) 240 days

Table 4.5.  $CMOD_{SUS}$  at 30, 100, 170 and 240 days

Load level [%]	$CMOD_{inst}$ [mm]	$CMOD_{SUS}$ [mm] after:				% increase in $CMOD_{SUS}$		
		30 days	100 days	170 days	240 days	(30-100)	(100-170)	(170-240)
30	0.059	0.023	0.040	0.047	0.054	72.47	18.38	13.24
50	0.133	0.064	0.096	0.105	0.116	50.71	10.01	9.70
70	0.347	0.261	0.352	0.375	0.396	35.18	6.31	5.76
85	0.581	0.823	1.072	1.169	1.219	30.29	9.02	4.25

Table 4.6.  $CMOD_{sus}$  rate at 30, 100, 170 and 240 days

Load level [%]	$CMOD_{sus}$ rate [ $\mu\text{m}/\text{day}$ ] at:				% decrease in $CMOD_{sus}$ rate		
	30 days	100 days	170 days	240 days	(30-100)	(100-170)	(170-240)
30	0.324	0.155	0.112	0.091	52.085	27.694	19.001
50	0.630	0.270	0.182	0.143	57.161	32.530	21.590
70	2.086	0.846	0.339	0.253	59.469	59.920	25.309
85	8.874	1.795	1.160	0.873	79.772	35.394	24.716

Figure 4.18. Graphic representation of the  $CMOD_{sus}$  rates at 30, 100, 170 and 240 days for each load level

In uncracked cement-based composites the creep-time response is used to evaluate the creep performance by determining the coefficient of creep, defined as the ratio of creep strain to the instantaneous/elastic strain. Some scholars defined a similar expression in terms of crack width or deflection (Babafemi, 2015; Blanco, 2013; Buratti & Mazzotti, 2012). This was done for situations where the strain values cannot be determined directly, e.g. cracked FRC. To further analyse the time-dependent performance of cracked SFRC, the  $CMOD_{sus}$ -time responses at the various load levels was used to determine the ratio of  $CMOD_{sus}$  to  $CMOD_{inst}$ , which is defined as:

$$\gamma(t) = \frac{CMOD_{sus}}{CMOD_{inst}} \quad (4.3)$$

where  $t$  is the generic time instance at which the  $CMOD_{sus}$  is determined. The coefficient of  $CMOD_{sus}$  ( $\gamma(t)$ ) are determined at 30, 100, 170 and 240 days, see Table 4.7.

Table 4.7. Coefficient of  $CMOD_{sus}$  at 30, 100, 170 and 240 days

Load level [%]	$CMOD_{inst}$ [mm]	$CMOD_{sus}$ [mm] after:				$\gamma(30)$	$\gamma(100)$	$\gamma(170)$	$\gamma(240)$
		30 days	100 days	170 days	240 days				
30	0.067	0.023	0.040	0.047	0.054	0.394	0.679	0.804	0.912
50	0.133	0.064	0.096	0.105	0.116	0.480	0.723	0.795	0.873
70	0.347	0.261	0.352	0.375	0.396	0.751	1.016	1.080	1.142
85	0.581	0.823	1.072	1.169	1.219	1.416	1.845	2.012	2.097

While Table 4.7 shows the  $\gamma(t)$  at generic time instances, Figure 4.19 shows the progression of  $\gamma(t)$  at each stress level over a period of 240 days. The results show that the  $\gamma(t)$  response is almost similar up to a load level of 50 %, confirming that the time-dependent CMOD behaviour is linear up to this load level. For higher load levels a significant increase in the  $\gamma(t)$  response is observed. At each stress level it is also established that the  $\gamma(t)$  increases with age at a decreasing rate. This is expected as the  $\gamma(t)$  is a ratio between  $CMOD_{sus}$  and  $CMOD_{inst}$ , which is a factor that represents the increase in the CMOD due to a sustained load. Because the  $CMOD_{sus}$  increases with age at a decreasing rate (see Tables 4.5 and 4.6), so will  $\gamma(t)$ . The  $\gamma(t)$  in Figure 4.19 and Table 4.7 shows that for load levels up to 50 % the CMOD increased at almost the same magnitude (0.912 and 0.873 for load levels 30 % and 50 %, respectively) as the  $CMOD_{inst}$  after 240 days. This increment increased to more than twice the magnitude (2.097) of the  $CMOD_{inst}$  when the load level was increased to 85 %. Zhao et al. (2014) performed uni-axial sustained load tests on cracked SFRC specimens at a load level of 30 % of the maximum pre-cracking load of the specimen. The results showed an average value of 1.24 for the  $\gamma(t)$  after 100 days. This value cannot be compared to the values in Table 4.7 since the applied sustained loads in this research project are based on the residual strength ( $\sigma_r$ ) and not the maximum pre-cracking load. Nevertheless, the average value of the  $\gamma(t)$  obtained by Zhao et al. (2014) falls in the range of the values obtained after a 100 days, see Table 4.7 (between 0.679 and 1.845); hence this gives some perspective on the values obtained in Table 4.7.

### 4.3.3 Effect of crack plane fibre count on the variability of $CMOD_{sus}$

In the results presented in Figures 4.10 to 4.13 some variance between the  $CMOD_{sus}$ -time responses are observed for specimens subjected to the same required load level. The variance between the responses could be a combination of different factors such as the crack plane fibre count ( $N_f$ ), fibre orientation and the fibre distribution on crack plane. Studies done on

these factors have been reported to affect the variability of the post-crack behaviour in fibre reinforced concrete (Babafemi & Boshoff, 2015; Ding, 2011; de Oliveira, 2010), therefore it could be the possible cause for the variability in the  $CMOD_{sus}$ -time responses at each required load level. In this section only the crack plane fibre count ( $N_f$ ) was considered. The investigation of the effect of fibre orientation on a single fibre level is presented in Chapter 5. The same method as in Section 4.2.4 was used to count the fibres on the crack plane for each specimen and the results are presented in Table 4.8. The results for sustained load levels 30 % and 85 % are depicted graphically in Figure 4.20(a) and 4.20(b), respectively.

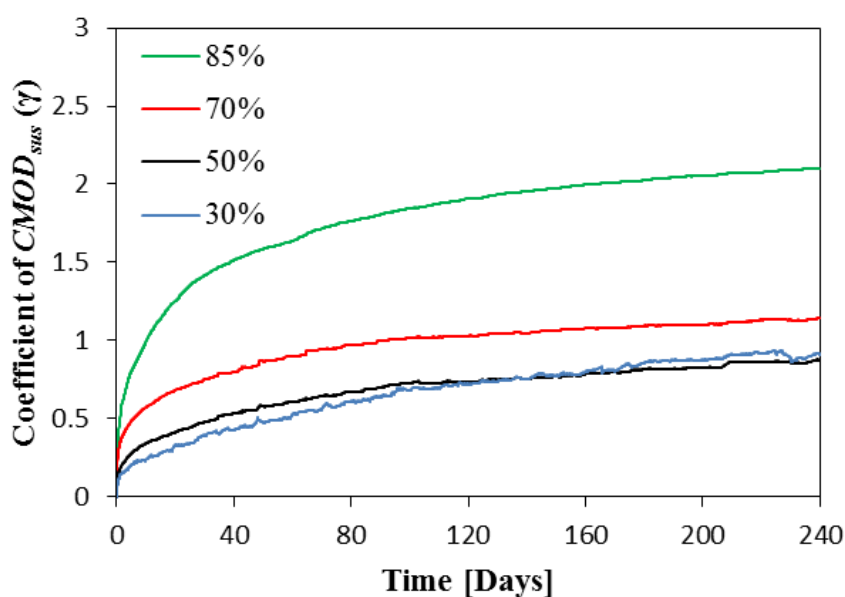


Figure 4.19. Coefficient of  $CMOD_{sus}$  for cracked SFRC at different applied load levels

After careful examination of the results, the fibre count on the crack plane of each specimen is considered as a reason for the variability noticed in the  $CMOD_{sus}$ -time responses at each load level as previously discussed. It is observed at each load level that the  $CMOD_{sus}$  decreases with increasing crack plane fibre count. For example, at 50 % load level, Specimen 1 had the highest crack plane fibre count (52); hence it had the least  $CMOD_{sus}$  after 240 days (0.069 mm). It was concluded that the specimens with the highest fibre count showed the least CMOD under sustained loading within a load level. Similar results were found by Babafemi (2015) who did sustained uni-axial tensile tests on pre-cracked macro-synthetic FRC. Buratti and Mazzotti (2012a) also found that the  $CMOD_{sus}$  decreased with increasing crack plane fibre count under sustained flexural loading for SFRC. This behaviour is consistent with the

results found in Section 4.2.4, that the fibre count has a greater influence on the mechanical properties after cracking.

Table 4.8. Fibre count on crack plane of the individual specimens at different load levels

Required load level	$\bar{\eta}$ [%]	Specimen no.	$CMOD_{sus}$ after 240 days [mm]	$N_f$
30%	31.02	1	0.061	37
	34.60	2	0.042	53
	29.18	3	0.058	43
50%	50.00	1	0.093	52
	44.16	2	0.108	40
	47.77	3	0.146	38
70%	72.71	1	0.531	25
	72.67	2	0.408	38
	67.10	3	0.251	42
85%	84.87	1	1.624	34
	87.49	2	1.367	37
	82.44	3	0.665	51

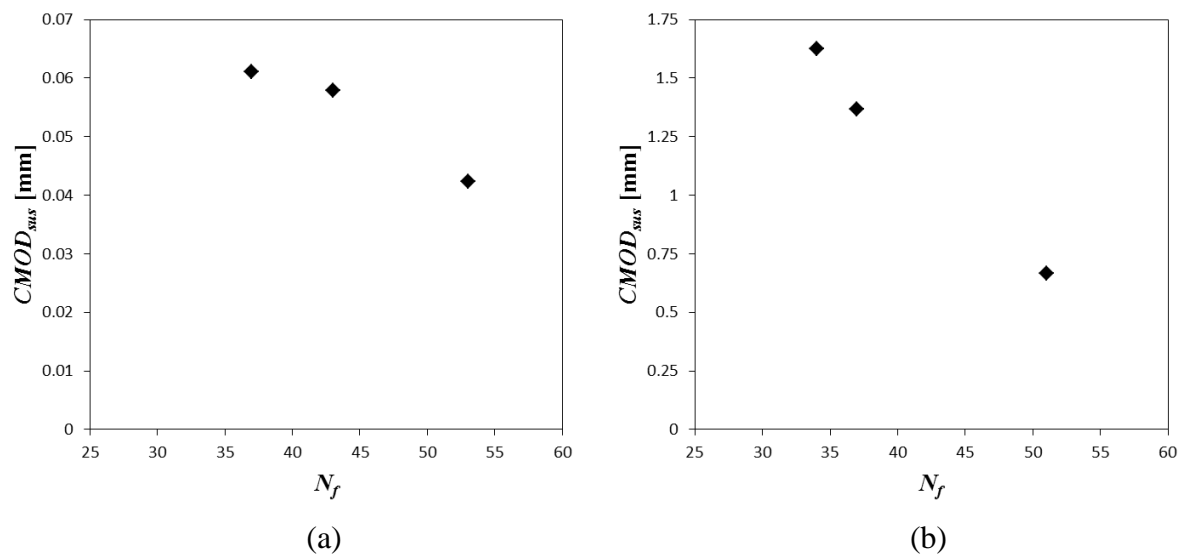


Figure 4.20. Relationship between the crack plane fibre count and the  $CMOD_{sus}$  after 240 days

#### 4.4 Drying Shrinkage Test

As mentioned in Section 3.2.4 the drying shrinkage of SFRC was measured on three 100 x 100 x 500 mm<sup>3</sup> unrestrained beams. The investigation was done to distinguish between time-dependent CMOD and drying shrinkage. The drying shrinkage deformations were subtracted



from the deformations measured during the pre-cracked sustained load tests to get the time-dependent CMOD.

#### 4.4.1 Results

Figure 4.21 shows the drying shrinkage strain-time responses for each individual specimen over a period of 240 days measured over a gauge length ( $L_{gauge}^{shrinkage}$ ) of 300 mm as described in Section 3.2.4. The time is expressed in days with the zero point at the time when the tests were commenced, i.e. at a curing age of 28 days.

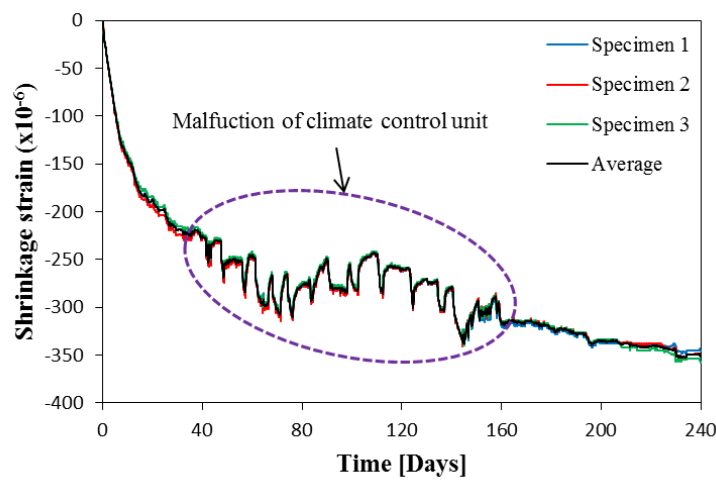


Figure 4.21. Drying shrinkage strain measured on  $100 \times 100 \times 500 \text{ mm}^3$  SFRC beams

The shrinkage deformation was calculated as the average displacement of the two adjacent LVDT readings over the measured gauge length. Since the shrinkage strains were subtracted from the displacements measured during the sustained uni-axial tensile load tests, the strains were converted to shrinkage displacements ( $\delta_{sh}$ ) over a gauge length the same as the pre-cracked sustained load specimens ( $L_{gauge}^{pre-cracked}$ ) as:

$$\delta_{sh} = \frac{\text{Average LVDT reading}}{L_{gauge}^{shrinkage}} \times L_{gauge}^{pre-cracked} \quad (4.4)$$

#### 4.4.2 Discussions

Little variation between the three specimens was observed over the measured period of 240 days. The drying shrinkage showed a non-linear rapid increase at a decreasing rate at the onset of the test. An anomaly in the results is observed between 40 and 160 days (circled in Figure 4.21). The cause of this anomaly is due to changes in the humidity and temperature

due to malfunctioning of the control unit in the climate control room where the tests were performed. After the control unit was fixed (beyond 160 days), the shrinkage deformation continued its normal trend. It is evident from the results that even after 240 days the specimens had not reached an asymptotic limiting value. This is an indication that the specimens had not yet reached equilibrium, i.e. there was still a loss of water from the specimen to the environment through evaporation.

Experimental investigations done by scholars on the effect of fibres on drying shrinkage have showed contradicting results. Some scholars observed that the introduction of fibres tends to reduce the shrinkage of the concrete matrix (Filho & Sanjuan, 1999; Mangat & Azari, 1984; Swamy & Stavrides, 1979; Zhang & Li, 2001). Whereas, others claimed that fibres do not have much influence on drying shrinkage, irrespective of the fibre geometry or content (Bissonnette, et al., 2007; Hannant, 1978). To validate the restraining behaviour of the steel fibres on normal concrete, the experimental results were compared with the prediction model of the final draft of *fib* Model Code 2010 (*fib* Special Activity Group 5, 2010). In Figure 4.22 the average experimental results and the *fib* Model are compared.

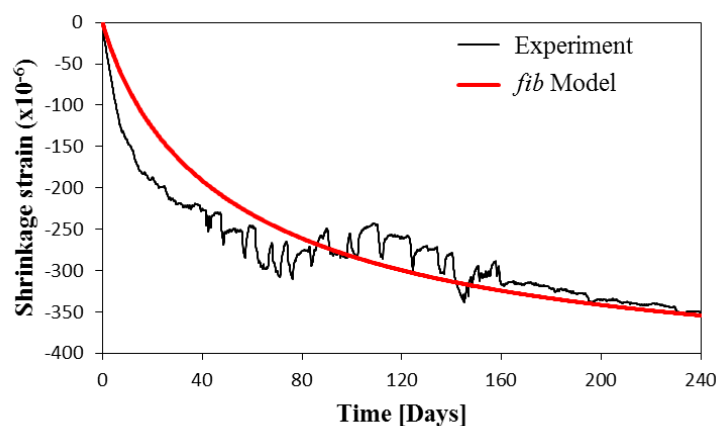


Figure 4.22. The average drying shrinkage and *fib* Model Code 2010 shrinkage prediction model

To analyse in detail the comparison between the experimental ( $\epsilon_{exp}$ ) and predicted ( $\epsilon_{model}$ ) drying shrinkage strain, the results were compared at generic time instances, see Table 4.9. Also presented in Table 4.9 are the normalised errors ( $\bar{\epsilon}$ ) between the predicted and experimental results at generic time instances, calculated as:

$$\bar{\epsilon} = \left| \frac{\epsilon_{exp} - \epsilon_{model}}{\epsilon_{exp}} \right| \quad (4.5)$$

From Table 4.9 it is evident that the normalised error ( $\bar{\epsilon}$ ) decreases with age, except for the period between 60 and 120 days where it appeared that the normalised error ( $\bar{\epsilon}$ ) increased. This behaviour is due to the malfunctioning of the control unit of the climate control room, between 40 and 160 days, as previously mentioned. The results show significant variability between  $\epsilon_{exp}$  and  $\epsilon_{model}$  at early-ages, i.e. for time instances younger than 160 days the  $\epsilon_{exp}$  is smaller than the  $\epsilon_{model}$ . However, for a time instance older than 160 days a resemblance between  $\epsilon_{model}$  and  $\epsilon_{exp}$  is observed. It is acknowledged that the drying shrinkage was not compared to that of the same concrete without fibres. Therefore, no conclusions can be reached on the restraining ability of steel fibres on the drying shrinkage of normal concrete. Nevertheless, it can be stated that the significant variance at early-ages is due to the additional defects that are induced to the matrix, e.g. more voids and increased porosity, when steel fibres are added to the concrete matrix; hence drying shrinkages depends on the size and type of voids in the concrete (Pelisser, et al., 2010). On the contrary it can be stated that the addition of steel fibres did not significantly influence the drying shrinkage.

*Table 4.9. Experimental and predicted drying shrinkage strain at generic time instances*

Time [Days]	$\epsilon_{exp}$ [x 10 <sup>-6</sup> ]	$\epsilon_{model}$ [x 10 <sup>-6</sup> ]	$\bar{\epsilon}$ [%]
1	-25.6	-10.2	60.1
30	-220.0	-163.4	25.7
60	-245.6	-232.2	5.5
120	-259.4	-299.7	15.5
160	-316.1	-324.5	2.6
240	-351.3	-354.4	0.9

## 4.5 Concluding Summary

Experimental tests were performed at a macroscopic level to investigate the behaviour of SFRC under two loading conditions, namely short- and long-term loading. The investigations performed under short-term loading conditions were compressive and uni-axial tensile strength tests. The long-term loading investigations were sustained uni-axial tensile load tests on cracked SFRC and drying shrinkage tests.

Compressive strength test were performed on concrete with and without fibres. The results have shown that the addition of 0.5 % of TYPE A hooked-end steel fibres to the concrete matrix increased the compressive strength with 10.8 %. Also an important observation made

---

during the compressive strength tests are that the specimens without fibres showed a more brittle failure mode whereas SFRC showed a more ductile failure mode under compression.

The uni-axial tensile tests showed a strain softening response. The crack formation phase appeared abruptly causing a large amount of dissipated energy which resulted in a significant crack width opening. After the cracking phase the fibres were fully engaged and the crack width opening was then controlled by the engaged fibres. During the post-cracking phase a slight pseudo-hardening behaviour was observed. Three possible reasons for the pseudo-hardening behaviour were provided, namely: The improved bond strength provided by the hooked-ends of the steel fibres, the number of effective fibres increases as the crack width opening increases, and the fibre orientation at the crack plane. It was also found that the post-cracking behaviour shows a linear dependence on the crack plane fibre count.

The pre-cracked sustained loading tests indicated that the time-dependent CMOD is dependent on the applied load level. An increase in the load level led to an increase in the time-dependent CMOD. None of the specimens tested fractured during the measured period of 240 days, even for load levels as high as 85 % of the residual strength of the specimen. With age an increase in the time-dependent CMOD at a decreasing rate was observed at each load level. The crack plane fibre count has been considered as a possible reason for the variability found in the results at each load level, i.e. the higher the crack plane fibre count, the lesser the time-dependent CMOD.

The drying shrinkage response of SFRC was compared to the predicted shrinkage of *fib* Model Code 2010. The results showed significant variability between the drying shrinkage of SFRC and the predicted shrinkage at early-ages of the test period. However, similarity was observed at time instances older than 160 days. It was acknowledge that the drying shrinkage was not compared to that of the same concrete without fibres. Therefore, no conclusions were drawn on the restraining ability of steel fibres on that of normal concrete without fibres. The shrinkage response of the predicted model has shown to be close to the shrinkage of SFRC; hence it was stated that the addition of steel fibres did not significantly influenced the drying shrinkage.

# Chapter 5

---

## Mechanical and Time-dependent Behaviour on a Single Fibre Level

In order to understand the mechanisms causing the time-dependent crack width opening of cracked SFRC, it is essential to understand the nature of the interface between the fibre and the surrounding concrete matrix. The bond strength between straight steel fibres and the matrix is relatively low and to compensate for this low bond strength geometrical modifications to the fibres are typically made to provide a mechanical bond. Numerous types of steel fibres with different longitudinal profiles are currently available commercially, see Section 2.1.2.1. Each of these fibres is designed to perform in a specific way. In this study hooked-end steel fibres were used.

The results of two types of loading conditions are reported in this chapter, namely: short- and long-term loading conditions. For the short-term loading condition quasi-static single fibre pull-out rate tests were performed to investigate the factors that can have an effect on the pull-out behaviour. Under the long-term loading condition single fibre sustained load tests were performed to identify the mechanisms causing the pull-out creep and to investigate which factors have an influence on it.

## 5.1 Quasi-Static Single Fibre Pull-out Tests

The pull-out behaviour of deformed steel fibres under quasi-static loading conditions has been well documented by a number of scholars (Banthia & Trottier, 1994; Cunha, et al., 2010; Kim, et al., 2008; Naaman, 2003). Nevertheless, in this study several factors were investigated to characterise the effect of each factor on the load-slip relationship as a precursor to the single fibre sustained load tests.

As mentioned in Section 3.3.1.1, the investigation was restricted to the influence of the fibre embedment inclination angle, the fibre embedment length, fibre mechanical anchorage and the rate of loading application. The results are expressed in terms of the labels given to each factor tested (see Section 3.3.1.4). Also discussed in this section are the different failure modes observed during the pull-out tests.

### 5.1.1 Results

#### 5.1.1.1 Pull-out loading rate

Pull-out rate tests were performed on straight and TYPE A hooked-end steel fibres. The pull-out rates was varied over five orders of magnitude ranging between 2.5 mm/s and 0.00025mm/s. The load-slip responses for each loading rate are depicted in Figures I.1 and I.2 of Appendix I. The average pull-out load-slip curves for each loading rate are depicted in Figures 5.1 and 5.2 for straight and TYPE A hooked-end fibres, respectively.

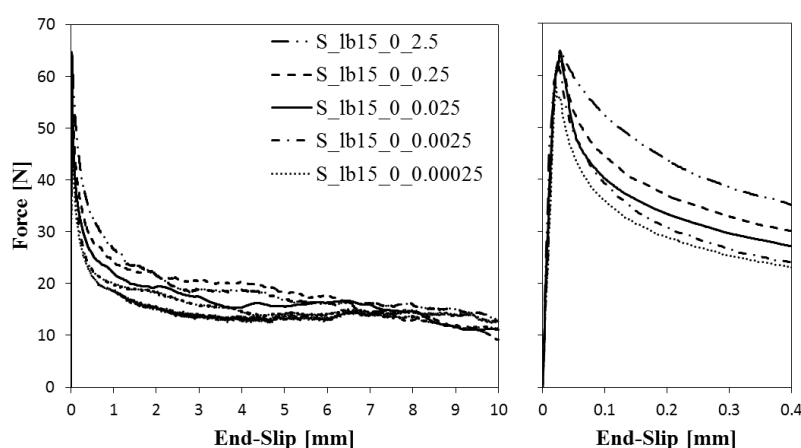


Figure 5.1. Average pull-out load-slip curves at different loading rates for straight fibres

The pull-out load-slip relationships showed similar characteristics to those found by Cunha (2010). From the pull-out load-slip relationships a pre-peak and post-peak response are

observed for both the straight and TYPE A hooked-end fibres. The pre-peak response is made up of a linear and a non-linear part, see Figures 5.1 and 5.2. The linear part is associated with the elastic bond between the fibre and the matrix surrounding the fibre. The non-linear part starts with the micro-cracking of the matrix surrounding the fibre. This corresponds to the debonding process of the matrix surrounding the fibre. The non-linear part of the pre-peak response is not that pronounced in straight fibres as in TYPE A hooked-end fibres. This is because the debonding process for straight fibres occurs relatively close to the peak load. This phenomenon results in an irrecoverable deformation between the fibre and the matrix due to micro-cracking that occurs at the interface between the fibre and the matrix. For TYPE A hooked-end fibres the micro-cracking is more severe at the zone of the hooked-end causing a significant amount of irrecoverable deformation. After the peak load is reached in straight fibres a sudden drop in the pull-out load occurs. The sudden drop is a result of the abrupt (unstable) debonding between the fibre and the matrix surrounding the fibre. Once this debonding has occurred the friction caused between the fibre and the matrix is the dominating mechanism of the pull-out behaviour. During this part of the post-peak response the load decreases as the slip increases. This is attributed to the decrease in the friction area between the fibre and the surrounding concrete matrix, as well as the roughness of the concrete matrix surrounding the fibre. In the case of hooked-end fibres the decrease in the post-peak load was not as abrupt as for straight fibres, since the mechanical anchorage of the fibre hook is activated as the pull-out slip increases. When the hooked-end is straightened the pull-out behaviour occurs under frictional resistance similar to that of straight fibres. This phenomenon occurs at approximately 4.5 mm which corresponds to the straightened hook length.

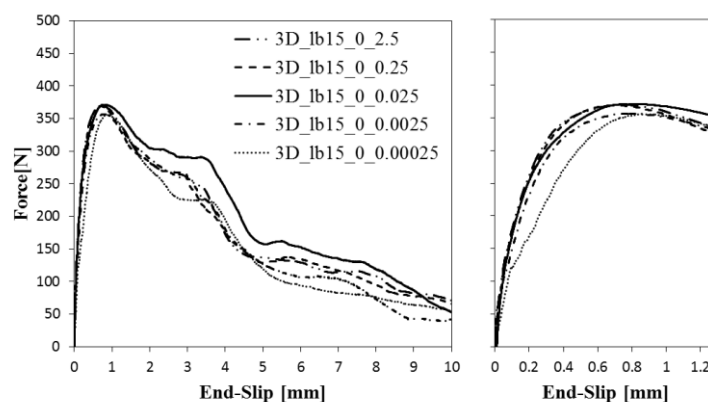


Figure 5.2. Average pull-out load-slip curves at different loading rates for TYPE A hooked-end fibres

To analyse the pull-out load-slip curves presented in Figures 5.1 and 5.2 in detail the average maximum force ( $N_{max}$ ), the average slip at maximum force ( $S_{max}$ ), and the average pull-out energy at maximum force ( $G_{max}$ ) for straight and TYPE A hooked-end fibres are presented in Table 5.1. The results are graphically presented in Figures 5.3 and 5.4 with error bars indicating the minimum and maximum values.

Table 5.1. Average values of the maximum force ( $N_{max}$ ), the slip at maximum force ( $S_{max}$ ) and the pull-out energy at maximum force ( $G_{max}$ ) at different pull-out rates

	$\dot{\Delta}$ [mm/s]	$N_{max}$ [N]	CoV [%]	$S_{max}$ [mm]	CoV [%]	$G_{max}$ [N.mm]	CoV [%]
Straight	0.00025	66.9	18.3	0.023	17.0	1.031	15.0
	0.0025	67.1	23.6	0.023	14.7	1.009	17.9
	0.025	69.0	29.4	0.021	29.0	1.078	32.9
	0.25	68.7	22.9	0.023	23.0	1.070	29.0
	2.5	67.1	18.0	0.022	40.0	1.109	22.4
TYPE A	0.00025	358.7	4.6	0.902	8.3	237.1	11.1
	0.0025	366.6	10.7	0.808	9.2	237.7	4.3
	0.025	375.8	11.7	0.760	8.8	229.4	9.1
	0.25	371.5	5.2	0.738	17.2	208.5	24.2
	2.5	372.3	7.7	0.738	17.0	209.7	26.1

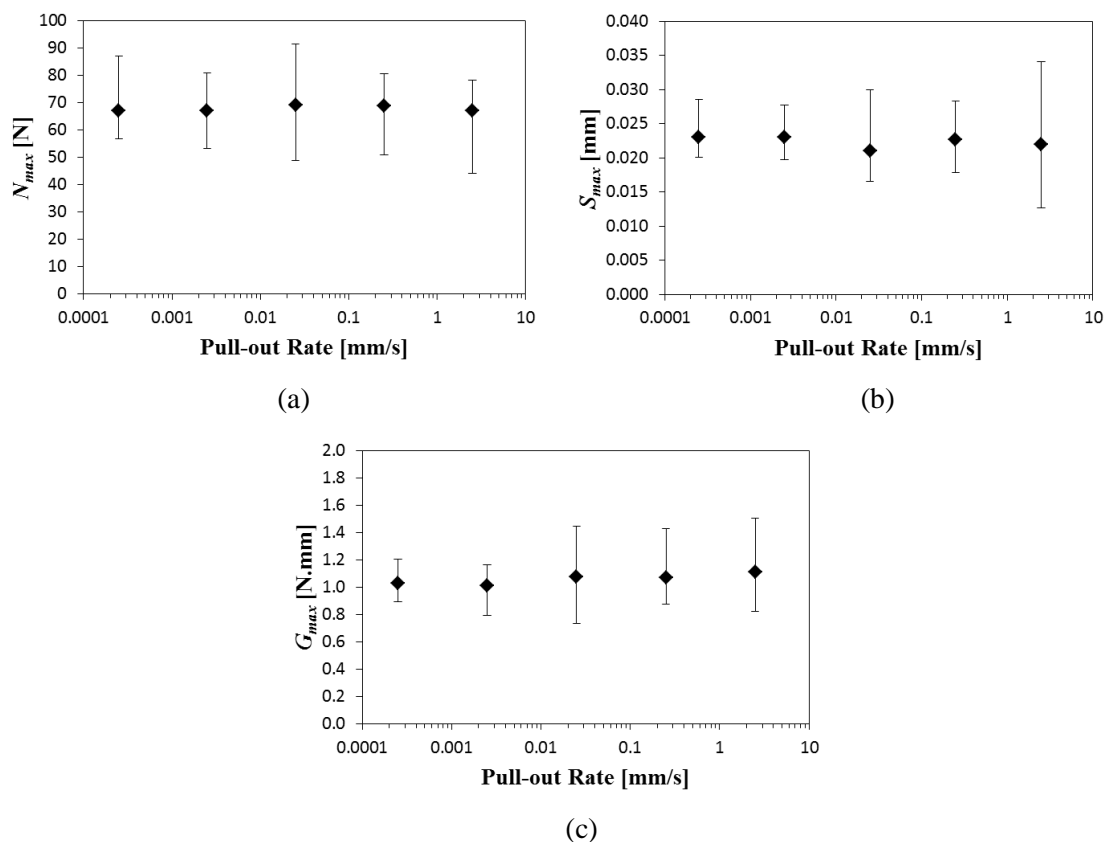


Figure 5.3. The range and average values for straight fibres at different pull-out rates with regard to (a) the maximum pull-out force ( $N_{max}$ ), (b) the slip at maximum pull-out force ( $S_{max}$ ) and (c) the pull-out energy at maximum force ( $G_{max}$ )



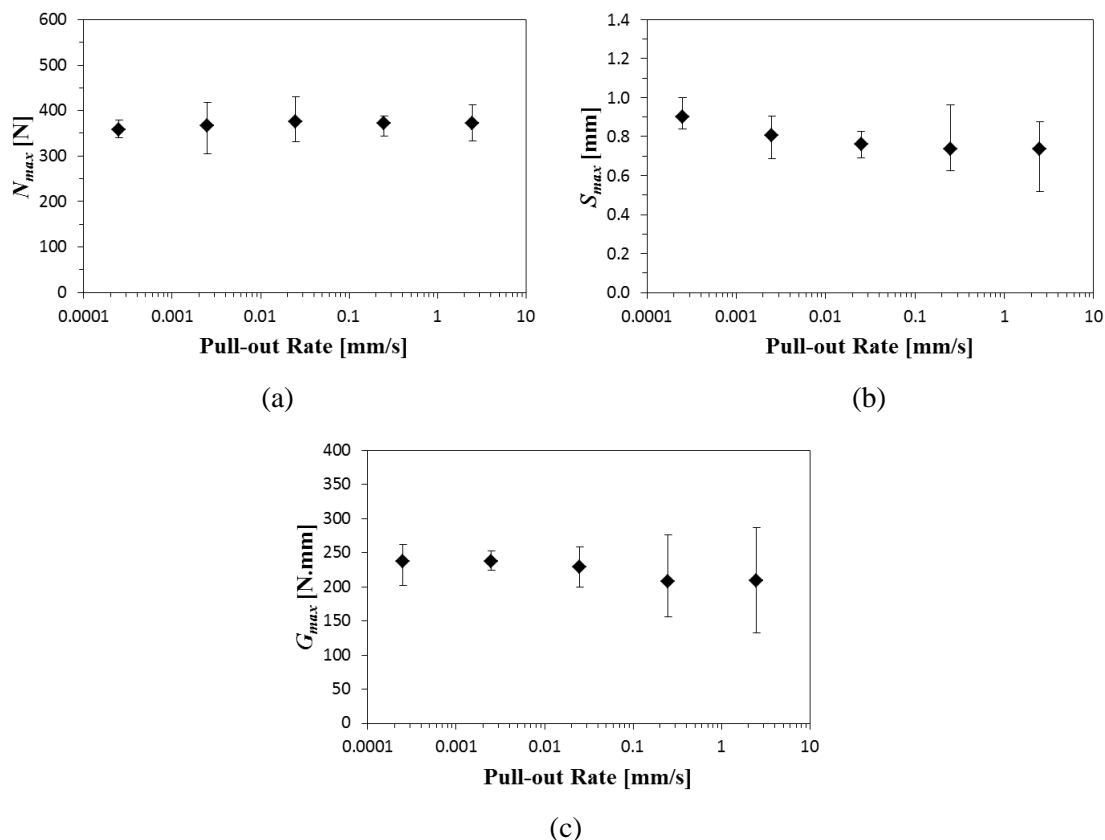


Figure 5.4. The range and average values for TYPE A hooked-end fibres at different pull-out rates with regard to (a) the maximum pull-out force ( $N_{max}$ ), (b) the slip at maximum pull-out force ( $S_{max}$ ) and (c) the pull-out energy at maximum force ( $G_{max}$ )

### 5.1.1.2 Fibre embedment length

The influence of the fibre embedment length was investigated for TYPE A hooked-end fibres. Note that all embedment lengths that were investigated were greater than the length of the hooked-end of the fibre. The pull-out load-slip responses for each embedment length are depicted in Figure I.3, see Appendix I. The average pull-out load-slip response for each embedment length is presented in Figure 5.5.

The pull-out load-slip response for each embedment length showed similar characteristics as explained in Section 5.1.1.1. A marked difference in the magnitude of the pull-out load-slip response is observed for an embedment length ( $l_b$ ) of 7.5 mm when compared to 15 mm and 30 mm. This is further discussed in Section 5.1.2.2.

The average maximum force ( $N_{max}$ ), the average slip at maximum force ( $S_{max}$ ), and the average pull-out energy at maximum force ( $G_{max}$ ) for each embedment length ( $l_b$ ) are

summarised in Table 5.2. The results are graphically presented in Figure 5.6 with error bars indicating the minimum and maximum values.

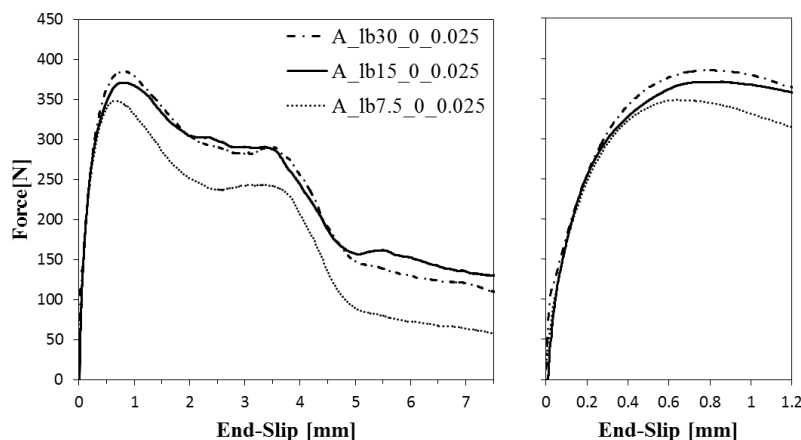


Figure 5.5. Average pull-out load-slip curves for different embedment lengths

Table 5.2. Average values of the maximum force ( $N_{max}$ ), the slip at maximum force ( $S_{max}$ ) and the pull-out energy at maximum force ( $G_{max}$ ) for different embedment lengths

$l_b$ [mm]	$N_{max}$ [N]	CoV [%]	$S_{max}$ [mm]	CoV [%]	$G_{max}$ [N.mm]	CoV [%]
7.5	350.2	10.0	0.668	13.2	180.2	11.3
15	375.8	11.7	0.760	8.8	229.4	9.1
30	387.8	7.1	0.763	19.9	240.9	25.0

### 5.1.1.3 Fibre inclination angle

Five different fibre embedment inclination angles were investigated for TYPE A hooked-end fibres, ranging from  $0^\circ$  to  $60^\circ$ . The pull-out load-slip responses for each embedded inclination angle are depicted in Figure I.4, see Appendix I. The average pull-out load-slip response for each embedded inclination angle is presented in Figure 5.7.

The pull-out load-slip responses for the different fibre embedded inclination angles showed similar characteristics as the aligned series (A\_lb15\_0\_0.025). However, a significant increase in the magnitude of the pull-out load-slip response is observed as the inclination angle ( $\theta$ ) increases. The magnitude of the non-linear part in the pre-peak response is more pronounced for higher embedded inclination angles, due to cracking and spalling of the matrix at the bend and the exiting point of the fibre from the matrix. The aforementioned is a result of additional stress concentration induced to the matrix through the bend of the inclined fibre. The post-peak response for inclined fibres also showed an increment in the pull-out force, even after the hooked-end was straightened (at a slip of approximately 4.5 mm) and the

pull-out behaviour was controlled through friction between the fibre and the surrounding matrix. The increase in frictional resistance for inclined fibres is induced between the bend of the inclined fibre and the matrix at this zone.

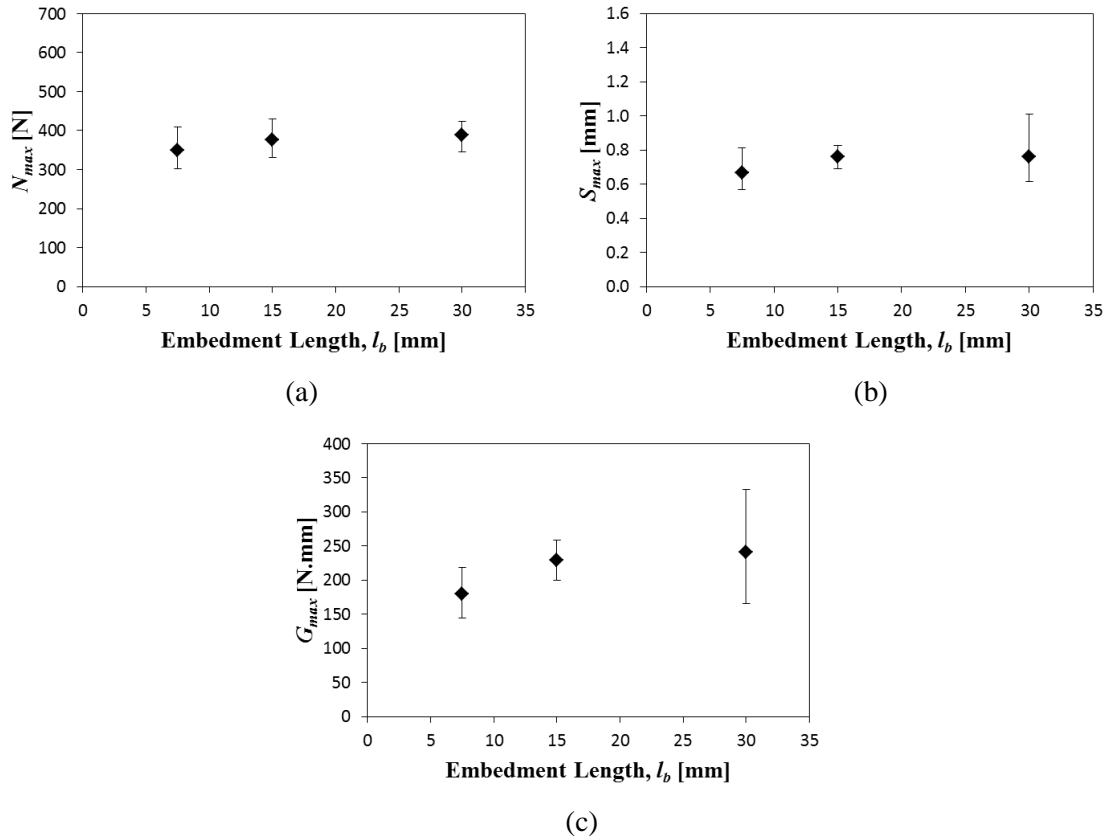


Figure 5.6. The range and average values for different embedment lengths with regard to (a) the maximum pull-out force ( $N_{max}$ ), (b) the slip at maximum pull-out force ( $S_{max}$ ) and (c) the pull-out energy at maximum force ( $G_{max}$ )

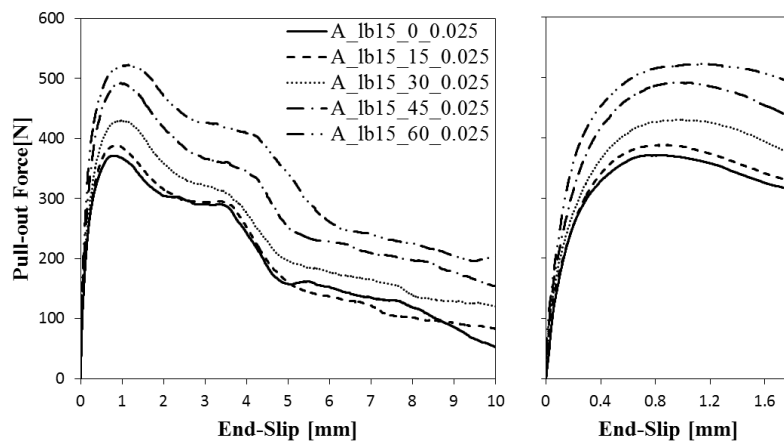


Figure 5.7. Average pull-out load-slip curves for the different fibre embedment inclination angles

The average maximum force ( $N_{max}$ ), the average slip at maximum force ( $S_{max}$ ), and the average pull-out energy at maximum force ( $G_{max}$ ) for different embedment inclination angles are summarised in Table 5.3. The results are graphically presented in Figure 5.8 with error bars indicating the minimum and maximum values.

Table 5.3. Average values of the maximum force ( $N_{max}$ ), the slip at maximum force ( $S_{max}$ ) and the pull-out energy at maximum force ( $G_{max}$ ) for different fibre embedment inclination angles

$\theta$ [°]	$N_{max}$ [N]	CoV [%]	$S_{max}$ [mm]	CoV [%]	$G_{max}$ [N.mm]	CoV [%]
0	375.8	11.7	0.760	8.8	229.4	9.1
15	392.6	7.3	0.875	23.1	269.4	19.6
30	440.8	8.8	0.980	28.1	334.0	31.3
45	501.0	6.2	1.047	29.0	419.9	29.4
60	539.1	12.1	1.182	30.9	528.3	34.9

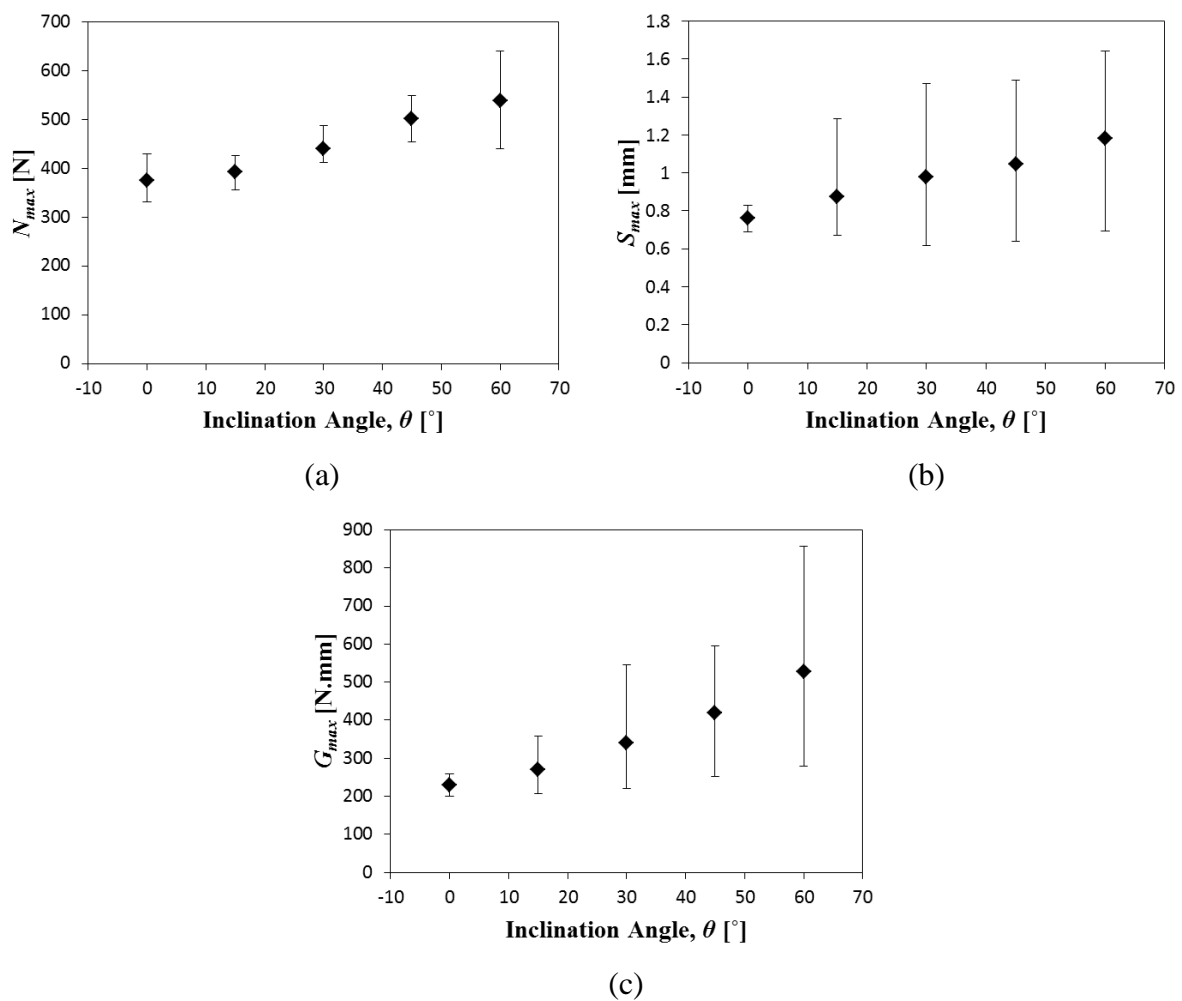


Figure 5.8. The range and average values for different fibre embedment inclination angles with regard to (a) the maximum pull-out force ( $N_{max}$ ), (b) the slip at maximum pull-out force ( $S_{max}$ ) and (c) the pull-out energy at maximum force ( $G_{max}$ )

### 5.1.1.4 Fibre mechanical anchorage

Single fibre pull-out tests were performed on three different hooked-end steel fibres, namely TYPE A, TYPE B and TYPE C. The hooked-end of each of these fibres had different geometrical properties, see Table 3.1. The pull-out load-slip responses for each fibre mechanical anchorage are depicted in Figure I.5, see Appendix I. The average pull-out load-slip response (Curve 1) for each fibre mechanical anchorage is presented in Figures 5.9(a) to 5.9(c) together with the contribution of the hooked-end mechanism (Curve 3). The average mechanical bond mechanism (Curve 3) was obtained by subtracting the average straight fibre series, S\_lb15\_0\_0.025 (Curve 2), from the hooked-end series (Curve 1).

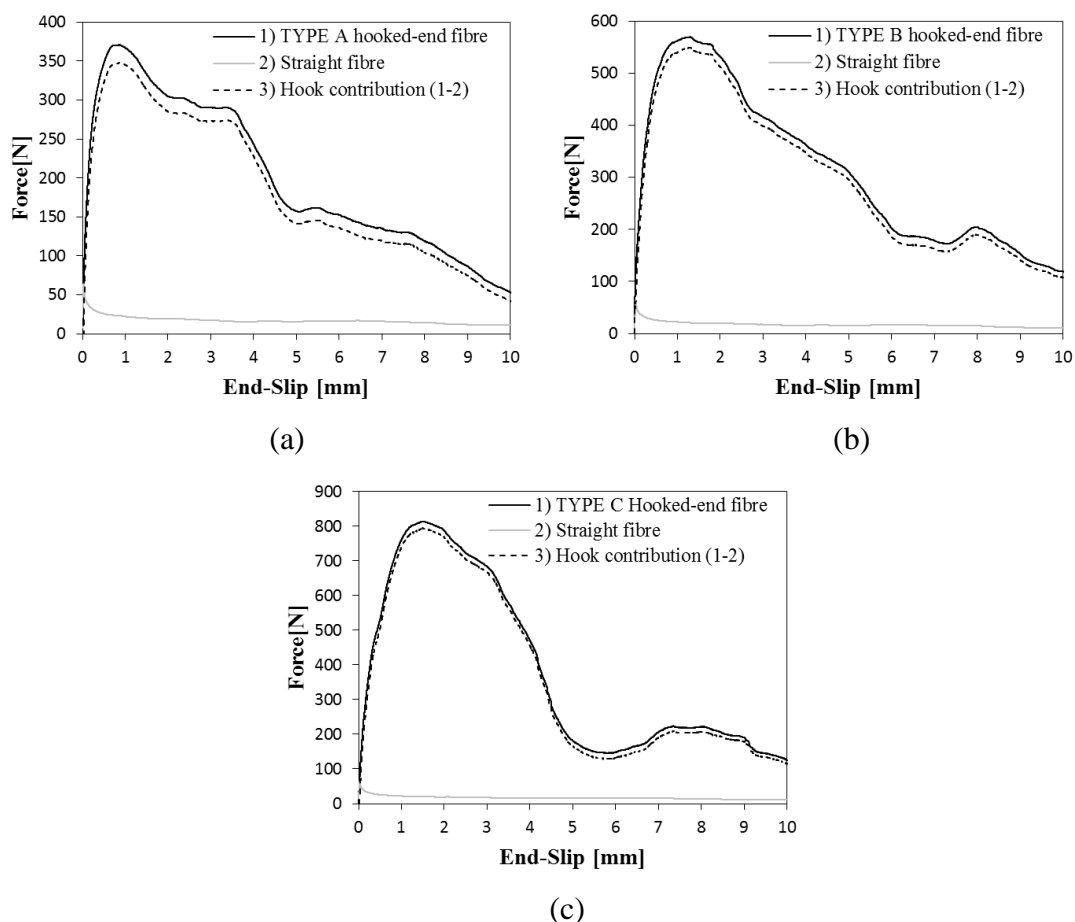


Figure 5.9. The average contribution of the hooked-end to the overall pull-out load-slip response for (a) TYPE A hooked-end fibres, (b) TYPE B hooked-end fibres and (c) TYPE C hooked-end fibres

Figure 5.9 shows that the geometry of the hooked-end of the fibre significantly affects the shape of the pull-out load-slip response. The TYPE A, TYPE B, and TYPE C hooked-end fibres differ from each other by the amount of bends or kinks in the hooked-end, see Figure

5.10. The TYPE A fibre has only two kinks, the TYPE B fibre has three kinks and the TYPE C fibre has four kinks. The pre-peak response is significantly affected by the amount of kinks in the hooked-end. The magnitude of the non-linear part in the pre-peak response is more pronounced for fibres with more kinks in the hooked-end. As the amount of kinks in the hooked-end increases more micro-cracking is induced to the surrounding concrete matrix at the zone of the kinks, causing the amount of irrecoverable deformation to increase with the amount of kinks, see Figure 5.10. The post-peak part was also significantly affected by the amount of kinks in the hooked-end. After the peak-load was reached the hooked-end of the fibre was deformed due to straightening of the kinks in the hook as the slip increased. After the hooked-end was completely straightened the pull-out behaviour was controlled under frictional resistance. Complete straightening of the hooked-end occurred at approximately 4.5 mm, 8.5 mm and 10 mm for TYPE A, TYPE B and TYPE C hooked-end fibres, respectively. These values correspond to the straightened hook length of the respective fibres.

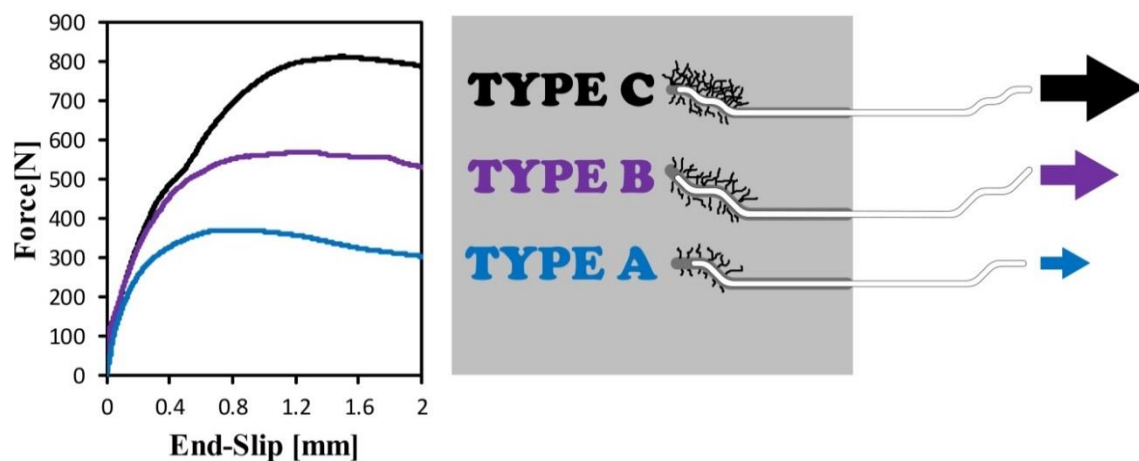


Figure 5.10. Comparison of average pre-peak pull-out behaviour for TYPE A, TYPE B and TYPE C fibres

In general, the contribution of the mechanical bond mechanism on the pull-out load-slip response increased with the amount of kinks in the hook-end of the fibre (see Figure 5.9). It would be thought that after the hooked-end is straightened that the pull-out load (frictional resistance) would be of the same magnitude as that of the straight fibre. However a higher pull-out load is observed in Figure 5.9 after the hooked-end is straightened. This is due to micro-cracking and crushing of the concrete matrix at the kinks, which resulted in the fibre not being perfectly straightened when passing through the imprint made by the hooked-end. This caused an increase in the frictional resistance after the fibre passed the last corner of the hooked-end imprint in the concrete matrix. The contribution of the additional frictional

resistance provided by the hooked-end that is not perfectly straightened is depicted by the hook contribution response (curves 3 in Figure 5.9) after a slip of approximately 4.5 mm, 8.5 mm, and 10 mm for TYPE A, TYPE B and TYPE C hooked-end steel fibres, respectively.

The average maximum force ( $N_{max}$ ), the average slip at maximum force ( $S_{max}$ ), and the average pull-out energy at maximum force ( $G_{max}$ ) for the different fibre mechanical anchorages are summarised in Table 5.4. The results are graphically presented in Figure 5.11 with error bars indicating the minimum and maximum values.

*Table 5.4. Average values of the maximum force ( $N_{max}$ ), the slip at maximum force ( $S_{max}$ ) and the pull-out energy at maximum force ( $G_{max}$ ) for different fibre mechanical anchorages*

Anchorage type	$N_{max}$ [N]	CoV [%]	$S_{max}$ [mm]	CoV [%]	$G_{max}$ [N.mm]	CoV [%]
Straight	69.0	29.4	0.021	29.0	1.1	32.9
A	375.8	11.7	0.760	8.8	229.4	9.1
B	608.7	14.9	1.087	41.8	527.4	48.6
C	849.8	17.5	1.480	28.0	937.6	42.2

## 5.1.2 Discussions

### 5.1.2.1 Failure modes

A schematic representation along the longitudinal cross-section of the specimen of the typical failure modes observed during the pull-out tests are presented in Figure 5.12. For both straight and hooked-end aligned fibres (TYPE A, TYPE B and TYPE C) complete pull-out was the dominating failure mode, see Figure 5.12(a). In the case of hooked-end fibres, after debonding between the fibre and the surrounding matrix interface, the hook was completely straightened. This failure mode is assigned as *FM1*. A failure mode observed for some aligned hooked-end fibres (TYPE A and TYPE C) was complete pull-out, however the hooked-end was not completely straightened, Figure 12(b). These pull-out load-slip responses showed a completely different behaviour than the rest of the specimens and are depicted in blue in Appendix I. This failure was assigned as *FM2*. A failure mode (*FM3*) that was only observed for some aligned TYPE B hooked-end fibres was rupturing of the hooked-end of the fibre, Figure 12(c). After the hooked-end ruptured the pull-out occurred under frictional resistance as for straight fibres. These pull-out load-slip responses are depicted in red in Appendix I. For TYPE A hooked-end fibres embedded at different inclination angles, complete pull-out of the fibre was observed, however spalling of the matrix at the exiting point was detected that was

induced by the bend of the inclined fibre, Figure 12(d). This type of failure mode was assigned as *FM4*.

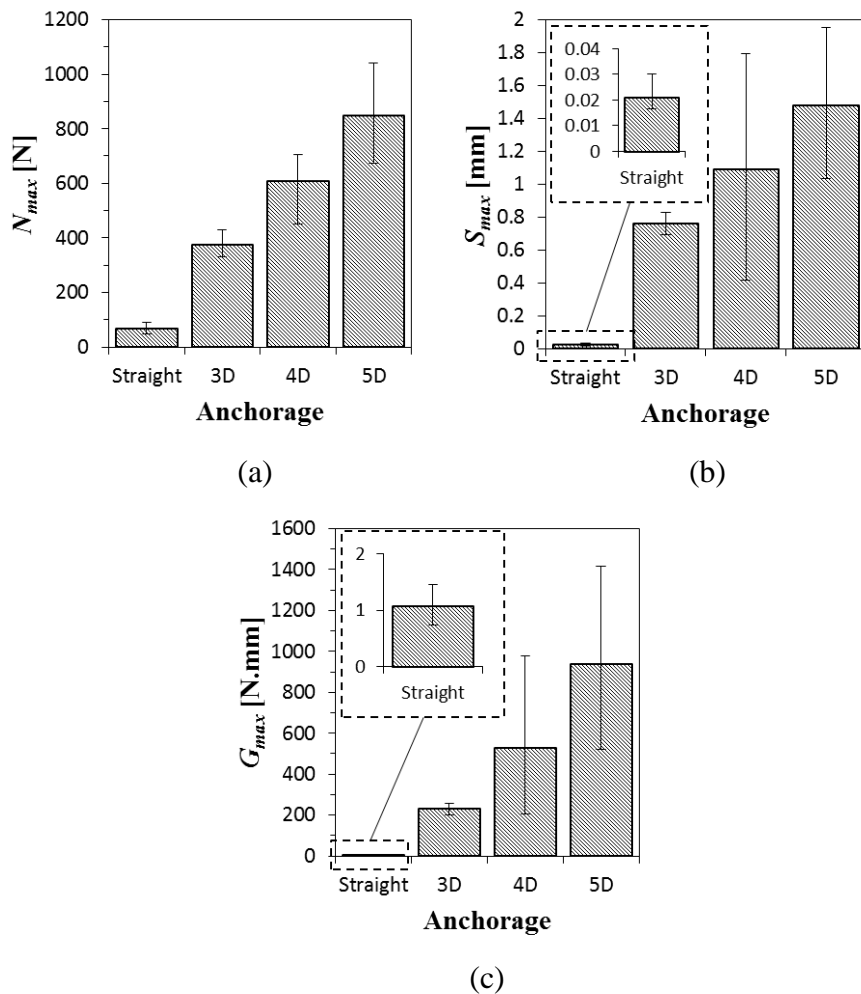


Figure 5.11. The range and average values for different fibre mechanical anchorages with regard to (a) the maximum pull-out force ( $N_{max}$ ), (b) the slip at maximum pull-out force ( $S_{max}$ ) and (c) the pull-out energy at maximum force ( $G_{max}$ )

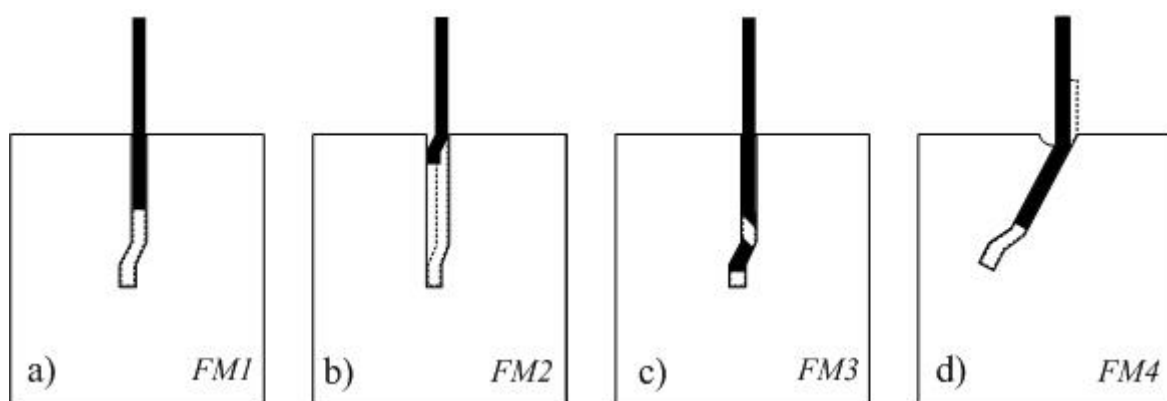


Figure 5.12. Typical failure modes observed during the fibre pull-out tests



Table 5.5 presents a summary of all the failure modes that were observed during each pull-out series. When more than one failure mode was observed for a specific series, the number of specimens corresponding to the type of failure mode is indicated in parentheses.

The tensile strength specified by the manufacturers of the TYPE A hooked-end fibres was lower (1160 MPa) compared to that of the TYPE B hooked-end fibres (1500 MPa). However, some of the TYPE B hooked-end fibres fractured during the pull-out tests (Failure mode *FM3*). This is a result of the improved anchorage mechanism as compared to the TYPE A hooked-end fibre. The anchorage mechanism of the TYPE C hooked-end fibres is more beneficial than that of the TYPE B hooked-end fibres. Nevertheless all the pull-out tests performed on TYPE C hooked-end fibres showed complete pull-out (Failure mode *FM1*). This is due to the high tensile strength of the TYPE C hooked-end fibres (2300 MPa).

*Table 5.5. Summary of the failure modes observed for each pull-out series*

Series	Failure mode
S_lb15_0_0.00025	<i>FM1</i>
S_lb15_0_0.0025	<i>FM1</i>
S_lb15_0_0.025	<i>FM1</i>
S_lb15_0_0.25	<i>FM1</i>
S_lb15_0_2.5	<i>FM1</i>
A_lb15_0_0.00025	<i>FM1</i>
A_lb15_0_0.0025	<i>FM1</i> (5); <i>FM2</i> (2)
A_lb15_0_0.025	<i>FM1</i> (6); <i>FM2</i> (2)
A_lb15_0_0.25	<i>FM1</i>
A_lb15_0_2.5	<i>FM1</i> (7); <i>FM2</i> (2)
A_lb7.5_0_0.025	<i>FM1</i>
A_lb30_0_0.025	<i>FM1</i>
A_lb15_15_0.025	<i>FM4</i>
A_lb15_30_0.025	<i>FM4</i>
A_lb15_45_0.025	<i>FM4</i>
A_lb15_60_0.025	<i>FM4</i>
B_lb15_0_0.025	<i>FM1</i> (4); <i>FM3</i> (4)
C_lb15_0_0.025	<i>FM1</i>

### 5.1.2.2 Pull-out loading rate

The totality of both hooked-end and straight fibres were completely pulled out from the matrix. This corresponds to failure mode *FM1*, see Figure 5.12(a). For test series A\_lb15\_0\_2.5, A\_lb15\_0\_0.025 and A\_lb15\_0\_0.0025 a distinct pull-out load-slip response

is observed, these results are shown in blue in Figure I.2, see Appendix I. This pull-out behaviour corresponds to failure mode *FM2*, see Figure 5.12(b).

An insignificant rate-dependent trend was found for the maximum pull-out force ( $N_{max}$ ) for TYPE A hooked-end fibres.  $N_{max}$  increased with 3.81 % from the lowest to the highest pull-out rate, and was therefore considered insignificant. Kim et al. (2008) also found that the increase in  $N_{max}$  was insignificant for pull-out rates ranging between 0.018 mm/s to 18 mm/s for hooked-end steel fibres embedded in a mortar matrix. Banthia & Trottier (1991) concluded that the pull-out load for hooked-end steel fibres embedded in cement-based matrixes is generally higher under impact (1500mm/s) than under static pull-out ( $8.46 \times 10^{-3}$  mm/s). Similar results were found by Abu-Lebdeh et al. (2010) at a dynamic rate of 25.4 mm/s and a static rate of 0.021 mm/s for hooked-end steel fibres embedded in a normal concrete matrix. For straight fibres, a steady behaviour was found averaging 67.75 N. Gokoz & Naaman (1981) found similar results for straight steel fibres, embedded in a mortar matrix, tested under static ( $4.2 \times 10^{-2}$  mm/s) and high loading rates (500 mm/s). The results found by Abu-Lebdeh et al. (2010) on straight steel fibres contradicts the results found by Gokoz & Naaman (1981) and the results found in this study. They found that  $N_{max}$  was significantly higher for high dynamic pull-out rates (25.4 mm/s) than for low static pull-out rates (0.021 mm/s). From the results it is concluded that  $N_{max}$  is not rate sensitive for both straight and TYPE A hooked-end steel fibres subjected to loading rates ranging between 0.00025 mm/s and 2.5 mm/s. An interesting result observed in Table 5.1 is that the coefficient of variation (CoV) for straight fibres is significantly higher than for TYPE A hooked-end fibres at each loading rate. The unstable debonding process for straight fibres, as explained in Section 5.1.1.1, is thought to be the reason that the CoV's are higher in straight fibres than in TYPE A hooked-end fibres.

The slip at maximum force ( $S_{max}$ ) showed a steady behaviour for straight fibres averaging 0.022 mm for pull-out rates ranging between 0.00025 mm/s and 2.5 mm/s. Abu-Lebdeh et al. (2010) found that  $S_{max}$  is significantly lower at high dynamic pull-out rates (25.4 mm/s) than for low static pull-out rates (0.021 mm/s) for straight steel fibres embedded in a normal concrete matrix. A significant rate-dependence was found for TYPE A hooked-end steel fibres.  $S_{max}$  decreased by 18.2 % from the lowest to the highest pull-out rate. Kim et al. (2008) showed that for hooked-end steel fibres embedded in a mortar matrix,  $S_{max}$  showed a steady behaviour for pull-out rates ranging between 0.018 mm/s to 18 mm/s. It is therefore

concluded that  $S_{max}$  for straight steel fibres is not rate sensitive for pull-out rates ranging between 0.00025 mm/s and 2.5 mm/s, however TYPE A hooked-end steel fibres are. It is also noted in Table 5.1 that the CoV for straight fibres is significantly higher than for TYPE A hooked-end fibres at each loading rate. The same reason as mentioned for  $N_{max}$  is thought to be the cause of this effect.

The pull-out energy at maximum force ( $G_{max}$ ) showed a steady behaviour for straight fibres. Gokoz & Naaman (1981) showed that for straight steel fibres embedded in a mortar matrix the pull-out energy at complete pull-out is independent from the pull-out loading rate ranging between static ( $4.2 \times 10^{-2}$  mm/s) and high loading rates (500 mm/s). The pull-out energy at maximum force ( $G_{max}$ ) for TYPE A hooked-end fibres showed rate sensitivity for the tested pull-out rate range (0.00025 mm/s to 2.5 mm/s). An 11.56 % decrease is found from the lowest to the highest pull-out rate. Kim et al. (2008) found that the pull-out energy up to the initiation of the mechanical bond increased for hooked-end fibres embedded in a mortar matrix for pull-out rates ranging between 0.018 mm/s and 1.8 mm/s. However, a reduction was found when the rate was increased from 1.8 mm/s to 18 mm/s. From the results presented in Table 5.1 it is concluded that the work done up to the maximum pull-out force is equivalent over the tested pull-out rate range (0.00025 mm/s to 2.5 mm/s) for straight steel fibres. However, for TYPE A hooked-end steel fibres the energy dissipated to reach  $N_{max}$  increased as the pull-out rate decreased.

From the discussions above it is concluded that straight steel fibres showed no rate sensitivity over the tested pull-out rate range. However, TYPE A hooked-end steel fibres showed rate sensitivity. It is evident that the contribution of the mechanical bond (hooked-end) is the cause of the relative significant rate sensitivity. The decrease in  $S_{max}$  from the lowest to the highest pull-out rate is induced by the visco-elastic behaviour of the interface between the hook and the matrix.

### 5.1.2.3 Fibre embedment length

The totality for all embedment lengths was complete pull-out. Failure mode *FM1* (Figure 5.12(a)) was observed in all the specimens tested except for two specimens in test series A\_lb15\_0\_0.025 that failed under *FM2* (Figure 5.12(b)) as previously mentioned in Section 5.1.2.2.

As previously mentioned, the magnitude of the pull-out load-slip responses for embedment lengths of 15 mm and 30 mm were essentially the same, however for 7.5 mm a marked difference in the magnitude of the response is observed. Similar results were found by Robins et al. (2002). They performed pull-out tests on hooked-end steel fibres embedded at four different embedment lengths (5 mm, 10 mm, 15 mm and 20mm) in normal concrete. They showed that the pull-out load-slip responses for embedment lengths ranging from 10 mm to 20 mm were essentially the same. However, with a 5 mm embedment length they showed that the shape and magnitude of the curve was significantly different from those found with an embedment length ranging from 10 mm to 20 mm. A significant reduction in the maximum pull-out force ( $N_{max}$ ) was observed. They mentioned that the pull-out response is predominantly influenced by the mobilisation and straightening of the hooked-end and can only occur fully if the embedment length is greater than the length of the hooked-end, which typically ranged between 4-5 mm for the fibres they used.

From the results in Table 5.2 an increase in the maximum pull-out force ( $N_{max}$ ) was observed with an increase in the embedment length. The percentage increase in  $N_{max}$  was more pronounced for the embedment length increase from 7.5 mm to 15 mm than for the increase from 15 mm to 30 mm. The percentage increases in  $N_{max}$  for the two intervals were 7.29 % and 3.20 %, respectively. This corresponds with the results found by Robins et al. (2002) as mentioned above.

A similar behaviour was observed for the slip at maximum force ( $S_{max}$ ) and the pull-out energy at maximum force ( $G_{max}$ ) for the two aforementioned embedment length intervals.  $S_{max}$  and  $G_{max}$  increased by 13.74 % and 27.29 %, respectively, for the interval of 7.5 mm to 15 mm. For the interval of 15 mm to 30 mm an insignificant increase of 0.37 % and 4.97 % was observed for  $S_{max}$  and  $G_{max}$ , respectively. Cunha (2010) also showed a slight increase in  $S_{max}$  with an increase in the embedment length ( $l_b$ ) for hooked-end fibres embedded in a self-compacting concrete (SCC) matrix. He also found that the dissipated energy up to a slip of 1 mm increased as the embedment length increased.

It is concluded from the discussions above that the embedment length does not significantly influence the pull-out behaviour of TYPE A hooked-end fibres. However, this is only valid if the embedment length is greater than the length of the hooked-end.

#### 5.1.2.4 Fibre inclination angle

Failure mode *FM4* (Figure 5.12(d)) was observed for all fibres embedded at inclination angles. Cunha (2010) and Robins et al. (2002) found that for fibre inclination angles equal and greater than  $30^\circ$ , fibre rupture was the dominating failure mode. It should be noted that the cross-sectional diameter of the hooked-end fibres used by Cunha (2010) and Robins et al. (2002) were smaller (0.74 mm and 0.5 mm, respectively) than the fibres used in this research program (0.9 mm). Therefore, the TYPE A hooked-end fibres used in this research programme could withstand a higher pull-out load.

In general, the maximum pull-out force ( $N_{max}$ ) increased up to an inclination angle of  $60^\circ$ . From Figure 5.8(a) the increase in  $N_{max}$  appears to have a linear response. Fibres with an embedded inclination angle of  $60^\circ$  had on average a 43.5 % higher  $N_{max}$  than the aligned ( $0^\circ$ ) series. Cunha (2010) and Robins et al. (2002) also found that  $N_{max}$  increased up to a fibre embedment inclination of  $30^\circ$  for hooked-end fibres. For fibre embedment inclination angles higher than  $30^\circ$  they observed a decrease in  $N_{max}$ . They concluded that this type of failure is a consequence of the increased stress concentration induced by the bend at the fibre exiting point from the matrix as previously explained, and therefore the matrix will be more prone to cracking and spalling that causes a decrease in the load level. Cunha (2010) also mentioned that due to the spalling of the matrix at the exiting point of the fibre, a longer fibre length can be bend more easily which decreases the stiffness up to the peak load.

The slip at maximum pull-out force ( $S_{max}$ ) increased linearly with the fibre embedment inclination angle ( $\theta$ ), see Figure 5.8(b).  $S_{max}$  increased on average by 55.5 % when  $\theta$  was increased from  $0^\circ$  to  $60^\circ$ . Cunha (2010) also observed a significant increase in  $S_{max}$  with the embedment inclination angle. According to him this significant increase can be ascribed to other additional mechanisms that only occur during the pull-out behaviour of inclined fibres. As the fibre embedment inclination angle increases so does the stress concentration at the bending point of the fibre. This results in a more significant part of the matrix to be crushed at the exiting point of the fibre. Therefore a large protruding length (i.e. the fibre length that extends beyond the concrete matrix) is exposed and is deformed due to bending (see Figure 2.12). This additional displacement due to deformation of the protruding part of the fibre is included in the measured slip. This explains the increase in  $S_{max}$  with the embedment inclination angle.

In general, the pull-out energy at maximum force ( $G_{max}$ ) increased linearly with the embedment inclination angle, see Figure 5.8(c). A significant increase of 130.3 % was observed when the embedment inclination angle was increases from  $0^\circ$  to  $60^\circ$ . This increase is the result of the increased frictional resistance between the bending point of the inclined fibre and the matrix at the exiting zone of the fibre. Hence, more energy is needed to pull-out the fibre. Cunha (2010) investigated the influence of fibre embedment inclination angle on pull-out energy up to a slip of 1 mm ( $G_{1mm}$ ). He observed an increase in  $G_{1mm}$  up to a fibre inclination angle of  $30^\circ$  followed by a decrease for a  $60^\circ$  angle. The same reason as explained above was the cause of the increase in  $G_{1mm}$  up to a fibre inclination angle of  $30^\circ$ . The cause for the decrease in  $G_{1mm}$  for fibre inclination angles higher than  $30^\circ$  is the same as for the decrease in  $N_{max}$  as mentioned previously.

It is concluded from the preceding discussions that the fibre embedment inclination angle significantly influences the pull-out behaviour of TYPE A hooked-end fibres embedded in a concrete matrix. The increase in frictional resistance, matrix spalling, and deformation of the fibre at the bending point of the fibre were the dominating mechanisms during the pull-out behaviour of inclined fibres.

### 5.1.2.5 Fibre mechanical anchorage

The type of failure mode observed for each series is presented in Table 5.6. If more than one failure mode was observed for a specific series, the number of specimens corresponding to each failure mode is indicated in parentheses. Refer to Section 5.1.2.1 for the explanation of types of failure modes.

Table 5.6. Failure modes observed during the pull-out tests on different fibre mechanical anchorage types

Series	Failure mode
S_lb15_0_0.025	FM1
A_lb15_0_0.025	FM1(6); FM2(2)
B_lb15_0_0.025	FM1(4); FM3(4)
C_lb15_0_0.025	FM1(6); FM2(2)

The maximum pull-out force ( $N_{max}$ ) was significantly influenced by the type of hooked-end mechanical anchorage used. For straight fibres  $N_{max}$  depends on the bond between the fibre and the surrounding matrix. However, for hooked-end fibres  $N_{max}$  is dependent on several mechanisms, namely: the cohesive bond between fibre and surrounding matrix, frictional resistance between fibre and matrix, and the geometry of the hooked-end of the fibre.

Figure 5.9 shows that the hook mechanism significantly contributed to the maximum pull-out load ( $N_{max}$ ) and can be considered as the principle mechanisms during the straightening phase of the hooked-end. The contribution of the hook mechanism on  $N_{max}$  was, 93.76 %, 96.38 % and 97.56 % for TYPE A, TYPE B and TYPE C hooked-end fibres, respectively. Cunha (2010) found a slight decrease in the contribution of the hook mechanism on  $N_{max}$  with an increase in fibre embedment length. This is due to the increase in the cohesive bond and frictional resistance as the embedment length increases, thus increasing its contribution to  $N_{max}$ .

The slip at maximum force ( $S_{max}$ ) increased significantly with the amount of kinks in the hooked-end of the fibre. As the amount of kinks in the hooked-end are increased more micro-cracking is induced to the surrounding concrete matrix at the zone of the kinks during the debonding phase, hence the amount of irrecoverable deformation that contributes to the slip up to maximum pull-out force ( $S_{max}$ ) is increased.

For straight fibres, the pull-out energy at maximum force ( $G_{max}$ ) is dependent on the amount of energy needed to break the bond between the fibre and the surrounding matrix. It is perceived that when the amount of kinks is increased more energy would be required to pull-out the fibre, due to the improved mechanical bond. This is justified by the pull-out results in Table 5.4.  $G_{max}$  increased significantly with the amount of kinks in the hooked-end of the fibre. The energy dissipated during the pull-out process is divided into three categories, namely: (1) the energy needed to break the bond between the fibre and the matrix, (2) the energy dissipated due to frictional resistance between the fibre and the matrix, and (3) the energy dissipated during the straightening of the hooked-end of the fibre. Regarding  $G_{max}$ , the energy dissipated on the mobilisation of the hooked-end was 91.24 %, 94.29 %, and 95.67 % of the total energy dissipated for TYPE A, TYPE B and TYPE C hooked-end fibres, respectively.

From the results it was concluded that increasing the amount of kinks in the hooked-end of the fibre significantly improves the pull-out behaviour. The pull-out behaviour is governed by three mechanisms, namely: (1) the cohesive bond mechanism, (2) the frictional resistance mechanism, and (3) the mechanical bond mechanism. For hooked-end fibres the mechanical bond is the principle mechanism that controls the pull-out behaviour as its magnitude is far greater than the other two mentioned mechanisms.



---

## 5.2 Single Fibre Sustained Load Tests

In Chapter 4 an increase in the crack width was found due to sustained uni-axial tensile loading on pre-cracked SFRC beams. It should be noted that on the crack plane the fibres were randomly orientated. During the pre-cracked sustained load tests (see Section 4.3) no fibre fracture occurred. Hannant (1978) showed that when composite failure occurred due to fibre pull-out the average pull-out length was a quarter of the fibre length ( $l_f/4$ ). Therefore, all single fibre sustained load tests performed had a constant embedment length of  $l_f/4$ .

This investigation was performed to characterise the effect of certain factors on the pull-out creep behaviour. The factors investigated in this experimental program were restricted to the applied sustained load, the fibre embedment inclination angle and the fibre mechanical anchorage. In Chapter 4 the specimens were pre-cracked before the sustained load was applied. The pre-cracking process caused damage between the fibres bridging the crack and the surrounding concrete matrix interface. This caused a pull-out of the fibres equal to that of the pre-crack width. To investigate whether this pre-damage due to pre-cracking would have an effect on the pull-out creep behaviour, a series of pre-damaged single fibre sustained load tests were performed on pre-damaged single fibre specimens. The pull-out creep of the fibres was measured using the method of microscope images as mentioned in Section 3.3.2.3.

### 5.2.1 Results

#### 5.2.1.1 Applied sustained load

Four sustained load levels were investigated on TYPE A hooked-end fibres, namely: 30 %, 50 %, 70 % and 85 % of the average maximum pull-out rate force that was determined from the results of the single fibre pull-out rate tests (see Section 5.1.1.1). It was noted that the maximum pull-out force was not significantly affected over the investigated pull-out rate range. The average of the average maximum pull-out force over the investigated pull-out rate range was calculated as 369.8 N. The sustained load levels were based on percentages of this value. A typical pull-out load-slip response of an aligned TYPE A hooked-end fibre is depicted up to a slip of 2 mm in Figure 5.13. The arrows indicate the magnitude of the applied sustained loads. The measurement of the pull-out creep was commenced immediately after the load was applied. The fibre pull-out observed during the load application is defined as the instantaneous pull-out ( $\delta_{inst}$ ).



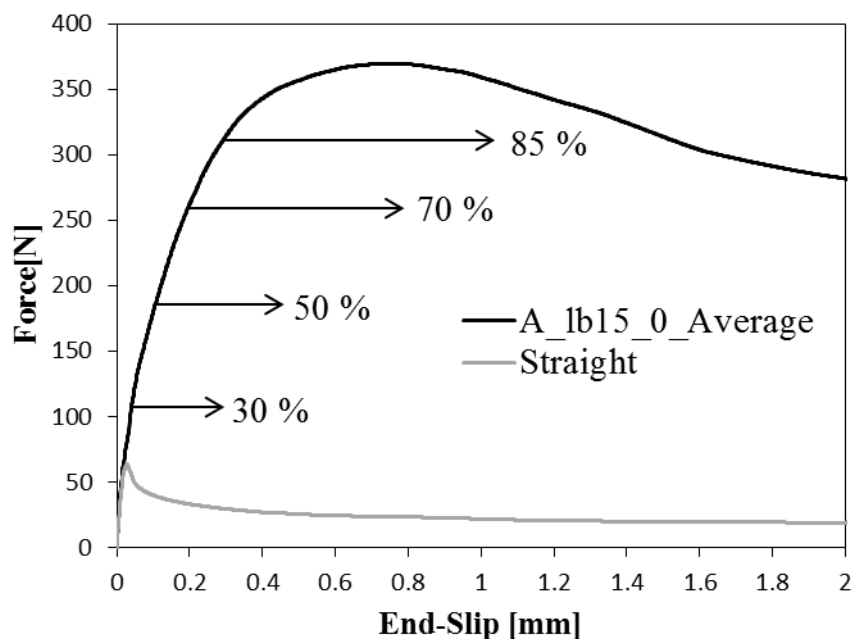


Figure 5.13. Schematic representation of the loading procedure for the single fibre sustained load tests

The calculated fibre pull-out creep over time for each individual specimen subjected to different load levels are depicted in Figure II.1, see Appendix II. The average pull-out creep-time responses for each load level are shown in Figure 5.14.

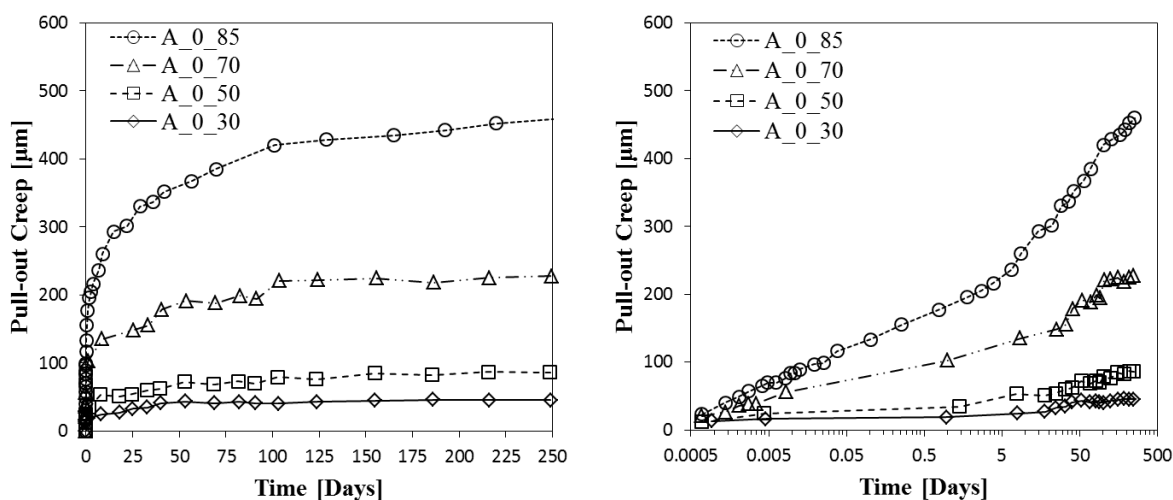


Figure 5.14. Average pull-out creep-time response for each load level for TYPE A hooked-end fibres: (a) linear plot and (b) semi-logarithmic plot

All specimens tested showed an initial increase in the pull-out creep just after the sustained load was applied. The rate of pull-out creep shows a clear trend at each load level, a decrease in the pull-out creep rate is observed with time. Another important effect observed from the

results is that the magnitude of pull-out creep is dependent on the applied load level. Babafemi & Boshoff (2015) performed single fibre sustained load tests on macro-synthetic fibres and concluded that the time-dependent pull-out displacement is dependent on the sustained applied load. However, the pull-out was found to be a combination of the fibre lengthening and the fibre pulling out. It is expected that time-dependent fibre lengthening will not occur for steel fibres.

Figure 5.13 shows that the magnitude of the applied sustained load for TYPE A hooked-end fibres for load levels equal and higher than 30 % is significantly higher than the maximum pull-out force for straight fibres. This entails that the pull-out creep ( $\delta_{creep}$ ) is exclusively induced by the mechanical hooked-end mechanism. The tensile sustained load applied to the fibre is transferred as a localised compressive sustained load at the zone of the hook (see Figure 5.15), which induces a compressive creep deformation of the concrete matrix. This causes a movement between the fibre and the surrounding matrix which was defined as pull-out creep ( $\delta_{creep}$ ).

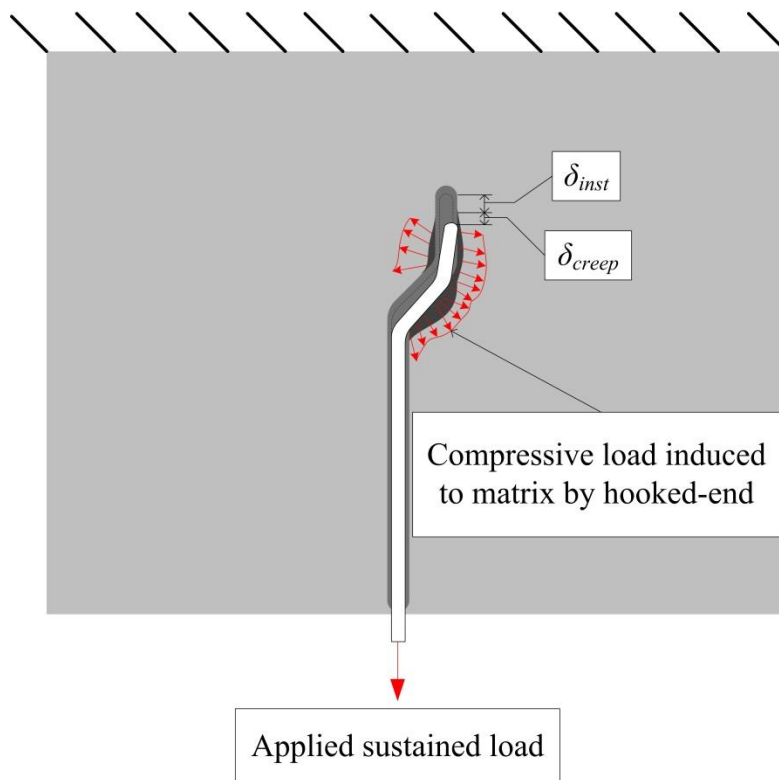


Figure 5.15. Schematic representation of pull-out creep

With the aim to analyse in detail the calculated pull-out creep, the values of the calculated instantaneous pull-out ( $\delta_{inst}$ ) and pull-out creep ( $\delta_{creep}$ ) at various load levels after 30, 100, 170

and 240 days are presented in Table 5.7. Also presented in Table 5.7 is the coefficient of pull-out creep, which is defined as:

$$\gamma_{creep}(t) = \frac{\delta_{creep}(t)}{\delta_{inst}} \quad (5.1)$$

where  $t$  is the generic time instance at which  $\gamma_{creep}(t)$  is determined. The coefficient of pull-out creep ( $\gamma_{creep}(t)$ ) is an indication of the increase in pull-out relative to the instantaneous pull-out. The coefficient of pull-out creep ( $\gamma_{creep}(t)$ ) is determined at 30, 100, 170 and 240 days, see Table 5.7. In Figure 5.16 the pull-out creep results ( $\delta_{creep}$ ) after each time instance presented in Table 5.7 are graphically presented against the load level.

Table 5.7. The coefficients of pull-out creep ( $\gamma_{creep}(t)$ ) at various load levels after 30, 100, 170 and 240 days

Load level [%]	$\delta_{inst}$ [ $\mu\text{m}$ ]	$\delta_{creep}$ [ $\mu\text{m}$ ] after:				$\gamma_{creep}$ after:			
		30 days	100 days	170 days	240 days	30 days	100 days	170 days	240 days
30	95	33	40	45	45	0.35	0.42	0.47	0.48
50	187	58	77	84	86	0.31	0.41	0.45	0.46
70	317	152	213	221	227	0.48	0.67	0.70	0.72
85	351	331	419	436	457	0.94	1.19	1.24	1.30

### 5.2.1.2 Fibre inclination angle

The effect of fibre embedment inclination angle on the pull-out creep of TYPE A hooked-end fibres was investigated by performing single fibre sustained load tests on three different embedment inclination angles, namely:  $0^\circ$ ,  $30^\circ$  and  $60^\circ$ . The sustained load applied at each inclination angle was 50 % of the average maximum pull-out force ( $N_{max}$ ), see Section 5.1.1.3, except for the  $0^\circ$  series. The applied sustained load for the  $0^\circ$  series was 50 % of the average of the average maximum pull-out rate force (369.8 N), the same as in the previous section. A summary of the applied sustained load for each fibre embedment inclination angle is presented in Table 5.8. In Figure 5.17 the typical pull-out load-slip response for TYPE A hooked-end fibres embedded at different inclination angles is presented. The arrows indicate the magnitude of the applied sustained load for each embedment inclination angle. The measurement of the pull-out creep was commenced immediately after the load was applied. The fibre pull-out observed during the load application is defined as the instantaneous pull-out.

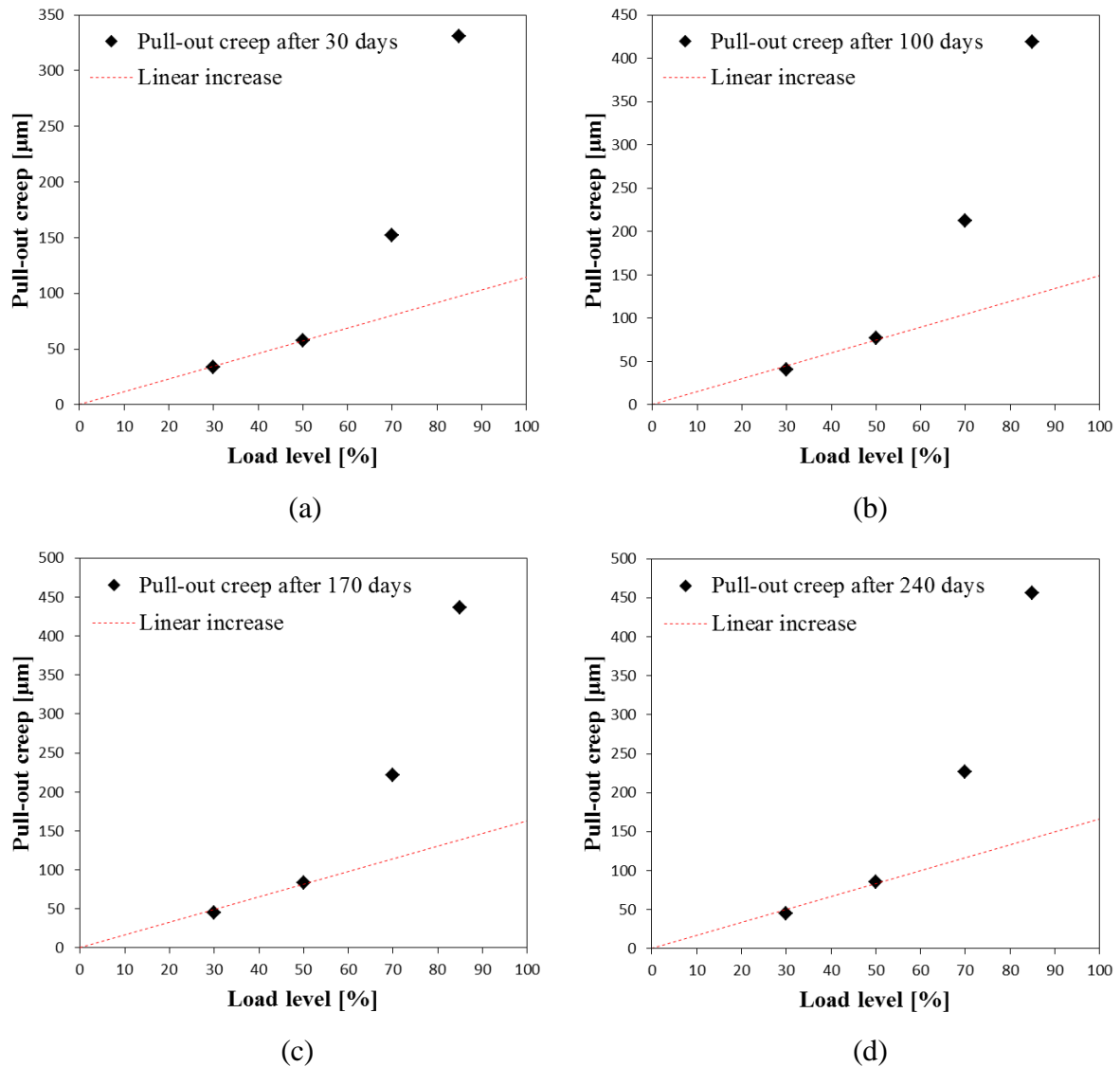


Figure 5.16. The pull-out creep at various load levels after (a) 30 days, (b) 100 days, (c) 170 days and (d) 240 days

Table 5.8. The applied sustained loads for different fibre embedment inclination angles

$\theta$ [ $^{\circ}$ ]	$N_{max}$ [N]	Applied load ( $0.5 \cdot N_{max}$ ) [N]
0	369.8	184.9
30	440.8	220.4
60	539.1	269.6

The pull-out creep-time responses for each embedment inclination angle is presented in Figure II.2, see Appendix II. The Average pull-out creep-time response for each embedment inclination angle is presented in Figure 5.18.

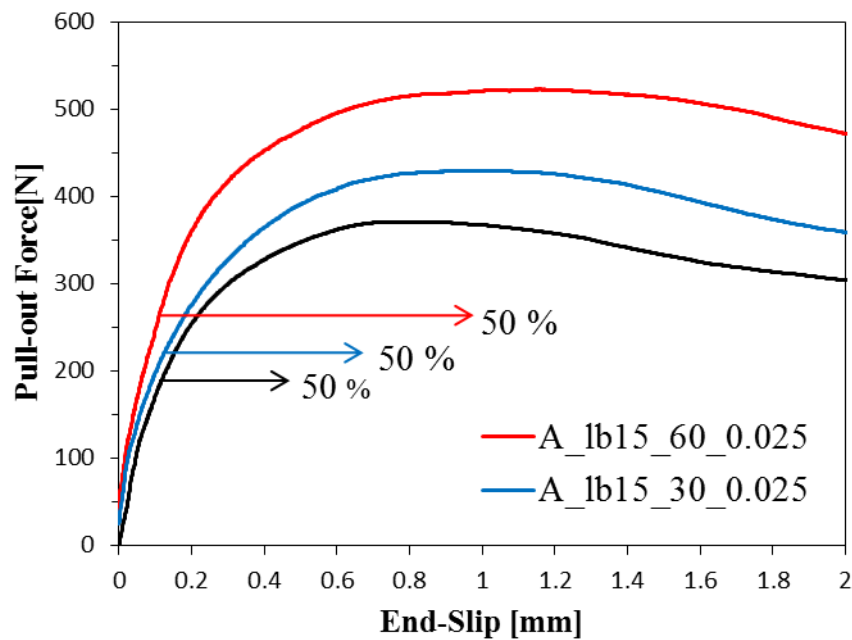


Figure 5.17. Schematic representation of the loading procedure for the single fibre sustained load tests embedded at different inclination angles

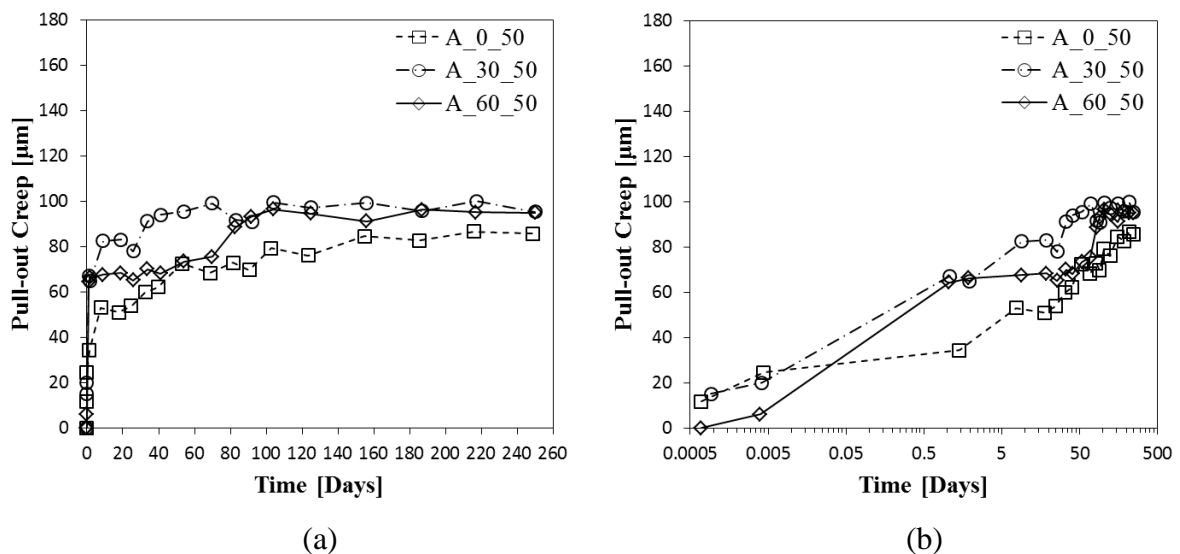


Figure 5.18. Average pull-out creep-time responses for different fibre embedment inclination angle: (a) linear plot and (b) semi-logarithmic plot

An initial increase in the pull-out creep was observed for all specimens just after the sustained load was applied. The pull-out creep-time responses for the different fibre embedment inclination angles appeared to be similar over the measured time period. This entails that the pull-out creep was independent from the fibre inclination angle. It should be noted that the applied sustained load increased with the fibre embedment inclination angle. Thus, with a

constant applied sustained load for all fibre embedment inclination angles, it is perceived that the pull-out creep would decrease with the increase in fibre embedment inclination angle.

To further analyse the results, the instantaneous pull-out ( $\delta_{inst}$ ) and the pull-out creep ( $\delta_{creep}$ ) for each fibre embedment inclination angle were determined at the following time instances, namely: 30, 100, 170 and 240 days (see Table 5.9). Further, for each inclination angle the coefficient of pull-out creep ( $\gamma_{creep}(t)$ ) was determined after each time instance (see Equation 5.1). Figure 5.19 graphically presents the pull-out creep ( $\delta_{creep}$ ) against the fibre embedment inclination angle after each time instance as presented in Table 5.9.

Table 5.9. The coefficients of pull-out creep ( $\gamma_{creep}(t)$ ) for different fibre embedment inclination angle after 30, 100, 170 and 240 days

$\theta$ [°]	$\delta_{inst}$ [ $\mu\text{m}$ ]	$\delta_{creep}$ [ $\mu\text{m}$ ] after:				$\gamma_{creep}$ after:			
		30 days	100 days	170 days	240 days	30 days	100 days	170 days	240 days
0	187	58	77	84	86	0.31	0.41	0.45	0.46
30	183	85	97	98	97	0.46	0.53	0.53	0.53
60	180	68	95	93	95	0.38	0.53	0.52	0.53

### 5.2.1.3 Fibre mechanical anchorage

The essence of this research programme was to investigate the behaviour of pull-out creep for fibres with different mechanical hooked anchorages. Three different hooked-end anchorages were investigated, namely: TYPE A, TYPE B and TYPE C. The sustained load applied to hooked-end anchorage was 50 % of the maximum pull-out force ( $N_{max}$ ), see Section 5.1.1.4, except for the TYPE A hooked-end. The applied sustained load for the TYPE A hooked-end series was 50 % of the average of the average maximum pull-out rate force (369.8 N) as explained in Section 5.2.1.1. The applied sustained load for each mechanical anchorage series is presented in Table 5.10. The pull-out load-slip responses for the different mechanical hooked-end anchorages are presented in Figure 5.20 up to a slip of 2 mm. The magnitude of the applied sustained load for each mechanical hooked-end anchorage is schematically represented by the arrows. The responses presented in Figure 5.20 are a representation of the behaviour during the application of the loads. The measurement of the pull-out creep ( $\delta_{creep}$ ) was commenced immediately after the load was applied. The fibre pull-out observed during the loading phase was defined as the instantaneous pull-out ( $\delta_{inst}$ ).

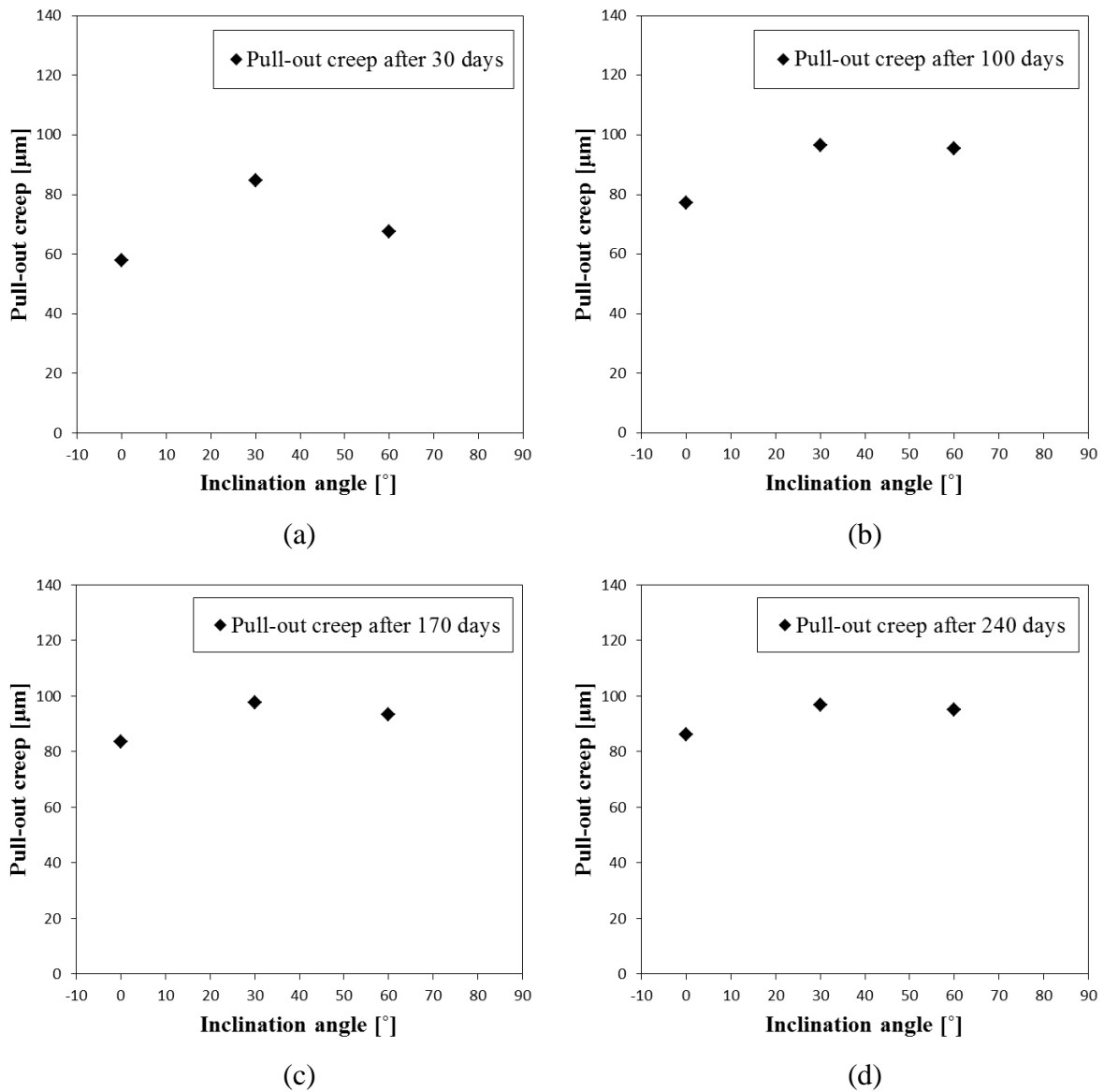


Figure 5.19. The pull-out creep for different fibre embedment inclination angles after (a) 30 days, (b) 100 days, (c) 170 days and (d) 240 days

Table 5.10. The applied sustained loads for different fibre mechanical anchorages

Anchorage type	$N_{max}$ [N]	Applied load ( $0.5 \cdot N_{max}$ ) [N]
A	369.8	184.9
B	608.7	304.3
C	849.8	424.9

The pull-out creep responses for the different fibre hooked-end anchorages are presented in Figure II.3, see Appendix II. The Average pull-out creep responses for the different fibre hooked-end anchorages are depicted in Figure 5.21.

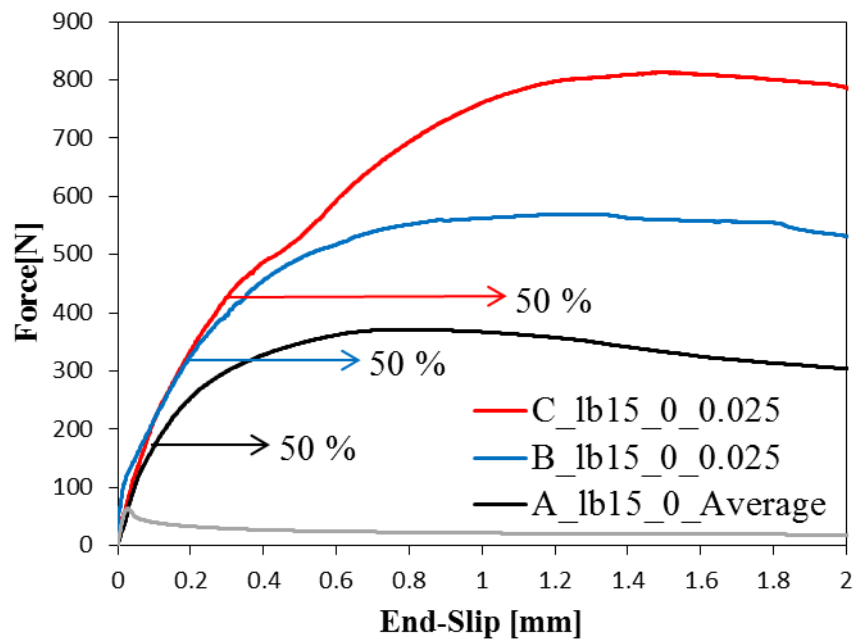


Figure 5.20. Schematic representation of the loading procedure for the single fibre sustained load tests with different fibre mechanical anchorages

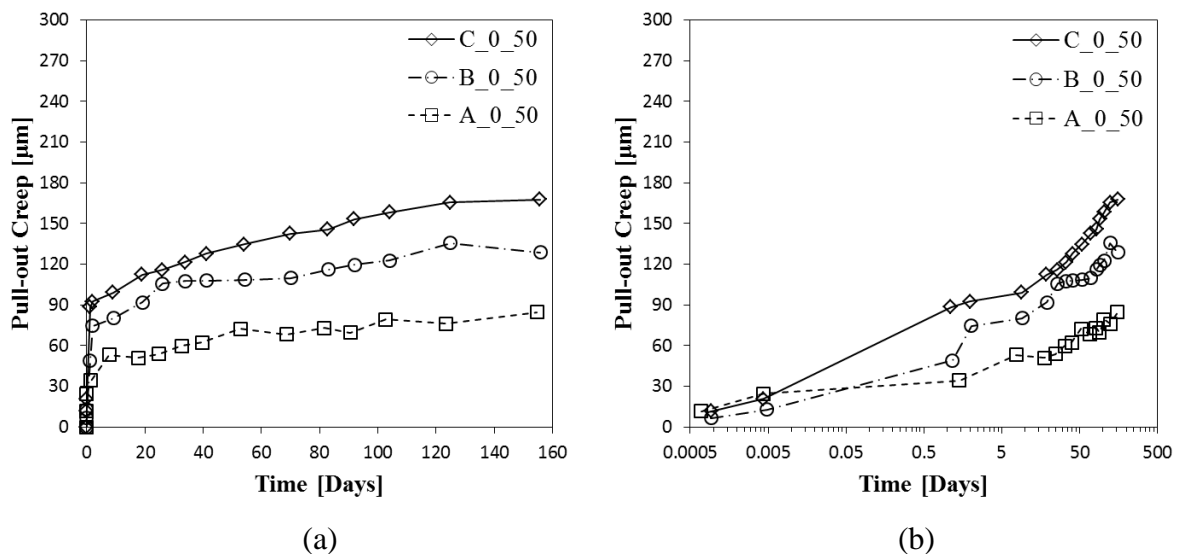


Figure 5.21. Average pull-out creep-time responses for different fibre hooked-end anchorages: (a) linear plot and (b) semi-logarithmic plot

Each hooked-end fibre within a series showed an initial increase in pull-out creep at a decreasing rate just after the load was applied. As previously explained in Section 5.1.1.4, the TYPE A, TYPE B and TYPE C hooked-end fibres differ from each other by the amount of kinks in the hooked-end. The results in Figure 5.21 show that the geometry of the hooked-end significantly affects the magnitude of pull-out creep. The magnitude increased significantly



with the amount of kinks. Figure 5.20 shows that the magnitude of the applied sustained load for each mechanical hooked-end anchorage series significantly exceeds the maximum pull-out force for straight fibres. This entails that the pull-out creep is exclusively induced by the mechanical hooked-end mechanism as previously mentioned in Section 5.2.1.1.

The pull-out creep for hooked-end series TYPE B and TYPE C was measured over a time period of 155 days due to unforeseen circumstances and not 249 days as for the TYPE A hooked-end series. To further analyse the results, the instantaneous pull-out ( $\delta_{inst}$ ) and pull-out creep ( $\delta_{creep}$ ) for the different fibre hooked-end anchorages were determined at 30, 100 and 150 days (see Table 5.11). The coefficient of creep ( $\gamma_{creep}(t)$ ) was determined after each time instance and presented in Table 5.11, see Equation 5.1 for the determination of  $\gamma_{creep}(t)$ . The pull-out creep values after each time instance are presented against the fibre hooked-end anchorage in Figure 5.22.

*Table 5.11. The coefficients of pull-out creep ( $\gamma_{creep}(t)$ ) for different fibre mechanical hooked-end anchorages after 30, 100 and 150 days*

Anchorage	$\delta_{inst}$ [ $\mu\text{m}$ ]	$\delta_{creep}$ [ $\mu\text{m}$ ] after:			$\gamma_{creep}$ after:		
		30 days	100 days	150 days	30 days	100 days	150 days
A	187	58	77	84	0.31	0.41	0.45
B	199	107	121	130	0.54	0.61	0.65
C	210	119	156	167	0.56	0.74	0.80

#### 5.2.1.4 Pre-damage sustained load test

As previously mentioned the pre-cracking process of the macroscopic specimens caused the fibres bridging the crack to pull-out equal to that of the pre-crack width. This pull-out of the fibres causes damage between the interface of the fibres and the surrounding concrete matrix. Therefore, the essence of this research programme was to investigate the effect of the pre-damage on the pull-out creep behaviour.

The specimens were pre-damage up to a slip equal to that of the average  $w_r$  (see Section 4.2.1). In Figure 5.23 the force-slip response of a specimen that was pre-damaged to a slip of 0.53 mm then unloaded and reloaded up to a slip of 1 mm is presented. This behaviour is a representative of the behaviour of the specimens that were pre-damaged, unloaded and then taken to the pull-out creep frames where they were subjected to sustained loads. The applied sustained load was 50 % of the average of the average maximum pull-out rate force (369.8 N)

as explained in Section 5.2.1.1. The arrow represents the magnitude of the applied sustained load to each pre-damaged specimen in the pull-out creep frame. The average irrecoverable slip after unloading is 0.45mm, which is almost similar to that of the average  $CMOD_{irr}$  (see Section 4.3.2).

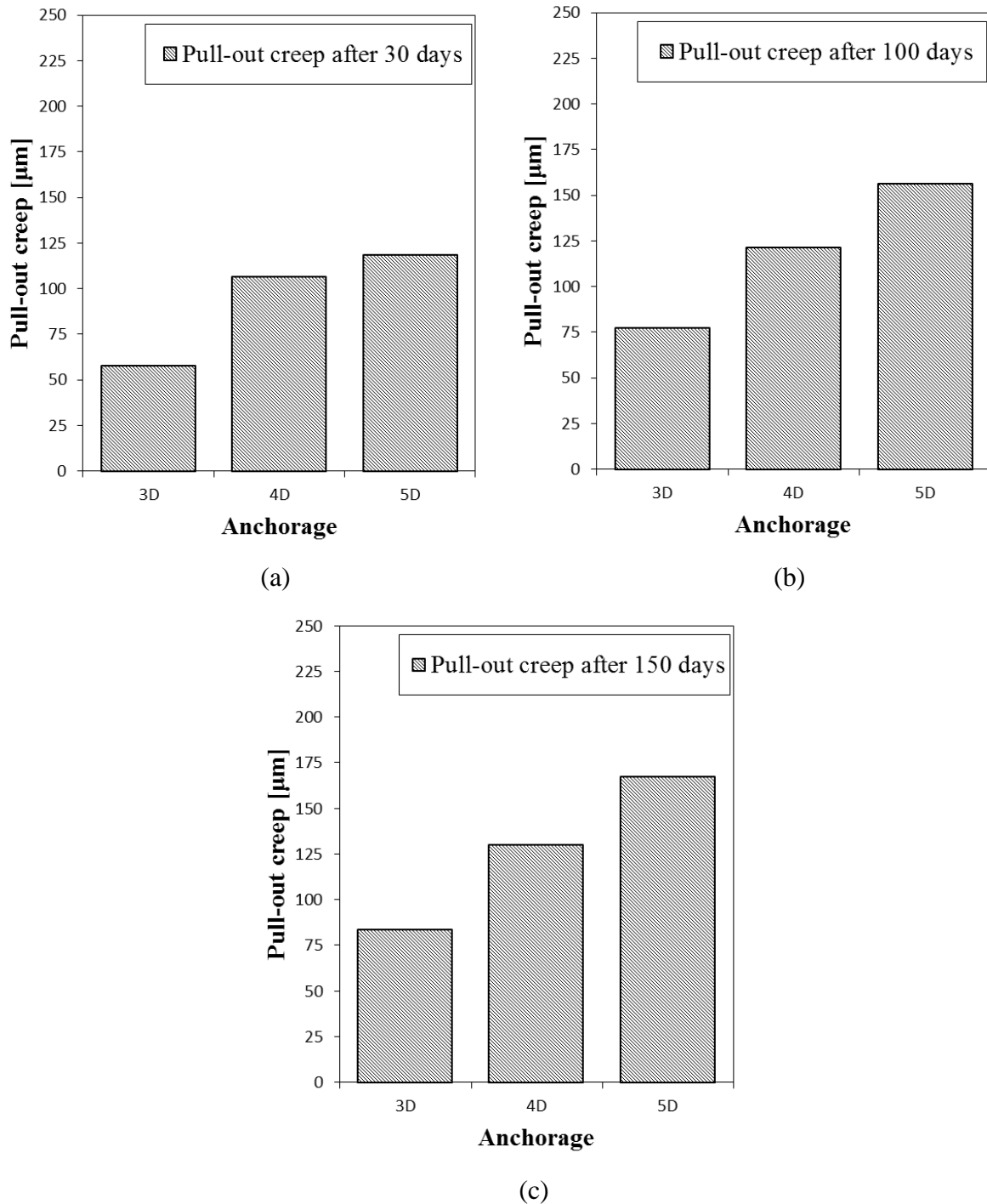


Figure 5.22. The pull-out creep for different fibre mechanical hooked-end anchorages after (a) 30 days, (b) 100 days and (c) 150 days

The pull-out creep responses for each pre-damaged specimen are presented in Figure II.4, see Appendix II. The average pull-out creep response for the pre-damaged specimens is depicted in Figure 5.24. Also presented in Figure 5.24 is the average response of the sustained load Series A\_0\_50.

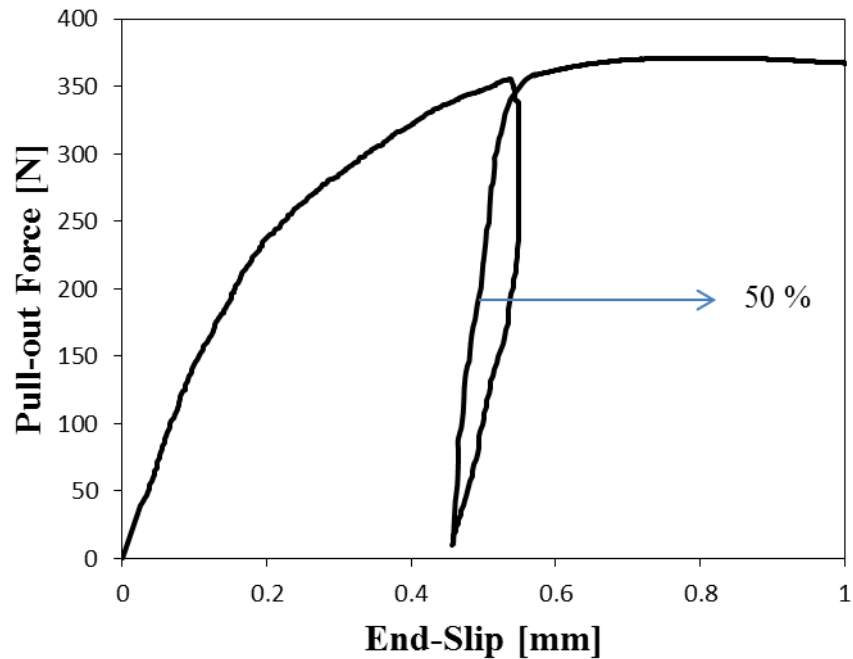


Figure 5.23. The force-slip response of a specimen that was unloaded and reloaded during a single fibre pull-out test

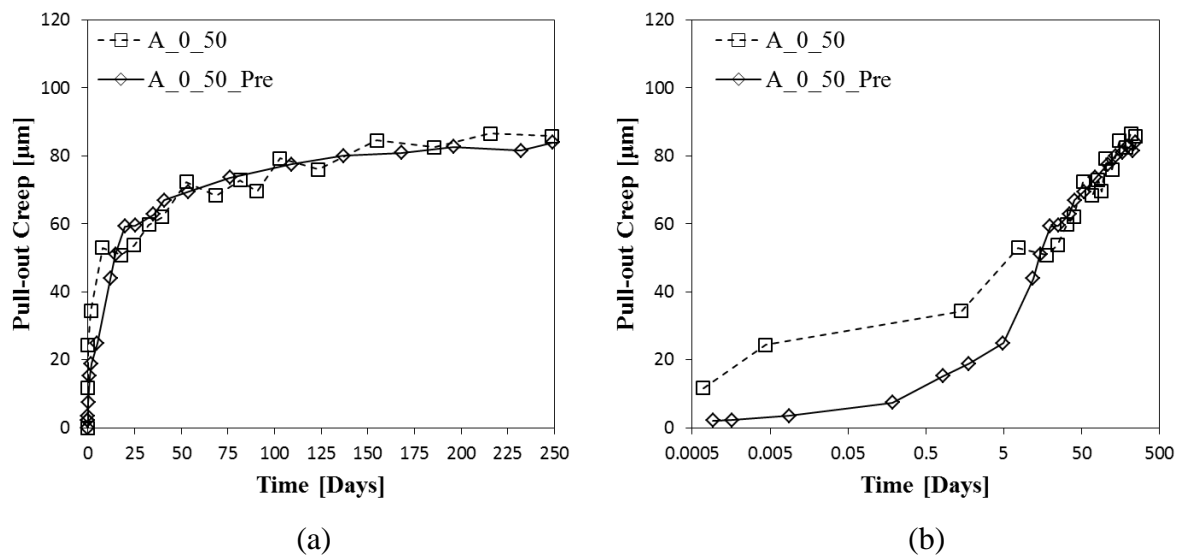


Figure 5.24. Average pull-out creep-time responses for pre-damaged specimens: (a) linear plot and (b) semi-logarithmic plot

At first the pre-damaged pull-out creep behaviour appears to be similar to that of the undamaged specimens, see Figure 5.24(a). However, from Figure 24(b) a significant difference in the two responses is observed at early ages. To analyse the results in detail, the instantaneous pull-out ( $\delta_{inst}$ ) and pull-out creep ( $\delta_{creep}$ ) for the pre-damaged and undamaged responses were determined at 5, 15, 30 and 240 days (see Table 5.12). The coefficient of creep ( $\gamma_{creep}(t)$ ) was determined after each time instance and presented in Table 5.12, see Equation 5.1 for the determination of  $\gamma_{creep}(t)$ .

Table 5.12. The coefficients of pull-out creep ( $\gamma_{creep}(t)$ ) for undamaged and damaged specimens after 5, 15, 30 and 240 days

Damage type	$\delta_{inst}$ [ $\mu\text{m}$ ]	$\delta_{creep}$ [ $\mu\text{m}$ ] after:				$\gamma_{creep}$ after:			
		5 days	15 days	30 days	240 days	5 days	15 days	30 days	240 days
Undamaged	187	45	51	58	86	0.24	0.27	0.31	0.46
Pre-damaged	6	25	51	61	83	4.30	8.84	10.48	14.18

## 5.2.2 Discussions

### 5.2.2.1 Applied sustained load

None of the fibres pulled out completely during the measured time period (249 days), even for sustained load levels as high as 85 % of the of the average maximum pull-out force. The results depicted in Figure 5.16 show that the pull-out creep increased linearly up to a load level of 50 %. However, for higher load levels an exponential increase is observed. A similar behaviour was observed for the Crack Mouth Opening Displacement due to the applied sustained load ( $CMOD_{sus}$ ), refer to Section 4.3.2. To further investigate the mechanisms causing the non-linear increase in the pull-out creep, Computed Tomography (CT) scans were performed on a specimen at each load level at the end of 249 days. The CT scans were performed on the specimens after the load was removed. CT scans were also performed on a specimen that was not subjected to any loading, which was used as the control.

Figure 5.25(a) presents the CT scans performed on a specimen that was not subjected to any loading (0 %). A defect in the concrete matrix is observed, Point D in Figure 5.25(a). The reason for this defect is unknown, however it was not due to an applied load since no load was subjected to the fibre. Regardless of the defect in the concrete matrix no other damage can be observed from the CT scans. The CT scans showed that the pull-out (Point E) increased with the sustained load level. The pull-out observed in the CT scans was a

combination of instantaneous pull-out, pull-out creep and pull-out creep recovery. Pull-out recovery was possible since the CT scans was performed after 249 days on specimens after the load was removed. Also observed in the CT scans is that the separation between the fibre and the concrete matrix at the zone of the hook (Point F) is more severe as the sustained load increases. This separation is due to a combination of two phenomena. Firstly, as the load is applied to the fibre, the hook of the fibre transfers most of the load as a localised compressive force to the concrete matrix. This will cause an instantaneous deformation as the interface transition zone (ITZ) between the fibre and the bulk matrix is a porous layer that consist mostly out of calcium-hydroxide (CH) crystals, see Section 2.1.2.1. It is perceived that the CH layer is crushed and compacted during the loading phase, which results in the instantaneous deformation. Secondly, the applied sustained load causes a localised compressive creep of the concrete matrix at the zone of the hooked-end. This creep contributed to the relative movement between the fibre and the concrete matrix interface (Point F), which was referred to as pull-out creep. It is believed that pull-out creep was dominated by the same mechanisms as in bulk normal concrete, i.e. the movement of moisture, breaking and rebinding of bonds and micro-cracking, see Section 2.2.3. The CT scans performed on the specimens subjected to sustained loads of 70 % and 85 % showed severe localised micro-cracking in the concrete matrix (Point G) at the hooked-end of the fibre, which was not observed in the CT scans of specimens subjected to load levels up to 50 %. Therefore, can it be concluded that the non-linear increase in the pull-out creep observed in Figure 5.16 is due to the severe localised micro-cracking damage at the zone of the hooked-end of the fibre.

The coefficient of pull-out creep ( $\gamma_{creep}(t)$ ) incremented at more or less the same magnitude up to a load level of 50 % for each time instance (see Table 5.7), confirming that the pull-out creep behaviour is linear up to this load level. For higher load levels the  $\gamma_{creep}(t)$  increased significantly. At each stress level an increase in the  $\gamma_{creep}(t)$  is observed with age at an decreasing rate. This behaviour was also observed for the coefficient of  $CMOD_{sus}$  at each load level, refer to Section 4.3.2. After 240 days the coefficient of pull-out creep ( $\gamma_{creep}(t)$ ) at a load level of 30 % was 0.48. This indicates that the fibre pull-out almost increased by 50 % of the instantaneous pull-out due to fibre pull-out creep. A significant increase in the  $\gamma_{creep}(t)$  is observed at a load level of 85 %. The fibre pull-out increased with more than 100 % of the instantaneous pull-out.

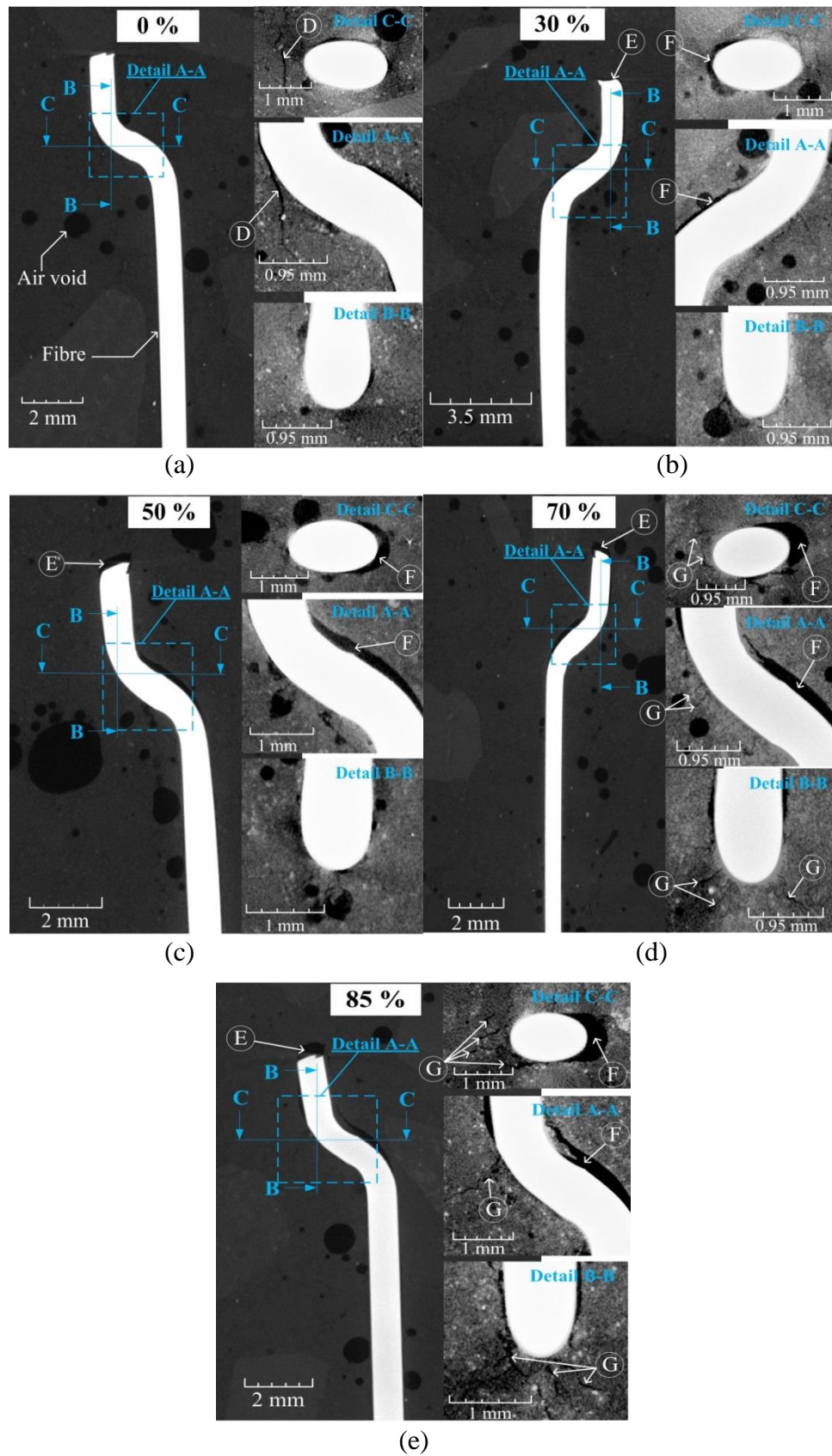


Figure 5.25. CT scan performed on single fibre sustained load specimens after 249 days at different load levels: (a) specimen that was not loaded (0 %), (b) 30 %, (c) 50 %, (d) 70 % and (e) 85 %



From the results and discussion above it is concluded that the fibre pull-out creep is one of the principle mechanisms involved during the  $CMOD_{sus}$ . It is believed that the pull-out creep is dominated by the same mechanisms as for the creep in bulk normal concrete. However, it was observed by CT scans that when the load level is increased to more than 50 %, micro-cracking seems to be the predominant mechanism causing the pull-out creep.

### 5.2.2.2 Fibre inclination angle

During the measured time period (249 days) none of the fibres pulled out completely. The results in Figure 5.19 show that there is no clear trend between the pull-out creep and the fibre embedment inclination angle after 30 days and 100 days. However after 170 days and 240 days a steady result is observed between the pull-out creep and the fibre embedment inclination angles. An increase in the slip at maximum pull-out force ( $S_{max}$ ) with the fibre embedment inclination angle was observed during quasi-static single fibre pull-out tests. This was a result of matrix spalling at the fibre bending point (refer to Section 5.1.2.4). Therefore, it was anticipated that an increase in fibre embedment inclination angle would result in a higher pull-out creep. However, this was not the case as shown by the results. Also no significant matrix spalling at the exiting point of the fibre during the measured time period was observed for each specimen with a fibre embedment inclination angle of 30° and 60°. This could be due to that at a sustained load level of 50 % no severe matrix spalling occurred. This is confirmed with the pull-out load-slip responses presented in Figure 5.17. The pre-peak responses were more or less linear up to 50 % of the maximum pull-out force. However, for loads higher than 50 % a non-linear behaviour is observed in the pre-peak responses, which is a result of matrix spalling at the fibre exiting point.

As previously mentioned in Section 5.2.1.2 the applied sustained load increased with the fibre embedment inclination angle and if a constant sustained load was applied to each fibre inclination angle a decrease in the pull-out creep would have been observed with an increase of embedment inclination angle. Therefore, higher fibre embedment inclination angles show better resistance against pull-out creep.

The coefficient of pull-out creep ( $\gamma_{creep}(t)$ ) for an aligned fibre (0°) increased with age at a decreasing rate (see Table 5.9). For fibre embedment inclination angles of 30° and 60° an increase in the  $\gamma_{creep}(t)$  with age is observed between 30 days and 100 days. However, for ages older than 100 days a stable result in the  $\gamma_{creep}(t)$  is observed. This entails that the pull-out

creep for fibre inclination angles 30° and 60° reached an asymptotic value after 100 days. This confirms with the judgement that higher fibre embedment inclination angles exhibit better resistance against pull-out creep.

### 5.2.2.3 Fibre mechanical anchorage

During the measured time period (155 days) none of the fibres pulled out completely. It was mentioned in Section 5.2.1.1 that the pull-out creep was induced by the anchorage mechanism. From Figure 5.22 it is evident that the pull-out creep after each time instance increased with the amount of kinks in the hooked-end. This increase in the pull-out creep is due to a combination of two factors. The first is that the applied sustained load increased with the amount of kinks. This phenomenon alone will increase the pull-out creep as it was showed in Section 5.2.2.1 that the pull-out creep increased with the applied sustained load level. Secondly, the hooked length increased with the amount of kinks, entailing that the interface between the fibre and surrounding concrete matrix increased with the amount of kinks. Hence, the area of surrounding concrete matrix at the zone of the hooked-end, which is subjected to a localised compressive sustained loading as explained in Section 5.2.1.1, increases with the amount of kinks. This resulted in an increase in the pull-out creep with the amount of kinks.

The coefficient of pull-out creep ( $\gamma_{creep}(t)$ ) for each fibre mechanical hooked-end anchorage increased with age at a decreasing rate. After 150 days the increase in fibre pull-out relative to the instantaneous pull-out due to pull-out creep was 45 %, 65 % and 80 % for TYPE A, TYPE B and TYPE C hooked-end fibres respectively.

An important factor that was not considered in this research programme is the effect of the mechanical hooked-end anchorage on the pull-out creep if a constant sustained load is applied to the different hooked-end fibre types. However, a 50 % load level for a TYPE B hooked-end fibre (304.3 N) is the same as an 82.3 % load level applied to a TYPE A hooked-end fibre. After 30 days and 100 days the pull-out creep for the TYPE A hooked-end fibre at a 70 % load level was already higher than the pull-out creep of the TYPE B hooked-end fibre subjected to a 50 % load level (see Table 5.13). This entails that the pull-out creep of the TYPE A hooked-end fibre should be even higher for a load level of 82.3 %. The method of linear interpolation (Table 5.7) was used to determine the pull-out creep values for the TYPE A hooked-end fibre at a load level of 82.3 %, see Table 5.13. Therefore, can it be concluded



that an increase in the amount of kinks decreases the pull-out creep, if a constant sustained load is applied to all fibre types. However when TYPE A hooked-end fibres are typically replaced by TYPE C hooked-end fibres, less fibres are added and the average load a fibre has to resist will increase. Thus, using TYPE C hooked-end fibres will result in increased fibre pull-out creep.

*Table 5.13. Pull-out creep of TYPE A and TYPE B hooked-end fibres subjected to a constant load at time instances 30 days and 100 days*

Anchorage type	Load level [%]	Equivalent load [N]	$\delta_{creep}$ [ $\mu\text{m}$ ] after:	
			30 days	100 days
A	70	258.8	152	213
A	82.3	304.3	299	382
B	50	304.3	106	122

#### 5.2.2.4 Pre-damaged sustained load tests

None of the fibres for the pre-damaged specimens pulled out completely during the measured time period of 249 days. From Figure 5.24(a) it seems that the pull-out creep behaviour is similar for the undamaged and pre-damaged specimens. However, on a logarithmic scale a significant difference between the two responses is observed at early ages, see Figure 5.24(b). This is confirmed by the results presented in Table 5.12. The results showed that for time instances younger than 15 days a significant difference in the pull-out creep is observed between the two responses. The magnitude of the pull-out creep for the pre-damaged specimens is significantly smaller than that of the undamaged specimens for time instances younger than 15 days. For older time instances the pull-out creep is almost the same magnitude for the two responses. In Figure 5.26 the pull-out creep rates at various time instances for pre-damaged and undamaged specimens are presented. It is shown that the pull-out creep rate for undamaged specimens is significantly higher than that of the pre-damaged specimens for time instances younger than 10 days. This explains why the pull-out creep is higher for the undamaged specimens than for the pre-damaged specimens at early ages. The reason for this phenomenon is still unknown and further investigations in this field are required. However, it is thought that the Interfacial Transition Zone (ITZ) is the cause of this phenomenon. The ITZ largely consists out of calcium-hydroxide (CH) crystals which have a significantly lower strength and stiffness compared to the bulk cement matrix, see Section 2.1.2.1. Thus, during the pre-damage process the ITZ is compressed together and when the sustained load is applied the measured pull-out creep is only that of the localised creep of the

bulk matrix. The perceived reason for the aforementioned phenomenon is thought to be the reason for the decrease in the percentage increase in the  $CMOD_{sus}$  as the sustained load level increases (see Section 4.3.2).

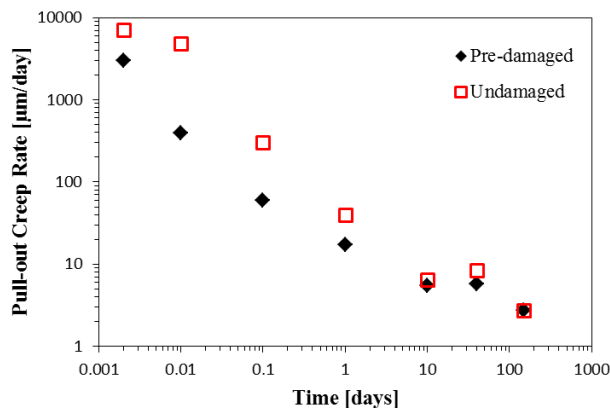


Figure 5.26. The average pull-out creep rate at various time instances for pre-damage and undamaged specimens

Also observed in Table 5.12 is that the average instantaneous pull-out ( $\delta_{inst}$ ) of the pre-damaged specimens is significantly lesser than that of the undamaged specimens. The same reason as postulated above as the cause for the lower pull-out creep is the reason for this phenomenon.

From the results and discussions above it is concluded that the pull-out creep behaviour is significantly affected by the pre-damage process at time instances younger than 10 days. However, for time instances older than 10 days the pull-out creep behaviour between the undamaged specimen and the pre-damaged specimen is similar.

### 5.2.3 Mechanisms causing the crack widening under sustained loading

In Chapter 4 it was shown that the Crack Mouth Opening Displacement due to the applied sustained load ( $CMOD_{sus}$ ) increases with time. This phenomenon is associated with the pull-out creep of the fibres at the crack plane. In this research it has been proven that the pull-out creep is induced by the interface between the hooked-end of the fibre and surrounding matrix, see Section 5.2.1.1. The mechanisms causing the pull-out creep is believed to be the same mechanisms that dominate the creep in bulk normal concrete, i.e. the movement of moisture, breaking and rebinding of bonds and micro-cracking. The latter has been discussed in Section 5.2.2.1 to be the predominant mechanism if the applied sustained load level is higher than 50 %.

The above mentioned mechanisms were only investigated on fibres embedded at inclination angles parallel to the applied load ( $0^\circ$ ). In Section 5.1.2.3 it was shown that the slip at maximum pull-out force increases with the increase in fibre embedment inclination angle. This phenomenon is associated with matrix spalling at the exit point of the fibre. The effect of the fibre embedment inclination angle on the pull-out creep was investigated in Section 5.2.2.2, at an applied load level of 50 %. At this applied load level no severe matrix spalling occurred. It is conceived that at higher load levels severe matrix spalling under sustained load will occur. Thus further investigations in this field are required to investigate whether this mechanism will contribute to the crack widening under sustained loading.

### 5.3 Concluding Summary

In this chapter the time-dependent pull-out behaviour of steel fibres was investigated under two types of loading conditions, namely short and long term loading conditions. For the short term loading conditions quasi-static single fibre pull-out tests were performed to investigate the effect of several factors on the force-slip behaviour. The investigation was restricted to the influence of the fibre embedded inclination angle, the fibre embedment length, fibre mechanical anchorage and the rate of loading application. For the long term loading conditions single fibre sustained load tests were performed. The factors investigated were restricted to the applied sustained load, the fibre embedment inclination angle and the fibre mechanical anchorage. Also a set of sustained load tests were performed on pre-damaged specimens to investigate what effect it has on the pull-out creep behaviour.

Pull-out rate tests were performed on straight and TYPE A hooked-end steel fibres. The straight fibres showed no rate sensitivity over the tested pull-out rate range. However, TYPE A hooked-end steel fibres showed rate sensitivity for the slip at maximum force. This rate effect is induced by the interface between the hooked-end of the fibre and the matrix.

The quasi-static single fibre pull-out results showed that the fibre embedment length does not significantly influence the pull-out behaviour of TYPE A hooked-end fibres. This is however only valid if the embedment length is greater than the length of the hooked-end of the fibre.

The quasi-static single fibre pull-out tests performed on inclined fibres disclosed that the fibre embedment inclination angle significantly influenced the pull-out behaviour of TYPE A hooked-end fibres. The increase in frictional resistance, matrix spalling, and deformation of

---

the fibre at the bending point of the fibre were the dominating mechanisms during the pull-out behaviour of inclined fibres.

The geometry of the mechanical hooked-end mechanism of the fibre has been found to have a significant effect on the pull-out behaviour. It was proven that by increasing the amount of kinks in the hooked-end of the fibre significantly improves the pull-out behaviour. The pull-out behaviour is governed by three mechanisms, namely: cohesion, friction and mechanical bond. The latter has been found to be the predominant mechanism for hooked-end fibres as its magnitude is far greater than the other two mentioned mechanisms.

The single fibre sustained load tests showed that the pull-out creep is dependent on the applied load level. The pull-out creep increases linearly up to a load level of 50 % and for higher load levels a non-linear behaviour is observed. It is believed that the pull-out creep is dominated by the same mechanisms as for creep in bulk normal concrete. Further investigations in this field are required to confirm this. The non-linear pull-out creep behaviour is a result of micro-cracking which is the predominant mechanism at load levels higher than 50 %.

The pull-out creep behaviour is dependent on the fibre embedment inclination angle. It was proven that an increase in the fibre embedment inclination angle will reduce the pull-out creep. However, this was only investigated at an applied sustained load level of 50 % and at this load level no severe matrix spalling was observed at the fibre exiting point. It is thought that for higher load levels severe matrix spalling may occur and this can have an effect on the pull-out creep behaviour. Thus, further investigations in this field are required to confirm this.

As in the case of single fibre pull-out, the geometry of the mechanical hooked-end mechanism showed an effect on the pull-out creep behaviour. It was proven that by increasing the amount of kinks in the hooked-end of the fibre will reduce the pull-out creep. However, using fibres with more kinks will probably result in increased pull-out creep as fewer fibres are then typically used.

From the sustained load tests performed on pre-damaged specimens it is concluded that the pull-out creep behaviour is significantly affected by the pre-damage process at time instances younger than 10 days. However, for time instances older than 10 days the pull-out creep behaviour between the undamaged specimen and the pre-damaged specimen is similar.

# Chapter 6

---

## Predicting the Single Fibre Pull-out Creep Behaviour

Some scholars have successfully predicted the single fibre pull-out behaviour of hooked-end fibres (Cunha, 2010; Sujivorakul, et al., 2000), however predicting the single fibre pull-out creep behaviour of hooked-end fibres has not yet been resolved. A comprehensive investigation on the pull-out creep behaviour was performed in the previous chapter. The experimental results showed that the pull-out creep behaviour is linearly dependent on the sustained load up to load levels of 50 % of the average maximum pull-out rate force. For higher sustained load levels a non-linear increase is observed in the pull-out creep behaviour.

This chapter aims to provide a straightforward method to predict the pull-out creep behaviour of TYPE A hooked-end fibres. Refer to Table 3.1 for the different steel fibre types. Firstly a model for predicting the linear pull-out creep behaviour is presented. The model is then adapted to incorporate the non-linear pull-out creep behaviour. Finally, a time-dependent pull-out model is proposed to predict the pull-out rate behaviour. The time-dependent pull-out model incorporates the pull-out creep model and was used to validate the pull-out creep model against the pull-out rate test results.

---

## 6.1 Constitutive Pull-out Creep Model

It has been shown in this dissertation that the pull-out creep for a TYPE A hooked-end fibre is linearly related to the applied load up to a sustained load level of 50 % of the average maximum pull-out force and for higher sustained load levels the pull-out creep showed a non-linear behaviour (see Section 5.2.1.1). The linear pull-out creep behaviour due to the localised compressive creep at the zone of the hooked-end was thought to be dominated by the same mechanisms as the creep for bulk normal concrete at low compressive load levels, i.e. the movement of moisture, breaking and rebinding of bonds and micro-cracking. This was explained in detail in Section 2.2.3. This linear pull-out creep behaviour is due to the linear visco-elastic behaviour of the concrete matrix at the hooked-end zone. Furthermore, the non-linear pull-out creep behaviour was due to a significant increase in the micro-cracking damage at the zone of the hooked-end of the fibre. In Section 5.2.2.1 it is concluded that micro-cracking is the predominant mechanism causing this behaviour.

The behaviour of the linear pull-out creep mechanisms can be modelled with rheological components which consist of mechanical components such as springs and dashpots (see Figure 6.1). The behaviour of these components can be represented by simple mathematical expressions. During the linear pull-out creep behaviour the micro-cracking was considered as insignificant, i.e. for sustained load levels up to 50 % of the average maximum pull-out force. However, for sustained load levels higher than 50 % the micro-cracking damage contributed significantly to the pull-out creep behaviour. The contribution by micro-cracking incremented the pull-out creep deformation non-linearly and therefore can only be modelled with a non-linear component. A mathematical expression to describe the behaviour of this non-linear component will be presented in the course of this chapter.

### 6.1.1 Mathematical derivation of linear pull-out creep behaviour

The matrix of concrete is an inhomogeneous structure and has a visco-elastic response when subjected to sustained loads. The hooked-end of the fibre transmits the applied sustained load to the concrete matrix at the zone of the hooked-end. The experimental results in Section 5.2.1.1 showed that the pull-out creep behaviour exhibits a visco-elastic response over time. These responses can be described by ordinary differential equations in time. As previously mentioned, a convenient way for developing these relationships and to visualise them is by using mechanical components such as springs and dashpots, see Figure 6.1.

The force in a spring can be described by Hooke's law as follows:

$$N = ks \quad (6.1)$$

where  $N$  and  $s$  are the spring force and displacement, respectively, and  $k$  is the stiffness of the spring with units N/mm.

The force in a dashpot is directly proportional to the rate of change of displacement ( $s$ ) and is described as follows:

$$N = v \frac{ds}{dt} = v\dot{s} \quad (6.2)$$

where  $v$  is the viscosity of the viscous material with units N.s/mm.

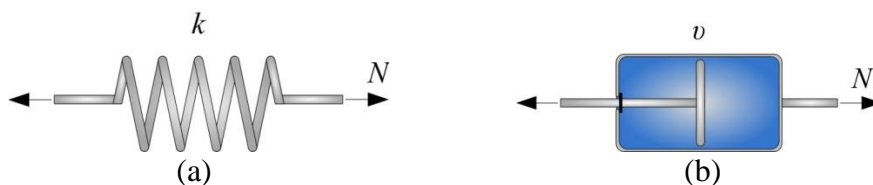


Figure 6.1. (a) Spring and (b) dashpot

These mechanical components can be used in combination to construct rheological models. A number of rheological models (Kelvin-Voigt model, Maxwell, Standard Linear Solid, amongst others) have been developed over time by scholars to describe the behaviour of polymers. Each of the developed models contain components that represent certain intrinsic (matrix composition) and extrinsic (environmental conditions, time history) factors and are arranged accordingly to represent the desired behaviour of the polymer.

The Kelvin-Voigt model consists of a spring and a dashpot connected in parallel (see Figure 6.2). It is assumed that no bending occurs in the parallel connection, so that the displacement experienced by the spring is the same as that experienced by the dashpot. The total force ( $N$ ) is the sum of the force in the spring ( $N_{spring}$ ) and the force in the dashpot ( $N_{dashpot}$ ) and can be expressed as a first order differential equation:

$$N = N_{spring} + N_{dashpot} \quad (6.3)$$

$$N = ks + v \frac{ds}{dt} \quad (6.4)$$

If the applied load ( $N$ ) is constant, Equation 6.4 can be solved to yield:

$$s = \frac{N}{k} \left[ 1 - e^{-\left(\frac{k}{v}\right)t} \right] \quad (6.5)$$

In the relations to follow it is sometimes convenient to express the ratio of viscosity to stiffness as:

$$\tau = \frac{v}{k} \quad (6.6)$$

where  $\tau$  refers to the retardation time and is a measure of the time taken for the displacement to increase during the measured time period, namely immediately after the load is applied to the removal of the load. The shorter the retardation time, the more rapid is the increase in displacement. Equation 6.6 is rewritten with the retardation time as,

$$s = \frac{N}{k} \left[ 1 - e^{-\left(\frac{t}{\tau}\right)} \right] \quad (6.7)$$

Equation 6.7 represents the basic shape of the displacement against time curve for a Kelvin-Voigt model. The pull-out creep behaviour of a TYPE A hooked-end fibre embedded in a concrete matrix is too complex to be described by a single Kelvin-Voigt Model. More complex models can be constructed by adding more Kelvin-Voigt elements. The pull-out creep behaviour can then be represented by the generalised Kelvin-Voigt chain. This model consists of  $R$  different Kelvin-Voigt elements in series, see Figure 6.3. Each Kelvin-Voigt element has different material constants, i.e.  $k$  and  $v$ . The total displacement of the generalised Kelvin-Voigt model is the sum of the displacement of each Kelvin-Voigt element,

$$s = s_1 + s_2 + \dots + s_R \quad (6.8)$$

$$s = N \sum_{i=1}^R \frac{1}{k_i} \left[ 1 - e^{-\left(\frac{t}{\tau_i}\right)} \right] \quad (6.9)$$

It should be noted that Equation 6.9 is only valid when a constant force is applied to the model. When the force varies over time the concept of superposition can be used to derive a formulation that represents the complete force history over time. The derivation of these formulations is presented in Section 6.2.2.1.

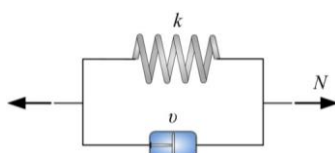


Figure 6.2. Kelvin-Voigt Model



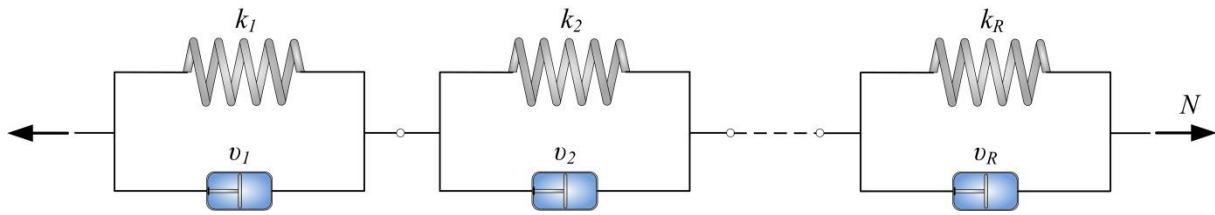


Figure 6.3. Generalised Kelvin-Voigt model

### 6.1.2 Model adaption to include non-linear pull-out creep behaviour

In the previous section a formulation was presented that can be used to model the linear pull-out creep behaviour. This formulation is valid for applied sustained load levels up to 50 % of the average maximum pull-out force. For higher loading percentages the pull-out creep behaviour is non-linear. This non-linear increase in the pull-out creep is due to significant micro-cracking damage. To incorporate this behaviour a non-linear component was introduced in series with the generalised Kelvin-Voigt model. Boshoff (2007) proposed a method which incorporates the non-linear creep of cementitious composites. He described the non-linear behaviour by introducing a factor,  $\varphi$ , into Equation 6.9 as follow:

$$s = [(\varphi - 1)f(t)]_{non-linear} + [f(t)]_{linear} \quad (6.10)$$

where  $f(t) \equiv s$  in Equation 6.9. The first set of square brackets represents the non-linear component and the second set the linear component. In Equation 6.10  $\varphi$  is defined as:

$$\varphi = 1 \text{ for } \frac{N_1}{N_u} \leq \eta \quad (6.11)$$

$$\varphi = 1 - A + Ae^{B\left(\frac{N_1}{N_u} - \eta\right)} \text{ for } \frac{N_1}{N_u} > \eta \quad (6.12)$$

where  $N_1$  is the applied sustained load,  $N_u$  is the maximum pull-out force,  $\eta$  is the non-linear pull-out creep load ratio, i.e. the load ratio at which non-linear pull-out creep starts, and  $A$  and  $B$  are two constants defining the shape of the non-linearity.  $A$  and  $B$  are the same for each Kelvin-Voigt element.

By simplifying Equation 6.10 the expression given in Equation 6.14 is obtained which will be used to describe the pull-out creep behaviour,

$$s = \left[ (\varphi - 1)N \sum_{i=1}^R \frac{1}{k_i} \left( 1 - e^{-\left(\frac{t}{\tau_i}\right)} \right) \right] + N \sum_{i=1}^R \frac{1}{k_i} \left( 1 - e^{-\left(\frac{t}{\tau_i}\right)} \right) \quad (6.13)$$

$$s = N \sum_{i=1}^R \frac{\varphi}{k_i} \left[ 1 - e^{-\left(\frac{t}{\tau_i}\right)} \right] \quad (6.14)$$

### 6.1.3 Implementation of pull-out creep model

Equation 6.14 is described by two sets of unknown parameters, namely the linear visco-elastic material parameters and the non-linear parameters. In this section the procedure for calibrating the unknown parameters with the experimental results is explained.

#### 6.1.3.1 Linear visco-elastic material parameters

A seven element generalised Kelvin-Voigt model was used to describe the linear pull-out creep behaviour. An iterative numerical method was used to determine the required material parameters as described in Equation 6.9 so that it accurately predicts the experimental pull-out creep behaviour. The average pull-out creep results obtained from the 30 % load level series, i.e. series A\_0\_30 as presented in Section 5.2.1.1, was use in the numerical method to determine the material parameters. The values for the material parameters obtained during the iterative numerical method, which defines the pull-out creep behaviour, are included in Table 6.1. The simulated pull-out creep behaviour for each loading percentage for the material parameters given in Table 6.1 is presented in Figure 6.4.

*Table 6.1. Linear pull-out creep material parameters*

Element no.	$k$ [N/mm]	$\tau$ [Days]
1	1.578E+04	1.718E+02
2	2.096E+04	4.308E+03
3	2.798E+04	9.627E+03
4	1.113E+04	6.035E+05
5	7.291E+03	5.052E+06
6	4.650E+03	2.147E+08
7	2.786E+03	4.738E+08

To further analyse the results shown in Figure 6.4, the average experimental and modelled pull-out creep is plotted against the sustained load level after 1 day, 30 days, 100 days and 249 days (see Figure 6.5). The normalised error ( $\bar{e}$ ) for each load level at each time instance is presented in Table 6.2 and was calculated as follow:

$$\bar{e} = \frac{|s_{model} - s_{exp}|}{s_{exp}} \quad (6.15)$$

where  $s_{model}$  and  $s_{exp}$  are the modelled and average experimental pull-out creep, respectively.

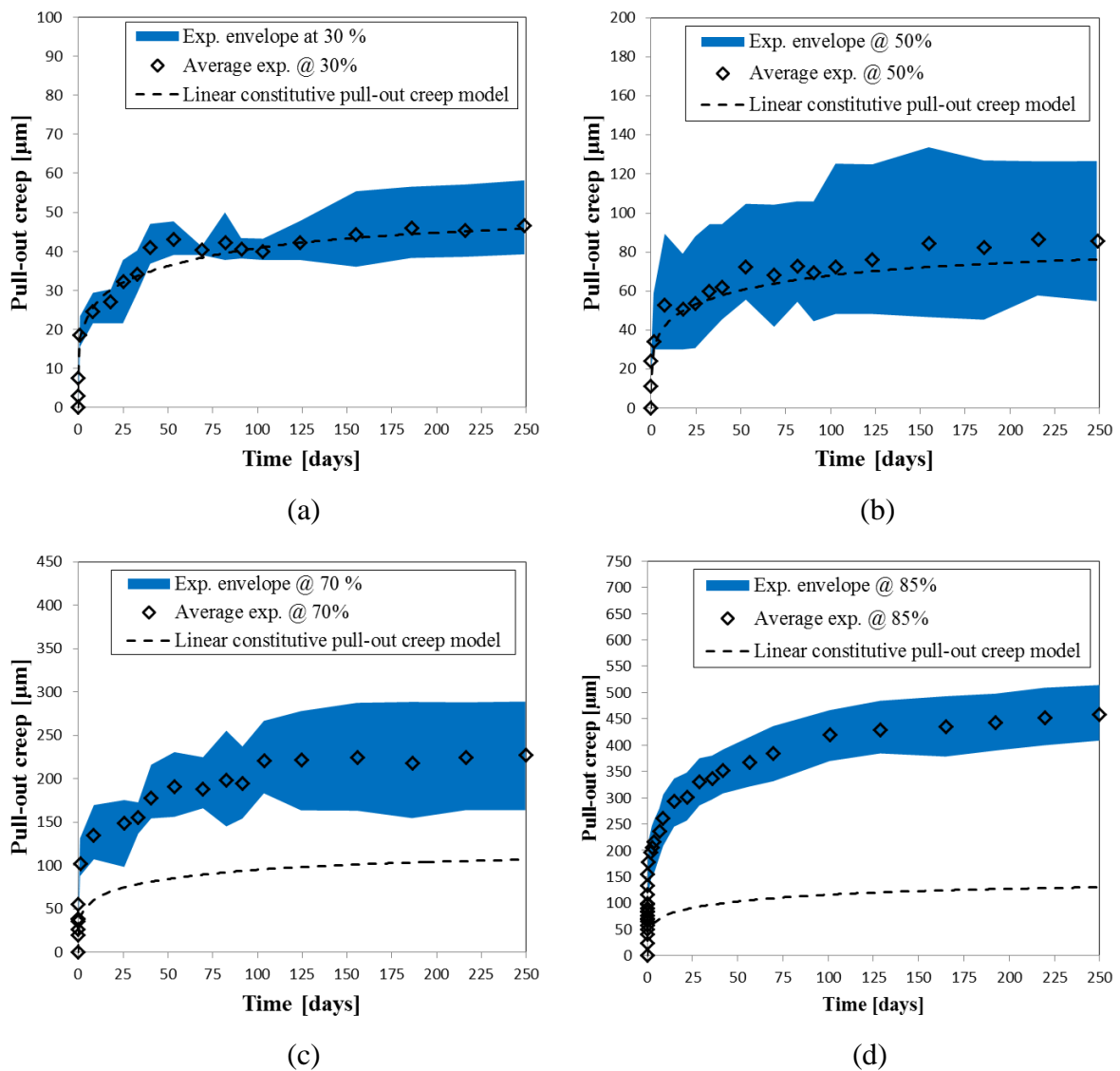


Figure 6.4. Simulated pull-out creep behaviour with linear constitutive pull-out creep model at various sustained load levels: (a) 30 %, (b) 50 %, (c) 70 % and (d) 85 %

Table 6.2. Calculated normalised errors for each load level at each time instance for linear pull-out creep model

Load level [%]	1 day			30 days			100 days			249 days		
	Exp. [ $\mu\text{m}$ ]	Model [ $\mu\text{m}$ ]	$\bar{\epsilon}$ [%]	Exp. [ $\mu\text{m}$ ]	Model [ $\mu\text{m}$ ]	$\bar{\epsilon}$ [%]	Exp. [ $\mu\text{m}$ ]	Model [ $\mu\text{m}$ ]	$\bar{\epsilon}$ [%]	Exp. [ $\mu\text{m}$ ]	Model [ $\mu\text{m}$ ]	$\bar{\epsilon}$ [%]
30	19	18	2.6	33	33	1.1	40	41	1.7	45	46	0.9
50	34	31	8.8	58	55	4.6	72	68	5.0	86	76	10.9
70	103	42	58.8	152	77	49.3	213	95	55.2	228	107	53.1
85	181	51	71.7	331	94	71.7	419	116	72.4	458	130	71.7

It is evident from the results in Table 6.2 and Figure 6.5 that the linear constitutive pull-out creep model can predict the pull-out creep behaviour with relative high accuracy up to a load

level of 50 %. This is evident in the relatively low normalised errors presented in Table 6.5. However, for load levels higher than 50 % a significant increase in the normalised errors are observed at each time instance. This indicates that the linear constitutive pull-out creep model is unable to accurately simulate the non-linear pull-out creep behaviour. To include this behaviour in the model a non-linear component was added in series with the linear constitutive pull-out creep model. As previously mentioned, the non-linear pull-out creep behaviour is due to the significant increase in micro-cracking damage at load levels higher than 50 %. The non-linear contribution of micro-cracking to the pull-out creep behaviour is included in the non-linear factor,  $\phi$ , (Equation 6.14).

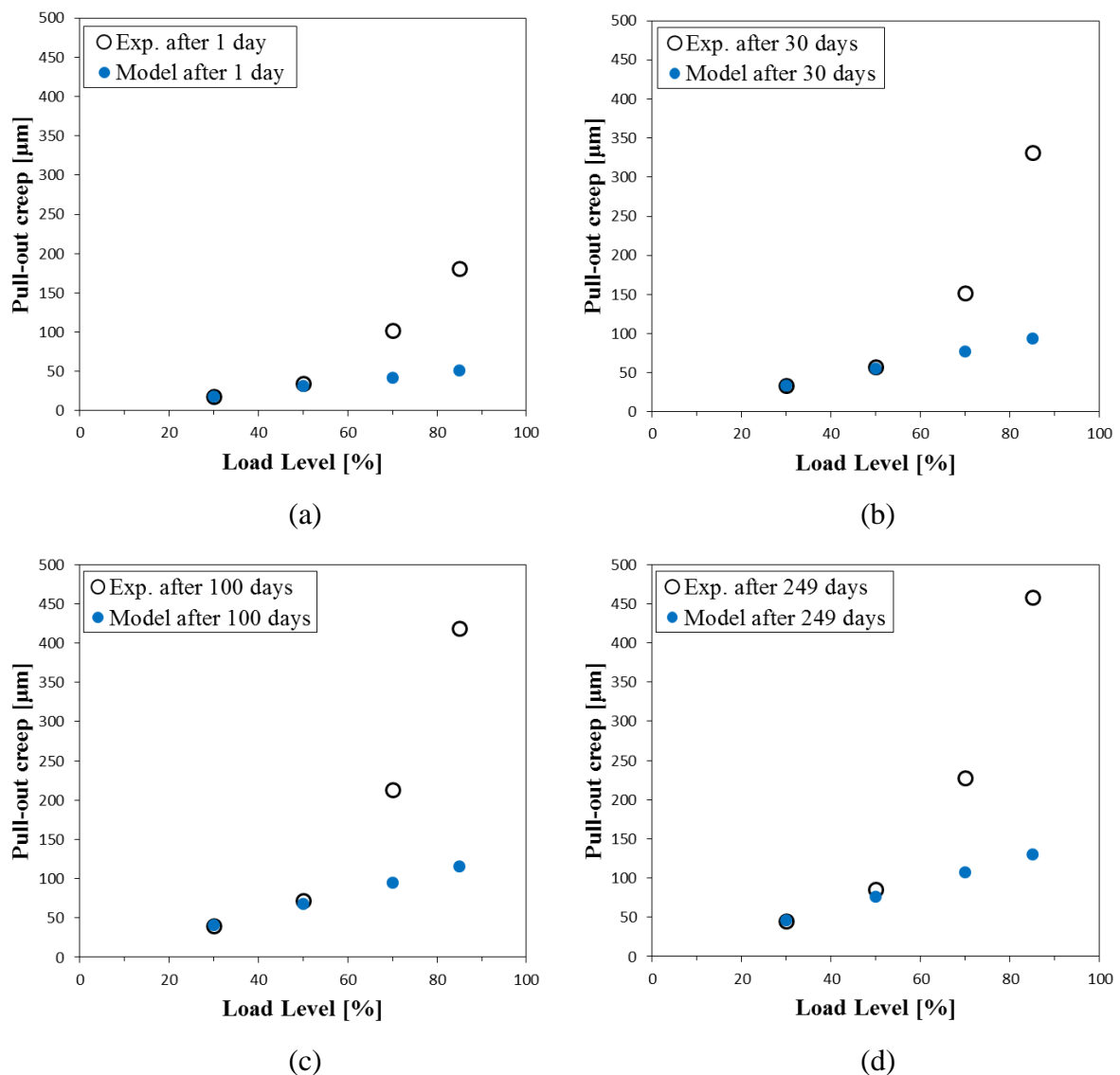


Figure 6.5. The average experimental and linear constitutive pull-out creep model results at each load level after: (a) 1 day, (b) 30 days, (c) 100 days and (d) 240 days

### 6.1.3.2 Non-linear pull-out creep behaviour

Equations 6.11 and 6.12 describe the behaviour of the non-linear factor ( $\varphi$ ). The parameters describing the non-linear behaviour were calibrated with the pull-out creep results at different load levels after 249 days. The non-linear factor ( $\varphi$ ) is a dimensionless factor that scales the linear constitutive pull-out creep model so that it can describe the non-linear behaviour. To calibrate the parameters describing the non-linear behaviour, it was required to quantify the experimental non-linear behaviour. This was done by normalising the specific pull-out creep, i.e. the pull-out creep per unit force, at each load level with the specific pull-out creep at 30 % load level. This dimensionless factor is called the experimental non-linear factor ( $\varphi_{exp}$ ), see Table 6.3. An iterative numerical method was used during the calibration process of the non-linear parameters. The calibrated non-linear parameters that describe the predicted non-linear factor ( $\varphi_{predicted}$ ) are presented in Table 6.4. The normalised error ( $\bar{e}$ ) between the experimental non-linear factor ( $\varphi_{exp}$ ) and predicted non-linear factor ( $\varphi_{predicted}$ ) for each load level is presented in Table 6.5 and was calculated as follow:

$$\bar{e} = \frac{|\varphi_{exp} - \varphi_{predicted}|}{\varphi_{exp}} \quad (6.16)$$

The experimental non-linear factor ( $\varphi_{exp}$ ) increased slightly up to a load level of 50 %. However, the increase was insignificant when compared to the increase for sustained load levels higher than 50 %. This confirms that the pull-out creep behaviour is non-linear for sustained load levels higher than 50 %. The predicted non-linear factor ( $\varphi_{predicted}$ ) calculated using the calibrated non-linear parameters in Table 6.4 simulated the experimental non-linear factor ( $\varphi_{exp}$ ) with high accuracy. This is evident from the relatively low normalised errors ( $\bar{e}$ ) presented in Table 6.5.

Table 6.3. Experimental non-linear factor ( $\varphi_{exp}$ )

Load Level [%]	Pull-out creep [ $\mu\text{m}$ ]	Applied load [N]	Specific pull-out creep [ $\mu\text{m}/\text{N}$ ]	$\varphi_{exp}$
30	45	110.9	0.41	1.00
50	86	184.9	0.46	1.13
70	228	258.8	0.88	2.15
85	458	314.3	1.46	3.56

*Table 6.4. Calibrated non-linear parameters*

$\eta$	A [-]	B [-]	$N_u$ [N]
0.5	1.38	2.97	369.8

*Table 6.5. Normalised errors for the predicted non-linear factor ( $\varphi_{predicted}$ )*

Load Level [%]	$\varphi_{exp}$	$\varphi_{predicted}$	$\bar{e}$ [%]
30	1.00	1.00	0.00
50	1.13	1.00	11.77
70	2.15	2.12	1.28
85	3.56	3.53	0.95

The parameters describing the non-linear behaviour are implemented in Equation 6.14 to predict the pull-out creep at various sustained load levels. For sustained load levels up to 50 %  $\varphi_{predicted} = 1$ , which reduces the non-linear pull-out creep (Equation 6.14) formulation to the linear pull-out creep formulation (Equation 6.9). In Figure 6.6 the pull-out creep behaviour at different load levels are simulated by the non-linear constitutive pull-out creep model.

To analyse in detail the difference in accuracy between the non-linear and linear constitutive pull-out creep model, the experimental and modelled pull-out creep at each sustained load level after 1 day, 30 days, 100 days and 249 days are depicted in Figure 6.7. The calculated normalised errors (Equation 6.15) for the non-linear constitutive pull-out creep model after each time instance are presented in Table 6.6.

*Table 6.6. Calculated normalised errors for each load level after each time instance for the linear constitutive pull-out creep model*

Load level [%]	1 day			30 days			100 days			249 days		
	Exp. [ $\mu\text{m}$ ]	Model [ $\mu\text{m}$ ]	$\bar{e}$ [%]	Exp. [ $\mu\text{m}$ ]	Model [ $\mu\text{m}$ ]	$\bar{e}$ [%]	Exp. [ $\mu\text{m}$ ]	Model [ $\mu\text{m}$ ]	$\bar{e}$ [%]	Exp. [ $\mu\text{m}$ ]	Model [ $\mu\text{m}$ ]	$\bar{e}$ [%]
30	19	18	2.6	33	33	1.1	40	41	1.7	45	46	0.9
50	34	31	8.8	58	55	4.6	72	68	5.0	86	76	10.9
70	103	90	12.6	152	164	7.6	213	202	4.9	228	227	0.3
85	181	181	0.2	331	331	0.0	419	409	2.5	458	458	0.0

The addition of the non-linear component significantly improved the performance of the model for sustained load levels higher than 50 %. This is evident from the normalised errors presented in Table 6.6 compared with those presented in Table 6.2. From Table 6.6 and

Figure 6.7 it is evident that the non-linear model is able to predict pull-out creep behaviour with high accuracy over relatively short and long time periods.

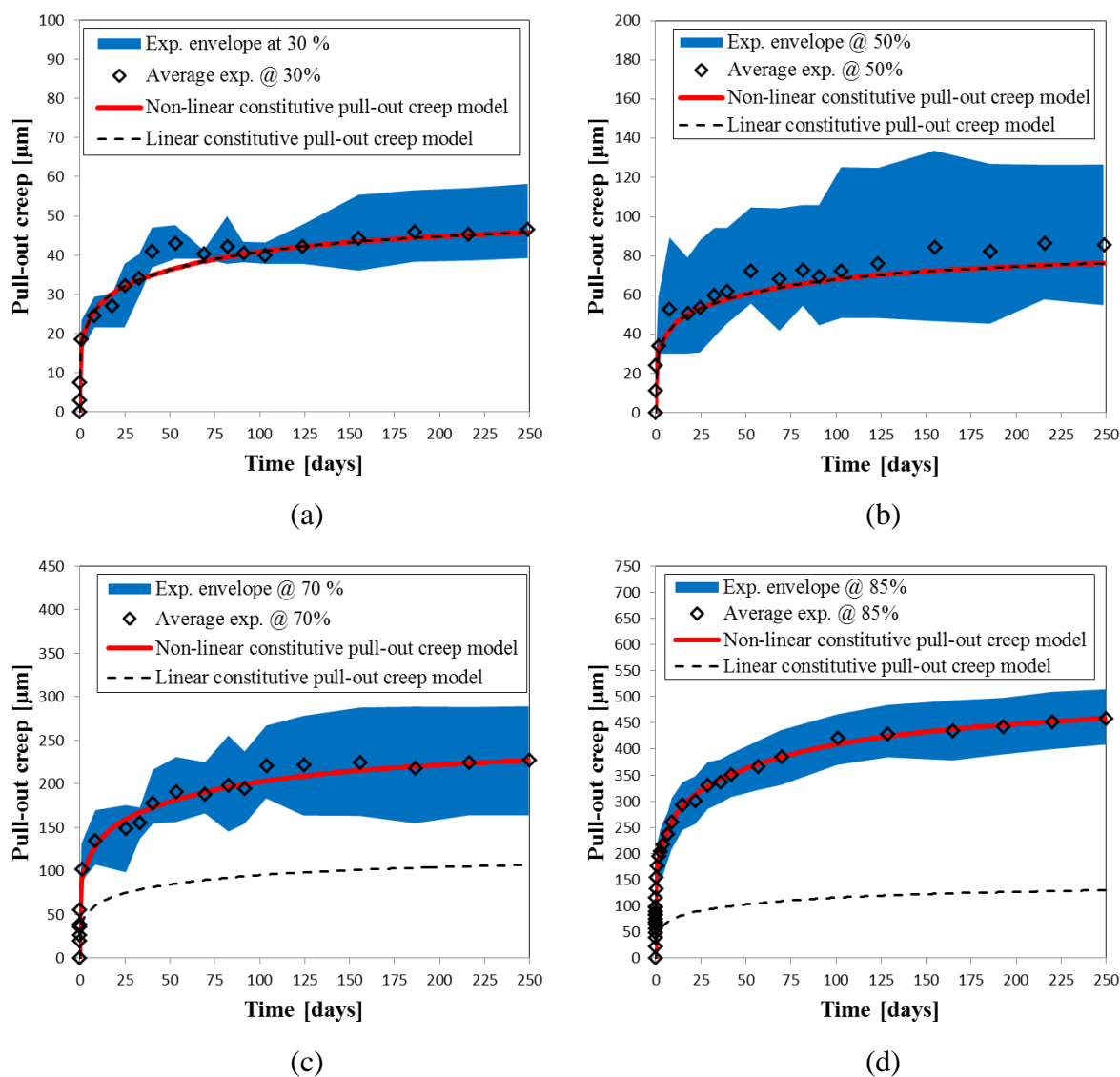


Figure 6.6. Simulated pull-out creep behaviour with non-linear constitutive pull-out creep model at various sustained load levels: (a) 30 %, (b) 50 %, (c) 70 % and (d) 85 %

## 6.2 Verification of Pull-out Creep Model using Rate Tests

To verify the performance of the proposed constitutive pull-out creep model, the experimental pull-out rate results on TYPE A hooked-end fibres presented in Section 5.1.1.1 were used. The pull-out rate results showed a relative significant rate effect on the pull-out behaviour. This behaviour is perceived to be induced by the visco-elastic behaviour between the fibre and the surrounding concrete matrix at the zone of the hooked-end. The quasi-static pull-out behaviour of TYPE A hooked-end fibres was described by the model proposed by Cunha

(2010). To incorporate the rate effect the model of Cunha (2010) was adapted by incorporating the constitutive pull-out creep model presented in the previous section. The response at a pull-out rate of 2.5 mm/s was used as the static response where it was assumed that no pull-out creep occurred due to the short time duration of the test. It is acknowledged that this assumption could lead to an underestimation of the magnitude of the pull-out creep, but for the purpose of this research this is deemed sufficient.

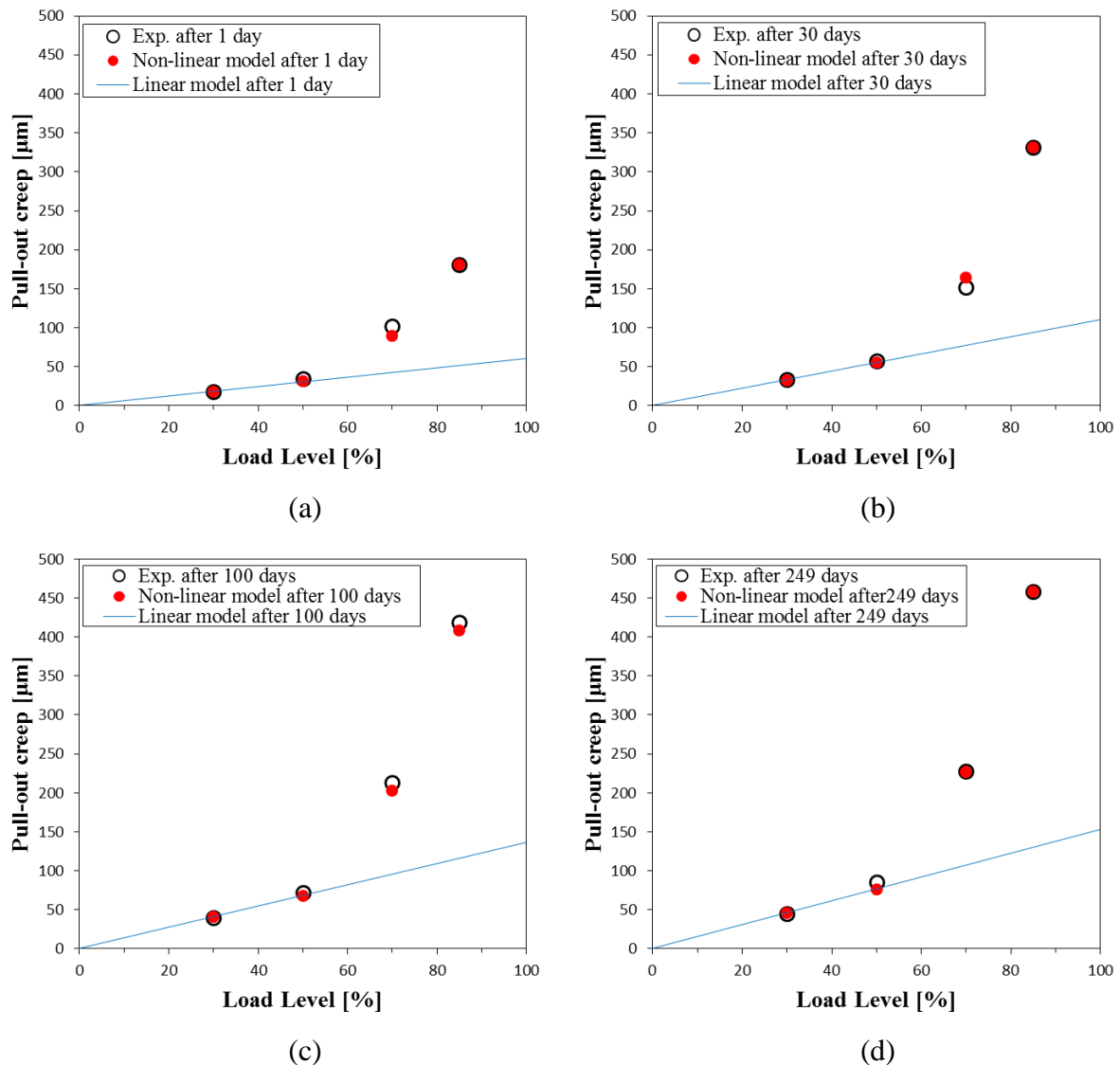


Figure 6.7. The average experimental pull-out creep, non-linear and linear constitutive pull-out creep model for each load level after: (a) 1 day, (b) 30 days, (c) 100 days and (d) 240 days

In this section a summary of the single fibre pull-out model proposed by Cunha (2010) is given, followed by the incorporation of the constitutive pull-out creep model proposed in



Section 6.1.3.2. The model presented in Section 6.1.3.2 is only valid for constant applied loads. However, the pull-out load for the experimental rate tests varied with time. With the concept of superposition the model presented in Section 6.1.3.2 was modified so that the complete force history could be considered. Finally, the adapted model is verified with the experimental pull-out rate results to ascertain its performance.

## 6.2.1 Analytical modelling of the quasi-static pull-out behaviour

The bond mechanisms that contribute to the ductile behaviour during aligned pull-out of TYPE A hooked-end steel fibres from a concrete matrix are: adhesion, friction and mechanical bond. Therefore, in general the pull-out phenomenon is a complex multi-dimensional problem. However, Cunha (2010) simplified this into a two dimensional axisymmetric problem by simulating the adhesion and frictional mechanisms with a local bond slip relationship and treating the mechanical anchorage mechanism as a spring component, see Figure 6.8. This was feasible since the length of the TYPE A hook is significantly shorter than the length of the fibre. A detailed description of the relationships given in the following subsections can be found in Cunha (2010).

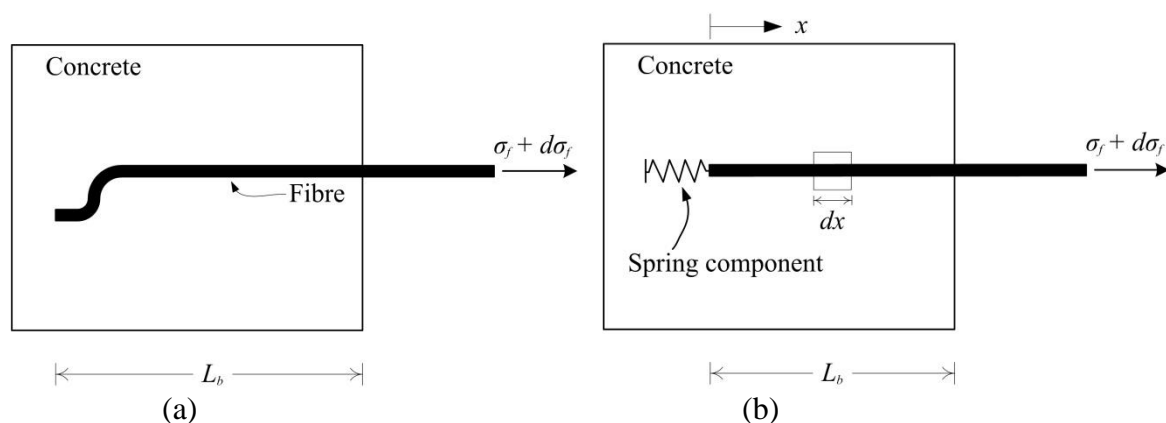


Figure 6.8. Axisymmetric pull-out model based on Cunha (2010): (a) general problem, (b) simplified model

### 6.2.1.1 Local bond-slip relationship

Taking the equilibrium of the free body diagram of an infinitesimal length  $dx$  of a fibre embedded in a concrete matrix (Figure 6.9) the following second order differential equation that describes the local bond phenomena between the fibre and the matrix interface is established:

$$\frac{d^2s}{dx^2} = \frac{P_f}{E_f A_f} \tau \quad (6.17)$$

where  $\tau = \tau[s(x)]$  is the local bond shear stress between the fibre and the concrete matrix, and  $s$  = slip, i.e. the relative displacement between the fibre and the surrounding concrete matrix.  $A_f$ ,  $E_f$  and  $P_f$  are the cross-sectional area, Young's modulus and the cross-sectional perimeter of the fibre, respectively.

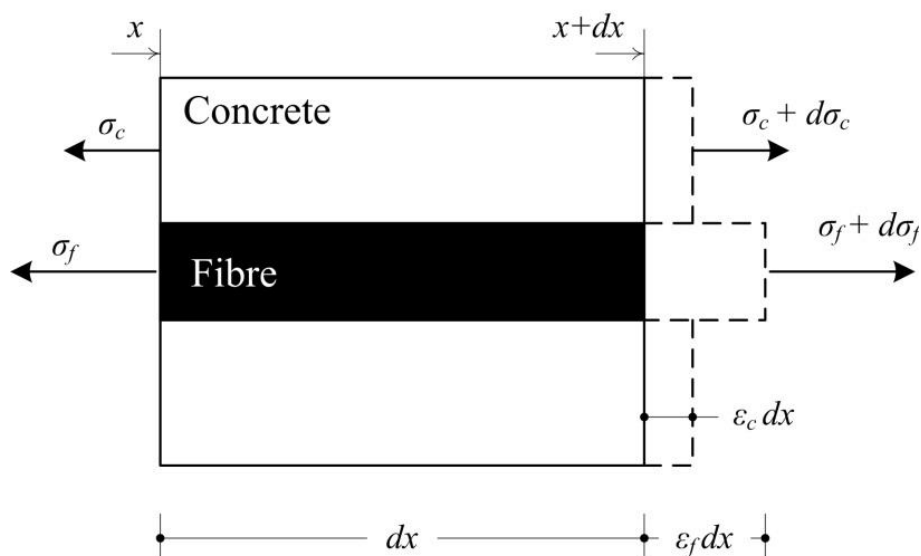


Figure 6.9. Equilibrium of an infinitesimal fibre length embedded in a concrete matrix (based on Cunha 2010)

### 6.2.1.2 Pull-out load-slip relationship

It should be noted in the following expressions developed by Cunha (2010), both numerical and experimental entities are simultaneously used, hence the experimental data is distinguished by an overline, e.g.  $\bar{N}$  is the pull-out force data captured during the pull-out test.

Consider a steel fibre embedded in a concrete matrix with a bond length of  $\bar{L}_b = L_b$ , subjected to a generic applied pull-out force  $N$ , where  $s_f$  and  $s_l$  are the free and loaded end slips, respectively [ $s_f = s(x=0)$ ;  $s_l = s(x=\bar{L}_b)$ ]. The following functions can be determined along the fibre bond length when the fibre is slipping due to an applied pull-out load,  $\bar{N}$ : slip along the fibre bond length,  $s(x)$ ; bond shear stress,  $\tau(x)$ ; fibre strain,  $\epsilon_f(x)$ ; and the axial force,  $N(x)$ .

An energy or equilibrium approach can be used to determine the pull-out load-slip relationship, see Focacci et al. (2000) and Naaman et al. (1991), respectively. Cunha (2010) adopted the energy approach to determine the pull-out load-slip relationship. The following

expression is obtained by balancing the external work with the internal work performed on the fibre:

$$N'(\bar{L}_b) = \sqrt{2E_f \cdot A_f \cdot P_f \int_{s_f}^{s(x=\bar{L}_b)} \tau(s) ds} \quad (6.18)$$

With Equation 6.18 the generic applied pull-out force for a straight fibre can be determined.

For TYPE A hooked-end fibres the generic applied force is  $\bar{N} = N'(x = \bar{L}_b) + N_{sp}$  and is given by

$$\bar{N} = N_{sp} + \sqrt{2E_f \cdot A_f \cdot P_f \int_{s_f}^{s(x=\bar{L}_b)} \tau(s) ds} \quad (6.19)$$

where  $N_{sp}$  is the contribution of the mechanical bond component which is simulated by the spring component.

The bond stress-slip relationship,  $\tau(s)$ , used in Equations 6.18 and 6.19 is defined as follows:

$$\tau(s) = \begin{cases} \tau_m \left( \frac{s}{s_m} \right)^\alpha & \text{for } s \leq s_m \\ \tau_m \frac{1}{1 + \left( \frac{s - s_m}{s_1} \right)^{\alpha'}} & \text{for } s > s_m \end{cases} \quad (6.20)$$

where  $\tau_m$  and  $s_m$  are the bond strength and its corresponding slip, respectively. Parameter  $\alpha$  defines the shape of the pre-peak branch, whereas  $\alpha'$  and  $s_1$  define the shape of the post-peak branch of the curve.

The contribution of the mechanical bond,  $N_{sp}$ , was obtained by subtracting the experimental average curve of the straight fibres from the experimental curves of the TYPE A hooked-end fibres. Both the envelope and the average of the contribution of the mechanical bond for the 2.5 mm/s pull-out rate series (A\_lb15\_0\_2.5 series) are depicted in Figure 6.10(a). An analytical relationship of the average contribution of the mechanical bond was obtained by non-linear regression and is given by:

$$N_{sp} = \begin{cases} 1445.7732 \cdot s - 1656.7085 \cdot s^2 & \text{for } s \leq 0.4 \\ 6.5353 \cdot s^5 - 84.7224 \cdot s^4 + 401.6657 \cdot s^3 & \\ -850.9486 \cdot s^2 + 732.9955 \cdot s + 129.9825 & \text{for } 0.4 < s \leq 4.5 \\ 175.0 - 12.9987 \cdot s & \text{for } s > 4.5 \end{cases} \quad (6.21)$$

Both the envelope and the analytical simulation of the contribution of the mechanical bond are depicted in Figure 6.10(b). The unknown parameters of the local bond stress-slip relationship (Equation 6.20) were obtained to fit the differential Equation 6.17 as accurately as possible, see Section 6.2.1.3. Computational code was developed and implemented using the algorithm and methods given by Cunha (2010) to determine these parameters.

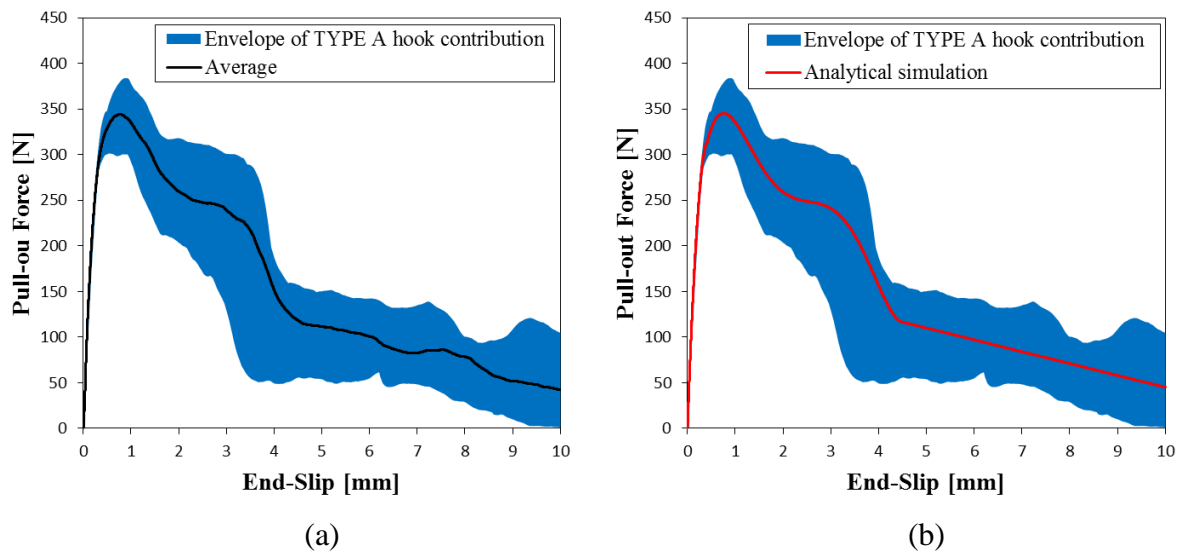


Figure 6.10. (a) The envelope and average of the TYPE A hook contribution for the 2.5 mm/s pull-out rate series, (b) the analytical simulation of the TYPE A hook contribution

### 6.2.1.3 Numerical simulations

The values of the parameters defining the quasi-static local bond stress-slip relationship for straight and TYPE A hooked-end fibres, determined using the numerical strategy described by Cunha (2010), for each specimen tested are included in Tables 6.7 and 6.8, respectively. Also included is the normalised error,  $\bar{e}$ , which was defined as follow:

$$\bar{e} = \frac{|A_{exp} - A_{num}|}{A_{exp}} \quad (6.22)$$

where  $A_{exp}$  and  $A_{num}$  are the area under the experimental and numerical force-slip graph, respectively. The adopted values of the material and geometrical properties used in the numerical strategy developed by Cunha (2010) were the following: a cross-sectional area ( $A_f$ ) of  $0.636 \text{ mm}^2$ , a Young's modulus ( $E_f$ ) of 210 GPa and a cross-sectional perimeter ( $P_f$ ) of 2.827 mm. Figure 6.11 depicts the simulated quasi-static force-slip relationship with the average of the 2.5 mm/s experimental series and the experimental envelope for straight and TYPE A hooked-end fibres. The parameters for the quasi-static bond-stress relationship depicted in Figure 6.11 were obtained by taking the average of the parameters as presented in Table 6.7 and 6.8 for straight and TYPE A hooked-end fibres, respectively.

*Table 6.7. Parameters for the quasi-static local bond stress-slip relationship for straight fibres*

Specimen No.	$s_m$ [mm]	$\tau_m$ [MPa]	$\alpha$	$\alpha'$	$s_l$ [mm]	$\bar{\epsilon}$ [%]
1	0.010	1.095	0.544	0.547	0.868	8.96E-10
2	0.029	1.448	0.262	0.184	0.149	2.99E-11
3	0.015	1.793	0.412	0.848	0.944	7.13E-11
4	0.014	2.022	0.548	0.206	0.041	2.46E-09
5	0.024	2.000	0.709	0.874	0.915	5.84E-11
6	0.033	1.643	0.863	0.321	0.047	1.54E-10
7	0.025	1.420	0.887	0.406	0.539	1.17E-09
Average	0.021	1.631	0.6036	0.4835	0.500	6.92E-10

*Table 6.8. . Parameters for the quasi-static local bond stress-slip relationship for TYPE A hooked-end fibres*

Specimen No.	$s_m$ [mm]	$\tau_m$ [MPa]	$\alpha$	$\alpha'$	$s_l$ [mm]	$\bar{\epsilon}$ [%]
1	0.014	1.454	0.851	0.388	0.376	1.45E-04
2	0.015	1.750	0.875	0.437	0.374	1.99E-03
3	0.02	1.375	0.613	0.450	0.825	1.05E-01
4	0.025	0.953	0.792	0.200	1.000	4.75E-01
5	0.015	1.500	0.500	0.413	0.513	3.10E-02
6	0.035	1.202	0.682	0.413	1.181	6.72E-04
7	0.019	1.133	0.680	0.400	1.200	2.18E-01
Average	0.020	1.338	0.713	0.386	0.781	1.19E-01

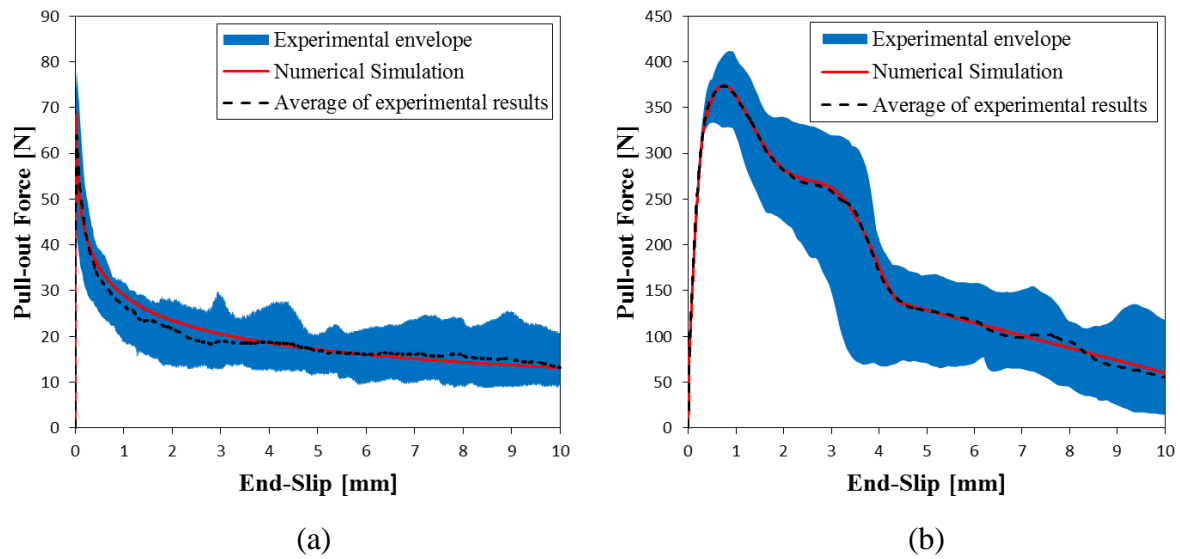


Figure 6.11. Numerical quasi-static pull-out force-slip simulation for (a) straight fibres and (b) TYPE A hooked-end fibres

The analytical model developed by Cunha (2010) was able to simulate the experimental force-slip results for both straight and TYPE A hooked-end fibres with high accuracy. This is evident in the relatively low values of the normalised errors presented in Tables 6.7 and 6.8. To further analyse the accuracy of the model developed by Cunha (2010) the numerical maximum pull-out force ( $N_{max}$ ) and the corresponding slip ( $s_{max}$ ) are compared with the experimental maximum pull-out force ( $\bar{N}_{max}$ ) and its corresponding slip ( $\bar{s}_{max}$ ), see Table 6.9. The normalised error ( $\bar{e}$ ) is also presented which is the ratio between the deviation (the difference between the experimental and numerical value) and the experimental value.

Table 6.9. Comparison between simulated and experimental quasi-static parameters

Series	$\bar{N}_{max}$ [N]	$N_{max}$ [N]	$\bar{e}$ [%]	$\bar{s}_{max}$ [mm]	$s_{max}$ [mm]	$\bar{e}$ [%]
S_lb15_0_2.5	67.1	68.5	2.02	0.022	0.021	2.79
A_lb15_0_2.5	372.3	374.1	0.47	0.738	0.736	0.23

The model developed by Cunha (2010) simulated the average quasi-static maximum pull-out force and the corresponding slip with high accuracy for both straight and TYPE A hooked-end fibres. This is evident in the relatively low normalised errors presented in Table 6.9.

## 6.2.2 Model adaption to include time-dependent behaviour

The constitutive pull-out creep model presented in Section 6.1 was added in series with the analytical model developed by Cunha (2010) shown in Section 6.2.1 to incorporate the rate

effect in the model (see Figure 6.12). The adapted model presented in Figure 6.12 will from here on be referred to as the time-dependent pull-out model. The constitutive pull-out creep model (the time-dependent component) contained two components, namely a non-linear component and a visco-elastic component. As previously mentioned the time-dependent component was derived for the condition of constant force, but the pull-out rate force varied with time. However, the principle of superposition can be used to modify Equation 6.14 so that the complete force history is considered.

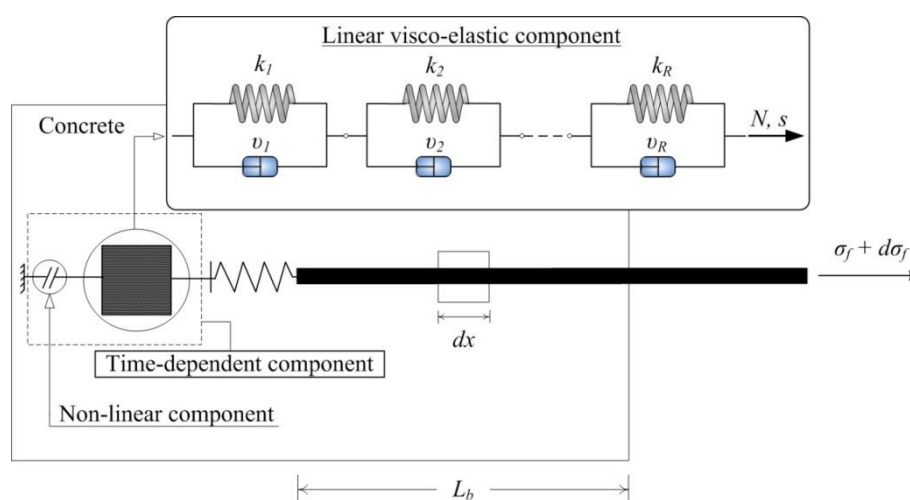


Figure 6.12. Time-dependent pull-out model: analytical model developed by Cunha (2010) adapted to include time-dependent behaviour

The concept of superposition implies that the sum of the separate pull-out creep displacements caused by each force and time increment equals the total pull-out creep displacement. This is schematically shown in Figure 6.13.

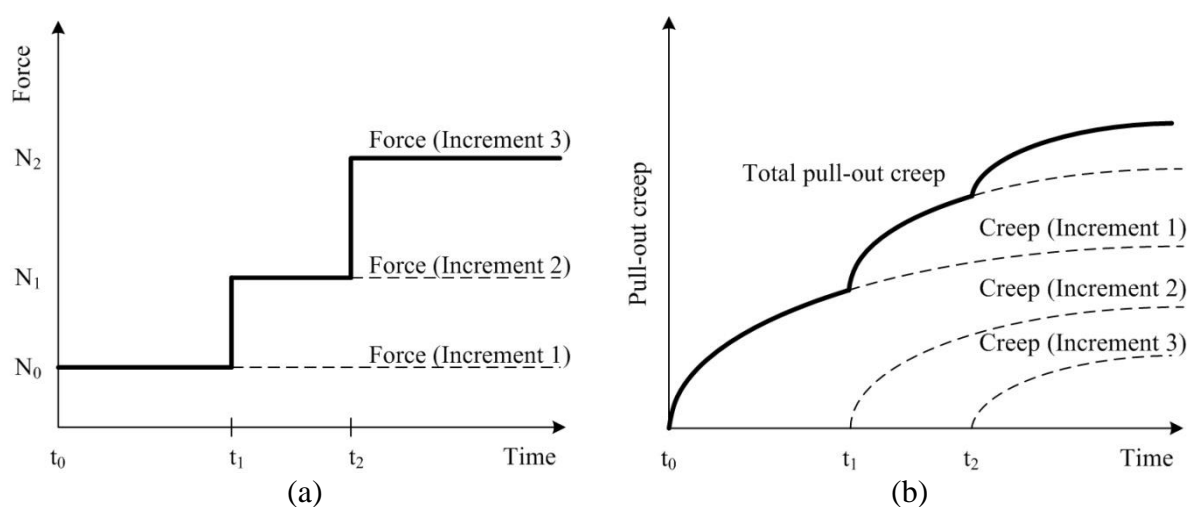


Figure 6.13. The principal of superposition: (a) The applied force increments that causes (b) the pull-out creep increments

### 6.2.2.1 Mathematical derivation of time-dependent model

Consider a specific time increment,  $t_0$  to  $t_1$ , and a force increment  $N_0$  to  $N_1$ . The total displacement at time  $t_1$  using the principle of superposition and Equation 6.14 is as follows:

$$s_1 = (N_1 - N_0) \sum_{i=1}^r \frac{\varphi}{k_i} \left[ 1 - e^{-\frac{(t_1-t_0)}{\tau_i}} \right] \quad (6.23)$$

To explain the application of superposition only one term of the sum will be used further on. Equation 6.23 then simplifies to:

$$s_1 = (N_1 - N_0) \frac{\varphi}{k} \left[ 1 - e^{-\frac{(t_1-t_0)}{\tau}} \right] \quad (6.24)$$

This simplifies to:

$$s_1 = \left[ (N_1 - N_0) \frac{\varphi}{k} \right] + e^{-\frac{t_1}{\tau}} \left[ (N_0 - N_1) \frac{\varphi}{k} e^{\frac{t_0}{\tau}} \right] \quad (6.25)$$

The next time increment,  $t_1$  to  $t_2$ , the force is increased from  $N_1$  to  $N_2$ . The total displacement,  $s_2$ , is:

$$s_2 = (N_1 - N_0) \frac{\varphi_1}{k} \left[ 1 - e^{-\frac{(t_2-t_0)}{\tau}} \right] + (N_2 - N_1) \frac{\varphi_2}{k} \left[ 1 - e^{-\frac{(t_2-t_1)}{\tau}} \right] \quad (6.26)$$

This simplifies to:

$$s_2 = \left[ (N_1 - N_0) \frac{\varphi_1}{k} + (N_2 - N_1) \frac{\varphi_2}{k} \right] + e^{-\frac{t_2}{\tau}} \left[ (N_0 - N_1) \frac{\varphi_1}{k} e^{\frac{t_0}{\tau}} + (N_1 - N_2) \frac{\varphi_2}{k} e^{\frac{t_1}{\tau}} \right] \quad (6.27)$$

From Equation 6.27 it is found that the parameters of the first term in each set of square brackets is known at the end of the first increment, i.e.,  $t_0$  to  $t_1$ , while the parameters of the second term are known at the end of the second increment,  $t_1$  to  $t_2$ . If another increment is added, i.e.,  $t_2$  to  $t_3$ , a third term would arise where all the parameters will be known at the end of the increment. This means that Equation 6.27 can be simplified to:

$$s_2 = \left[ H_1 + (N_2 - N_1) \frac{\varphi_2}{k} \right] + e^{-\frac{t_2}{\tau}} \left[ H_2 + (N_1 - N_2) \frac{\varphi_2}{k} e^{\frac{t_1}{\tau}} \right] \quad (6.28)$$



where  $H_1$  and  $H_2$  are two history variables, which describe the force history. At the end of the second increment, i.e.,  $t_1$  to  $t_2$ , the history variables are updated as follow:

$$H_{1,update} = H_1 + (N_2 - N_1) \frac{\varphi_2}{k} \quad (6.29)$$

$$H_{2,update} = H_2 + (N_1 - N_2) \frac{\varphi_2}{k} e^{\frac{t_1}{\tau}} \quad (6.30)$$

The generalised form of Equation 6.28 is as follow:

$$s_2 = \sum_{i=1}^r \left[ \left[ H_{1,i} + (N_2 - N_1) \frac{\varphi_2}{k_i} \right] + e^{-\frac{t_2}{\tau_i}} \left[ H_{2,i} + (N_1 - N_2) \frac{\varphi_2}{k_i} e^{\frac{t_1}{\tau_i}} \right] \right] \quad (6.31)$$

This formulation above will represent the rate effect of the single fibre pull-out behaviour. The applied force can change with time and the force history is only represented by two variables per Kelvin-Voigt element.

### 6.2.2.2 Verification of adapted model

To determine the performance of the time-dependent model, it was verified with the experimental single fibre pull-out rate results. Note that these results were not used to determine the parameters of the model. The experimental results showed a rate effect on the slip at maximum force ( $s_{max}$ ). The increase in  $s_{max}$  as the pull-out rate decreases is due to the increase in the pull-out creep at maximum pull-out force. To simulate the total pull-out creep at maximum pull-out force for each loading rate the method as described in Equations 6.24 to 6.31 was implemented using the material and non-linear parameters given in Tables 6.1 and 6.4, respectively. Figure 6.14 presents the calculated average experimental and simulated pull-out creep at maximum pull-out force for each loading rate. The linear pull-out creep simulations presented in Figure 6.14, constitute the pull-out creep behaviour when the non-linear factor,  $\varphi$ , is not included in Equations 6.24 to 6.31.

In Figure 6.14 it is observed that the average pull-out creep at maximum force increases exponentially as the pull-out rate decreases. Therefore, as observed in Figure 6.13 the non-linear constitutive pull-out creep model is more accurate in simulating the non-linear pull-out creep behaviour at maximum force.

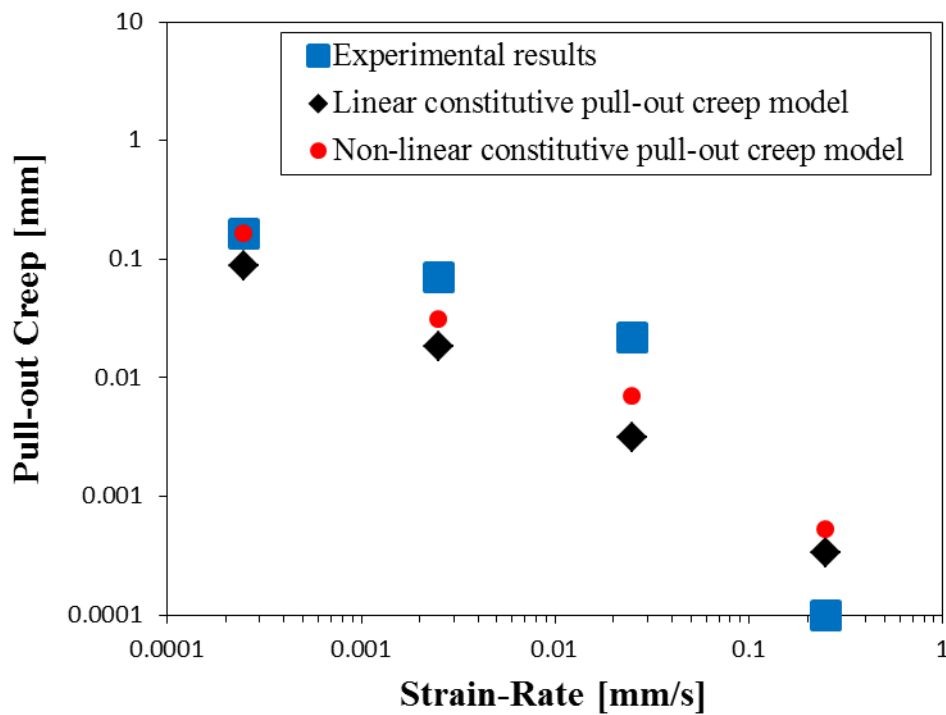


Figure 6.14. The average experimental and simulated pull-out creep at maximum pull-out force for different loading rates

The slip at maximum pull-out force,  $s_{max}$ , at each loading rate determined with the linear and non-linear time-dependent pull-out model (Figure 6.12) are depicted in Figures 6.15(a) and 6.15(b), respectively. The only difference between the linear and non-linear time-dependent pull-out model is that the non-linear component is excluded in the linear time-dependent pull-out model. The simulated slip at maximum pull-out force,  $s_{max}$ , at each loading rate is calculated as follow:

$$s_{max} = s_{max,static} + \Delta_{max,\dot{s}} \quad (6.32)$$

where  $s_{max,static}$  is the simulated slip at maximum pull-out force for the quasi-static response and  $\Delta_{max,\dot{s}}$  is the total simulated pull-out creep at maximum pull-out force for a specific pull-out rate,  $\dot{s}$ . Also presented in Figures 6.15(a) and 6.15(b) are the normalised error ( $\bar{e}$ ) calculated at each loading rate. The normalised errors ( $\bar{e}$ ) were calculated as follow:

$$\bar{e} = \frac{|s_{max,exp} - s_{max,sim}|}{s_{max,exp}} \quad (6.33)$$

where  $s_{max,exp}$  and  $s_{max,sim}$  are the average experimental and simulated slip at maximum pull-out force, respectively.

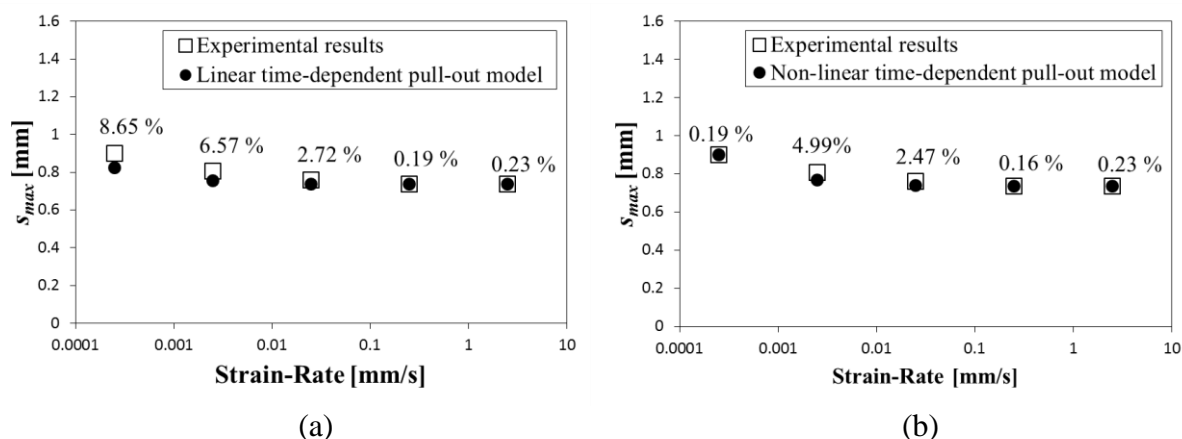


Figure 6.15. Verification of the time-dependent pull-out model by simulating the slip at maximum pull-out force ( $s_{max}$ ) at each loading rate with (a) the linear time-dependent pull-out model and (b) non-linear time-dependent pull-out model

The normalised errors ( $\bar{\epsilon}$ ) presented in Figure 6.15 for both the linear and non-linear time-dependent pull-out models are relatively low, however, it is evident that the non-linear time-dependent pull-out model is more accurate in simulating the rate effect, especially at lower loading rates. This is due to the non-linear pull-out creep behaviour which is observed in Figure 6.14.

The time-dependent component added in series with the model developed by Cunha (2010) simulated the rate effect with relative high accuracy, see Figure 6.15(b). This confirms that the material and non-linear parameters presented in Tables 6.1 and 6.4, respectively, describe the pull-out creep behaviour of TYPE A hooked-end fibres.

### 6.3 Concluding Summary

In this chapter a method was proposed to predict the pull-out creep of aligned TYPE A hooked-end fibres. The model is based on a rheological component and a non-linear component connected in series. The rheological component is a generalised Kelvin-Voigt model which describes the linear pull-out creep behaviour up to sustained load levels of 50 % of the average maximum pull-out force. The material parameters describing the linear pull-out creep behaviour were calibrated with the average experimental pull-out creep results at a 30 % load level. The non-linear component introduced a non-linear factor which incorporates the non-linear pull-out creep behaviour caused by micro-cracking damage. The non-linear parameters were calibrated with the average experimental pull-out creep results at different load levels after 249 days. By implementing the calibrated non-linear parameters the pull-out

creep model is able to simulate the pull-out creep behaviour for sustained load levels higher than 50 % of the average maximum pull-out force.

To validate the calibrated material and non-linear parameters the pull-out creep model was used in collaboration with a model developed by Cunha (2010) to predict the pull-out rate effect of TYPE A hooked-end fibres. In Section 5.1.1.1 it was concluded that the slip at maximum pull-out force is rate dependent. The constitutive pull-out creep model was added in series with the model of Cunha (2010) to incorporate the rate effect. The adapted model was referred to as the time-dependent pull-out model and is able to simulate the slip at maximum pull-out force with relative high accuracy.

The proposed model enables the prediction of the pull-out creep of a single TYPE A hooked-end fibre. The next step is to generalise the single fibre pull-out creep model to simulate the tensile time-dependent crack width opening behaviour of cracked SFRC on a macroscopic level.

# Chapter 7

---

## Predicting the Macroscopic Time-dependent Crack Mouth Opening Displacement

The post cracking behaviour of FRC has been successfully predicted by numerous scholars (Buratti, et al., 2011; Cunha, 2010; Dupont, 2003; de Oliveira, 2010). It was only recently that the prediction of the time-dependent CMOD of cracked FRC has been investigated. Babafemi (2015) proposed a numerical model that predicts the time-dependent CMOD of cracked notched macro-synthetic FRC beams. Even though recommendations and codes exist for the structural use of SFRC, information on the time-dependant behaviour after cracking is still lacking. For the optimal design of SFRC it is relevant to predict this time-dependent CMOD.

In Chapter 5 it was shown that the principle mechanism responsible for the time-dependent crack mouth opening displacement of cracked SFRC is the fibre pull-out creep. A constitutive model for predicting the pull-out creep of a single sided aligned TYPE A hooked-end fibre was proposed in Chapter 6. In this chapter the aim is to generalise the constitutive pull-out creep model so that it can predict the macroscopic crack mouth opening displacement under sustained loading ( $CMOD_{sus}$ ). An orientation factor was introduced into the model to incorporate the inclination angle of the fibres bridging the crack plane

## 7.1 Conceptual Basis

In Chapter 5 it was concluded that pull-out creep is exclusively induced by the mechanical hooked-end mechanisms. An aligned fibre crossing the crack plane in a macroscopic specimen is subjected to pull-out creep at both hooked-ends of the fibre. The constitutive pull-out creep model developed in Chapter 6 described the single sided pull-out creep for aligned TYPE A hooked-end fibres. However, a single aligned TYPE A hooked-end fibre crossing the crack plane in a macroscopic specimen is subjected to pull-out creep ( $s_{creep}$ ) at both hooked-ends of the fibre, see Figure 7.1. Thus, if it is assumed that the pull-out creep at both ends is the same, the crack width opening due to pull-out creep ( $w_{creep}$ ) of an aligned single fibre crossing the crack plane would be twice the amount of the single sided embedded fibre pull-out creep ( $s_{creep}$ ), which is expressed as follow:

$$w_{creep}(t) = 2 \cdot s_{creep}(t) = 2N \sum_{i=1}^R \frac{1}{k_i} \left[ 1 - e^{-\left(\frac{t}{\tau_i}\right)} \right] \quad (7.1)$$

Equation 7.1 represents the crack width opening due to pull-out creep ( $w_{creep}$ ) behaviour at a generic time instance,  $t$ , of a single aligned fibre bridging the crack plane in the macroscopic specimen. In the course of this chapter a method will be presented how to generalise the expression in Equation 7.1 so that it can be used to model the macroscopic  $CMOD_{sus}$ .

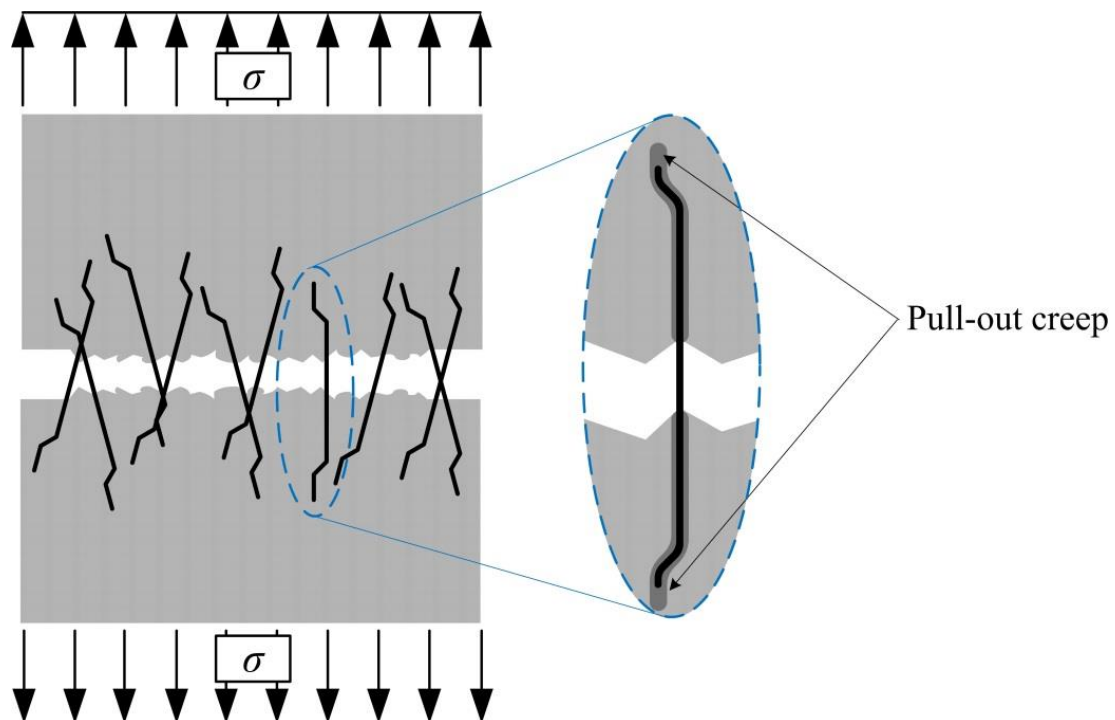


Figure 7.1. Schematic representation of a fibre bridging a crack plane under sustained loading

## 7.2 Generalised Constitutive Model (GCM)

The pull-out creep behaviour can be affected by numerous factors, e.g. the fibre embedded inclination angle, fibre embedment length, applied sustained load, mechanical anchorage etc. In Chapter 5 the factors investigated on the single sided pull-out creep behaviour of TYPE A hooked-end fibres were restricted to the applied sustained load and the fibre embedment inclination angle. Since the pull-out creep behaviour is the principle mechanism responsible for the  $CMOD_{sus}$  of cracked SFRC, it was perceived that the aforementioned factors will have an effect on the  $CMOD_{sus}$ .

The concept of the GCM was based on certain assumptions regarding the factors that can have an effect on the  $CMOD_{sus}$ . These assumptions were then used to construct a model, the GCM, which is used to predict the behaviour of the  $CMOD_{sus}$ . These assumptions were then validated by verifying the GCM with the  $CMOD_{sus}$  results presented in Chapter 4.

### 7.2.1 Identifying factors that affects the $CMOD_{sus}$

The following assumptions were made for the GCM on the factors that can have an effect on the  $CMOD_{sus}$ :

- The number of fibres is distributed uniformly over the crack plane area.
- The  $CMOD_{sus}$  propagates symmetrically.
- All fibres crossing the crack plane are aligned with the sustained load.
- The sustained load is distributed uniformly over the fibres bridging the crack.
- All fibres bridging the crack have the same embedment length at both sides.

The general problem and the GCM for predicting the  $CMOD_{sus}$  are schematically presented in Figure 7.2. The GCM is constructed based on the above mentioned factors. A brief discussion of the effect of the aforementioned factors on the  $CMOD_{sus}$  behaviour will follow next.

#### 7.2.1.1 Crack plane fibre distribution

It was assumed for the GCM that the fibres are distributed uniformly over the crack plane, however, in Section 4.2.3 it was shown that the fibres are not distributed uniformly over the crack plane, (see Figure 7.3). By assuming that the fibres are distributed uniformly over the crack plane area led to the following assumption discussed next.



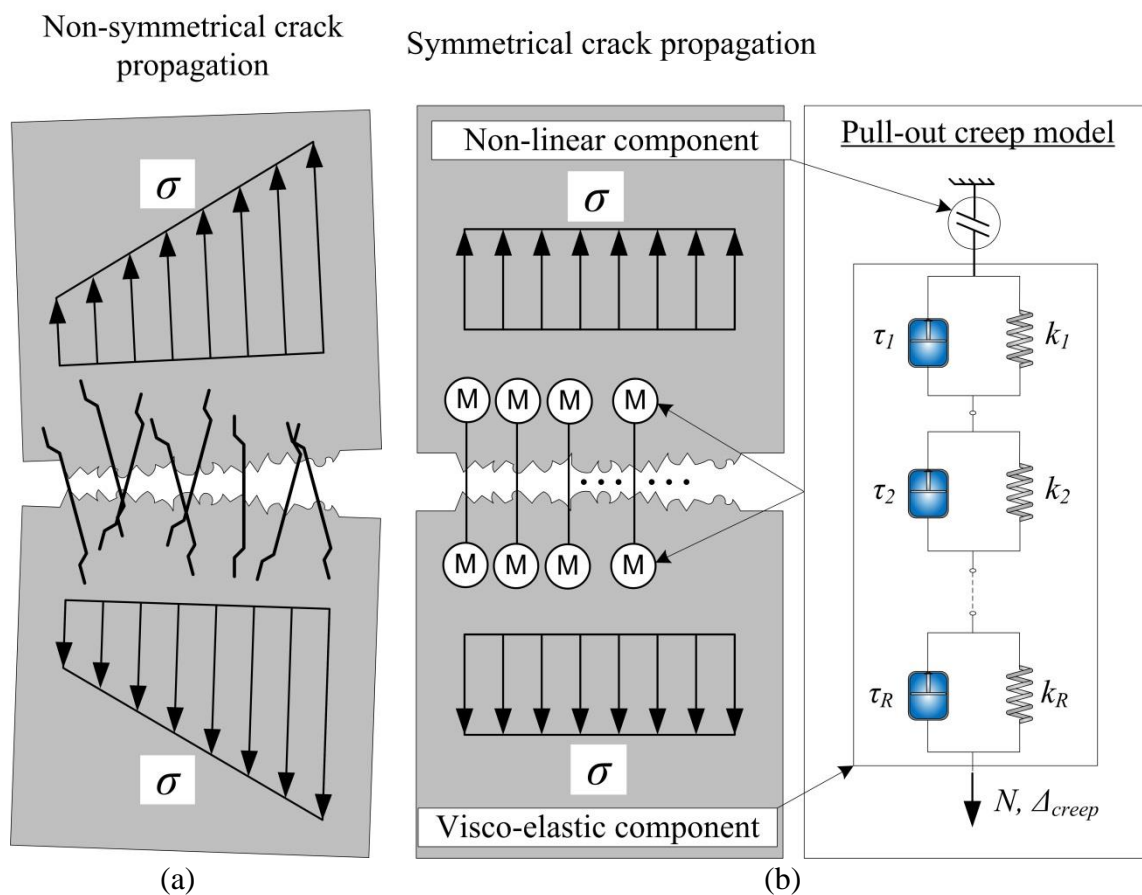


Figure 7.2. (a) The general problem, (b) The generalised constitutive model (GCM) for predicting the  $CMOD_{sus}$



Figure 7.3. Example of fibre distribution over the crack plane



### 7.2.1.2 Propagation of $CMOD_{sus}$

Since it is assumed that the fibres are distributed uniformly over the crack plane, it was perceived that the  $CMOD_{sus}$  will propagate symmetrically. However, as previously mentioned in Section 4.2.3 it was shown that the fibre distribution was not uniform over the crack plane, which was possibly the reason for the combination of non-symmetrical (out-of-plane) and symmetrical crack propagation observed during the uni-axial tensile tests. Assuming that the  $CMOD_{sus}$  propagates symmetrically implied that all the fibres undergo the same amount of crack width opening due to pull-out creep ( $w_{creep}$ ).

### 7.2.1.3 Fibre embedment inclination angle distribution over crack plane

In SFRC the fibres are randomly distributed and oriented in all directions. In Section 5.2.1.2 it was shown that the out-of-plane orientation, i.e. the embedment inclination angle between the fibre longitudinal axis and the loading direction, has an effect on the pull-out creep behaviour. This implies that the distribution of the fibre embedment inclination angle over the crack plane will have an effect on the  $CMOD_{sus}$ . However, for the GCM it is assumed that all the fibres are aligned in the direction of the sustained load.

### 7.2.1.4 Sustained load distribution over crack plane

Since the fibres are randomly orientated and distributed at the crack plane the stress distributed over the fibres will not be uniformly distributed. For the GCM it is assumed that the sustained load is distributed uniformly over the crack plane. This implies that each fibre is subjected to the same load magnitude.

### 7.2.1.5 Fibre embedment length distribution over crack plane

It was proven in Section 5.2.1.1 that the pull-out creep was induced by the anchorage mechanism, i.e. the TYPE A hooked-end of the fibre. Thus, the embedment length will have no effect on the pull-out creep behaviour. This is only true if the fibre embedment length is larger than the hooked-end of the fibre. For the GCM it was assumed that each fibre over the crack plane had an embedment length of half the fibre length ( $l_f/2$ ).

## 7.2.2 Generalised formulation

With the aforementioned assumptions an expression for predicting the  $CMOD_{sus}$  is derived next. Consider a crack plane with  $N_f$  number of fibres distributed uniformly over it. If a

sustained load,  $P$ , is applied over the crack plane and with the assumption that the load is uniformly distributed over the fibres bridging the crack, the applied load,  $N$ , subjected to each fibre is calculated as follow:

$$N = \frac{P}{N_f} \quad (7.2)$$

With the assumption that all fibres undergo the same amount of crack width opening due to pull-out creep ( $w_{creep}$ ), the  $CMOD_{sus}$  at a generic time instance,  $t$ , is determined as follow:

$$CMOD_{sus}(t) = \frac{\sum_{j=1}^{N_f} w_{creep,j}(t)}{N_f} = \frac{\sum_{j=1}^{N_f} 2N \sum_{i=1}^R \frac{1}{k_i} \left[ 1 - e^{-\left(\frac{t}{\tau_i}\right)} \right]}{N_f} \quad (7.3)$$

were  $w_{creep,i}(t)$  represents the crack width opening due to pull-out creep at generic time instance,  $t$ , of the  $i^{\text{th}}$  fibre bridging the crack plane and can be determined with Equation 7.1. Since the applied load,  $N$ , subjected to each fibre is the same (see Equation 7.2), Equation 7.3 is simplified to

$$CMOD_{sus}(t) = w_{creep}(t) = 2 \cdot s_{creep}(t) = 2N \sum_{i=1}^R \frac{1}{k_i} \left[ 1 - e^{-\left(\frac{t}{\tau_i}\right)} \right] \quad (7.4)$$

This implies that the concept of the GCM is based on the assumption that the behaviour of  $CMOD_{sus}$  is the same as the crack width opening due to pull-out creep ( $w_{creep}$ ) of a single fibre crossing the crack plane.

### 7.2.3 Experimental validation

The  $CMOD_{sus}$  results reported in Chapter 4 will be used to evaluate the suitability of the GCM on describing the  $CMOD_{sus}$  behaviour of cracked SFRC. The input parameters required for the GCM are the material and non-linear parameters for the constitutive pull-out creep model ( $s_{creep}(t)$ ) and the load,  $N$ , subjected to each fibre over the crack plane. The material and non-linear parameters for the constitutive pull-out creep model ( $s_{creep}(t)$ ) is presented in Tables 6.1 and 6.4. Table 7.1 summarises the average experimental parameters obtained from the  $CMOD_{sus}$  results reported in Section 4.3. With Equation 7.2 and the average experimental parameters presented in Table 7.1, the predicted uniform distributed load,  $N$ , subjected to each fibre at the crack plane at each load level is determined, see Table 7.2. The  $CMOD_{sus}$  simulated with the GCM at each sustained load level is presented in Figure 7.4.

Table 7.1. Average experimental parameters obtained from the pre-cracked sustained load results in Section 4.3

Experimental parameters			Load level			
			30%	50%	70%	85%
Average residual strength	$\sigma_r$	[MPa]	1.96	2.11	2.03	2.61
Average number of fibres	$N_f$	[-]	44.33	43.33	35.00	40.67
Area of cracked section	$A_{sec}$	[mm <sup>2</sup> ]	6400			
Required applied load		[MPa]	0.59	1.06	1.42	2.22
Actual applied load		[MPa]	0.62	1.01	1.43	2.22
Equivalent actual load level	$\bar{\eta}$	[%]	31.6	47.6	70.6	84.9

Table 7.2. Predicted uniform distributed load subjected to each fibre at the crack plane at each load level

Load Level [%]	30	50	70	85
Load subjected to each fibre [N]	89.5	148.7	262.1	348.9

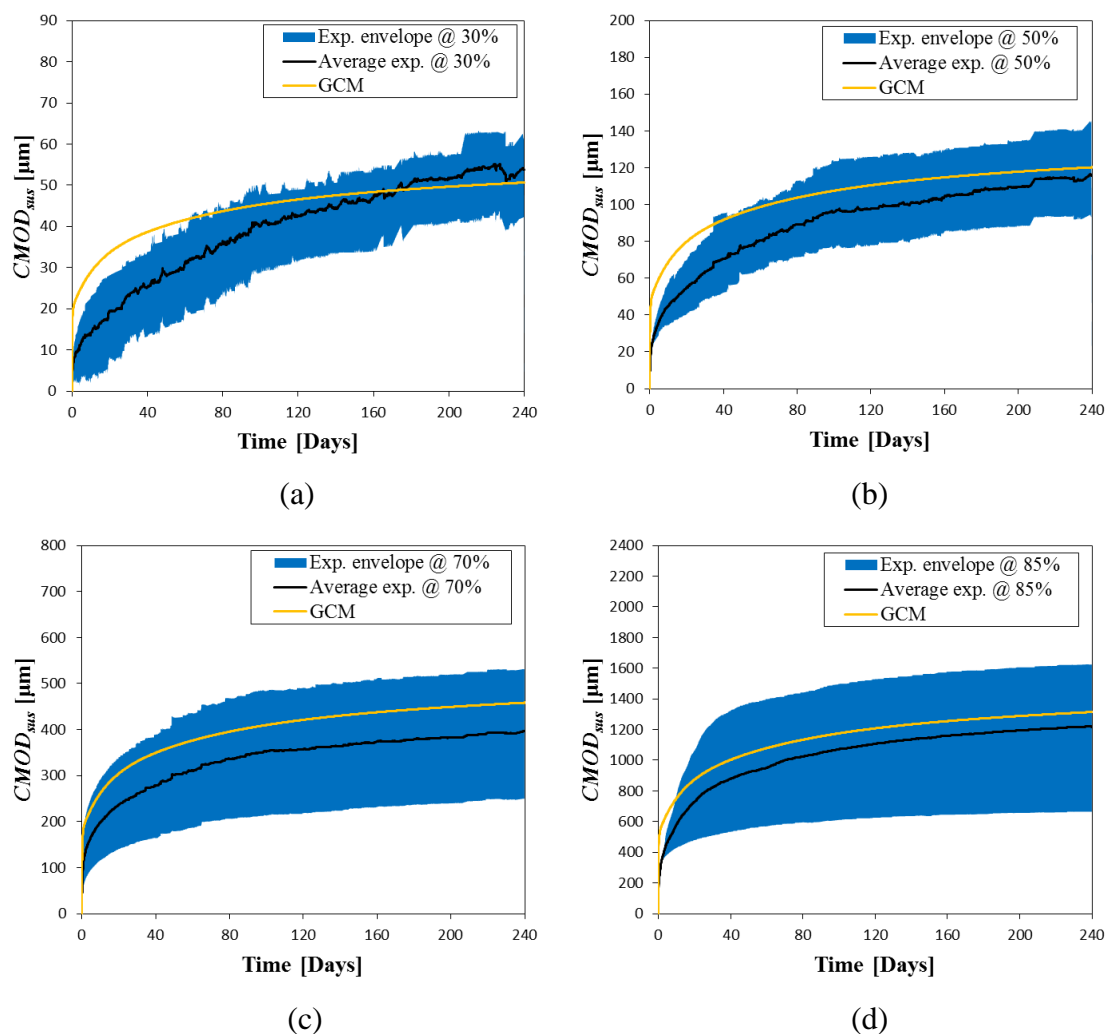


Figure 7.4. Simulated  $CMOD_{sus}$  behaviour with generalised constitutive model (GCM) at various sustained load levels: (a) 30 %, (b) 50 %, (c) 70 % and (d) 85 %

To investigate the suitability of the GCM, the average experimental and modelled  $CMOD_{sus}$  are plotted against the sustained load level after 1 day, 30 days, 100 days and 240 days (see Figure 7.5). The normalised error ( $\bar{e}$ ) for each load level after each generic time instance is presented in Table 7.3 and was calculated as follows:

$$\bar{e} = \frac{|CMOD_{sus}^{model} - CMOD_{sus}^{exp}|}{CMOD_{sus}^{exp}} \quad (7.5)$$

where  $CMOD_{sus}^{model}$  and  $CMOD_{sus}^{exp}$  are the modelled and average experimental  $CMOD_{sus}$ , respectively.

Table 7.3. Calculated normalised errors at each load level after certain generic time instances for the generalised constitutive model (GCM)

Load level [%]	1 day			30 days			100 days			240 days		
	Exp. [ $\mu\text{m}$ ]	GCM [ $\mu\text{m}$ ]	$\bar{e}$ [%]	Exp. [ $\mu\text{m}$ ]	GCM [ $\mu\text{m}$ ]	$\bar{e}$ [%]	Exp. [ $\mu\text{m}$ ]	GCM [ $\mu\text{m}$ ]	$\bar{e}$ [%]	Exp. [ $\mu\text{m}$ ]	GCM [ $\mu\text{m}$ ]	$\bar{e}$ [%]
30	8	21	172.4	23	37	57.4	40	45	13.0	54	51	5.8
50	23	50	110.8	64	87	36.6	96	108	12.2	116	120	4.0
70	117	189	62.0	261	331	26.9	352	410	16.3	396	458	15.6
85	278	542	94.9	823	949	15.3	1072	1175	9.6	1219	1314	7.9

From Table 7.3 and Figure 7.5 it is evident that the GCM is not suitable for predicting the  $CMOD_{sus}$  over the complete measured time period. At each sustained load, the calculated normalised errors ( $\bar{e}$ ) decrease with age. This is an indication that the simulated  $CMOD_{sus}$  rate is not a good representation of the experimental  $CMOD_{sus}$  rate. To get a better understanding of the simulated and average experimental  $CMOD_{sus}$  rate, the abscissa axis of the results presented in Figure 7.4 are scaled logarithmically, see Figure 7.6.

From the semi-logarithmic plots presented in Figure 7.6 a significant difference in the  $CMOD_{sus}$  rate is observed between the experimental and GCM results for generic time instances younger than 10 days. This poses two possible problems with the GCM, firstly, the assumptions made to construct the GCM do not represent the general problem and secondly, the material parameters of the constitutive pull-out creep model developed in Chapter 6 does not represent the pull-out creep behaviour of a single fibre bridging the crack plane in a macroscopic specimen. Concerning the aforementioned problem a similar trend was observed in Section 5.2.1.4 between the pull-out creep of an undamaged and a pre-damaged single fibre specimen before loading. The results showed a significant difference in the pull-out creep rate between the pre-damaged and undamaged single fibre specimens for generic time instances

younger than 10 days, similar to the case of the difference in the  $CMOD_{sus}$  rate between the experimental and GCM results as previously mentioned. This implies that the material parameters describing the undamaged single fibre pull-out creep behaviour do not represent the pull-out creep behaviour of a single fibre bridging the crack plane in a pre-cracked macroscopic specimen. The material parameters of the constitutive pull-out creep model presented in Section 6.1.1 should therefore be calibrated with the pre-damaged pull-out creep results. Since only pre-damaged sustained load tests were performed at a 50 % load level it was not possible to quantify the non-linear pull-out creep behaviour. However, it was assumed that the non-linear pull-out creep rate of the pre-damaged specimens is the same as the undamaged specimens, implying that the non-linear parameters are the same as that of the undamaged specimens.

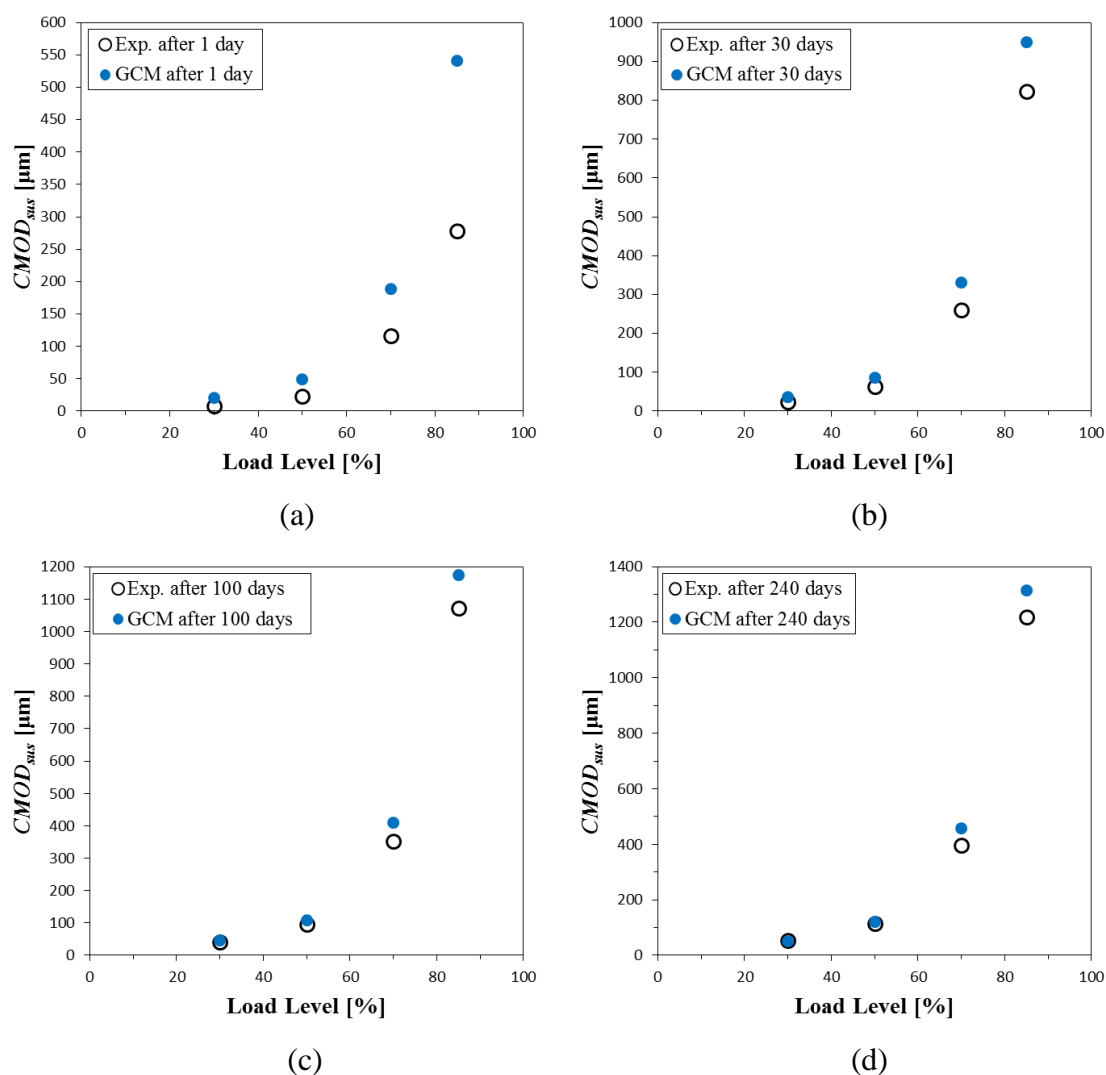


Figure 7.5. The average experimental and generalised constitutive model (GCM)  $CMOD_{sus}$  at each load level after: (a) 1 day, (b) 30 days, (c) 100 days and (d) 240 days

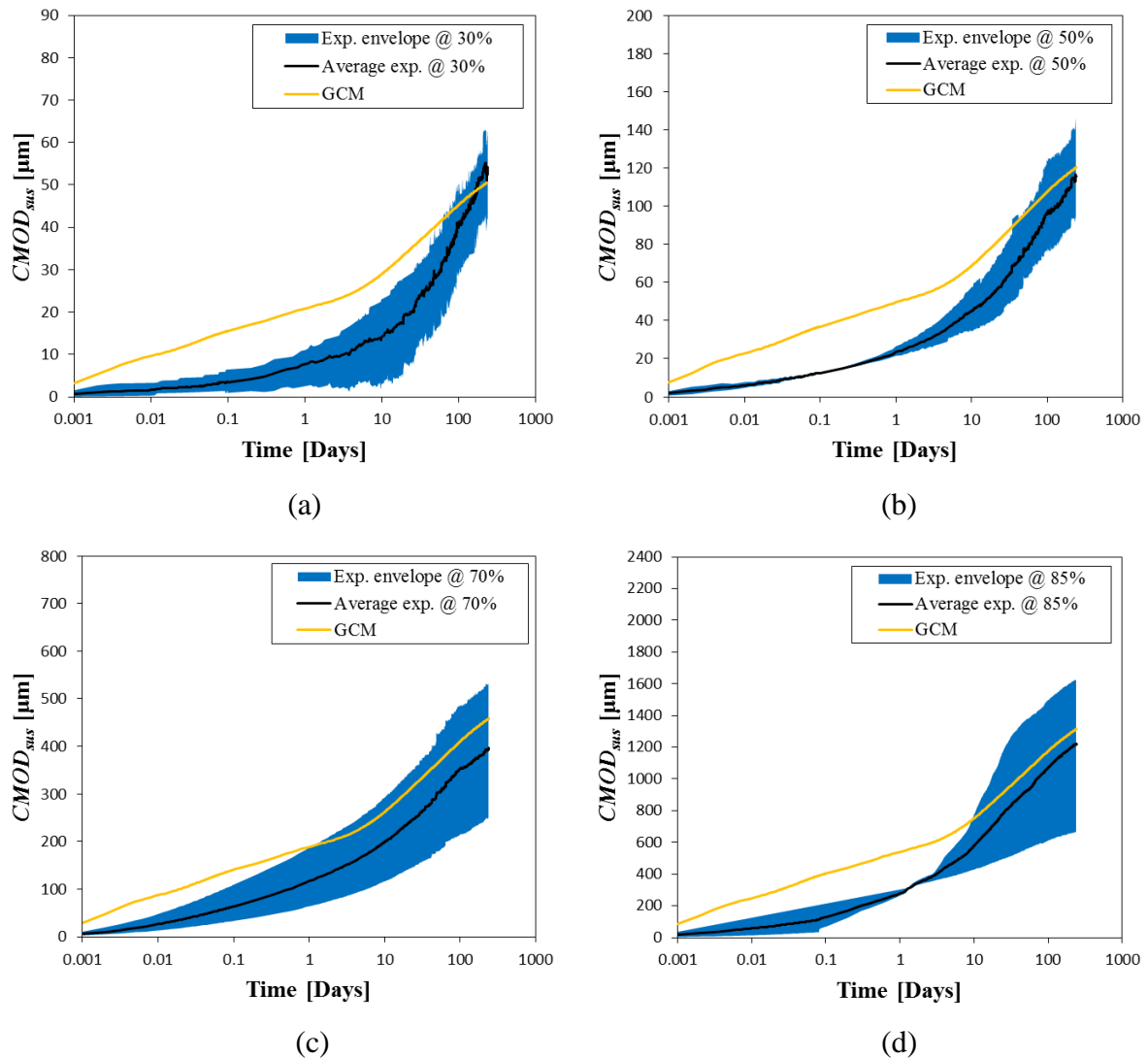


Figure 7.6. Semi-logarithmic plots of generalised constitutive model (GCM) simulations at various sustained load levels: (a) 30 %, (b) 50 %, (c) 70 % and (d) 85 %

## 7.2.4 Calibration of generalised constitutive model (GCM)

The average pre-damaged pull-out creep results presented in Section 5.2.1.4, i.e. series A\_0\_50\_Pre, were used to calibrate the material parameters, see Table 7.4. The simulated pre-damaged pull-out creep behaviour at a load level of 50 % for the material parameters given in Table 7.4 is presented in Figure 7.7.

Figure 7.8 presents the semi-logarithmic plots of the  $CMOD_{sus}$  simulated by the calibrated GCM at various load levels. The material and non-linear parameters for the constitutive pull-out creep model ( $s_{creep}(t)$ ) implemented in the calibrated GCM are presented in Table 7.4 and Table 6.4, respectively.

Table 7.4. Calibrated pre-damaged pull-out creep material parameters

Element no.	$k$ [N/mm]	$\tau$ [Days]
1	8.15E+04	3.97E+01
2	7.17E+04	2.00E+04
3	1.80E+04	2.68E+04
4	7.42E+04	5.40E+04
5	4.91E+03	1.82E+06
6	5.06E+03	1.04E+07
7	3.56E+03	6.82E+08

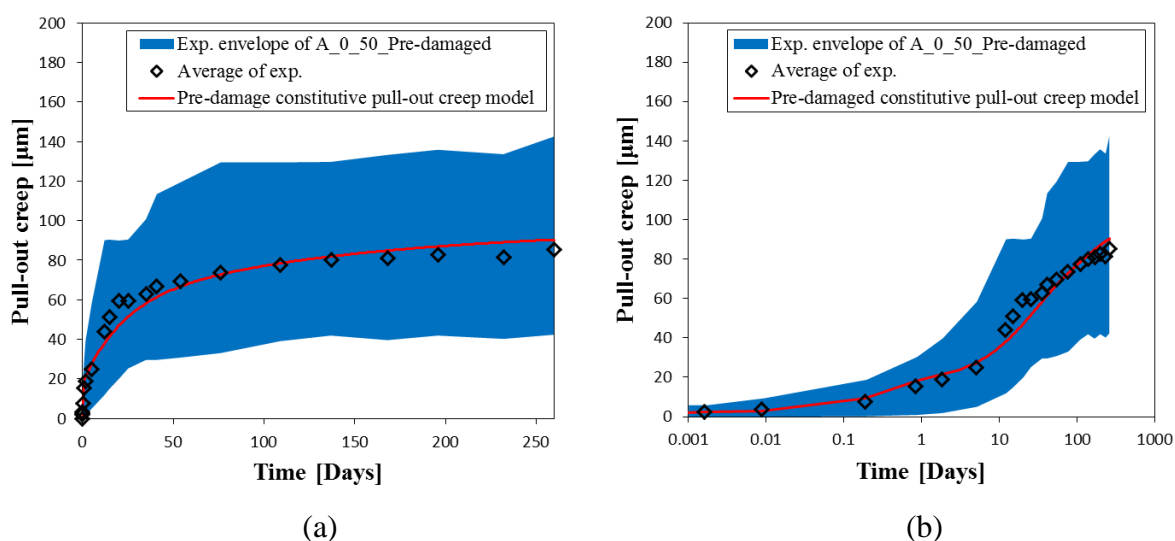


Figure 7.7. Simulated pre-damaged pull-out creep behaviour at a sustained load level of 50 %: (a) linear plot, (b) semi-logarithmic plot

From Figure 7.8 it is evident that the rate of the simulated  $CMOD_{sus}$  is almost similar to that of the average experimental rate for generic time instances younger than 10 days. However, significant deviations between the modelled and average experimental results are observed at generic time instances older than 10 days. The calibrated GCM seems to over predict the  $CMOD_{sus}$  over the measured time period (240 days). For sustained load levels up to 50 % the calibrated GCM prediction was almost similar to that of the maximum extreme value. For higher sustained load levels the prediction was between the boundaries of the experimental envelope, however significant deviations from the average experimental trend were observed for generic time instances older than 10 days. These results reveal that some of the assumptions made for the GCM are invalid for the purpose of predicting the  $CMOD_{sus}$ .

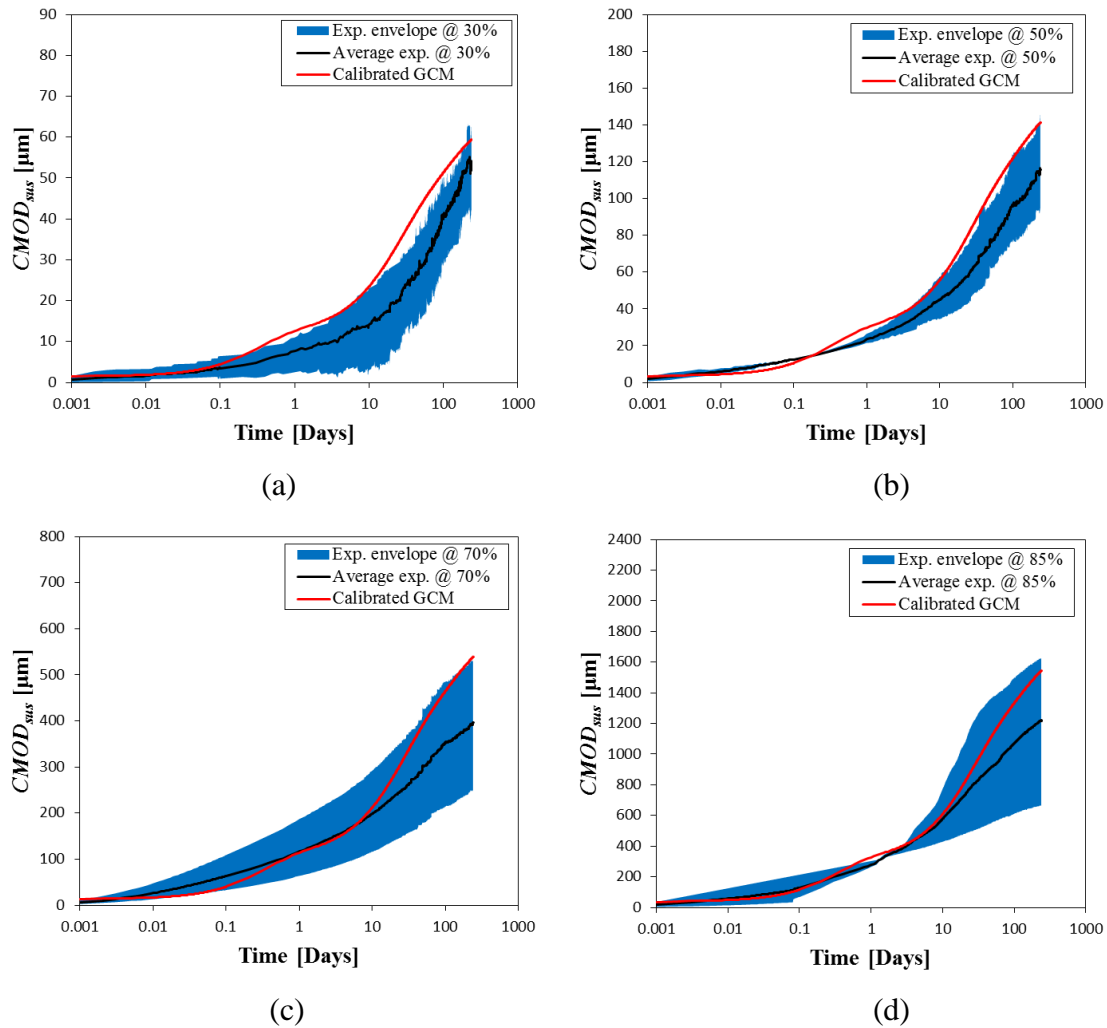


Figure 7.8. Simulated  $CMOD_{sus}$  behaviour with calibrated generalised constitutive model (GCM) at various sustained load levels: (a) 30 %, (b) 50 %, (c) 70 % and (d) 85 %

A factor that was investigated in this research project and which is not included in the calibrated GCM is the inclination angle of the fibres bridging the crack plane. As previously mentioned, the fibre inclination angle does have an effect on the single fibre pull-out creep behaviour. Since the fibres bridging the crack plane are randomly orientated relative to the applied load it is conceived that this factor will significantly affect the  $CMOD_{sus}$ . In the course of the next section a method is proposed how to include the fibre embedment inclination angle in the model.

### 7.3 Oriented Generalised Constitutive Model (OGCM)

In the GCM it was assumed that each fibre is orthogonal to the crack plane. This is however not the case for SFRC elements, since each fibre bridging the crack plane is randomly orientated relative to the orthogonal axis of the crack plane (Cunha, 2010; Dupont, 2003).



The average orientation of fibres at a crack plane is normally characterized through the orientation factor ( $\alpha$ ). According to Krenchel (1975) and Soroushian and Lee (1990) the factor  $\alpha$  can be determined as follow:

$$\alpha = \frac{N_f}{V_f} \cdot \frac{A_f}{A_c} \quad (7.6)$$

where  $N_f$  and  $V_f$  are, respectively, the number of fibres bridging the crack plane and the volumetric fraction of fibres added to the concrete matrix.  $A_f$  and  $A_c$  are the cross sectional area of a single fibre and the crack plane, respectively. According to de Oliveira (2010) can the average orientation angle ( $\theta$ ) of the fibres bridging the crack plane be expressed in degrees as follow:

$$\theta = \arccos(\alpha) \times \frac{180}{\pi} \quad (7.7)$$

The orientation factor ( $\alpha$ ) can vary between 0 and 1, referring to fibres that are parallel and orthogonal to the crack plane, respectively.

It is commonly assumed that that the fibres within a cementitious matrix are randomly orientated, i.e. isotropic uniformly randomly orientated. Analytical formulations proved that the rotational factor ( $\alpha$ ) under isotropic conditions for a one (1D), two (2D) and three-dimensional (3D) case equals to 1,  $2/\pi$  and 0.5 respectively (Kameswara Rao, 1979; Kooiman, 2000; Stroeven & Hu, 2006). However, nowadays it is widely accepted by scholars that certain factors can affect the orientation of the fibres within a structural element (Cunha, 2010; de Oliveira, 2010). Amongst these factors the following were considered to promote the re-orientation of fibres within a structural element, the fibre geometry, the casting procedure, the geometry of the mould, the compaction energy and the rheology properties of the concrete.

With the assumption of isotropic conditions and Equation 7.6 the average orientation factor ( $\alpha$ ) at each sustained load was determined, see Table 7.5. The fibre volume fraction adopted was 0.5 %. The cross sectional area of a single fibre and the crack plane were  $0.636 \text{ mm}^2$  and  $6400 \text{ mm}^2$ , respectively. The average number of fibres ( $N_f$ ) was adopted from Table 7.1. Also presented in Table 7.5 is the average orientation angle ( $\theta$ ), see Equation 7.7, at each sustained load level.

The calculated orientation factors ( $\alpha$ ) in Table 7.5 are significantly higher, between 9.3 % and 38.3 %, than the theoretical value of the orientation factor for a 2D isotropic random distribution, i.e.  $2/\pi \approx 0.637$ . There is thus a clear preferential orientation of the fibres at the crack plane, as the orientation factors calculated (Table 7.5) lay within the theoretical values for a 2D ( $\approx 0.637$ ) and 1D (1.0) uniform isotropic distribution.

Table 7.5. Calculated average orientation factor ( $\alpha$ ) and average orientation angle ( $\theta$ ) at various sustained load levels

Load Level	$N_f$	$\alpha$	$\theta$ [°]
30%	44.33	0.881	28.19
50%	43.33	0.861	30.52
70%	35.00	0.696	45.91
85%	40.67	0.808	36.05

In Chapter 5 the effect of fibre embedment inclination angle on the single fibre pull-out creep was investigated. The results showed that the pull-out creep at a sustained load level of 50 % of the maximum pull-out force is almost the same for fibre embedment inclination angles up to 60°. However, as mentioned in Section 5.2.2.2 the maximum pull-out force increased with the fibre embedment inclination angle. This implied that the pull-out creep would decrease with the increase in fibre embedment inclination angle if the same sustained load was considered for each inclination angle. To incorporate this behaviour into the GCM it was assumed that the single fibre pull-out creep is indirectly proportional to the increased pull-out force factor ( $\zeta$ ). Thus, from Equation 7.1 and the aforementioned assumption the crack width opening due to pull-out creep ( $w_{creep,\theta}$ ) of a fibre orientated at an angle of  $\theta$  relative to the orthogonal axis of the crack plane is as follow:

$$w_{creep,\theta}(t) = \frac{2 \cdot s_{creep}(t)}{\xi} \quad (7.8)$$

If it is assumed that all the fibres bridging the crack plane have a fibre orientation angle of  $\theta$ , then Equation 7.8 can be substituted into Equation 7.4. Thus, the  $CMOD_{sus}$  at a generic time instance,  $t$ , is determined as follow:

$$CMOD_{sus}(t) = \frac{w_{creep}(t)}{\xi} = \frac{2 \cdot s_{creep}(t)}{\xi} \quad (7.9)$$

This implies that the OGCM is based on the assumption that the behaviour of the  $CMOD_{sus}$  with and average fibre orientation angle of  $\theta$  at the crack plane is the same as the crack width

opening due to pull-out creep ( $w_{creep,\theta}$ ) of a single fibre crossing the crack plane at an angle of  $\theta$ .

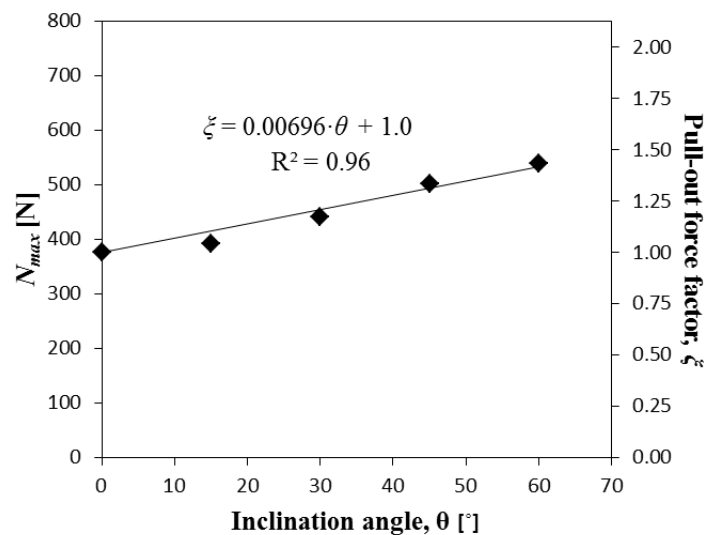
The pull-out force factor ( $\xi$ ) is determined as follow:

$$\xi = \frac{N_{max,\theta}}{N_{max,0^\circ}} \quad (7.10)$$

where  $N_{max,\theta}$  and  $N_{max,0^\circ}$  are the maximum single fibre pull-out force at an fibre embedment inclination angle of  $\theta$  and  $0^\circ$ , respectively. Table 7.6 presents the calculated pull-out force factors ( $\xi$ ) for the results presented in Table 5.3. Figure 7.9 presents a linear regression model that describes the pull-out force factor ( $\xi$ ) with a coefficient of determination ( $R^2$ ) of 0.96.

*Table 7.6. Calculated pull-out force factors ( $\xi$ ) at various fibre embedment inclination angels ( $\theta$ )*

$\theta$ [°]	Nmax [N]	$\xi$
0	375.8	1.000
15	392.6	1.045
30	440.8	1.173
45	501.0	1.333
60	539.1	1.435



*Figure 7.9. Linear regression model for the pull-out force factor*

In Table 7.7 the pull-out force factors for the macroscopic sustained load tests are presented. These values were determined with the regression model presented in Figure 7.9 and by adopting the predicted average crack plane fibre orientation angles presented in Table 7.5.

Table 7.7. The calculated pull-out factors for the macroscopic sustained load tests

Load Level	$\theta$ [°]	$\xi$
30%	28.19	1.196
50%	30.52	1.212
70%	45.91	1.320
85%	36.05	1.251

### 7.3.1 Experimental validation

The  $CMOD_{sus}$  simulated by the OGCM is presented in Figure 7.10. In Figure 7.11 the results are scaled logarithmically on the abscissa axis. The material and non-linear parameters for the constitutive pull-out creep model ( $s_{creep}(t)$ ) implemented in the OGCM (Equation 7.9) are presented in Table 7.4 and Table 6.4, respectively. The pull-out load factor ( $\xi$ ) adopted at each load level is presented in Table 7.7.

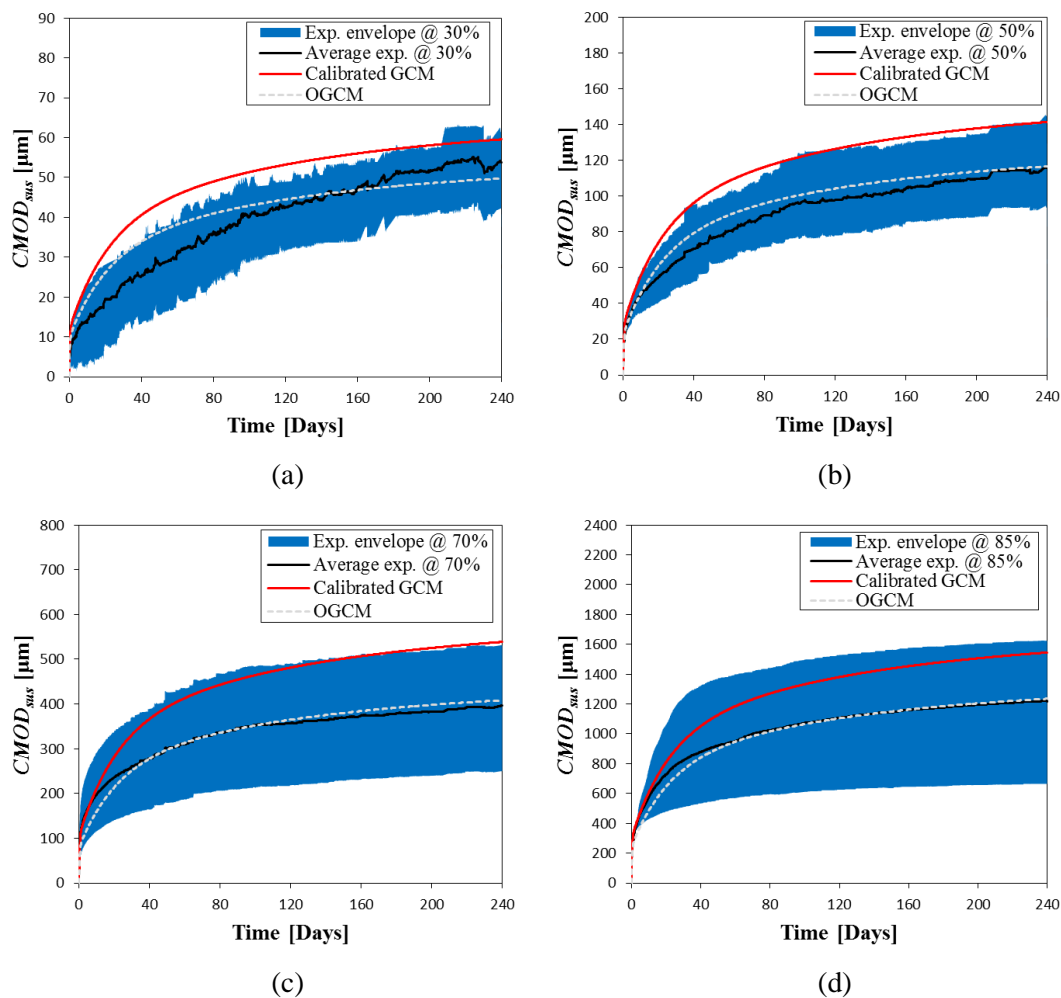


Figure 7.10. Simulated  $CMOD_{sus}$  behaviour with generalised constitutive model (GCM) and oriented generalised constitutive model (OGCM) at various sustained load levels: (a) 30 %, (b) 50 %, (c) 70 % and (d) 85 %

From Figures 7.10 and 7.11 it is evident that the OGCM is the most accurate model for predicting the  $CMOD_{sus}$ . To investigate the suitability of the OGCM in detail, the average experimental and modelled  $CMOD_{sus}$  are plotted against the sustained load level after 1 day, 30 days, 100 days and 240 days (see Figure 7.12). The calculated normalised errors ( $\bar{\epsilon}$ ) are presented in Table 7.8, see Equation 7.5.

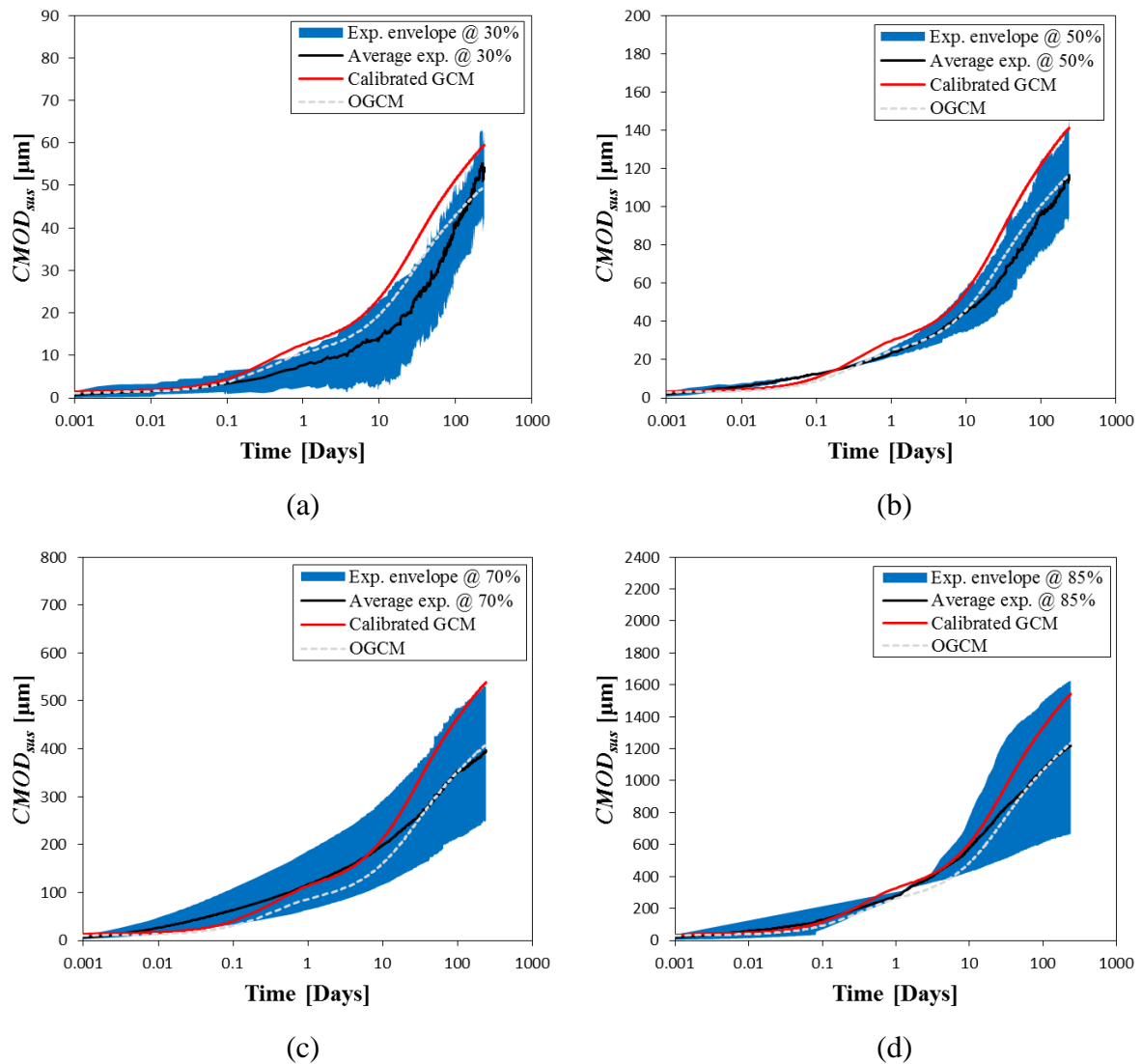


Figure 7.11. Semi-logarithmic plots of generalised constitutive model (GCM) and oriented generalised constitutive model (OGCM) simulations at various sustained load levels: (a) 30 %, (b) 50 %, (c) 70 % and (d) 85 %

Overall the calculated normalised errors ( $\bar{\epsilon}$ ) presented in Table 7.8 are relatively low. However, the OGCM significantly deviated at certain points from the average experimental results. Nevertheless, the OGCM simulated the  $CMOD_{sus}$  within the boundary of the experimental envelope.

Through the observation of Figures 7.10 to 7.12 it is possible to conclude that the proposed OGCM is capable of predicting the  $CMOD_{sus}$  behaviour of cracked SFRC with TYPE A hooked-ends with reasonable accuracy.

Table 7.8. Calculated normalised errors at each load level after certain generic time instances for the oriented generalised constitutive model (OGCM)

Load level [%]	1 day			30 days			100 days			240 days		
	Exp. [ $\mu\text{m}$ ]	OGCM [ $\mu\text{m}$ ]	$\bar{e}$ [%]	Exp. [ $\mu\text{m}$ ]	OGCM [ $\mu\text{m}$ ]	$\bar{e}$ [%]	Exp. [ $\mu\text{m}$ ]	OGCM [ $\mu\text{m}$ ]	$\bar{e}$ [%]	Exp. [ $\mu\text{m}$ ]	OGCM [ $\mu\text{m}$ ]	$\bar{e}$ [%]
30	8	11	37.5	23	31	32.0	40	43	7.1	54	50	7.5
50	23	25	5.0	64	72	13.0	96	101	4.9	116	117	0.8
70	117	86	25.9	261	251	3.5	352	352	0.1	396	408	3.0
85	278	261	5.9	823	761	7.6	1072	1065	0.7	1219	1235	1.4

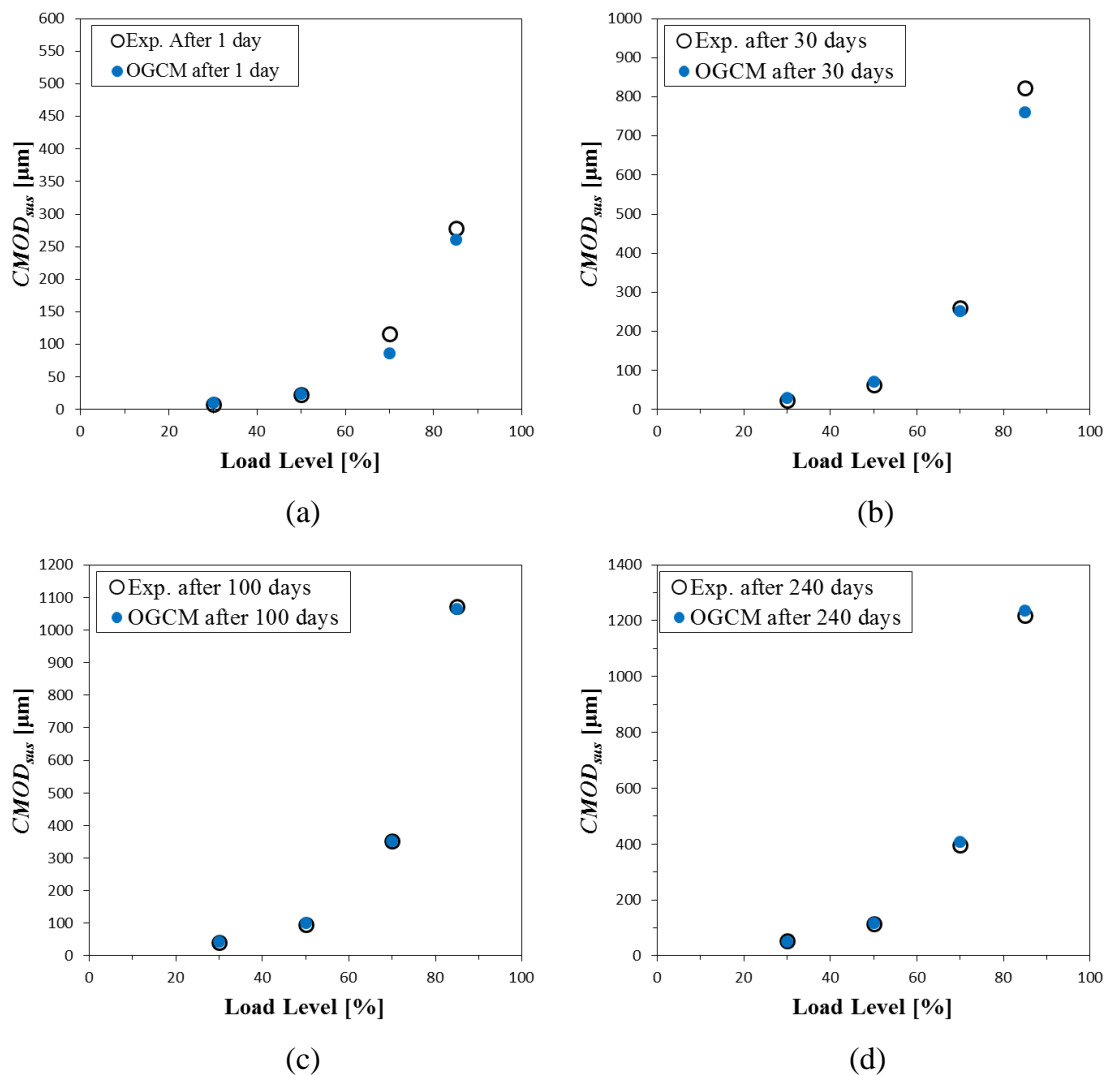


Figure 7.12. The average experimental and oriented generalised constitutive model (OGCM)  $CMOD_{sus}$  at each load level after: (a) 1 day, (b) 30 days, (c) 100 days and (d) 240 days

---

## 7.4 Concluding summary

This chapter presented the development of a constitutive model for predicting the  $CMOD_{sus}$  behaviour of cracked SFRC by combining Chapters 4, 5 and 6.

The pull-out creep behaviour was emphasised as the principle mechanism causing the  $CMOD_{sus}$ . A constitutive model was proposed in Chapter 6 based on the theory of rheology to predict the single fibre pull-out creep behaviour. This model was generalised to a macroscopic level by assuming a uniform fibre distribution over the crack plane. Assumptions regarding the emphasised factors that affect the pull-out creep behaviour were made to simplify the generalised constitutive model (GCM). The orientation of the fibres at the crack plane was emphasised as a relevant factor that affects the  $CMOD_{sus}$  behaviour. A method was proposed to incorporate the orientation of the fibres at the crack plane into the GCM. Finally, the macroscopic sustained load tests on cracked SFRC reported in Chapter 4 were considered for validation purposes. A reasonable agreement with the  $CMOD_{sus}$  behaviour predicted by the oriented generalised constitutive model (OGCM) was observed.

# Chapter 8

---

## Conclusions and Recommendations

### 8.1 Conclusions

In this research project the time-dependent behaviour of cracked SFRC under sustained uni-axial tensile loading was investigated. The major contribution of the study is a model which predicts the crack width opening of steel fibre reinforced composite concrete material over time by considering the behaviour at a single fibre level.

A comprehensive study at the single fibre level has been performed in order to identify the mechanisms involved during the time-dependent crack width opening and to investigate the factors that affect it. A constitutive model that predicts the time-dependent single fibre pull-out behaviour was developed. This model was generalised to predict the macroscopic time-dependent behaviour of cracked SFRC under sustained uni-axial tensile loading.

The conclusions drawn from the work presented in this dissertation are presented in the following sections.

#### 8.1.1 Macroscopic Level

- The sustained uni-axial tensile response of cracked SFRC is dependent on the applied load level, i.e. the crack mouth opening displacement due to sustained loading ( $CMOD_{sus}$ ) increased with the applied sustained load level. None of the specimens



tested fractured during the measured period of 240 days, even for load levels as high as 85 % of the residual strength of the specimen.

- As the applied load level was increased the  $CMOD_{sus}$  rate increased at a decreasing rate. However, it was shown that the percentage decrease in the  $CMOD_{sus}$  rate increased with the applied load level. It was found that after 240 days the  $CMOD_{sus}$  has not yet reached an asymptotic value for applied load levels up to 85 % of the residual strength of the specimen.
- Detailed analyses of the results revealed that at a certain time instance the  $CMOD_{sus}$  increased linearly up to a sustained load level of 50 % and for higher load levels the increase is non-linear.
- After 240 days the average  $CMOD_{sus}$  at a 30 % load level increased by 91.2 % relative to the average instantaneous crack mouth opening displacement ( $CMOD_{ins}$ ). The increase is more than twice the magnitude of the  $CMOD_{ins}$  for a load level of 85 %.
- The crack plane fibre count for each specimen is considered as a possible reason for the variability on the behaviour of the  $CMOD_{sus}$  within a specific load level, i.e. the higher the fibre count on a crack plane the lower  $CMOD_{sus}$  and vice versa.

## 8.1.2 Single Fibre Level

### 8.1.2.1 Quasi-static single fibre pull-out tests

- Straight steel fibres showed insignificant rate sensitivity for pull-out rates ranging from 0.00025 mm/s – 2.5 mm/s. However, TYPE A hooked-end steel fibres showed rate sensitivity for the slip at maximum pull-out force. This behaviour is induced by the interface between the mechanical end anchorage of the fibre and the matrix.
- The embedment length does not significantly influence the pull-out behaviour of TYPE A hooked-end steel fibres. However, this is only valid if the embedment length is greater than the length of the hooked-end.
- The fibre embedment inclination angle significantly influenced the pull-out behaviour of TYPE A hooked-end steel fibres. The increase in frictional resistance, matrix spalling and deformation of the fibre at the bending point of the fibre were the dominating mechanisms during the pull-out behaviour of inclined fibres.
- The geometry of the hooked-end of the fibre significantly influenced the pull-out behaviour. By increasing the amount of kinks in the hooked-end of the fibre, the pull-

---

out behaviour was significantly improved. Also for hooked-end fibres the mechanical bond is the principle mechanism that controls the pull-out behaviour.

### 8.1.2.2 Single fibre sustained load tests

- The sustained load tests showed that the pull-out creep is related to the applied load. The pull-out creep increases linearly up to a load level of 50 % of the average maximum pull-out force. For higher sustained load levels the pull-out creep increases exponentially. It is believed that the pull-out creep is dominated by the same mechanisms as for the creep in bulk normal concrete. However, CT scans showed that the non-linear pull-out creep behaviour is due to the increase in micro-cracking damage mechanism. It is concluded that the fibre pull-out creep is one of the principle mechanisms involved during the time-dependent crack width opening.
- The magnitude of the pull-out creep behaviour showed to be similar for fibre inclination angles ranging from 0° to 60°. The applied load level to each fibre inclination angle was 50 % of the average maximum pull-out force. It was thus conceived that an applied load of the same magnitude subjected to each fibre inclination angle will result in a decrease in the pull-out creep for the tested fibre inclination angle range.
- The geometry of the mechanical hooked-end mechanism significantly influenced the pull-out creep behaviour. The pull-out creep increased with the amount of kinks in the hooked-end. This increase is due to a combination of two factors. Firstly, the applied sustained load increased with the amount of kinks, i.e. 50 % of the average maximum pull-out force. Secondly, the area of the surrounding concrete matrix at the zone of the hooked-end that is subjected to a localised compressive sustained load increases with the amount of kinks, thus resulting in an increase in the pull-out creep with the amount of kinks. However, it was proven that when the applied sustained load to each fibre type is of the same magnitude the pull-out creep decreased with the amount of kinks in the hooked-end. However, using fibre with more kinks will probably result in increased pull-out creep as fewer fibres are then typically used.
- The pull-out creep behaviour is significantly affected by the pre-damaging process at time instances younger than 10 days. However, for time instances older than 10 days the pull-out creep behaviour between the undamaged specimen and pre-damaged specimen is similar.

### 8.1.3 Single Fibre Pull-out Creep Modelling

- The proposed constitutive pull-out creep model predicted the pull-out creep behaviour with high accuracy. The pull-out creep behaviour up to a load level of 50 % was successfully modelled with a linear visco-elastic model. The non-linear pull-out creep behaviour is incorporated successfully with a non-linear factor.
- The proposed time-dependent pull-out model included the constitutive pull-out creep model. This model was used to validate the calibrated material and non-linear parameters of the constitutive pull-out creep model by simulating the pull-out rate effect, i.e. the slip at maximum pull-out force. The constitutive pull-out creep model simulated the rate effect with relative high accuracy. This provided evidence that the proposed constitutive pull-out creep model is suitable for predicting the pull-out creep behaviour.

### 8.1.4 Time-dependent Modelling of Cracked SFRC

- The constitutive pull-out creep model was generalised to simulate the macroscopic  $CMOD_{sus}$  behaviour. The constitutive pull-out creep model was implemented within the proposed generalised constitutive model (GCM) by adopting the calibrated material parameters and non-linear parameters that describe the single fibre pull-out creep behaviour.
- The material parameters calibrated with the pull-out creep results were not suitable to predict the  $CMOD_{sus}$  behaviour. This was a consequence of the pre-cracking process of the specimens. As the specimens are pre-cracked the localised interface at the zone of the hook for the fibres at the crack plane is damaged. The single fibre pull-out creep results performed on pre-damaged specimens showed that the pull-out creep behaviour is significantly different from those that were not pre-damaged. The material parameters were thus calibrated with the pre-damaged pull-out creep results.
- It was emphasised that the orientation of the fibres significantly influence the  $CMOD_{sus}$  behaviour. This was also confirmed on a single fibre level. A method was proposed to incorporate the orientation of the fibres at the crack plane into the GCM.
- The simulated  $CMOD_{sus}$  behaviour predicted by the oriented generalised constitutive model (OGCM) showed a reasonable agreement with the experimental results at each load level.

---

## 8.2 Recommendations

Based on the insight gained during the course of the research described in this dissertation the following aspects are recommended for further investigation.

- It was mentioned in Chapter 4 that the test machine used to perform the uni-axial tensile and pre-cracking tests of the macroscopic specimens has a slow reaction time, which resulted in an inadequate amount of data points measured during the cracking phase. Thus the calculated fracture energy, which is the area under the  $\sigma$ - $w$  graph, is deceptive. To get a stable crack growth for uni-axial tensile and pre-cracking tests a closed loop machine with a fast reaction time needs to be used. This will render the true tensile material parameters.
- The fibre count on the crack plane has been identified as one of the factors causing the significant variability observed in the uni-axial tensile sustained load results. It is anticipated that the orientations and distribution of the fibres on the crack plane could also have some influence on the results. It would be worthy to conduct an investigation on what the effect of these factors are on the  $CMOD_{sus}$ .
- Single fibre sustained load tests were performed on undamaged specimens. However, in Chapter 5 it was shown that the pull-out creep behaviour of pre-damaged specimens is different from those that are undamaged. In Chapter 7 it was shown that the pre-damaged pull-out creep behaviour is more suitable for representing the behaviour of a single fibre at the crack plane. It would therefore be advised for future studies in this field to perform single fibre sustained load tests on pre-damage specimens.
- In Chapter 7 it was assumed that the non-linear pull-out creep rate of the pre-damaged single fibre specimens is the same as the undamaged specimens. This implies that the parameters of the non-linear factor that describes the non-linear behaviour are the same for the undamaged and pre-damaged specimens. It is recommended that this hypothesis be tested by conducting a comprehensive comparative study between the non-linear pull-out creep behaviour of undamaged and pre-damaged specimens. The understanding of the model would also be improved if some physical meaning could be attributed to the parameters that describe the non-linear behaviour of the material.
- The constitutive model proposed in Chapter 7 which predicts the  $CMOD_{sus}$  of cracked SFRC needs to be extended so that it can predict the flexural behaviour. This will

require a comparative study between the behaviour of flexural and uni-axial tensile time-dependent CMOD.

# References

---

RILEM TC 162-TDF, 2001. Test and design methods for steel fibre reinforced concrete: uniaxial tension test for steel fibre reinforced concrete. *Materials and Structures*, Volume 34, pp. 3-6.

Abrishambaf, A., Barros, J. & Cunha, V., 2015. Tensile stress-crack width law for steel fibre reinforced self-compacting concrete obtained from indirect (splitting) tensile tests. *Cement & concrete composites*, Volume 57, pp. 153-165.

Abrishambaf, A., Barros, J. & Cunha, V., 2015. Time-dependent flexural behaviour of cracked steel fibre reinforced self-compacting concrete panels. *Cement and Concrete Research*, Volume 72, pp. 21-36.

Abu-Lebdeh, T., Hamoush, S. & Zornig, B., 2010. Rate Effect on Pullout Behavior of Steel Fibers Embedded in Very-High Strength Concrete. *American Journal of Engineering and Applied Sciences*, 3(2), pp. 454-463.

Adam, I. & Taha, M., 2011. Identifying the Significance of Factors Affecting Creep of Concrete: nA Probabilistic Analysis of RILEM Database. *International Journal of Concrete Structures and Materials*, 5(2), pp. 97-111.

- 
- Alani, A. & Aboutalebi, M., 2013. Mechanical properties of fibre reinforced concrete - A comparative experimental study. *International Journal of Civil, Structural, construction and Architectural Engineering*, 7(9), pp. 203-208.
- Alexander, M. & Beushausen, H., 2009. Deformation and Volume Change of Hardened Concrete. In: G. Owens, ed. *Fulton's concrete technology*. 9th ed. Midrand, South Africa: Cement & Concrete Institute, pp. 111-144.
- Altoubat, S. & Lange, D., 2003. A New Look at Tensile Creep of Fiber Reinforced Concrete. *ACI Special Publications on Fiber Reinforced Concrete*, pp. 143-160.
- Alwan, J., Naaman, A. & Guerrero, P., 1999. Effect of Mechanical Clamping on the Pull-Out Response of Hooked Steel Fibers Embedded in Cementitious Matrices. *Concrete Science and Engineering RILEM*, 1(1), pp. 15-25.
- Arango, S., Taengua, E., Vargas, J. & Ros, P., 2012. *A Comprehensive Study on the Effect of Fibers and Loading on Flexural Creep of SFRC*. Minho, RILEM Publications.
- ASTM C496, 2004. Standard test method for splitting tensile strength of cylindrical concrete specimens. *Annual Book of ASTM Standards: American Society of Testing Materials*.
- Atrushi, D. S., 2003. *Tensile and Compressive Creep of Early Age Concrete: Testing and Modelling*, The Norwegian University of Science and Technology, Trondheim: Unpublished PhD thesis.
- Aveston, J., Mercer, R. & Sillwood, J., 1974. *Fibre-Reinforced Cements - Scientific Foundations for Specifications*. Teddington, National Physical Laboratory, pp. 9-16.
- Babafemi, A., 2015. *Tensile creep of cracked macro synthetic fibre reinforced concrete*, Stellenbosch University Faculty of Engineering, Stellenbosch: Unpublished PhD thesis.
- Babafemi, A. & Boshoff, W., 2015. Tensile creep of macro-synthetic fibre reinforced concrete (MSFRC) under uni-axial tensile loading. *Cement & Concrete Composites*, Volume 55, pp. 62-69.
- Babafemi, A. & Boshoff, W., 2015. Tensile creep of macro-synthetic fibre reinforced concrete (MSFRC) under uni-axial tensile loading. *Cement & Concrete Composites*, Volume 55, pp. 62-69.

- 
- Banthia, N., 1990. Study of Some Factors Affecting the Fibre-Matrix Bond in Steel Fibre Reinforced Concrete. *Canadian Journal of Civil Engineering*, 17(4), pp. 610-620.
- Banthia, N., Chokri, K., Ohama, Y. & Mindess, S., 1993. Fiber-Reinforced Cement Based Composites Under Tensile Impact. *Advanced Cement Based Materials*, Volume 1, pp. 131-141.
- Banthia, N., Mindess, S. & Trottier, J.-., 1996. Impact Resistance of Steel Fiber Reinforced Concrete. *ACI Materials Journal*, 93(5), pp. 472-479.
- Banthia, N. & Trottier, J., 1989a. Effects of Curing Temperature and Early Freezing on Pull-out Resistance of Steel Fibers from a Cementitious Matrix. *Cement and Concrete Research*, 19(5), pp. 727--736.
- Banthia, N. & Trottier, J., 1989b. Effects of curing temperature and early freezing on the pullout behaviour of steel fibres. *Cement and Concrete* , 19(3), pp. 400-410.
- Banthia, N. & Trottier, J.-F., 1991. Deformed Steel Fiber-Cementitious Bond Under Impact. *Cement and Concrete Research*, Volume 21, pp. 158-168.
- Banthia, N. & Trottier, J., 1994. Concrete Reinforced with Deformed Steel Fibres, Part I: Bond-slip Mechanisms. *ACI Materials Journal*, 91(5), pp. 435-446.
- Banthia, N. & Trottier, J., 1995. Test methods for flexural toughness characterization of fiber reinforced concrete: Some concerns and a proposition. *ACI Materials Journal*, 92(1), pp. 48-57.
- Barragan, B., Gettu, R., Martin, M. & L, Z. R., 2003. Uniaxial tension test for steel reinforced concrete-a parametric study. *Cement & Concrete composites*, Volume 25, pp. 767-77.
- Barragan, B. & Zerbino, R., 2008. *Creep behaviour of cracked steel fibre reinforced concrete beams*. Chennai, Proceedings of the 7th International RILEM Symposium on Fibre Reinforced Concrete: Design and Applications (BEFIB 2008), pp. 577-586.
- Barros, J., Cunha, V., Ribeiro, A. & Antunes, J., 2005. Post-cracking Behaviour of Steel Fibre Reinforced Concrete. *Materials and Structures*, Volume 38, pp. 47-56.
- Barros, J. & Figueiras, J. A., 1999. Flexural Behavior of SFRC: Testing and Modeling. *Journal of Materials in Civil Engineering*, 11(4), pp. 331-339.



- Bartos, P. & Duris, M., 1994. Inclined tensile strength of steel fibres in cement-based composites. *Composites*, 25(10), pp. 945-952.
- Bayramov, F., Tasdemir, C. & Tasdemir, M., 2004. Optimisation of Steel Fibre Reinforced Concretes by means of Statistical Response Surface Method. *Cement and Concrete Composites*, Volume 26, pp. 665-675.
- Benboudjema, F., Meftah, F. & Torrenti, J., 2003. An Unified Approach for the Modeling of Drying Shrinkage and Basic Creep of Concrete: analysis of intrinsic behaviour and structural effects. *Computational Modelling of Concrete Structures*, pp. 391-400.
- Benboudjema, F., Meftah, F., Torrenti, J. & Heinfling, 2001. *A Basic Creep Model for Concrete Subjected to Multiaxial Loads*. Cachan, France, s.n., pp. 161-168.
- Bencardino, F., 2014. Effects of fibre volume fraction on the compressive and flexural experimental behaviour of SFRC. *Contemporary Engineering Sciences*, 7(8), pp. 379-390.
- Bencardino, F., Rizzuti, L., Spadea, G. & Swamy, R., 2008. Stress-strain behavior of steel fiber-reinforced concrete in compression. *Journal of Materials in Civil Engineering*, 20(3), pp. 255-263.
- Bencardino, F., Rizzuti, L., Spadea, G. & Swamy, R., 2013. Implications of test methodology on post-cracking and fracture behaviour of steel fibre reinforced concrete. *Composites: Part B*, Volume 46, pp. 31-38.
- Bentur, A. & Mindess, S., 1990. *Fibre reinforced cementitious composites*. London: Elsevier Applied Science.
- Bentur, A. & Mindess, S., 2007. *Fibre Reinforced Cementitious Composites*. 2nd ed. London: Taylor and Francis.
- Bissonnette, B. & Pigeon, M., 1995. Tensile creep at early ages of ordinary, silica fume fiber reinforced concretes. *Cement and Concrete Research*, 25(5), pp. 1075-1085.
- Bissonnette, B., Pigeon, M. & Vaysburd, A., 2007. Tensile creep of concrete: study of its sensitivity to basic parameters. *ACI Material Journal*, 104(4), pp. 360-368.
- Blanco, A., 2013. *Characterization and modelling of SFRC elements*, Barcelona, Spain: Unpublished Doctoral dissertation.

- 
- Boshoff, W. & Adendorff, C., 2013. Effect of sustained tensile loading on SHCC crack widths. *Cement and Concrete Composites*, Volume 37, pp. 119-125.
- Boshoff, W., Mechtcherine, V. & van Zijl, G., 2009a. Characterising the Time-Dependant Behaviour on the Single Fibre Level of SHCC: Part 1: Mechanism of fibre pull-out creep. *Cement and Concrete Research*, Volume 39, pp. 779-786.
- Boshoff, W., Mechtcherine, V. & Zijl, G., 2009b. Characterising the Time-dependant Behaviour on the Single Fibre Level of SHCC: Part 2: The Rate Effects on Fibre Pull-out Tests. *Cement and Concrete Research*, Volume 39, pp. 787-797.
- Boshoff, W. P., 2007. *Time-Dependant Behaviour of Engineered Cement-Based composites*, Stellenbosch: University of Stellenbosch, South Africa: Unpublished PhD thesis.
- Boshoff, W. P. & van Zijl, G. P., 2007. Time-Dependent Response of ECC: Charaterisation and Modelling of Creep and Creep Fracture. *Cement and Concrete Research*, 37(5), pp. 725-734.
- Boulekbache, B., Hamrat, M., Chemrouk, M. & Amziane, S., 2012. Influence of yield stress and compressive strength on direct shear behaviour of steel fibre-reinforced concrete. *Construction and Building Materials*, Volume 27, pp. 6-14.
- Brandt, A. M., 2008. Fibre Reinforced Cement-based (FRC) Composites after over 40 years of Development in Building and Civil Engineering. *Composites Structures*, 86(1-3), pp. 3-9.
- BS EN 12350-2, 2000. *Testing fresh concrete-Slump test*. London, UK: British standard Institution.
- BS EN 12390-3, 2002. *Testing hardened concrete-compressive strength of test specimens*. London: British Standard Institution.
- Buil, M. & Acker, P., 1985. Creep of a Silica Fume Concrete. *Cement and Concrete Research*, Volume 15, pp. 463-466.
- Burakiewicz, A., 1996. Testing of Fibre Bond Strength in Cement Matrix. *RILEM International Symposium on Testing and Test Methos of Fibre Cement Composites*, pp. 355-365.

- 
- Buratti, N. & Mazzotti, C., 2012a. *Effects of different types and dosages of fibres on the long-term behaviour of fibre-reinforced self-compacting concrete*. Guimaraes, Portugal, 8th RILEM international symposium on fiber reinforced concrete BEFIB 2012, pp. 726-738.
- Buratti, N. & Mazzotti, C., 2012b. *Temperature effect on the long-term behaviour of macro-synthetic-and-steel-fibre reinforced concrete*. Guimaraes, Portugal, 8th RILEM international symposium on fiber reinforced concrete BEFIB 2012, pp. 715-725.
- Buratti, N., Mazzotti, C. & Savoia, M., 2011. Post-cracking behaviour of steel and macro-synthetic fibre-reinforced concretes. *Construction and Building Materials*, Volume 25, pp. 2713-2722.
- Buyukozturk, O. & Hearing, B., 1998. Crack Propagation in Concrete Composites Influenced by Interface Fracture Parameter. *International Journal of Solids and Structures*, 35(31-32), pp. 4055-4066.
- Chanvillard, G. & Aitcin, P.-C., 1996. Pull-out Behaviour of Corrugated Steel Fibres. *Advanced Cement Based Materials*, Volume 4, pp. 28-41.
- Chanvillard, G., Banthia, N. & Aitcin, P.-C., 1990. Normalized Load-Deflection Curves for Fibre Reinforced Concrete under Flexure. *Cement and Concrete Composites*, 12(1), pp. 41-45.
- Chanvillard, G. & Roque, O., 1999. *Behaviour of fibre reinforced concrete cracked section under sustained load*. Mainz, Germany, Proceedings of the 3rd International Workshop on High Performance Fiber Reinforced Cement Composites, pp. 239-250.
- Chen, B. & Liu, J., 2005. Contribution of hybrid fibers on the properties of high-strength lightweight concrete having good workability. *Cement and Concrete Research*, Volume 35, pp. 913-917.
- Chern, J.-C. & Chan, Y.-W., 1989. Deformations of Concretes Made With Blast-Furnace Slag Cement and Ordinary Portland Cement. *ACI Materials Journal*, 86(4), pp. 372-382.
- Chong, K. T., 2004. *Numerical Modelling of Time-dependant Cracking and Deformation of Reinforced Concrete Structures*, The University of New South Wales, Sydney, Australia: Unpublished PhD thesis.

- 
- Cigna, R. et al., 2003. *Corrosion of steel in reinforced concrete structures*, Italy: European Communities.
- CSIR, 1988. *The influence of low temperatures on the properties of OPC, FA concretes*, Pretoria: CSIR.
- Cunha, V., 2010. *Steel fiber reinforced self-compacting concrete (from micro-mechanics to composite behaviour)*, University of Minho, Portugal: Unpublished PhD thesis.
- Cunha, V. M., Barros, J. A. & Sena-Cruz, J. M., 2010. Pullout Behavior of Steel Fibers in Self-Compacting Concrete. *Journal of Materials in Civil Engineering*, 22(1), pp. 1-9.
- Darwin, D., Barham, S., Kozul, R. & Luan, S., 2001. Fracture Energy of High-Strength Concrete. *ACI Materials Journal*, 98(5), pp. 410-417.
- Davis, R. & Davis, H., 1931. Flow of Concrete under the Action of Sustained Loads. *ACI Journal*, Volume 27, p. 837.
- de Oliveira, F., 2010. *Design-oriented constitutive model for steel fiber reinforced concrete*, Spain, Barcelona: Unpublished PhD Thesis.
- Desarmot, G. & Favre, J., 1991. Advances in Pull-out testing and Data Analysis. *Composites Science and Technology*, 42(1-3), pp. 151-187.
- Dhakal, R., Wang, C. & Mander, J., 2005. *Behavior of Steel Fibre Reinforced Concrete in Compression*. Christchurch, University of Canterbury. Civil and Natural Resources Engineering.
- Diamond, S. & Huang, J., 2001. The ITZ in concrete - a different view based on image analysis and SEM observations. *Cement and Concrete Composites*, 23((2-3)), pp. 179-188.
- Ding, Y., 2011. Investigations into the relationship between deflection and crack mouth opening displacement of SFRC beam. *Construction and Building Materials*, Volume 25, pp. 2432-2440.
- Dupont, D., 2003. *Modelling and Experimental Validation of the Constitutive Law and Cracking Behaviour of Steel Fibre Reinforced Concrete*, Catholic University of Leuven, Heverlee, Belgium: PhD thesis.

- 
- Ezeldin, A. & Balaguru, P., 1992. Normal and High-Strength Fiber Reinforced Concrete under Compression. *Journal of Materials in Civil Engineering*, 4(4), pp. 415-429.
- Fanella, D. & Naaman, A., 1985. Stress-Strain Properties of Fiber Reinforced Mortar in Compression. *ACI Journal*, 82(4), pp. 475-483.
- Fantilli, A. P., Mihashi, H. & Vallini, P., 2009. Multiple Cracking and Strain Hardening in Fiber-Reinforced Concrete under Uniaxial Tension. *Cement and Concrete Research*, 39(12), pp. 1217-1229.
- fib Special Activity Group 5, 2010. *fib Model Code 2010 First Complete Draft Volume 1*, Lausanne, Switzerland: International Federation for Structural Concrete (fib).
- Filho, R. & Sanjuan, M., 1999. Effect of low modulus sisal and polypropylene fiber on the restrained shrinkage of mortars at early age. *Cement and Concrete Research*, Volume 29, pp. 1597-1604.
- Focacci, F., Nanni, N., ASCE & Bakis, C., 2000. Local bond-slip relationship for FRP reinforcement in concrete. *Journal of Composites for Construction*, 4(1), pp. 24-31.
- Garacia-Taengua, E., Arango, S., Marti-Vargas, J. & Serna, P., 2014. Flexural creep of steel fiber reinforced concrete in cracked state. *Construction and Building Materials*, Volume 65, pp. 321-329.
- Garas, V., Kahn, L. & Kurtis, K., 2009. Short-term creep and shrinkage of ultra-high performance concrete. *Cement and Concrete Composites*, Volume 31, pp. 147-152.
- Ghoddousi, P., Ahmadi, R. & Sharifi, M., 2010. Fiber Pullout Model for Aligned hooked-end Steel Fiber. *Canadian Journal of Civil Engineering*, 37(9), pp. 1179-1188.
- Ghoddousi, P., Ghasemi, R. & Parhizkar, T., 2004. *Evaluation of Plastic Shrinkage in Concrete*. Singapore, CI-Premier PTE LTD.
- Giaccio, G. & Zerbino, R., 1997. Combined Effects of Coarse Aggregates and Strength Level. *Advanced Cement Based Materials*, 7(2), pp. 41-48.
- Gokoz, U. & Naaman, A., 1981. Effect of Strain-rate on the Pull-out Behaviour of fibres in mortar. *The International Journal of Cement Composites*, 3(3), pp. 187-202.

- 
- Gopalaratnam, V. & Abu-Mathkour, H., 1987. Investigation of the Pullout Characteristics of Steel Fibres from Mortar Matrices. *International Symposium on Fibre Reinforced Concrete*, pp. 201-211.
- Gopalaratnam, V. & Shah, S., 1987. Tensile Failure of Steel Fiber-Reinforced Mortar. *Journal of Engineering Mechanics*, 113(5), pp. 635-651.
- Gorbatkina, Y., 1992. *Adhesive Strength of Fiber-Polymer Systems*. New York: Ellis Horwood.
- Granju, J. et al., 2000. *Delayed behaviour of cracked SFRC beams*. Lyon, France, 5th RILEM Symposium on Fibre-Reinforced Concretes, pp. 511-520.
- Gray, R. & Johnston, C., 1984. Effect of matrix composition on fibre/matrix interfacial bond shear strength in fibre-reinforced mortar. *Cement and Concrete Research*, 14(2), pp. 285-296.
- Groth, P., 2000. *Fibre Reinforced Concrete-Fracture Mechanics Method Applied on Self-Compacting Concrete and Energetically Modified Binders*, Lulea University of Technology, Lulea, Sweden: Unpublished PhD thesis.
- Guerrero, P. & Naaman, A., 2000. Effect of mortar finess and adhesive agents on pullout response of steel fibers. *ACI Materials Journal*, 97(1), pp. 12-20.
- Gutsch, A. & Rostasy, F., 1994. Young concrete under high tensile stresses-creep, relaxation and cracking. In: R. Springenschmid, ed. *Thermal cracking in concrete at early age*. London, RILEM: E & FN Spon, pp. 111-118.
- Hannant, J., 1978. *Fibre cements and fibre concretes*. illustrated ed. the university of Michigan: Wiley.
- Hasanain, G., Khallaf, T. & Mahmood, K., 1989. Water Evaporation from Freshly placed Concrete in Hot Weather. *Cement and Concrete Research*, Volume 19, pp. 465-475.
- Holschemacher, K., Mueller, T. & Ribakov, Y., 2010. Effect of steel fibres on mechanical properties of high-strength concrete. *Materials and Design*, Volume 31, pp. 2604-2615.
- Holt, E. E., 2001. *Early Age Autogenous Shrinkage of Concrete*, University of Washington, Seattle: Unpublished PhD thesis.

- 
- Htut, T., 2010. *Fracture Processes in Steel Fibre Reinforced Concrete*, University of New South Wales, Sydney, Australia: Unpublished PhD thesis.
- Japan Concrete Institute, 1999. Technical Committee on Autogenous Shrinkage of Concrete "Committee Report". In: E. Tazawa & F. Spon, eds. *Autogenous Shrinkage of Concrete*. London: Japan Concrete Institute, pp. 1-62.
- Jarrat, R., 2011. *Construction of In-situ Cast Flat Slabs using Steel Fibre Reinforced Concrete*, University of Stellenbosch, Stellenbosch: Unpublished MSc thesis.
- Johansen, R. & Best, C., 1962. Creep of concrete with and without ice in the system. *RILEM Bulletin*, pp. 47-57.
- Kamen, A., Denarie, E., Sadouki, H. & Bruhwiler, E., 2009. UHPFRC Tensile Creep at early Age. *Materials and Structures*, Volume 42, pp. 113-122.
- Kameswara Rao, C., 1979. Effectiveness of random fibres in composites. *Cement and Concrete Research*, Volume 9, pp. 685-693.
- Kanakubo, T., 2006. Tensile characteristics evaluation method for ductile fiber-reinforced cementitious composites. *Journal of Advanced Concrete Technology*, Volume 4, pp. 3-17.
- Kanstad, T. & Zirgulis, G., 2012. *Long-Term Creep Testing of Pre-Cracked Fibre Reinforced Concrete Beams*. Minho, RILEM Publications.
- Kim, D., El-Tawil, S. & Naaman, A., 2008. Loading Rate Effect on Pullout Behavior of Deformed Steel Fibers. *ACI Materials Journal*, 105(6), pp. 576-584.
- Kooiman, A., 2000. *Modelling steel fibre reinforced concrete for structural design*, PhD Thesis: Delf University of Technology.
- Kormeling, H. & Reinhardt, H., 1987. Strain Rate Effects on Steel Fibre Concrete in Uniaxial tension. *The International Journal of Cement Composites and Lightweight Concrete*, 9(4), pp. 197-204.
- Kosmatka, S. & Panarese, W., 1988. *Design and Control of Concrete Mixtures*. 13th ed. Skokie: Portland Cement Association.
- Kovler, K., 1999. A New Look at The Problem of Drying Creep of Concrete under Tension. *Journal of Materials in Civil Engineering*, 11(1), pp. 84-87.



- Krenchel, H., 1975. *Fibre spacing and specific fibre surface*. Horneby, Lencaster, Rilem Symposium: Fibre Reinforced Cement and Concrete, pp. 69-79.
- Lim, T., Paramasivam, P. & Lee, S., 1988. Analytical Model for Tensile Behavior of Steel-Fiber Concrete. *ACI Materials Journal*, 84(4), pp. 286-298.
- Lim, T., Paramasivam, P. & Lee, S., 1988. Bending Behavior of Steel-Fiber Concrete Beams. *ACI Structural Journal*, 84(6), pp. 524-536.
- Li, V. & Maalej, M., 1996. Toughening in cement based composites. Part II: Fiber reinforced cementitious composites. *Cement & Concrete Composites*, Volume 18, pp. 239-249.
- Li, V. & Stang, H., 1997. Interface Property Characterization and Strengthening Mechanisms in Fiber Reinforced Cement Based Composites. *Advanced Cement Based Materials*, 6(1), pp. 1-20.
- Li, V., Stang, H. & Krenchel, H., 1993. Micromechanics of Crack Bridging in Fibre-Reinforced Concrete. *Materials and Structures*, Volume 26, pp. 486-494.
- Löfgren, I., (2005) *Fibre-reinforced concrete for industrial construction - a fracture mechanics approach to material testing and structural analysis*, Chalmers University of Technology, Goteborg, Sweden: Unpublished PhD thesis.
- Maage, M., 1977. Interaction between steel fibers and cement based matrixes. *Materiaux Et Constructions*, 10(59), pp. 297-301.
- Majumdar, A. & Nurse, R., 1974. Glass Fibre Reinforced Cement. *Materials Science and Engineering*, Volume 15, pp. 107-127.
- Mangat, P. & Azari, M., 1984. A theory for the free shrinkage of steel fibre reinforced cement matrices. *Journal of Materilas Science*, 19(7), pp. 2183-2194.
- Markovic, I., Walraven, J. & Van Mier, J., 2003. Experimental evaluation of fibre pullout from plain and fibre reinforced concrete. *Fourth International Workshop on High Performance Fibre Reinforced Cement Composites (HPFRCC 4)*, pp. 419-436.
- Marzouk, H., 1992. Effect of low temperature on the creep behaviour of high strength concrete. In: *Creep and shrinkage of concrete; effect of materials and environment*. Detroit: American Concrete Institute, pp. 51-64.



- Mehta, P. & Monteiro, J., 1993. *Concrete: Structure, Properties and Materials*. 2nd ed. New Jersey: Prentice Hall.
- Mendes, P., Barros, J., Goncalves, D. & Sena-Cruz, J., 2012. *Steel Fibre Reinforced Self-Compacting Concrete for Lightweight and Durable Pedestrian Bridges: Creep Behaviour*. Minho, RILEM Publications.
- Mindess, S., 1995. Fibre reinforced concrete: Challenges and prospects. In: N. Banthia & S. Mindess, eds. *Fiber reinforced concrete - Modern developments*. Toronto, Canada: The second University-Industry workshop on fiber reinforced concrete and other composites , pp. 1-11.
- Montaignac, R., Massicotte, B., Charron, J. & Nour, A., 2011. Design of SFRC structural elements: post-cracking tensile strength measurement. *Materials and Structures*, Volume 45, pp. 609-622.
- Morton, J. & Groves, G., 1974. The cracking of composites consisting of discontinuous ductile fibres in a brittle matrix- effect of fibre orientation. *Journall of Materials Science*, 9(9), pp. 1436-1445.
- Mouton, C. & Boshoff, W., 2012. Intial Study on the Tensile Creep of Cracked Steel Fibre Reinforced Concrete. *8th Rilem Symposium on Fibre Reinforced Concrete: Challenges and Opportunities (BEFIB 2012)*, 19-21 September.pp. 326-337.
- Mouton, C. J., 2012. *Investigating the Tensile Creep of Steel Fibre Reinforced Concrete*, Stellenbosch University, Stellenbosch, South Africa: Unpublised MSc thesis.
- Naaman, A., 2003. Engineered Steel Fibers with Optimal Properties for Reinforcement of Cement Composites. *Journal of Advanced Concrete Technology*, 1(3), pp. 241-252.
- Naaman, A. E., Moavenzadeh, F. & McGarry, F. J., 1974. Probabilistic Analysis of Fiber-Reinforced Concrete. *Journal of the Engineering Mechanics Division*, 100(2), pp. 397-413.
- Naaman, A. & Najm, H., 1991. Bond-slip Mechanisms of Steel Fibres in Concrete. *ACI Materials Journal*, 88(2), pp. 135-145.
- Naaman, A., Namur, G., Alwan, J. & Najm, H., 1991. Fiber Pullout and Dond Slip. I: Analytical Study. *Journal of Structural Engineering*, 117(9), pp. 2769-2790.

- 
- Naaman, A. & Shah, S., 1987. Pullout Mechanisms in Steel Fibre-Reinforced Concrete. *Journal of the Structural Division*, 102(8), pp. 1537-1548.
- Nairn, J., 2000. Analytical Fracture Mechanics Analysis of the Pull-out Test including the Effects of Friction and Thermal Stresses. *Advanced Composites Letters*, Volume 9, pp. 373-383.
- Nakov, D. & Markovski, G., 2012. *Time Dependant Behaviour of SFRC Elements under Sustained Loads*. Minho, RILEM Publications.
- Nataraja, M., Dhang, N. & Gupta, A., 1999. Stress Strain Curve for Steel-Fiber Reinforced Concrete under Compression. *Cement and Concrete Composites*, 21(5-6), pp. 383-390.
- Neville, A., 1970. *Creep of Concrete: Plain, reinforced and prestressed*. Amsterdam: North Holland publishing company.
- Neville, A., 1996. *Properties of Concrete*. 4th ed. New York, USA: John Wiley & Sons.
- NG, T., Htut, T. & Foster, S., 2012. *Fracture of Steel Fibre reinforced Concrete-The Unified Vairiable Engagement Model*, The University of New South Wales, Sydney, Australia: Unpublished report.
- Oh, B., Kim, J. & Choi, Y., 2007. Fracture behavior of concrete members reinforced with structural synthetic fibers. *Engineering Fracture Mechanics*, 74(1-2), pp. 243-257.
- Olivito, R. & Zuccarello, F., 2010. An experimental study on the tensile strength of steel fiber reinforced concrete. *Composites Part B: Engineering*, 41(3), pp. 246-255.
- Oslejs, J., 2008. New Frontiers for Steel Fiber-Reinforced Concrete. *Concrete International*, pp. 45-50.
- Ostergaard, L., Lange, D., Altoubat, S. & stang, H., 2001. Tensile basic creep of early-age concrete under constant load. *Cement and Concrete Research*, 31(12), pp. 1895-1899.
- Otsuka, K. & Date, H., 2000. Fracture Process Zone in Concrete Tension Specimens. *Enineering Fracture Mechanics*, 66(2-3), pp. 111-131.
- Ouyang, C., Pacios, A. & Shah, S., 1994. Pullout of Inclined Fibres From Cementitious Matrix. *Journal of Engineering Mechanics*, 120(12), pp. 2641-2659.

- 
- Ou, Y.-C., Tsai, M.-S., Liu, K.-Y. & Chang, K.-C., 2012. Compressive Behaviour of Steel-Fiber-Reinforced Concrete with a High Reinforcing Index. *Journal of Materials in Civil Engineering*, 24(2), pp. 207-215.
- Pakotiprapha, B., Pama, R. & Lee, S., 1983. Analysis of a Bamboo Fibre-Cement Past composite. *Journal of Ferrocement*, 8(2), pp. 141-159.
- Pelisser, F., Neto, B., Rovere, H. & R.C, P., 2010. Effect of the addition of synthetic fibers to concrete thin slabs. *construction and BUilding Materials*, Volume 24, pp. 2171-2176.
- Pickett, G., 1942. The effect of change in moisture-content on the creep of concrete under a sustained load. *Journal of the ACI*, Volume 38, pp. 333-355.
- Pinchin, D. & Tabor, D., 1987. Interfacial contact pressure and frictional stress transfer in steel fibre cement. In: R. Swamy, ed. *Proceedings of RILEM Conference Testing and Test Methods of Fibre-Cement Composites*. England: The Construction Press, pp. 337-344.
- Ram, S., Timusk, T. G. & Timusk, J., 1981. Creep of Fly Ash Concrete. *ACI Journal*, 78(5), pp. 351-357.
- RILEM TC162-TDF, 2000. Test and design methods for steel fibre reinforced concrete: bending test. *Materials and Structures*, Volume 33, pp. 75-81.
- Robins, P., Austin, S. & Jones, P., 2002. Pull-out behaviour of hooked steel fibres. *Materials and Structures*, August, Volume 35, pp. 434-442.
- Ross, A., 2009. Steel Fibre Reinforced Concrete (SFRC) - Quality, Performance and Specification. *Conference Paper New Zealand Concrete Conference 09*, p. 7.
- Rossi, P., 1992. Mechanical behaviour of metal-fibre reinforced concretes. *Cement & Concrete Composites*, Volume 14, pp. 3-16.
- Scheer, R. & Nairn, J., 1995. A Comparison of Several Fracture Mechanics Methods For Measuring Interfacial Toughness with Microbond Tests. *The Journal of Adhesion*, 53(1-2), pp. 45-68.
- Schlangen, E. & van Mier, J., 1992. Experimental and Numerical Analysis of Micromechanisms of Fracture of Cement-Based Composites. *Cement and Concrete Composites*, Volume 14, pp. 105-118.

- 
- Shah, S., 1992. Do fibers increase the tensile strength of cement-based matrixes?. *ACI Material Journal*, 88(6), pp. 595-602.
- Shah, S., Ouyang, C. & Swartz, S., 1995. *Fracture Mechanics of Concrete: Applications of fracture mechanics to concrete, rock, and other brittle materials*. New York: John Wiley and Sons.
- Skocek, J. & Stang, H., 2008. Inverse analysis of the wedge-splitting test. *Engineering Fracture Mechanics*, 75(10), pp. 3173-3188.
- Song, H. & Saraswathy, 2007. Corrosion monitoring of reinforced concrete structures - A review. *International Journal of Electrochemical Science*, Volume 2, pp. 1-28.
- Soranakom, C. & Mobasher, B., 2007. Closed-form moment-curvature. *ACI Materials Journal*, Volume 104-M39, pp. 351-359.
- Soranakom, C. & Mobasher, B., 2007. Closed-form solutions for flexural response of Fibre-reinforced concrete beams. *Journal of Engineering Mechanics*, 133(8), pp. 933-941.
- Soranakom, C. & Mobasher, B., 2008. Correlation of Tensile and Flexural Response of Strain Softening and Strain Hardening Cement Composites. *cement and Concrete Composites*, Volume 30, pp. 465-477.
- Soroushian, P. & Bayasi, Z., 1991. Fiber-Type Effects on the Perfomance of Steel Fiber Reinforced Concrete. *ACI Materials Journal*, 88(2), pp. 129-134.
- Soroushian, P. & Lee, C., 1990. Distribution and orientaion of fibres in steel fibre reinforced concrete. *ACI Materials Journal*, 87(5), pp. 433-439.
- Sparavigna, A. C., 2011. *Cornell University: Libary*. [Online] Available at: <http://arxiv.org/abs/1110.5230> [Accessed 4 November 2012].
- Stang, H. & Shah, S., 1986. Failure of Fiber Reinforced Composites by Pull-out Fracture. *Journal of Materials Science*, 21(3), pp. 953-957.
- Stroeven, P. & Hu, J., 2006. Effectiveness near boundaries of fibre reinforcement in concrete. *Materials and Structures*, Volume 39, pp. 1001-1013.

- 
- Sujivorakul, C., Waas, A. & Naaman, A., 2000. Pullout response of a smooth fiber with an end anchorage. *Journal of Engineering Mechanics*, 126(9), pp. 986-993.
- Swaddiwudhipong, S., Lu, H. & Wee, T., 2003. Direct tension test and tensile strain capacity of concrete at early age. *Cement and Concrete Research*, 33(12), pp. 2077-2084.
- Swamy, R., 1974. The technology of steel fibre reinforced concrete for practical applications. *Proceedings, Institution of Civil Engineers*, Volume 56, pp. 143-59.
- Swamy, R. & Jojagha, A., 1982. Workability of steel reinforced lightweight aggregate concrete. *The International Journal of cement composites and lightweight concrete*, 4(2), pp. 103-109.
- Swamy, R. & Mangat, P., 1974. Compactibility of steel fibre reinforced concrete. *Concrete*, 8(5), pp. 34-35.
- Swamy, R. & Mangat, P., 1974. Influence of fibre geometry on the properties of steel fiber reinforced concrete. *Cement and Concrete Research*, Volume 4, pp. 451-465.
- Swamy, R. & Stavrides, H., 1979. Influence of fiber reinforcement on restrained shrinkage and cracking. *ACI Journal*, Volume 75, pp. 443-460.
- Tan, K.-H., Paramasivam, P. & Tan, K.-C., 1995. Cracking Characteristics of Reinforced Steel Fiber Concrete Beams under Short- and Long-Term Loadings. *Advanced Cement Based Materials*, 2(4), pp. 127-137.
- Tan, K. & Saha, M., 2005. Ten year study on steel fibre -reinforced concrete beams under sustained loads. *ACI Structural Journal*, Volume 102, pp. 472-480.
- Tasderi & Karihaloo, 2001. *Effect of Type and Volume Fraction of Aggregate on the Fracture Properties of Concrete*. Cachan, France, Balkema, pp. 123-129.
- Tazawa, E.-i., Miyazawa, S. & Kasai, T., 1995. Chemical Shrinkage and Autogenous shrinkage of Hydrating Cement Past. *Cement and Concrete Research*, 25(2), pp. 288-292.
- Toutanji, H., EI-Korchi, T. & Katz, R. L. G., 1993. The behaviour of carbon fiber reinforced cement composites in direct tension. *Cement and Concrete Research*, 23(3), pp. 618-626.
- Trckova, J. & Prochazka, P., 2009. *Study on the influence of the number of metallic fibres in concrete volume element*. Singapore, CI-Primier PTE LTD.

- 
- Van Dijk, J. & Boardman, V., 1971. *Plastic Shrinkage Cracking of Concrete*. Haifa, Technion, pp. 225-239.
- van Mier, J., 1991. Mode I Fracture of Concrete: Discontinuous crack growth and crack interface grain bridging. *Cement and Concrete Research*, Volume 21, pp. 1-15.
- van Mier, J., 1997. *Fracture Processes of Concrete*. Boca Raton, Florida: CRC Press.
- van Mier, J. & van Vliet, M., 2002. Uniaxial tension test for determination of fracture parameters of concrete: State of the art. *Engineering Fracture Mechanics*, Volume 69, pp. 235-247.
- Vrech, S. et al., 2010. Meso- and Macroscopic Models for Fibre-Reinforced Concrete. *Computational modelling of concrete structures*, pp. 241-250.
- Wei, S., Mandel, J. & said, S., 1986. Study of the interfacial strength of steel fibre reinforced cement based composites. *ACI Journal*, Volume 83, pp. 597-605.
- Wille, K., EI-Tawil, S. & Naaman, A., 2014. Properties of strain hardening ultra high performance fiber reinforced concrete (UHP-FRC) under direct tensile loading. *Cement & Concrete Composites*, Volume 48, pp. 53-66.
- Wille, K. & Naaman, A. E., 2012. Pullout behavior of high-strength steel fibres embedded in ultra-high-performance concrete. *ACI MATERIALS JOURNAL*, 109(4), pp. 479-487.
- Wu, K.-R., Chen, B., Yao, W. & Zhang, D., 2001. Effect of Coarse Aggregate Type on Mechanical Properties of High-Performance Concrete. *Cement and Concrete Research*, 31(10), pp. 1421-1425.
- Yakut, A., 2004. Reinforced Concrete Frame Construction. *World Housing Encyclopedia-Summary Publication*, pp. 9-1.
- Yang, E. & Li, V., 2005. *Rate dependence in Engineered Cementitious Composites*. Hawaii, USA, Honolulu.
- Yanni, V. Y. G., 2009. *Multi-Scale Investigation of Tensile Creep of Ultra-High Performance Concrete for Bridge Applications*, Georgia Institute of Technology, Georgia: Unpublished PhD thesis.

- 
- Yazici, S., Inan, G. & Tabak, V., 2007. Effect of aspect ratio and volume fraction of steel fiber on the mechanical properties of SFRC. *Construction and Building Materials*, Volume 21, pp. 1250-1253.
- Zerbino, R. L. & Barragán, B. E., 2012. Long-Term Behavior of Cracked Steel Fiber-Reinforced Concrete Beams under Sustained Loading. *ACI Materials Journal*, 109(2), pp. 215-224.
- Zhandarov, S. & Mader, E., 2005. Charaterization of Fiber/Matrix Interface Strength: Applicability of Different tests, Approaches and Parameters. *Composites Science and Technology*, Volume 65, pp. 149-160.
- Zhang, J. & Li, V., 2001. Influences of fibers on drying shrinkage of fiber-reinforced cementitious composites. *Journal of Engineering Mechanics*, 127(1), pp. 37-44.
- Zhang, X. & Xu, S., 2007. Fracture Resistance on Aggregate Bridging Crack in Concrete. *Frontiers of Structural and Civil Engineering*, 1(1), pp. 63-70.
- Zhao, G., Prisco, M. & Vandewalle, L., 2014. Experimental investigation on uniaxial tensile creep behaviour of cracked steel fibre reinforced concrete. *Materials and Structures*, pp. 1-13.
- Zhou, F., 1992. *Time-dependent Crack Growth and Fracture in Concrete*, University of Lund, Sweden: Unpublished PhD thesis.

# APPENDIX I

---

## Experimental Quasi-Static Single Fibre Pull-out Results

### **I.1 Pull-out loading rate**

Presented in Figure I.1 are the pull-out load-slip responses for each specimen tested at the various pull-out loading rates for straight fibres.



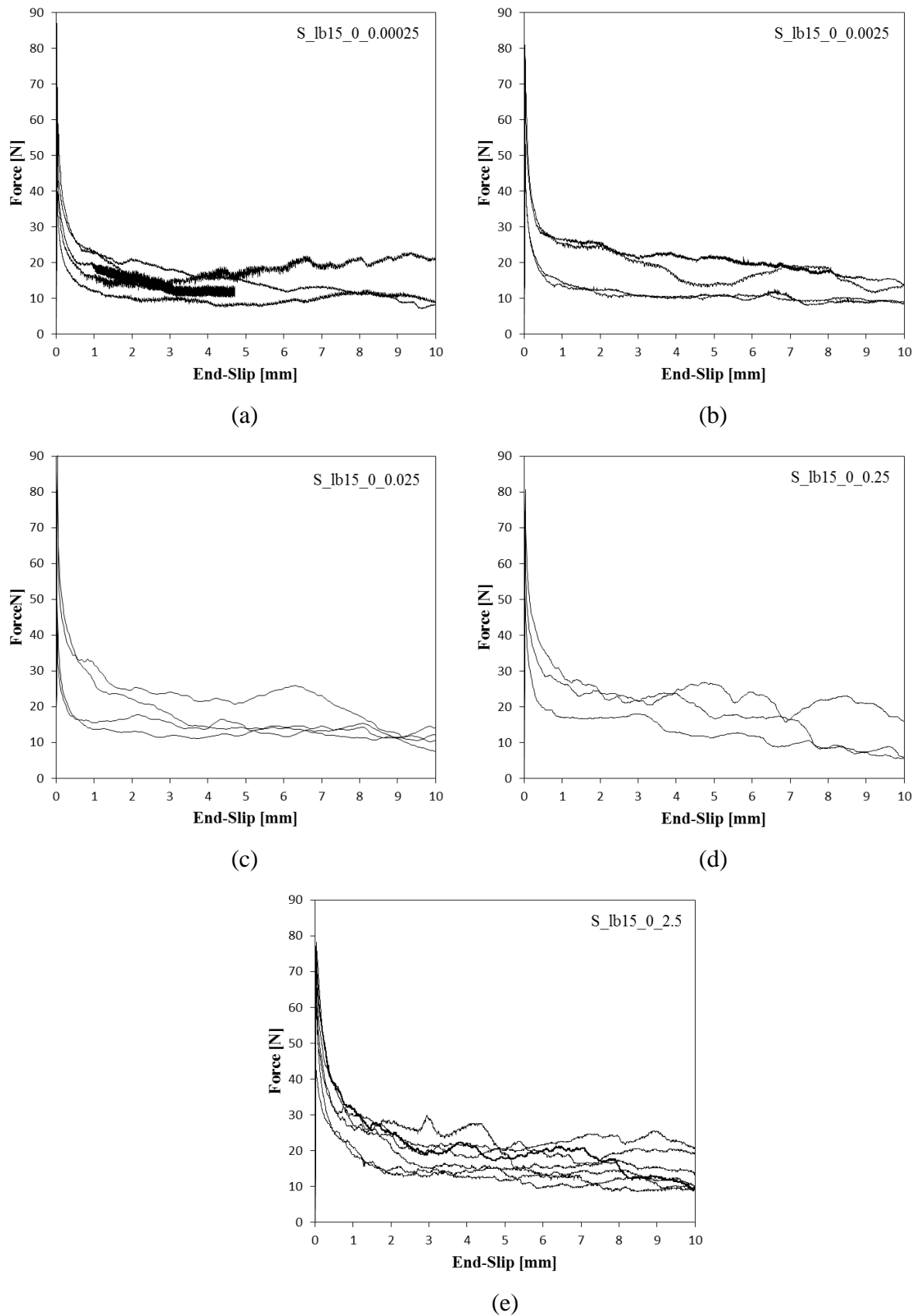


Figure I.1. Pull-out load-slip responses for straight fibres at various pull-out loading rates: (a) 0.00025 mm/s, (b) 0.0025 mm/s, (c) 0.025 mm/s, (d) 0.25 mm/s and (e) 2.5 mm/s

Presented in Figure I.2 are the pull-out load-slip responses for each specimen tested at the various pull-out loading rates for TYPE A hooked-end fibres.

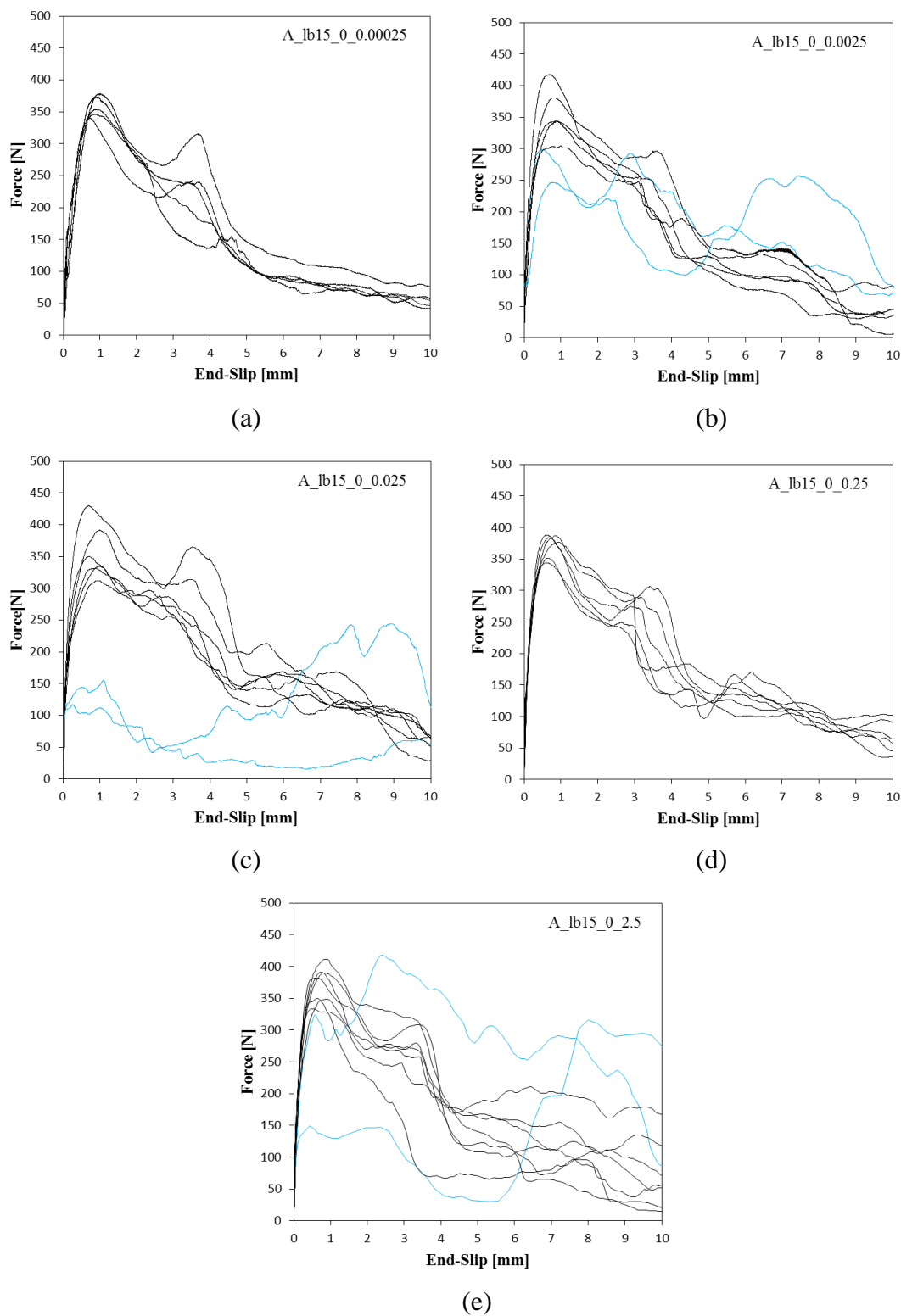


Figure I.2. Pull-out load-slip responses for TYPE A hooked-end fibres at various pull-out loading rates: (a) 0.00025 mm/s, (b) 0.0025 mm/s, (c) 0,025 mm/s, (d) 0.25 mm/s and (e) 2.5 mm/s

## I.2 Fibre embedment length

Presented in Figure I.3 are the pull-out load-slip responses for each specimen tested at the different embedment lengths for TYPE A hooked-end fibres.

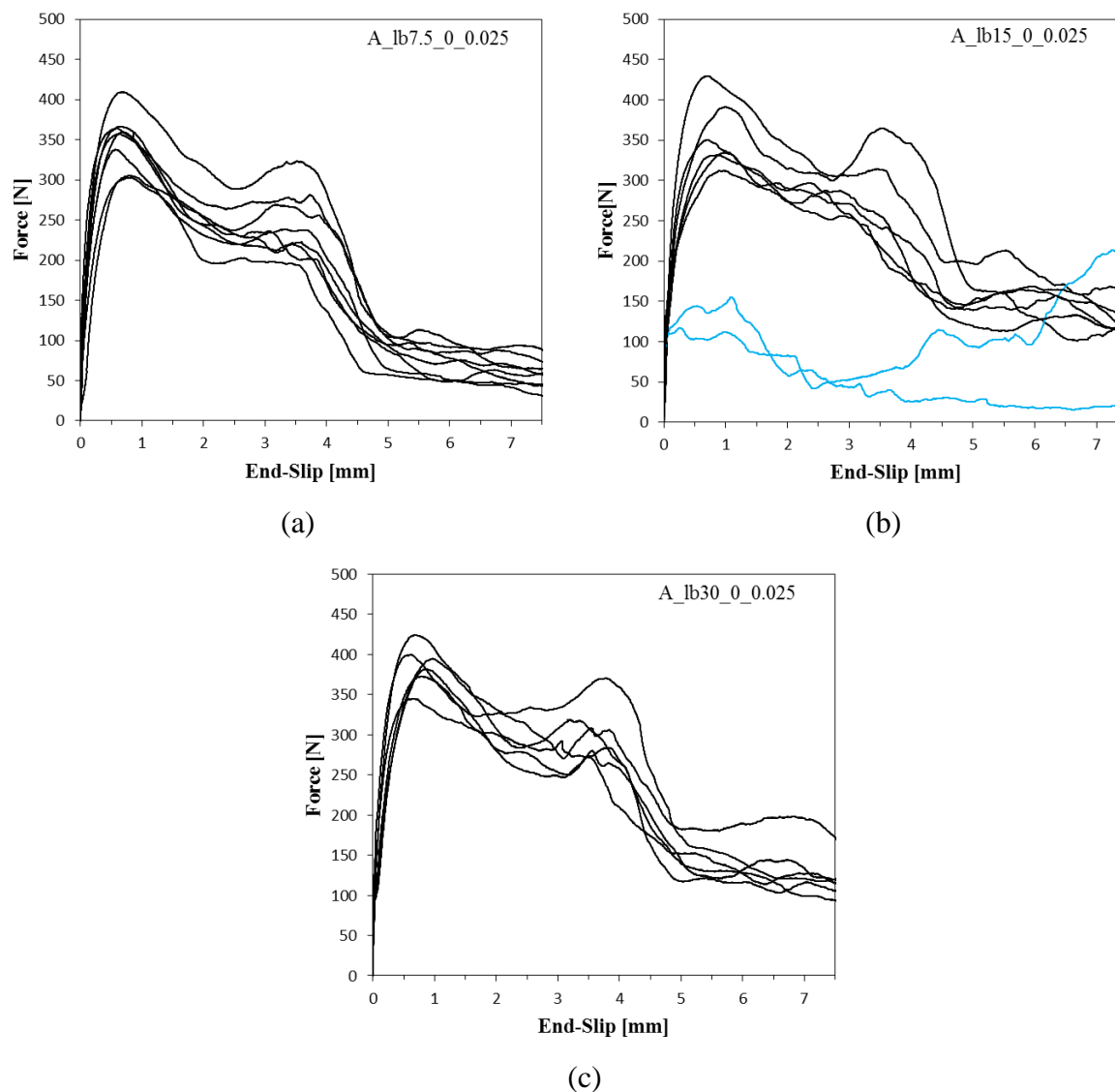


Figure I.3. Pull-out load-slip responses for TYPE A hooked-end fibres at different embedment lengths: (a) 7.5 mm, (b) 15 mm and (c) 30 mm

## I.3 Fibre inclination angle

Presented in Figure I.4 are the pull-out load-slip responses for each specimen tested at the different fibre embedment inclination angles for TYPE A hooked-end fibres.

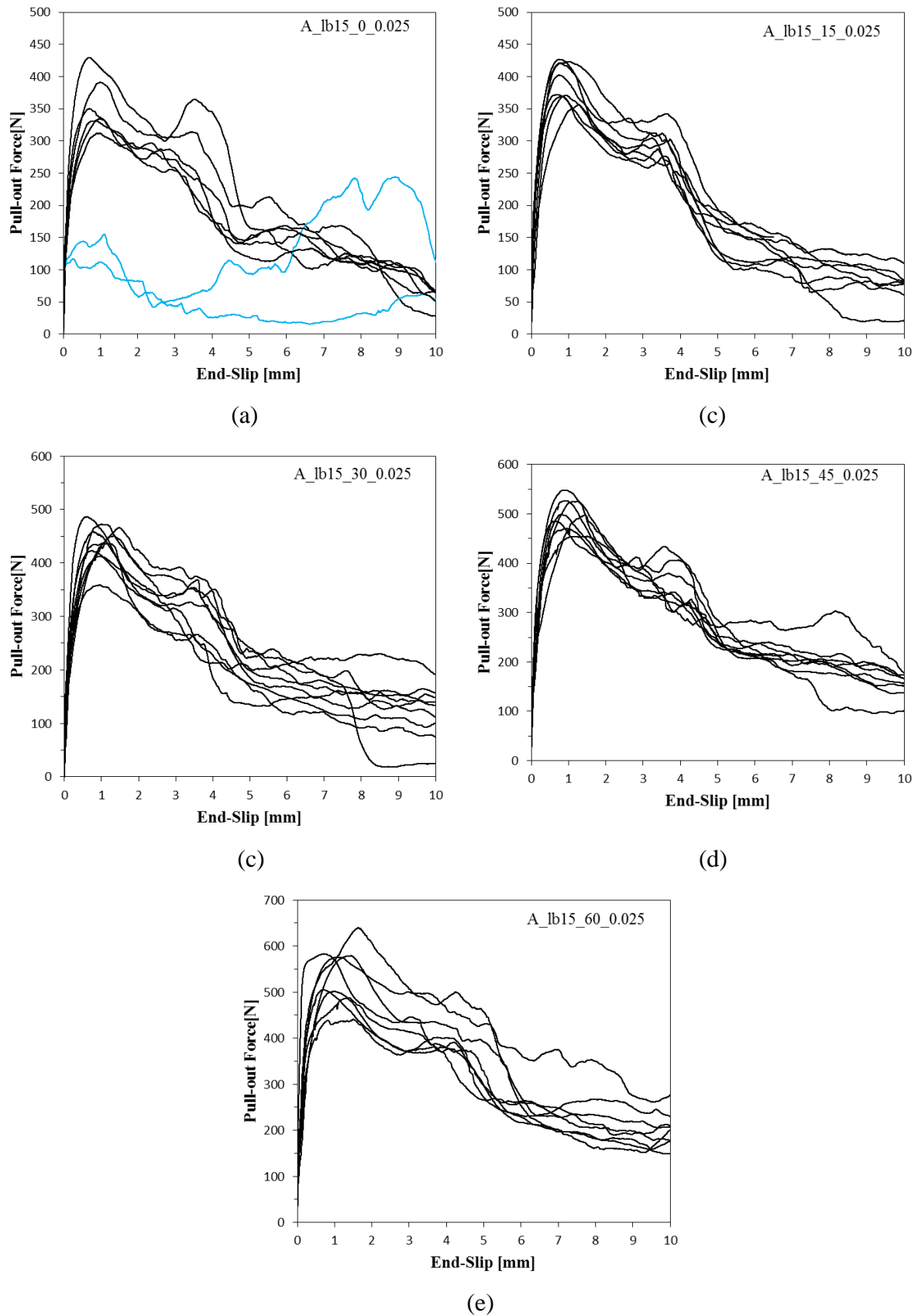


Figure I.4. Pull-out load-slip responses for TYPE A hooked-end fibres at different fibre embedment inclination angles: (a)  $0^\circ$ , (b)  $15^\circ$ , (c)  $30^\circ$ , (d)  $45^\circ$  and (e)  $60^\circ$

## I.4 Fibre mechanical anchorage

Presented in Figure I.5 are the pull-out load-slip responses for each specimen tested with different fibre mechanical anchorages.

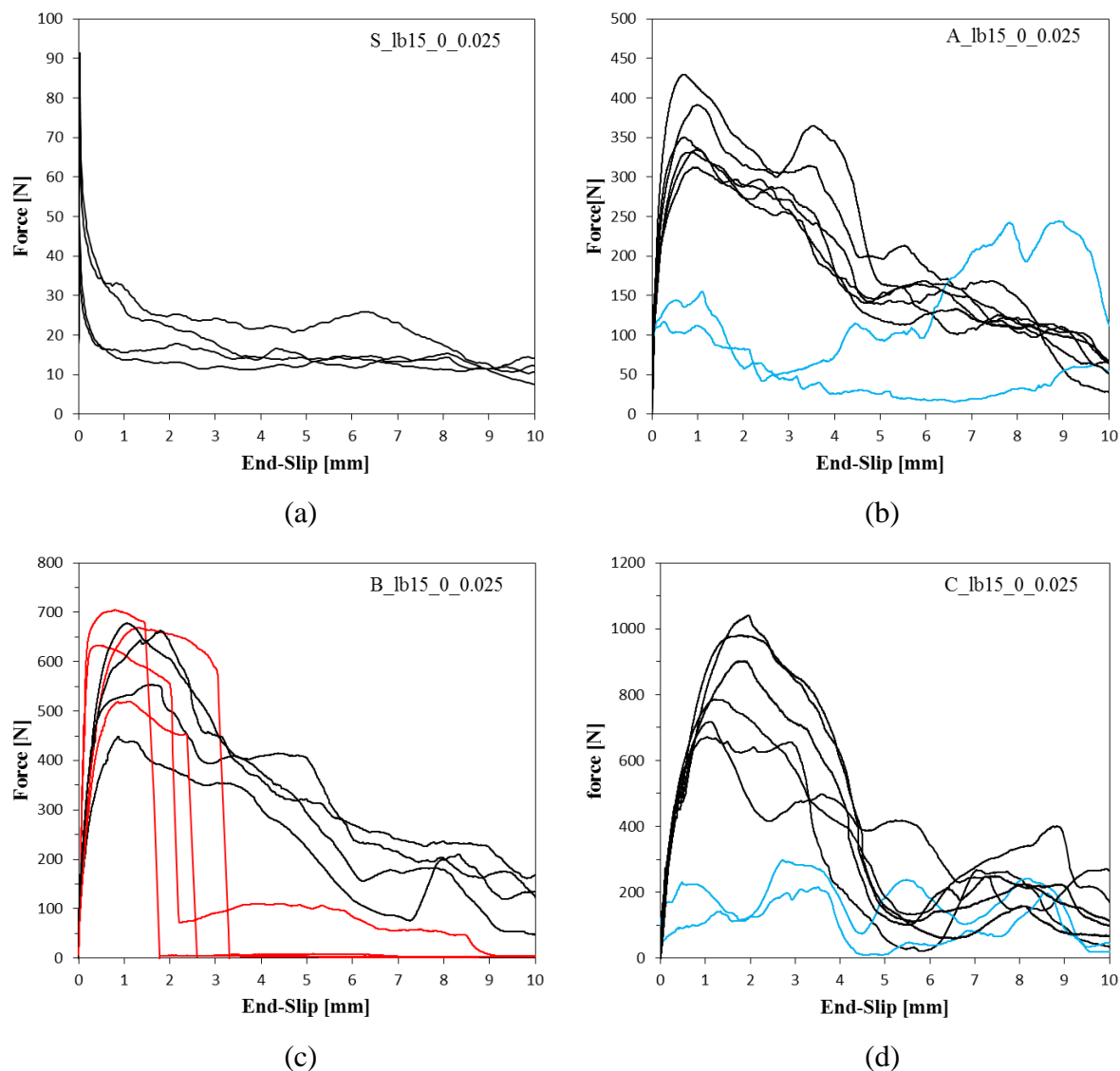


Figure I.5. Pull-out load-slip responses for different fibre mechanical anchorages: (a) straight fibres, (b) TYPE A hooked-end fibres, (c) TYPE B hooked-end fibres and (d) TYPE C hooked-end fibres

# APPENDIX II

---

## Experimental Single Fibre Pull-out Creep Results

### **II.1 Applied sustained load**

Presented in Figure II.1 are the pull-out creep-time responses at the different applied sustained load levels for TYPE A hooked-end fibres.

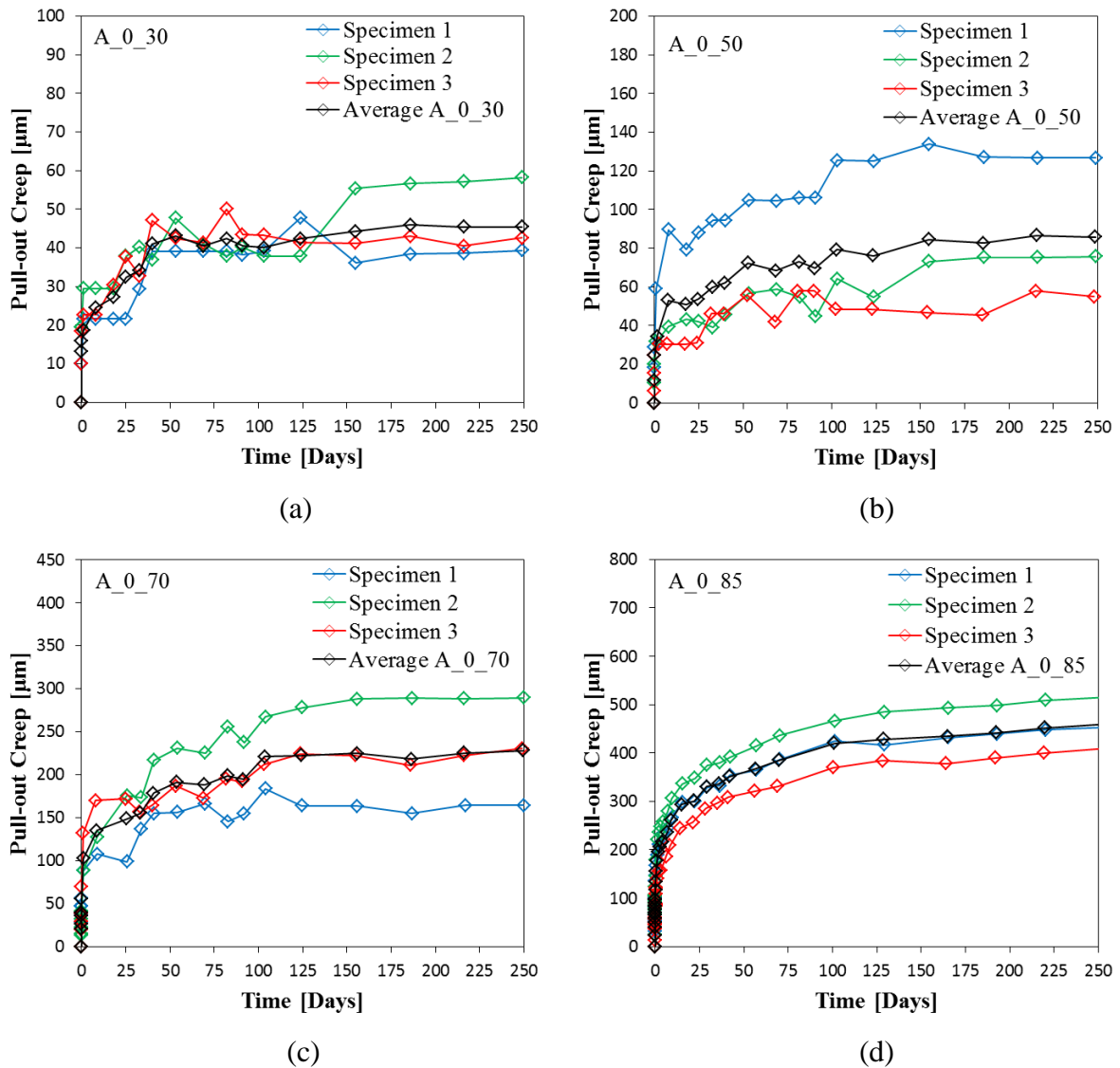


Figure II.1. Pull-out creep-time responses for TYPE A hooked-end fibres at different applied sustained load levels: (a) 30 %, (b) 50 %, (c) 70 % and (d) 85 %

## II.2 Fibre inclination angle

Presented in Figure II.2 are the pull-out creep-time responses for different fibre embedment inclination angles for TYPE A hooked-end fibres.

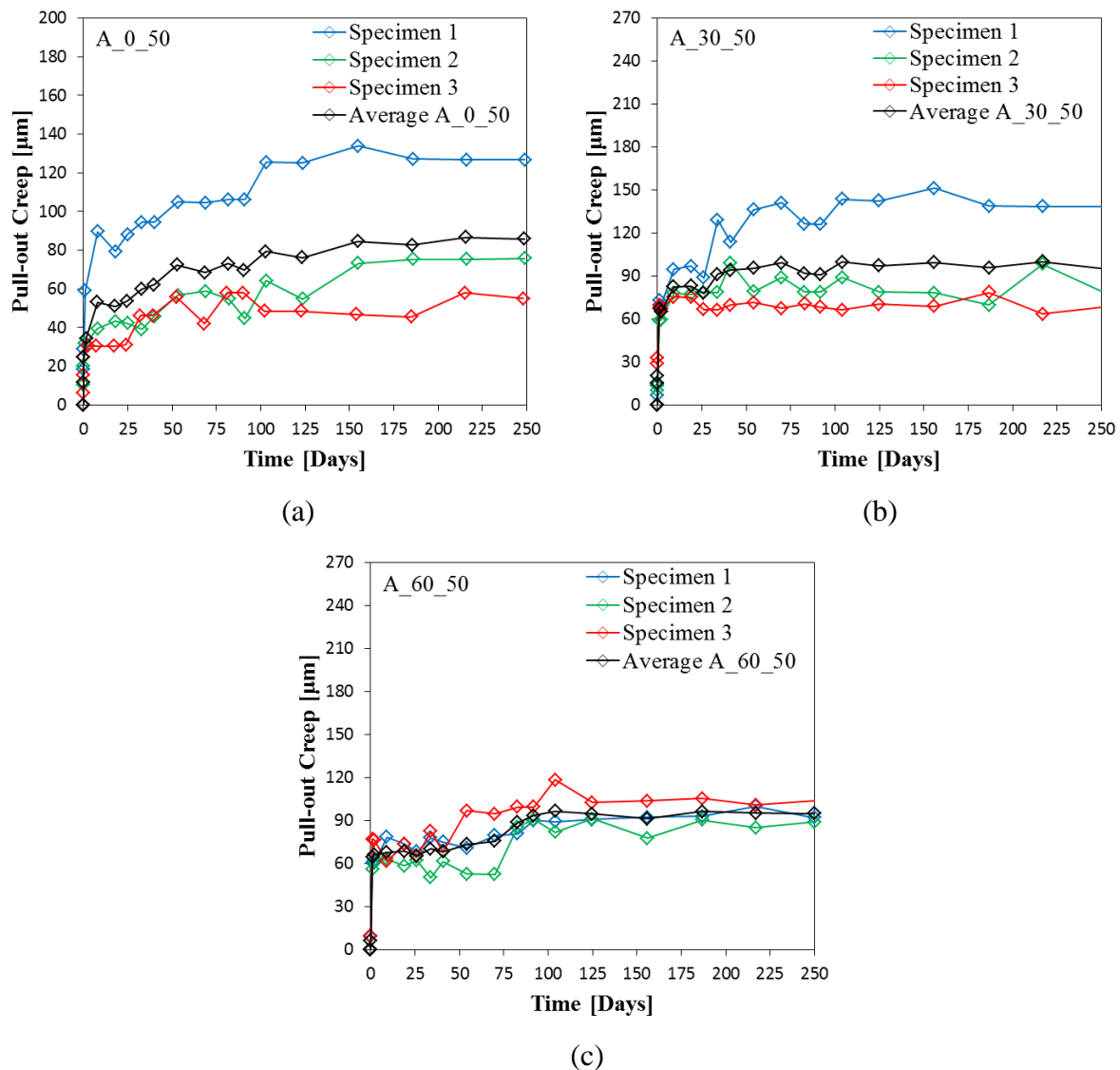


Figure II.2. Pull-out creep-time responses for TYPE A hooked-end fibres embedded at different fibre inclination angles: (a)  $0^\circ$ , (b)  $30^\circ$  and (c)  $60^\circ$

### II.3 Fibre mechanical anchorage

Presented in Figure II.3 are the pull-out creep-time responses for different fibre mechanical anchorages.



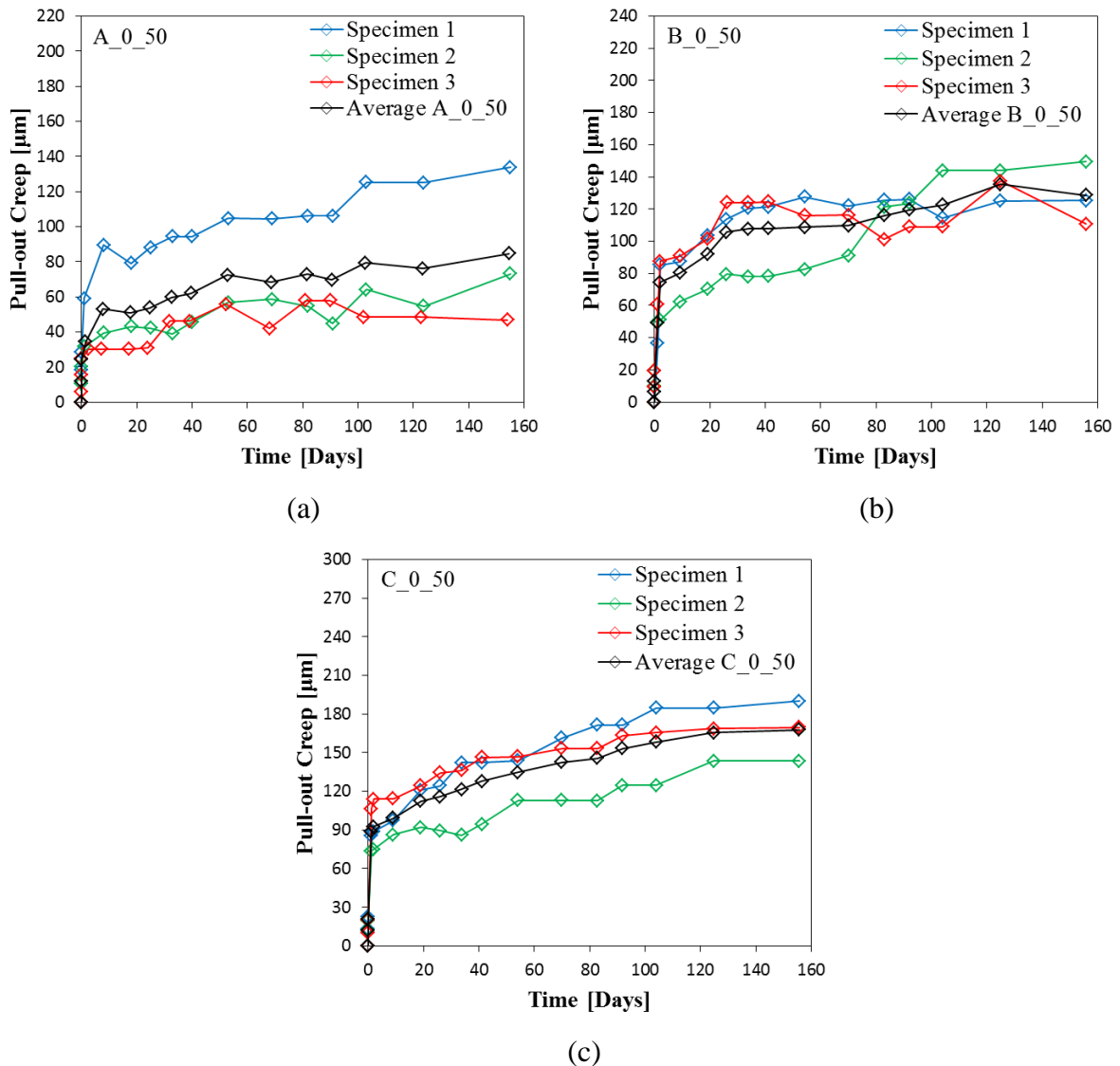


Figure II.3. Pull-out creep-time responses for different fibre mechanical anchorages: (a) TYPE A hooked-end, (b) TYPE B hooked-end and (c) TYPE C hooked-end

## II.4 Pre-damage sustained load tests

Presented in Figure II.4 are the pull-out creep-time responses for pre-damaged TYPE A hooked-end fibres.

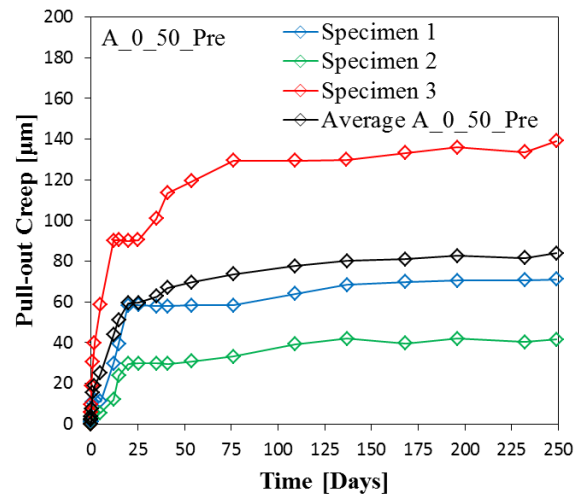


Figure II.4. Pull-out creep-time responses for pre-damaged TYPE A hooked-end fibres